

COMPUTATIONAL MODELING STUDIES OF COBALT PENTLANDITE (Co₉S₈)

By

Mofuti Amos Mehlape

THESIS

Submitted in fulfilment of the requirements for the degree of

Doctor of Philosophy (PhD)

in

Physics

in the

Faculty of Science and Agriculture,

(School of Physical and Mineral Sciences)

at the

UNIVERSITY OF LIMPOPO (Turffloop Campus)

SUPERVISOR: PROF. P.E. NGOEPE

Co-SUPERVISOR: PROF. S.C. PARKER

2013

Declaration

I declare that the thesis hereby submitted to the University of Limpopo (Turfloop Campus) for the degree of Doctor of Philosophy (PhD) has not been previously submitted by me for a degree at this or any other university; that this is my work in design and in execution, and that all material contained herein has been duly acknowledged.

Mehlape M.A.

Date

Abstract

The intention of the current study is to investigate structure, ion transport and reactivity of various forms of the cobalt pentlandite, Co_9S_8 , at different temperatures using atomistic simulation methods with the support of electronic structure calculations. The first interatomic potentials of Co_9S_8 were derived with input data as structure and elastic properties from experiment and electronic structure calculations respectively. The potentials were validated by running energy minimization and molecular dynamics calculations. Structure, elastic properties and phonon spectra were well reproduced, together with the complex high temperature transformations and melting of Co_9S_8 as deduced from crystal structure, radial distribution functions, density profiles and diffusion coefficients.

Amongst the high symmetry surfaces $\{111\}$, $\{101\}$ and $\{100\}$ atomistic surface energy calculations proposed the $\{111\}$ surface of Co_9S_8 as the most stable in agreement with experimental morphologies, and water adsorption energies on the such surfaces which mostly agreed with those from electronic structure calculations. The structural and ion transport variations with temperature were investigated and predicted surface melting at lower temperatures than the bulk. The effects of hydration on the surfaces at low and high temperatures were also studied.

The structural and ion transport properties of Co_9S_8 nanoparticles of varying sizes, covered by high symmetry surfaces $\{111\}$, $\{101\}$ and $\{100\}$ were predicted using molecular dynamics method based on our derived interatomic potentials. The

structural and ion transport properties of Co_9S_8 nanoparticles of varying sizes, covered by high symmetry surfaces $\{111\}$, $\{101\}$ and $\{100\}$ were predicted using molecular dynamics method based on our derived interatomic potentials. Generally for $\{111\}$, $\{101\}$ nanoparticles, high temperature transitions were abrupt for smaller nanoparticles and these tended to disintegrate and form voids. However, for larger nanoparticles the transitions were more gradual. Transitions in the $\{100\}$ bound nanoparticles were less dramatic for all sizes and the formation of voids was reduced at high temperatures. Generally, the melting temperatures of different sizes of nanoparticles increases with the particle size hence approach the bulk limit. The interaction of nanoparticles with water was investigated.

Acknowledgements

I would like to thank my supervisor, Professor P.E. Ngoepe and co-supervisor Professor S.C. Parker, for the support, patience and guidance throughout this project. Thanks must also go to my colleagues at the Materials Modelling Centre (University of Limpopo), and members of The Parker group at the University of Bath, UK for the help and fruitful discussions during my visits in 2008 and 2010.

I would like to acknowledge the Anglo Platinum, National Research Foundation (South Africa), and The Royal Society (UK) for their financial support. The Centre for High Performance Computing (CHPC) is acknowledged for the provision of computer resources.

Studying for PhD is not always easy. Many times the excitement of getting encouraging results comes with many failed efforts. Hard work and persistence are not really enough. With stress, tiredness and sense of giving up taking its toll, it is important to get the support, encouragement and understanding. I was fortunate that my family and friends provided these in abundance. To all of them I am grateful.

Finally, my son *Matome* who unknowingly allowed me to be away from him for extended periods and also his mom for taking care of him during my absence.

Dedications

Dedicated:

To my son: *Matome*,

My mom: *Henrietta* and

My sisters: *Stella* and *Maite*

Table of contents

Abstract.....	i
Acknowledgements	iii
List of Figures.....	viii
List of Tables	xviii
Chapter 1: Introduction	1
1.1. General Background	1
1.2. Literature Review.....	3
1.2.1. Experimental Studies	3
1.2.2. Computer Simulation Studies	6
1.2.3. Nanoparticles Study of Co_9S_8	8
1.3. Structural Aspects of Pentlandite, Co_9S_8	10
1.4. Rationale of the Study.....	12
1.5. Objectives of the Study	14
1.6. Outline of the Study	14
Chapter 2: Theoretical Studies and Computational Methods	16
2.1. Atomistic Simulation	16
2.1.1. Energy Minimisation	17
2.1.2. Molecular Dynamics.....	21
2.1.3. Surface Energy Calculations.....	32
2.3. Crystal Morphology	38
Chapter 3: Computational Models for Co_9S_8.....	40
3.1. Quantum Mechanical Methods	40

3.1.1 Many-Body Schrödinger Equation	40
3.1.2. Born-Oppenheimer Approximation	42
3.1.3. Density Functional Theory	42
3.1.4. Approximation Exchange Correlation Functional	43
3.1.5. Convergence for Bulk Co_9S_8	44
3.2. Atomistic Potential Model	47
3.2.1. The Born Model of Solids.....	48
3.2.2. Long Range Interactions	49
3.2.3. Short Range Interactions.....	52
3.3. Derivation of Interatomic Potentials	56
3.4. The Atomistic Potentials Used In This Work	57
3.5. Validation of the Atomistic Potentials Model.....	63
3.5.1. Structural and Elastic Properties	63
3.5.2. Phonon Calculations of Co_9S_8	67
3.5.3. X-Ray Diffraction Pattern.....	73
Chapter 4: Structure and Stability of Bulk and Surfaces of Co_9S_8 ...	75
4.1. MD study of bulk Co_9S_8	75
4.2. Surfaces of Co_9S_8	85
4.2.1 Surface Energy Calculations.....	86
4.2.2. Crystal Morphology	89
4.2.3. MD study of Co_9S_8 Surfaces	91
4.2.3.1. {111} Surface.....	91
4.2.3.2. {101} Surface.....	95
4.2.3.3. {100} Surface.....	99
4.2.4. Interaction of Water with the Surfaces of Co_9S_8	104

4.2.4.1 {111} Co ₉ S ₈ Surface	105
4.2.4.2. {101} Co ₉ S ₈ Surface	110
4.2.4.3. {100} Co ₉ S ₈ Surface	115
Chapter 5: The Structure and Stability of Co₉S₈ Nanoparticles.....	121
5.1. Construction of nanoparticles	124
5.2. Effect of Size on Melting Temperature of Co ₉ S ₈ Nanoparticles	125
5.2.1. Surface {111} Co ₉ S ₈ nanoparticle	126
5.2.2. Surface {101} Co ₉ S ₈ nanoparticle	140
5.2.3. Surface {100} Co ₉ S ₈ nanoparticle	152
5.3. Co ₉ S ₈ Nanoparticle in Pure water	166
Chapter 6: Conclusions and Recommendations	171
6.1. Conclusions.....	171
6.2. Recommendations.....	174
References	176
Appendix A	197
Appendix B	198
Appendix C	200

List of Figures

Figure 1.1: A picture of pentlandite rich in cobalt [8].	2
Figure 1.2: Conventional unit cell (on the left hand side) and primitive unit cell (on the right hand side) of pentlandite structure (Co_9S_8). Blue and yellow spheres represent cobalt (Co) and sulphur (S) atoms respectively.	11
Figure 2.1: Schematic representation of the radial distribution function.....	28
Figure 2.2: Example of a Cobalt-Sulphur RDF in a crystalline solid on the left and in a liquid phase on the right.....	28
Figure 2.3: Schematic representation of the periodic boundary conditions where the simulation cell is highlighted in bold. [52].	31
Figure 2.4: The two region approach used in METADISE, the left hand case for a complete crystal unit (BULK) and the right hand case a half crystal exposing a surface [56].	34
Figure 2.5: Three types of stacking sequences described by Tasker [70] and the reconstructed type III by Oliver et al, 1993 [71].	37
Figure 2.6: Schematic representation of equilibrium morphology due to two faces with equal specific free energy in two dimensions.	39
Figure 3.1: The graph of total energy against K points for the chosen cut off of 700 eV.	46
Figure 3.2: The graph of total energy against plane wave cut off energy for different k-points.	46
Figure 3.3: Schematic representation of the shell model.	55
Figure 3.4: The total density of states of bulk Co_9S_8	59
Figure 3.3: Cubic unit cell of bulk Co_9S_8	63
Figure 3.4: Phonon DOS and dispersion curve of Co_9S_8 phase.	68

Figure 3.5: The primitive unit cell of Co_9S_8 . Co1 (O) is octahedral type 1 cobalt; Co2 (T) is tetrahedral type 2 cobalt; S1 (l) is linking type 1 sulphurs; S2 (f) is face-capping type sulphurs.	69
Figure 3.6: A comparison of the total phonon densities of states (DOS) of Co_9S_8 calculated using a) ab initio method with the VASP code and b) our derived interatomic potentials using the GULP program.	70
Figure 3.7: Phonon density of states for different types of cobalt and sulphur in a Co_9S_8 phase and the total DOS.	71
Figure 3.8: Heat capacity C_v as a function of temperature for Co_9S_8 phase using VASP code.....	72
Figure 3.9: X-Ray diffraction patterns of Co_9S_8 bulk structure for a) this work and b) experimental [11].....	74
Figure 4.1: The 3x3x3 supercell of Co_9S_8 bulk structure used in the MD calculations.	77
Figure 4.3: The total energy variation with temperature for Co_9S_8 bulk structure.	79
Figure 4.4: Radial distribution functions of the Co_9S_8 bulk structure at different temperatures.....	80
Figure 4.5: The total radial distribution functions of the Co_9S_8 bulk structure at different temperatures.	81
Figure 4.6: Snapshots of MD simulation at different temperatures for Co_9S_8 bulk structure.....	83
Figure 4.7: Total Mean square displacements (MSD) as a function of time for the Co_9S_8 bulk structure at different temperatures.....	84
Figure 4.8: Diffusion coefficient as a function of temperature for Co_9S_8 bulk structure.....	84

Figure 4.9: Top view of the adsorption site of adsorbed water on a) {111}, b) {100} and c) {101} Co ₉ S ₈ surfaces. Purple, yellow, red, white spheres are cobalt, sulphur, oxygen, and hydrogen atoms, respectively.	89
Figure 4.10: Morphology of Co ₉ S ₈ showing a) {111}, b) {100} and c) {101} surfaces.....	90
Figure 4.11: The experimental morphology of the {111} facet [15]......	91
Figure 4.12: The different views of the {111} surface of Co ₉ S ₈ a) side view and b) top view. The cobalt and sulphur atoms are represented by purple and yellow balls respectively.	92
Figure 4.13: Average diffusion coefficients of Co and S as a function of temperature for the slab constituting the {111} surface of Co ₉ S ₈	92
Figure 4.14: RDFs of the Co-Co, Co-S and S-S pairs for the {111} surface of Co ₉ S ₈ at various temperatures.	94
Figure 4.15: Density profiles of {111} Co ₉ S ₈ surface for cobalt (Co) and sulphur (S) at various temperatures.	94
Figure 4.16: Snapshots of MD simulation at a) 300 and b) 800K for the {111} surface of Co ₉ S ₈	95
Figure 4.17: The different views of the {101} surface of Co ₉ S ₈ a) side view and b) top view. The cobalt and sulphur atoms are represented by purple and yellow balls respectively.	96
Figure 4.18: Average diffusion coefficients of Co and S as a function of temperature for the slab constituting the {101} surface of Co ₉ S ₈	96
Figure 4.19: RDFs of the Co-Co, Co-S and S-S pairs for the {101} surface of Co ₉ S ₈ at various temperatures.	97

Figure 4.20: Density profiles of Co_9S_8 {101} surface for cobalt (Co) and sulphur (S) at various temperatures.	98
Figure 4.21: Snapshots of MD simulation at a) 300K and b) 900K for the {101} surface of Co_9S_8	99
Figure 4.22: The side view of the {100} surface of Co_9S_8 . The cobalt and sulphur atoms are represented by purple and yellow balls respectively.	100
Figure 4.23: Average diffusion coefficients of Co and S as a function of temperature for the slab constituting the {100} surface of Co_9S_8	101
Figure 4.24: RDFs of the Co-Co, Co-S and S-S pairs for the {100} surface of Co_9S_8 at various temperatures.	102
Figure 4.25: Density profiles of the Co_9S_8 {100} surface for cobalt (Co) and sulphur (S) at various temperatures.	102
Figure 4.26: Snapshots of MD simulation at a) 300K and b) 900K for a {100} surface of Co_9S_8	103
Figure 4.27: Snapshot of the initial configuration of interaction of water with {111} surface of Co_9S_8	105
Figure 4.28: Total energy variation as a function of temperature for {111} surface Co_9S_8 in water.	106
Figure 4.29: A temperature dependence of ion average diffusion coefficients on the slab constituting the {111} surface in contact with water.	107
Figure 4.31: Density profile of cobalt (Co) and sulphur (S) atoms at indicated temperatures for the {111} surface of Co_9S_8	109
Figure 4.32: Snapshots of the MD simulation for interaction of water with {111} surface of Co_9S_8 at a) 300K and b) 1050K.	110
Figure 4.34: Initial structure of interaction of water with {101} surface of Co_9S_8 . ..	111

Figure 4.35: Total energy as a function of temperature for {101} surface.....	111
Figure 4.36: Temperature dependence of the average diffusion coefficients of Co and S on the slab constituting the {101} surface with water, for Co ₉ S ₈	112
Figure 4.37: Radial distribution functions (RDFs) of Co-Co, Co-S and S-S pairs for {101} surface of Co ₉ S ₈ in contact with water at different temperatures.	113
Figure 4.38: Density profile of cobalt (Co) and sulphur (S) atoms of Co ₉ S ₈ at indicated temperatures for the {101} surface.	114
Figure 4.39: Snapshots of the MD simulation of interaction of water with {101} surface of Co ₉ S ₈ at a) 300K and b) 1000K.	114
Figure 4.40: Initial configuration of slab in contact with water of {100} surface for Co ₉ S ₈	115
Figure 4.41: Total energy as a function of temperature for {100} surface of Co ₉ S ₈ in contact with water.	116
Figure 4.42: Temperature dependence of the average diffusion coefficients of Co and S on the slab constituting the {100} surface of Co ₉ S ₈ in contact with water. ...	117
Figure 4.43: Radial Distribution functions of Co-Co, Co-S and S-S pairs of the {100} surface of Co ₉ S ₈ in contact with water at different temperatures.	118
Figure 4.44: Density profile of cobalt (Co) and sulphur (S) atoms of Co ₉ S ₈ in contact with water at indicated temperatures for the {100} surface.	119
Figure 4.45: Snapshots of the MD simulation of interaction of water with {100} surface of Co ₉ S ₈ at 300K and 850K.....	119
Figure 5.1: The predicted crystal morphologies together with the surface energies of {111}, {100} and {101} Miller indices.	125

Figure 5.2: Total energy variation with temperature for the {111} terminated Co_9S_8 nanoparticle with a) 342 atoms, b) 708 atoms, c) 1394 atoms and d) 2422 atoms.	128
Figure 5.3: Diffusion coefficients as a function of temperature for {111} terminated Co_9S_8 nanoparticle with a) 342 atoms, b) 708 atoms, c) 1394 atoms and d) 2422 atoms.	129
Figure 5.4: The RDFs of Co-Co, Co-S and S-S pairs for a {111} terminated Co_9S_8 nanoparticle with 342 atoms at the indicated temperatures.	130
Figure 5.5: The RDFs of Co-Co, Co-S and S-S pairs for a {111} terminated Co_9S_8 nanoparticle with 708 atoms at the indicated temperatures.	131
Figure 5.6: The RDFs of Co-Co, Co-S and S-S pairs for a {111} terminated Co_9S_8 nanoparticle with 1394 atoms at the indicated temperatures.	132
Figure 5.7: The RDFs of Co-Co, Co-S and S-S pairs for a {111} terminated Co_9S_8 nanoparticle with 2422 atoms at the indicated temperatures.	133
Figure 5.8: Atomic density profiles of {111} terminated Co_9S_8 nanoparticle with 342 atoms for cobalt (Co) and sulphur (S) at various temperatures.	134
Figure 5.9: Atomic density profiles of {111} terminated Co_9S_8 nanoparticle with 708 atoms for cobalt (Co) and sulphur (S) at various temperatures.	134
Figure 5.10: Atomic density profiles of {111} terminated Co_9S_8 nanoparticle with 1394 atoms for cobalt (Co) and sulphur (S) at various temperatures.	135
Figure 5.11: Atomic density profiles of {111} terminated Co_9S_8 nanoparticle with 2422 atoms for cobalt (Co) and sulphur (S) at various temperatures.	135
Figure 5.12: The initial configuration on the left and the structure at melting point on the right of the Co_9S_8 nanoparticle of {111} surface with 342 atoms. Purple, yellow spheres represent cobalt (Co), sulphur (S) atoms respectively.	136

Figure 5.13: The initial configuration on the left and the structure at melting point on the right of the Co_9S_8 nanoparticle of {111} surface with 708 atoms. Purple, yellow spheres represent cobalt (Co), sulphur (S) atoms respectively. 136

Figure 5.14: The initial configuration on the left and the structure at melting point on the right of the Co_9S_8 nanoparticle of {111} surface with 1394 atoms. Purple, yellow spheres represent cobalt (Co), sulphur (S) atoms respectively. 137

Figure 5.15: The initial configuration on the left and the structure at melting point on the right of the Co_9S_8 nanoparticle of {111} surface with 2422 atoms. Purple, yellow spheres represent cobalt (Co), sulphur (S) atoms respectively. 137

Figure 5.16: Radial distribution functions of Co_9S_8 {111} nanoparticle at 300K for the Co-Co, Co-S and S-S pairs for different number of atoms and bulk pairs. 138

Figure 5.17: Total energy as a function of nanoparticle size for surface {111} Co_9S_8 nanoparticle at 300 K, 700 K, 900 K and 1100 K..... 139

Figure 5.17 shows the approximate change in total energy versus nanoparticle size in nanometres. From the figure it is evident that as the nanoparticle size decreases the energy becomes more positive. As expected, the stability of nanoparticle is enhanced as the number of atoms increase. 140

Figure 5.18: Total energy variation with temperature for the {101} terminated Co_9S_8 nanoparticle with a) 360 atoms, b) 748 atoms, c) 1324 atoms and d) 2480 atoms. 141

Figure 5.19: Diffusion Coefficients as a function of temperature for {101} terminated Co_9S_8 nanoparticle with a) 360 atoms, b) 748 atoms, c) 1324 atoms and d) 2480 atoms. 142

Figure 5.20: The RDFs of Co-Co, Co-S and S-S pairs for a {101} terminated Co_9S_8 nanoparticle with 360 atoms at the indicated temperatures. 143

Figure 5.21: The RDFs of Co-Co, Co-S and S-S pairs for a {101} terminated Co_9S_8 nanoparticle with 748 atoms at the indicated temperatures.	144
Figure 5.22: The RDFs of Co-Co, Co-S and S-S pairs for a {101} terminated Co_9S_8 nanoparticle with 1324 atoms at the indicated temperatures.	145
Figure 5.23: The RDFs of Co-Co, Co-S and S-S pairs for a {101} terminated Co_9S_8 nanoparticle with 2480 atoms at the indicated temperatures.	146
Figure 5.24: Density profiles of the {101} terminated Co_9S_8 nanoparticle with 360 atoms for cobalt (Co) and sulphur (S) at various temperatures.	147
Figure 5.25: Density profiles of the {101} terminated Co_9S_8 nanoparticle with 748 atoms for cobalt (Co) and sulphur (S) at various temperatures.	147
Figure 5.26: Density profiles of the {101} terminated Co_9S_8 nanoparticle with 1324 atoms for cobalt (Co) and sulphur (S) at various temperatures.	148
Figure 5.27: Density profiles of the {101} terminated Co_9S_8 nanoparticle with 2480 atoms for cobalt (Co) and sulphur (S) at various temperatures.	148
Figure 5.28: The initial configuration on the left and the structure at melting on the right of the Co_9S_8 nanoparticle of {101} surface with 360 atoms. Purple, yellow spheres represent cobalt (Co), sulphur (S) atoms respectively.	149
Figure 5.29: The initial configuration on the left and the structure at melting on the right of the Co_9S_8 nanoparticle of {101} surface with 748 atoms. Purple, yellow spheres represent cobalt (Co), sulphur (S) atoms respectively.	149
Figure 5.30: The initial configuration on the left and the structure at melting on the right of the Co_9S_8 nanoparticle of {101} surface with 1324 atoms. Purple, yellow spheres represent cobalt (Co), sulphur (S) atoms respectively.	150

Figure 5.31: The initial configuration on the left and the structure at melting on the right of the Co_9S_8 nanoparticle of $\{101\}$ surface with 2480 atoms. Purple, yellow spheres represent cobalt (Co), sulphur (S) atoms respectively.	150
Figure 5.32: Total energy as a function of nanoparticle size for surface $\{101\}$ Co_9S_8 nanoparticle at 300K, 700K, 900K and 1100K.....	151
Figure 5.33: Total energy variation with temperature for $\{100\}$ surface Co_9S_8 nanoparticle with a) 442 atoms, b) 682 atoms, c) 1592 atoms and d) 2638 atoms.	153
Figure 5.34: Diffusion coefficients as a function of temperature for $\{100\}$ surface Co_9S_8 nanoparticle with a) 442 atoms, b) 682 atoms, c) 1592 atoms and d) 2638 atoms.	154
Figure 5.35: : The RDFs of Co-Co, Co-S and S-S pairs for a $\{100\}$ terminated Co_9S_8 nanoparticle with 442 atoms at the indicated temperatures.	156
Figure 5.36: The RDFs of Co-Co, Co-S and S-S pairs for a $\{100\}$ terminated Co_9S_8 nanoparticle with 682 atoms at the indicated temperatures.	157
Figure 5.37: The RDFs of Co-Co, Co-S and S-S pairs for a $\{100\}$ terminated Co_9S_8 nanoparticle with 1592 atoms at the indicated temperatures.	158
Figure 5.38: The RDFs of Co-Co, Co-S and S-S pairs for a $\{100\}$ terminated Co_9S_8 nanoparticle with 2638 atoms at the indicated temperatures.	158
Figure 5.39: Atomic density profiles along the nanoparticle axis for Co and S atoms in $\{100\}$ terminated Co_9S_8 nanoparticle with 442 atoms at temperatures leading up to melting.	159
Figure 5.41: Atomic density profiles along the nanoparticle axis for Co and S atoms in $\{100\}$ terminated Co_9S_8 nanoparticle with 1592 atoms at temperatures leading up to melting.	160

Figure 5.43: The initial configuration on the left and the structure at melting on the right of the Co_9S_8 nanoparticle of $\{100\}$ surface with 442 atoms. Purple, yellow spheres represent cobalt (Co), sulphur (S) atoms respectively.	162
Figure 5.44: The initial configuration on the left and the structure at melting on the right of the Co_9S_8 nanoparticle of $\{100\}$ surface with 682 atoms. Purple, yellow spheres represent cobalt (Co), sulphur (S) atoms respectively.	162
Figure 5.45: The initial configuration on the left and the structure at melting on the right of the Co_9S_8 nanoparticle of $\{100\}$ surface with 1592 atoms. Purple, yellow spheres represent cobalt (Co), sulphur (S) atoms respectively.	163
Figure 5.46: The initial configuration on the left and the structure at melting on the right of the Co_9S_8 nanoparticle of $\{100\}$ surface with 2638 atoms	163
Figure 5.47: Total energy as a function of nanoparticle size for $\{100\}$ terminated Co_9S_8 nanoparticle at 300, 700, 900 and 1100 K.....	164
Figure 5.48: The initial configuration of a) the $\{111\}$ Co_9S_8 nanoparticle immersed in water and b) the initial configuration without water.....	167
Figure 5.49: Cobalt-cobalt (Co-Co), Cobalt-sulphur (Co-S) and Sulphur-sulphur(S-S) RDFs of a) nanoparticle in water, b) bulk and c) nanoparticle in vacuum.	168
Figure 5.50: Snapshots of the $\{111\}$ nanoparticle in a) vacuum and b) water (removed water for clarity) after simulation.	170
Figure C1: Sketched representation of the atoms arrangement on the $\{111\}$ surface	200
Figure C2: Sketched representation of the atoms arrangement on the $\{101\}$ surface	201
Figure C3: Sketched representation of the atoms arrangement on the $\{100\}$ surface	202

List of Tables

Table 1.1: Atom Coordination and positions in pentlandite structure (Co ₉ S ₈).....	11
Table 3.1: Total energy of bulk Co ₉ S ₈ as a function of plane-wave cut-off and density of k-point.....	47
Table 3.2: Calculated elastic constants of Co ₉ S ₈	58
Table 3.3: Interatomic potential parameters for the Cobalt pentlandite (Co ₉ S ₈) as derived in the present study.	61
Table 3.4: Water potential parameters [105].	62
Table 3.5: Potential parameters for the cobalt pentlandite-water interactions.....	62
Table 3.5 shows the calculated lattice parameters obtained from different methods. The lattice parameters obtained using energy minimisation codes GULP and METADISE are smaller than those from the literature, but still within the acceptable range of 2%.	64
Table 3.5: Comparison of the lattice parameter of Co ₉ S ₈ , obtained from the derived interatomic potentials, with the other calculated and experimental values.	64
Table 3.6: Comparison of the interatomic distances (Å) calculated from the derived model with other calculated and experimental results.	65
Table 3.7: Calculated elastic constants and moduli of the Co ₉ S ₈ phase.	66
Table 4.1: Calculated surface energies of Co ₉ S ₈ using atomistic energy minimisation compared with surface energies using DFT.....	87
Table 4.2: Calculated hydrated surface energies of Co ₉ S ₈	88
Table 5.1: Simulation box sizes of different number of atoms for {111} terminated Co ₉ S ₈ nanoparticles.....	127
Table 5.2: Interatomic distances of different materials of Co ₉ S ₈	139

Table 5.3: Simulation box sizes of different number of atoms for {101} terminated Co ₉ S ₈ nanoparticles.....	140
Table 5.4: Simulation box sizes of different number of atoms for surface {100} Co ₉ S ₈ nanoparticles.	152
Table 5.5: The predicted melting temperatures of the three nanoparticles of different sizes.....	166
Table 5.6: The radial distance of nanoparticles in water and in a vacuum and bulk.	169
Table B1: Interatomic potential parameters for Co ₉ S ₈ . Model 1	198
Table B2: Interatomic potential parameters for Co ₉ S ₈ . Model 2	198
Table B3: Calculated structures and properties of the cubic Co ₉ S ₈ phase for different potential models, including comparison versus experiment, where known.	199

Chapter 1: Introduction

1.1. General Background

The transition metal sulphides (TMS) are a major group of minerals [1] and of vast industrial and economic importance; they are the main source of metals such as zinc, copper, nickel, cobalt, lead and others [2]. TMS play an important role as catalysts in the petroleum refining industry. They represent the only known class of stable catalytically active phases for strongly sulpho-reductive hydroprocessing conditions [3] [4]. Furthermore, metal-sulphur systems are of scientific and industrial interest in the fields of metallurgy, materials science, geochemistry and cosmochemistry [5]. Pentlandite $(\text{Fe,Ni})_9\text{S}_8$ and Co pentlandite $(\text{Co,Ni,Fe})_9\text{S}_8$, are well known, and are important sources of nickel and cobalt in continental deposits, which, over the last decade, have been found in mounds formed from ultramafic rocks on the ocean floor of the Mid-Atlantic Ridge (MAR) [6]. Pentlandite $(\text{Fe,Co,Ni})_9\text{S}_8$ is a major nickel-bearing mineral and plays a very important role in nickel metallurgy, and the mineral is distributed widely in mafic igneous rocks. In addition, precious metals appear as solid solution with pentlandite in the Merensky Reef; and with the Upper Ground 2 Reef (UG2) precious metals sulphides form intergrowths with pentlandites. These minerals have attracted attention as most common minerals in carbonaceous chondrites and interplanetary dust particles. Of the several cobalt minerals, cobalt pentlandite is the most abundant and has the widest geographical distribution. Cobalt pentlandite and cobaltian pentlandite are the most common species, accompanied by pyrrhotite,

pyrite, chalcopyrite, sphalerite and cobaltite [7]. A picture of pentlandite rich in cobalt is shown in Figure 1.1.

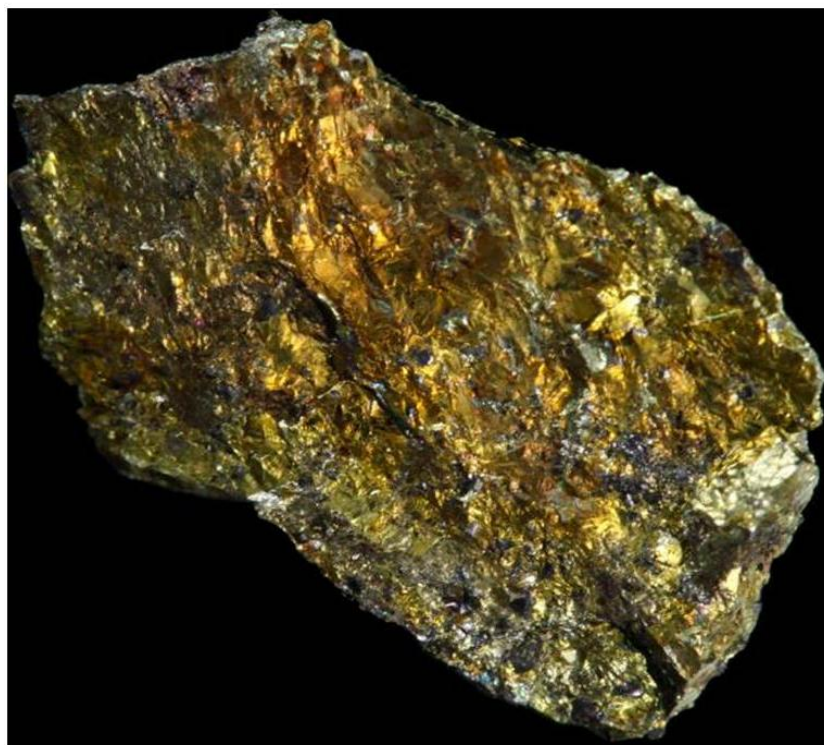


Figure 1.1: A picture of pentlandite rich in cobalt [8].

This work relates to problems in applied areas such as ceramic, mineralogy and geochemistry. In mineralogy and geochemistry a phase transition is modified by impurities, so there is the additional concern of the effect of high temperatures and high pressures. There are many phases of cobalt sulphides such as CoS , Co_3S_4 , CoS_2 , and Co_9S_8 . Among them, Co_9S_8 have attracted attention for their properties for a long time and is of importance in hydrodesulphurization catalysts and magnetic devices [9] [10]. The sulphides of cobalt and nickel attract significant attention due to their importance for catalysis [11]. Co_9S_8 as a pure material has an activity for hydrogenation and hydrodesulphurization [12]. Hydrodesulphurization (HDS) is the

process whereby sulphur is removed from organosulphur compounds that are present in petroleum distillates and other feedstocks by treatment with hydrogen gas (up to 200 atmosphere pressure) at temperatures of 300--450°C [13].

1.2. Literature Review

Several studies have been conducted on cobalt pentlandite (Co_9S_8) and they have been predominantly experimental; computational work has been scarce. The following sections review some previous studies on Co_9S_8 , using both techniques.

1.2.1. Experimental Studies

Several experimental techniques have been used to study cobalt pentlandite, Co_9S_8 . Farrell and Fleet in 2002 [14] studied phase relations for $(\text{Fe},\text{Co})_{1-x}\text{S}$ coexisting with cobalt pentlandite up to 450°C using sealed silica glass tube experiments, where all samples were characterized by X-ray powder diffraction (P-XRD), and a limited number of products were examined by X-ray precession photography, electron microscopy and electron-probe micro-analysis (EPMA). They found that the (Fe,Co) monosulfide solid-solution (*mss*) with the NiAs-type structure (Fe,Co -*mss*) unmixes abruptly below 425°C, to coexisting Fe-rich (Fe,Co -*mss*1; 1C structure) and Co-rich (Fe,Co -*mss*2; 3C structure) phases. Kitakaze and Sugaki [15] also investigated the phase relation along the join $\text{Fe}_{4.5}\text{Ni}_{4.5}\text{S}_8$ and Co_9S_8 in the system Fe-Ni-Co-S by the evacuated-silica-glass-tube method. Furthermore, they synthesized both crystals of high-form cobalt pentlandite (Co_9S_8) and a member of the solid solution containing 50 mol % Co_9S_8 by I2 vapor-transport and NaCl-KCL flux methods. The phases produced in the study were examined by ore microscopy, SEM, EPMA, high-temperature X-ray diffraction and DTA. They reported that a continuous solid-

solution (low form) between pentlandite and cobalt pentlandite transforms to a high-form solid-solution at temperatures from $615\pm 3^\circ\text{C}$ (pentlandite) to $831\pm 3^\circ\text{C}$ (cobalt pentlandite). They further observed that the high-form solid-solution melts incongruently to liquid and monosulfide solid-solution temperatures from $865\pm 3^\circ\text{C}$ (high-form pentlandite) to $930\pm 3^\circ\text{C}$ (high-form cobalt pentlandite), and then remnant monosulfide solid-solution melts completely at temperatures from $982\pm 5^\circ\text{C}$ for $(\text{Fe,Ni})_{1-x}\text{S}$ to $1069\pm 5^\circ\text{C}$ for Co_{1-x}S . Cemic and Kleppa [16] studied the high temperature calorimetry of Co_9S_8 (cobalt pentlandite), whereby the standard enthalpy of formation of Co_9S_8 have been determined by high temperatures between direct reaction calorimetry at temperatures between 700 K and 1021 K. They reported the standard enthalpy of formation to be $-855.66\pm 16.83\text{kJmol}^{-1}$, which was found to be in agreement with the other results from literature. Grzesik [17] determined the chemical diffusion coefficient in Co_9S_8 of temperatures (873-1073 K) and sulphur activity ($10^{-4} - 10^{-1}\text{Pa}$) using microthermo-gravimetric re-equilibrium technique. It was also observed that the chemical diffusion coefficient in Co_9S_8 can be described as a function of temperature. It was also found that the chemical diffusion coefficient in Co_9S_8 does not depend on the sulphur vapour pressure range studied, indicating that the mobility of cation vacancies in this sulphide does not depend on their concentration. In a follow-up work by Grzesik and Mrowec [18] the chemical diffusion coefficient and point defect concentration in metal-deficit sulphides (Co_yS_8 , Ni_{1-y}S and Mn_{1-y}S) has been studied as a function of temperature and sulphur activity using re-equilibration and two-stage kinetic methods. The results show clearly that the microthermogravimetry may successfully be utilized in studying the defect and transport properties of nonstoichiometric metal sulphides. Bezverkhyy et al [11] reported the synthesis of highly dispersed binary and ternary pentlandites, (Co_9S_8 ,

NiCo₈S₈, FeCo₈S₈, Ni₃Co₆S₈, Ni_{4.5}Fe_{4.5}S₈), their characterization with special emphasis on the distribution of cations, and their catalytic properties in the thiophene hydrodesulphurization reaction. The distribution of the cations in tetrahedral and octahedral sites of the pentlandite structure was characterized by EXAFS and Mossbauer spectroscopy. It was noted that the catalytic activity of the sulphides in the model thiophene hydrodesulphurization reaction increases in the following order: Ni_{4.5}Fe_{4.5}S₈, FeCo₈S₈ < Co₉S₈ < NiCo₈S₈ < Ni₃Co₆S₈.

In recent years there have been a number of studies of cobalt sulphide, Co₉S₈ (together with other cobalt sulphide phases) as a potential electrode for lithium ion batteries, some of which are detailed below.

Huang et al [19] synthesized cobalt sulfides/graphene composite by a facile one-pot solvothermal method and characterized by XRD, SEM and TEM. They observed that the as-prepared cobalt sulphides consisted of CoS₂, CoS and Co₉S₈ because of complex stoichiometric of cobalt chalcogenides and reactions under solvothermal conditions. Their results demonstrated that the cobalt sulphides/graphene composite exhibits a very high reversible capacity (as high as 1000 mAhg⁻¹) with the excellent cycle stability and good rate capability. They also reported that, even if the synthesized cobalt sulfides are complicated phases of CoS₂, CoS and Co₉S₈, the results demonstrated that cobalt sulfides/graphene composite exhibits the excellent electrochemical performances, and thus hold high potential as a promising anode material for high-performance Li-ion battery. Recently a facile biomolecule-assisted solvothermal route synthetic strategy was developed by Chen and co-workers [20] to prepare cobalt sulphide (Co₉S₈) hollow microspheres and plate-like microcrystals under mild conditions. The shape evolution and morphologies of the as-prepared

products were investigated in details by X-ray diffraction (XRD), scanning electron microscopy (SEM) and energy dispersive spectrometry (EDS). The shapes, morphologies and sizes of the final products were strongly depended on the reaction time and surfactants. They also investigated the electrochemical properties of the as-prepared cobalt sulphides as an electrode material for lithium-ion batteries. Their electrochemical studies reveal that cobalt sulphide with plate-like structure has larger lithiation capacities than hollow microspheres which could give further insights of the effect of crystal structure transformation on physical properties. Wang et al [21] studied a series of novel Co–S composites composed of metallic Co and Co_9S_8 were prepared via a facile hydrothermal method and investigated as negative electrodes for secondary alkaline batteries. Their instrumental analyses reveal that the incorporation of Co_9S_8 nanoflakes leads to better dispersion of Co particles and increases the interspacing between Co particles, greatly increasing the surface area. They also found that the Co-S composites show high discharge capacities of 420mAhg^{-1} and excellent cycle stability.

1.2.2. Computer Simulation Studies

Reports on computational modeling work of cobalt pentlandite, Co_9S_8 , are scarce. The noticeable study is the electronic structure calculation of Co_9S_8 and related alloys, with the unique structure of pentlandite, by Chauke and coworkers [22] using density-functional methods within the local-density approximation (LDA), in particular TB-LMTO. Convergence to self-consistency was achieved with the use of $4 \times 4 \times 4$ number of k points. They computed the total-energy calculations for Co_9S_8 and $(\text{Fe,Ni})_9\text{S}_8$ alloys and predicted equilibrium lattice parameters that are on average 1% smaller than in the experiment. Furthermore, they determined the individual bond

energies for Co_9S_8 and Co_8S_8 to stress the contribution of the octahedral metal cobalt to the stability of the Co_9S_8 phase. They determined on signature for the stability of $(\text{TM})_9\text{S}_8$. The most recent work is by Sidik and Anderson in 2005 [23], who used the slab band quantum computational approach in the Vienna *ab initio* simulation package (VASP) to calculate the adsorption energies of reactants, reaction intermediates, and products in O_2 reduction and in water oxidation on three crystallographic surfaces of pentlandite structure Co_9S_8 . Their calculations were performed in a plane-wave basis and the exchange correlation used is the local density approximation. The plane-wave cut-off energy is 400eV and the k-point mesh of $5 \times 5 \times 1$ was used. Their findings were that the adsorption bond strengths of the reactants, reaction intermediates, and products for water oxidation and O_2 reduction, the partially OH-covered (202) surface of Co_9S_8 should be active toward O_2 reduction. They also found that water molecules do not block the active sites on this surface and the prediction of O bonding to S, a non-metallic surface site.

Raybaud et al [3], in their paper investigated the structural and cohesive properties of a wide series of transition-metal sulphides (Co_9S_8 being one of them) of various stoichiometries and crystal structures using density functional theory, with the aim of establishing a correlation between the strength of the metal–sulphur bond and the catalytic activities of these materials. Their calculations were performed in a plane-wave basis and the exchange correlation used is the local density approximation. The plane-wave cut-off energy is 250eV and the k-point grids varying from $2 \times 2 \times 2$ and $4 \times 4 \times 4$ (depending on the size of the unit cell). Their results demonstrated that in the local density approximation there is a quite pronounced trend towards an overbinding which manifests itself in the prediction of too small atomic volumes and too large

cohesive energies. Their finding on the Co_9S_8 phase is that at low temperatures it is stabilized.

The recent computational study of Co_9S_8 is by Ramos et al [24]. The density functional theory was used to calculate the total energy in density of states (DOS) using CASTEP code [25], which is contained in Accelrys Materials Studio package. They used plane wave basis (PWB) and the exchange-correlation was revised by Perdew-Burke-Ernzerhof (RPBE) [25]. The PWB cut-off energy was 300 eV. In section 1.3 we explained that Co_9S_8 presents two types of cobalt atoms: an octahedrally coordinated cobalt atom with six sulphur neighbours and a tetrahedrally coordinated cobalt atom forming a cubic array through coordination to three other cobalt neighbours. They found that due to the presence of these Co–Co bonds, the DOS for Co_9S_8 presents a metallic character.

1.2.3. Nanoparticles Study of Co_9S_8

In this section we review some of the studies on nanoparticles of Co_9S_8 . Recently, Yin *et al* [26] successfully prepared Co_9S_8 nanocrystals and nanorods by using cobalt chloride ($\text{CoCl}_2 \cdot 6\text{H}_2\text{O}$), dimethyl sulfoxide (DMSO) and non-aqueous alcohol as reactants and starting materials, and by taking dimethyl sulfoxide as both sulphur source and strong infiltrator in nanorods preparation. Their results show that as-prepared Co_9S_8 nanocrystal with a size of 6 nm has weak paramagnetism at room temperature. Nanocrystalline Co_9S_8 has been successfully prepared by a hydrothermal-reduction method at 120°C by Wang *et al* [27]. The X-ray diffraction (XRD) patterns revealed that the product is a single phase of Co_9S_8 and transmission electron microscopy (TEM) shows that the average particle size of Co_9S_8 is approximately 20 nm. Most recently the polycrystalline Co_9S_8 nanotubes were

successfully fabricated by using $\text{Co}(\text{CO}_3)_{0.35}\text{Co}_{0.20}(\text{OH})_{1.10}$ nanorod bunches as sacrificial hard templates through a hydrothermal route [28]. The samples were characterized by X-ray powder diffraction (XRD), X-ray photoluminescence spectroscopy (XPS), scanning electron Microscopy (SEM) and TEM methods. The Co_9S_8 nanotubes were formed due to the nanoscale Kirkendall effect, which can be explained by the difference in diffusion rates between the cobalt source and the sulphur ion. The magnetic measurements indicated that the Co_9S_8 nanotubes are paramagnetic rather than ferromagnetic, which can be attributed to the tiny sizes of the component nanoparticles. The single-phase nanocrystalline Co_9S_8 was prepared by hydrothermal treatment of $\text{Co}(\text{Ac})_2$ and NH_2CSNH_2 in hydrazine solution at 170°C [29]. It was characterized by XRD, TEM and wet chemical analysis methods. XRD indicated a cubic Co_9S_8 phase, with the relative crystallite size of 6.3 nm. TEM images showed the particles were agglomerative. The synthesis and structural characterization of a mixture of $\text{CoS}_{1.035}$ (30%) and Co_9S_8 (70 %) nanoparticles were prepared by the method of hydrothermal reduction synthesis of transition-metal sulphide nanophase, which is the treatment of aqueous solutions of precursors such as cobalt acetate and thiourea at elevated temperatures in pressurised vessels [30]. In this technique, they found that size, morphology, and phase homogeneity can be controlled, rendering materials with a wide range of magnetic properties over the temperature range of 2.0-300K.

Co_9S_8 was recently studied by Du *et al* [23], and they described the synthesis of novel Co_9S_8 -nanowire-filled carbon nanotubes (CNTs) by a simple method involving the pyrolysis of thiophene on a cobalt catalyst in a conventional chemical vapour decomposition system. Finally, the Co_9S_8 nanoparticles were prepared from single source precursors [31] and it was found that the Co_9S_8 nanoparticles aggregates are

composed of numerous small cuboid Co_9S_8 nanoparticles with average diameters of 10-20 nm. Recently, along with many other metal sulphides, cobalt sulphides (Co_9S_8) have attracted great attention due to their potential application in lithium ion batteries [32]. Wang et al [33] studied the phase controlled synthesis of cobalt sulphides for lithium ion batteries. They obtained phases and microstructures of CoS_2 , Co_3S_4 , CoS , Co_9S_8 , and CoO depended on heating temperature and time. They found that these cobalt materials, possessed good cycling stability in lithium ion batteries, if they are successfully used as the electrodes of lithium ion batteries. Wang et al [34] examined the possibility of using cobalt sulphide nanopowders as cathode materials for lithium-rechargeable batteries through electrochemical testing. Their cyclic voltammetry measurements revealed that the $\text{Li}/\text{Co}_9\text{S}_8$ cell discharges in a two-step process. They improved the discharge capacities with increasing contents of electronic conductors in the electrodes. Shi et al [35] developed a novel solvothermal process for the synthesis of carbon-coated Co_9S_8 nanodandelions using 1-dodecanethiol as the sulphur source and the soft template. They replaced the 1-dodecanethiol with sulphur powder, which lead to the formation of 20 nm Co_9S_8 nanoparticles. In their study they found that the carbon coated Co_9S_8 dandelion exhibits excellent high-capacity-rate performance than the Co_9S_8 nanoparticles, which makes it attractive as the anode material to build high-energy-density and high-power-density lithium ion batteries.

1.3. Structural Aspects of Pentlandite, Co_9S_8

The conventional unit cell of the cobalt pentlandite has the formula $\text{Co}_{36}\text{S}_{32}$ and contains a cubic close-packed arrangement of sulphide ions containing 64 tetrahedral holes and 32 octahedral holes. Of the 64 tetrahedral holes, 32 are occupied by Co^{2+} ions, these being distributed through the lattice in groups of eight which lie at the

corners of sub-cubes of edge length 0.250 nm. Of the 32 octahedral holes, 28 are pseudo-octahedral, distorted, and empty, whereas four are truly octahedral and each contains a Co atom in a formally zero oxidation state. Thus the solid attains the overall stoichiometry Co_9S_8 [12].

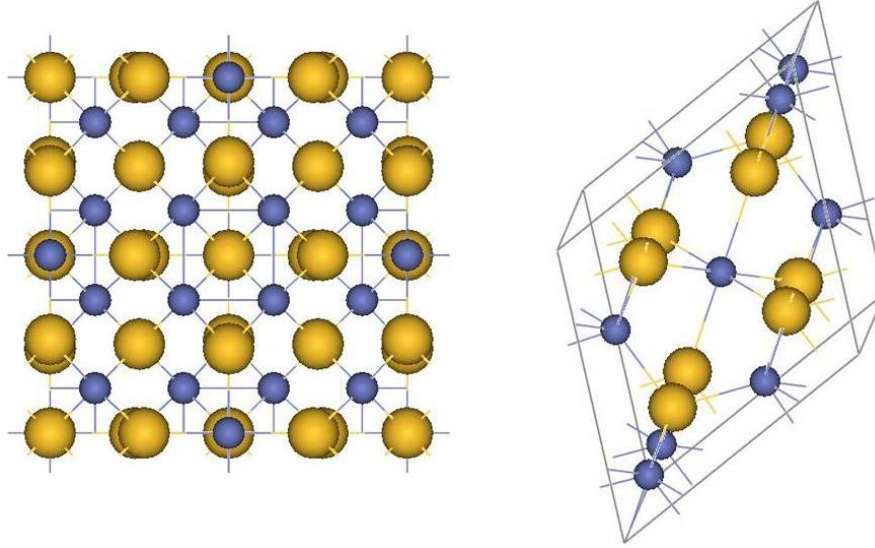


Figure 1.2: Conventional unit cell (on the left hand side) and primitive unit cell (on the right hand side) of pentlandite structure (Co_9S_8). Blue and yellow spheres represent cobalt (Co) and sulphur (S) atoms respectively.

Table 1.1 shows the atomic coordination and positions in cobalt pentlandite Co_9S_8 [22]. Figure 1.2 shows the conventional and primitive unit cells of Co_9S_8 . The Co_9S_8 has a space group $Fm\bar{3}m$ and a lattice parameter of $a = 9.928 \text{ \AA}$ [37].

Table 1.1: Atom Coordination and positions in pentlandite structure (Co_9S_8)

<i>Atom</i>	<i>Position</i>	<i>X</i>	<i>Y</i>	<i>Z</i>
<i>Co (t)</i>	<i>(4b)</i>	<i>0.5000</i>	<i>0.5000</i>	<i>0.5000</i>
<i>Co (o)</i>	<i>(32f)</i>	<i>0.1260</i>	<i>0.1260</i>	<i>0.1260</i>
<i>S</i>	<i>(8c)</i>	<i>0.2500</i>	<i>0.2500</i>	<i>0.2500</i>
<i>S</i>	<i>(24e)</i>	<i>0.2591</i>	<i>0.2591</i>	<i>0.2591</i>

Wyckoff notation [38]: Co (t), tetrahedral sites; Co (o), octahedral sites; space group, $Fm\bar{3}m(225)$

The conventional unit cell has an important feature of the structure which is the presence of three metal-metal bonds that extend from each tetrahedral cations (Figure 1.2). The pentlandite structures are transition-metal sulphides that contain distinguishable metal atom cubes and exist only for certain combinations of the Fe group elements, Co_9S_8 being the only known binary phase [38]. The metallic behaviour of Co_9S_8 is a result of metal-metal interactions, both direct and indirect [39] [40]. In terms of the bonding properties of Co_9S_8 , the S atoms are held together mainly through bonding with Co, the octahedrally coordinated Co (I) atoms are held together through bonding with S, while tetrahedrally coordinated Co(II) atoms are held together through bonding with S as well as through bonding between the special Co(II)-Co(II) pair [41].

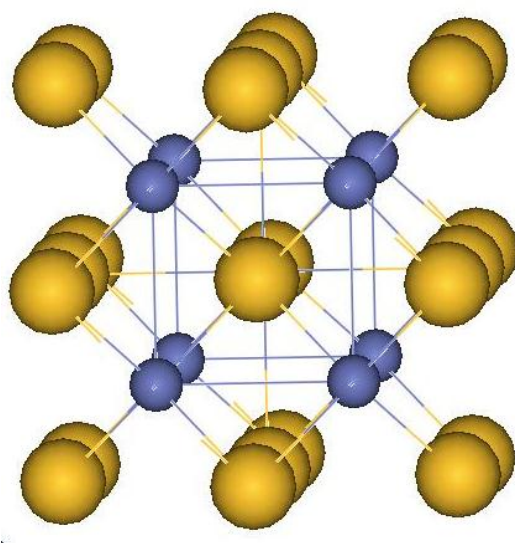


Figure 1.3: Cubic cluster of tetrahedral Co (II) in Co_9S_8 .

1.4. Rationale of the Study

The importance of pentlandite minerals as ore for provision of base metals has been highlighted when we depicted the significance of the current study and in our

literature review. Its co-existence with precious metal ores either as solid-solution and intergrowths has been indicated, hence rendering its detailed understanding important for efficient extraction of precious metals. In addition, the fundamental surface properties of metal sulphides and their existence in different nanophases, such as nanoparticles, nanorods, nanowires have been shown to play a crucial role in various areas of engineering and applied science, such as acid mine drainage, contaminant sorption, heterogeneous catalysis [42] and renewable energy storage [32-35]. Notwithstanding their current significance, pentlandites have not been studied as extensively as other sulphides, such as pyrite and metal oxides; though more experimental investigations are beginning to emerge. This could be emanating from their previous less technological prominence and homogenous large samples not being easily available. Hence, accumulation of all necessary experimental data could take a long time.

Computational modelling methods, including *ab-initio* and atomistic simulation techniques, have shed valuable insights on surface and nanostructural systems for a wide variety of materials. Such methods individually play unique roles along time and length scales of modelling. Although *ab-initio* methods tend to be more accurate, they are however, confined to smaller systems and currently do not address thermal properties of systems effectively. Atomistic simulations, on the other hand, are based on interatomic potentials that are not always transferable to other metal sulphides. They are, however, more appropriate for handling properties of bulk, surfaces and nanostructures consisting of a large number of atoms; and in addition, they enable high temperature studies. Atomistic simulations have not been carried out on pentlandite structures before, since related interatomic potentials are not available.

There is, consequently, a necessity for deriving such potentials for pentlandites, validating them and using them to predict surface and nanostructural properties at ambient and high temperatures.

1.5. Objectives of the Study

The objective of the study is to derive the interatomic potential model that can adequately describe structural and thermodynamic properties of the cobalt pentlandite (Co_9S_8) mineral. The bulk structural properties of Co_9S_8 will be calculated and compared with the available experimental and other data from literature, validating the newly derived potential model. We will employ molecular dynamics (MD) simulations, which will be used in conjunction with the derived interatomic potentials, to simulate the surfaces of Co_9S_8 at various temperatures and investigate the effect of water on the surface structures and stabilities. The surface energies of the dry and hydrated cobalt pentlandite surfaces will be calculated, and compared with the surface energies from *ab initio* methods. Calculated surface energies will provide crystal morphologies and be used to generate the Co_9S_8 nanoparticles. Molecular dynamics will be used to study the structure and stability of the generated Co_9S_8 nanoparticles at various temperatures; where the effect of size on the melting of those nanoparticles will be examined and the impact of hydration on the nanoparticles.

1.6. Outline of the Study

Chapter 1 contains the general background of the pentlandite structure, Co_9S_8 . The major experimental and computational and the nanoparticles studies of Co_9S_8 are reviewed. The structural aspects of the Co_9S_8 are discussed in this chapter. The rationale and objectives of the study are also outlined.

Chapter 2 discusses the theoretical aspects and methodology used throughout this work, in particular the computational techniques, such as energy minimisation, molecular dynamics and electronic structure methods

In Chapter 3, the derivation of the interatomic potential model of the cobalt pentlandite is discussed, together with its validation. We also discuss the convergence of the bulk Co_9S_8 using the density functional theory.

In Chapters 4 and 5 we outline the main results obtained in the present study. Chapter 4 discusses the molecular dynamics simulation of the bulk and surfaces of Co_9S_8 at ambient and high temperatures. Chapter 5 presents the structure of the nanocrystals of the Co_9S_8 using the molecular dynamics. The effect of size and water on the structure of the Co_9S_8 nanoparticles at different temperatures is discussed.

Finally, chapter 6 give summary of the main results presented in this thesis and several recommendations for future research are also listed.

Chapter 2: Theoretical Studies and Computational Methods

Computational methods are now a central technique in solid state science [43]. The field has changed qualitatively in recent years with the focus moving from reproduction (and illumination) of experimental data to detailed predictive calculations on highly complex systems. The methodology used in this thesis is computational, and in this chapter we will introduce electronic structure and atomistic simulation approaches. Energy minimisation and molecular dynamics techniques applicable in both approaches will be introduced. Levy [44] and Wimmer [45] also mentioned that for the past decades, computational materials science has made major strides in becoming a predictive; impacting fundamental science as well as the development programs of industrial materials.

2.1. Atomistic Simulation

One of the major reasons for computations in materials science is to gain a deeper understanding of materials on the atomic scale [46]. Atomistic computer modelling techniques now play a major role in both physical and biological sciences [47]. An atomistic simulation is now able to model the structure of mineral surfaces at the atomic level and is a valuable tool for interpreting and predicting surface structures [48]. The atomistic simulations are based on the Born model of ionic solids [49], in

which the ions interact *via* long-range electrostatic forces and short-range forces. The value of atomistic simulations in the earth and materials sciences lies in demonstrating the mechanisms of atomistic procedures, and extending this capability to evaluate material properties to regimes where direct laboratory measurements are difficult or impossible to perform [50]. Atomistic models are limited to small system sizes. The major disadvantage is their inability to explicitly model electronic properties. This problem is overcome by the use of electronic structure calculation density functional theory (DFT). The advantage of atomistic simulation is the reduction in computing time; we are able to model bigger system for a short period of time as compared to DFT. Energy minimization allows us to evaluate the most stable configurations and molecular dynamics provides the effect of temperature on the system. These techniques are discussed in the following sections.

2.1.1. Energy Minimisation

Energy minimisation allows us to evaluate energy of a system by adjusting the atom positions until a minimum energy configuration of the atoms is obtained. In this work we used energy minimisation throughout to calculate the energies and equilibrium structures of the bulk and surfaces of Co_9S_8 . As an example METADISE (minimum energy techniques applied to dislocations, interfaces, surface energies) codes [51], uses energy minimisation to calculate the structure of systems periodic in various dimensions (zero nanoparticles, one dislocations, two surfaces and three bulk). The advantage of energy minimisation is that (for systems it does not demand computationally, so it can be used to scan a range of possible configurations. The drawback of energy minimisation are that for large systems the inversion of the

matrix of second order derivatives becomes prohibitively expensive, something which the ever increasing power of computers and techniques such as molecular dynamics go some way to negating and that it does not take account of the vibrational properties of the system. There is no representation of temperature in the simulated system however this effect will be small for ideal solid systems.

The lowest energy configuration is found by using an iterative procedure to adjust the atom positions until the interaction energy is minimised. The calculated interaction energy should be the minimum interaction energy of the system, i.e., the system must be at its mechanical equilibrium and there should be no residual stresses. However, this is rarely the case on setting up a simulation cell and hence the interaction energy needs to be minimized so as to remove these residual stresses. There are two ways of achieving this: Firstly, via a constant volume or constant area minimization, where the cell dimensions are kept fixed but the position of the ions can be modified. Secondly, by means of a constant pressure minimization where both the cell dimensions and the ions can relax, i.e., forces on the atoms and the cell dimensions are both removed [52]. The ions are at their minimised positions when all the forces are zero, i.e., when

$$\frac{\partial U}{\partial r} = 0 \quad (2.1)$$

where U is the energy and r is the ion position.

The Newton-Raphson variable matrix method [53] has been employed for energy minimisation calculations throughout this work. This minimisation procedure optimises the energy of the systems modelled with the potential energy. In the Newton-Raphson method, $U(r)$ is expanded to second order by Taylor expansion:

$$U(r) = U(r_n) + g_n \cdot \delta r^T + \frac{1}{2} \delta r^T \cdot W_n \cdot \delta r \quad (2.2)$$

where δr is the displacement of a given ion

$$\delta r = r_{n+1} - r_n \quad (2.3)$$

and W_n is the second derivative matrix,

$$W_n = -\frac{\partial^2 U}{\partial r_n^2} \quad (2.4)$$

Then assuming equilibrium conditions where the change in energy with respect to ion position is zero

$$\frac{\partial U}{\partial r} = 0 = g_n + W_n \cdot \delta r \quad (2.5)$$

which gives

$$\delta r = -W_n^{-1} \cdot g_n \quad (2.6)$$

Hence

$$r_{n+1} = r_n - g_n \cdot H_n \quad (2.7)$$

where H_n is the Hessian matrix and is equivalent to W_n^{-1} . Therefore Equation 2.7 is the working equation for calculating the new atomic positions using the Newton-Raphson minimisation method. If the energy system was harmonic in r the minimum energy of the system would be obtained in a single step. However, the energy of the system is not harmonic, although the displacement gives rise to a lower energy configuration. Hence several iterations have to be performed before the equilibrium configuration is obtained. Since this method requires the calculation of both the first and the second derivative of energy with respect to the position of the ions and the inversion of the second derivative matrix, it can be computationally expensive for large systems. The speed of calculation can be increased if the inverted second

derivative matrix is approximated and the matrix is recalculated after a fixed number of iterations or when the changes in the energy are too large for the approximation to be valid [52] [54] [55][56]. There are a number of different ways that the inverse Hessian matrix can be approximated. The two methods that can be used to approximate the Hessian matrix are shown below.

The Davidon-Fletcher-Powell (DFP) method (54):

$$H_{n+1} \approx H_n + \frac{\delta r \times \delta r^T}{\delta r^T \cdot \delta g} - \frac{(H_n \cdot \delta g) \times (H_n \cdot \delta g^T)}{\delta g^T \cdot H_n \cdot \delta g} \quad (2.8)$$

where $\delta r = (r_{n+1} - r_n)$ and $\delta g = (g_{n+1} - g_n)$. The superscript corresponds to the transpose of the vector, and the new position $n+2$ can be calculated. The second method is the Broyden-Fletcher-Goldfarb-Shanno (BFGS) [57-60]. This is a more efficient approach. This is identical to the DFP equation with only the additional term:

$$H_{n+1} \approx H_n + \frac{\delta r \times \delta r}{\delta r \cdot \delta g} - \frac{(H_n \cdot \delta g) \times (H_n \cdot \delta g)}{\delta g \cdot H_n \cdot \delta g} + (\delta g \cdot H_n \cdot \delta g) u \times u \quad (2.9)$$

where the vector u is defined as:

$$u = \frac{\delta r}{\delta r \cdot \delta g} - \frac{H_n \cdot \delta g}{\delta g \cdot H_n \cdot \delta g} \quad (2.10)$$

2.1.2. Molecular Dynamics

Molecular dynamics simulation is a computational technique used to study the motions of atoms in a given system (e.g., a solid material or a solid solution could equally be liquids and gases) in order to understand and predict the structural , dynamic, kinetic, and /or equilibrium properties at a chosen conditions (e.g., compositions, temperatures, and pressures) [61]. Molecular dynamics (MD) is a powerful method for exploring the structure of solids, liquids and gases. It is a modern method which requires electronic computers and recently supercomputers. Molecular Dynamics simulations are in many respects very similar to real experiments. When we perform a real experiment, we proceed as follows. We prepare a sample of the material that we wish to study. We connect this sample to a measuring instrument (e.g. a thermometer, manometer, or viscometer), and we measure the property of interest during a certain time interval. If our measurements are subject to statistical noise (as most measurements are), then the longer we average, the more accurate our measurement becomes. In Molecular Dynamics simulation, we follow exactly the same approach. First, we prepare a sample: we select a model system consisting of N particles and we solve Newton's equations of motion for this system until the properties of the system no longer change with time (we equilibrate the system). After equilibration, we perform the actual measurement. In fact, some of the most common mistakes that can be made when performing a computer experiment are very similar to the mistakes that can be made in real experiments (e.g., the sample is not prepared correctly, the measurement is too short, the system undergoes an irreversible change during the experiment, or we do not measure what we think) [62]. We call molecular dynamics (MD) a computer simulation technique where the time evolution of a set of

interacting atoms is followed by integrating their equations of motion. The molecular dynamics can be used to investigate the detailed atomistic mechanisms. With MD technique it is possible to simulate the dynamic, thermal behaviour of atoms in solids. By performing simulations at different temperatures and studying the displacements of the ions as a function of time we can predict diffusion coefficients. The molecular dynamics technique involves solving Newton's laws of motion over a finite time period for all the particles of a system. The main difference with the energy minimization method discussed in the previous section, is that, molecular dynamics simulation gives the effect of temperature by assigning kinetic energy to the atoms in the simulation cell and thus allows us to follow the trajectory of the atoms and molecules with time. Hence, unlike in energy minimization calculations, atoms and molecules can potentially jump over energy barriers to reach a global minimum; however, due to the very short 'real time' accessible to molecular dynamics simulations, this only applies to small energy barriers, i.e., of the order of few $k_B T$. All molecular dynamics simulations in this work were performed using the computer code DL_POLY developed by W. Smith and T.R. Forester in Daresbury, UK [63].

In molecular dynamics simulation, the particles are initially assigned random velocities, such that the system starts with the required temperature and that the simulation cell has no translational momentum, i.e.,

$$\sum_{i=1}^N m_i \cdot v_i^2 = 3Nk_B T \quad (2.11)$$

and

$$\sum_{i=1}^N m_i \cdot v_i = 0 \quad (2.12)$$

where N is the number of particles, k_B is the Boltzmann constant, T is the temperature, m_i is the mass of ion i , and v_i its velocity.

The second step of a molecular dynamics simulation is to calculate the force acting on each particle. Once the forces, F_i , are obtained the accelerations, a_i , can be calculated and the velocities, v_i , and positions F_i , are updated, for an infinitely small time step, according to

$$a_i(t) = \frac{F_i(t)}{m_i} \quad (2.13)$$

$$v_i(t + \delta t) = v_i(t) + a_i(t) \cdot \delta t \quad (2.14)$$

$$r_i(t + \delta t) = r_i(t) + v_i(t) \cdot \delta t \quad (2.15)$$

These are the Newton's equations of motion and can only be applied strictly for an infinitesimal time step. In practice, computer codes use integration algorithms such as the Verlet algorithm [64] to solve Newton's laws of motion, as explained in the next section. The choice of the time step δt , in these equations is very important. Indeed if δt is too large, the molecular vibrations will occur within the time step, giving rise to large errors. However, if δt is too small, the particles will take too long to move a significant distance. In addition, another factor needs to be considered to choose the time factor. After each step, run time properties such as the potential energy, the temperature, or the pressure of the system are calculated. Then the process is repeated several thousand or million times to reach the required simulation time. In the first few tens of thousands steps, the particles' velocities are scaled to meet the desired temperature. This period is called the equilibrium period and it allows for the system to come to equilibrium at a given temperature and pressure before data are collected. Then, the simulation is run as long as possible, without scaling the particles'

velocities, to obtain converged averages of the properties of interest and reduce statistical noise.

In molecular dynamics we follow the laws of classical mechanics, and most notably Newton's law of motion:

$$\vec{F}_i = m_i \vec{a}_i \quad (2.16)$$

for each atom i in a system constituted by N atoms. Here, m_i is the atom mass, $\vec{a}_i = \frac{d^2 \vec{r}_i}{dt^2}$ its acceleration, and \vec{F}_i the force acting upon it, due to the interactions with other atoms.

In the next section we discuss the integration algorithm, the different types of ensembles used in this work and we will discuss the properties that are calculated from molecular dynamics simulations i.e. Radial distribution functions, diffusion coefficients and mean squared displacement.

Integration Algorithms

An integration algorithm is used to perform the step by step solution of the equations of motion using a finite difference algorithm. The algorithm used in this work is the Verlet algorithm [64]. The positions, velocities as well as accelerations are obtained by a Taylor expansion of the positions about time t :

$$\begin{aligned} r(t + \delta t) &= r(t) + v(t)\delta t + \frac{1}{2}a(t)\delta t^2 + \frac{1}{6}b(t)\delta t^3 + \dots \\ v(t + \delta t) &= v(t) + a(t)\delta t + \frac{1}{2}b(t)\delta t^2 + \dots \\ a(t + \delta t) &= a(t) + b(t)\delta t + \dots \\ b(t + \delta t) &= b(t) + \dots \end{aligned} \quad (2.17)$$

where r is the particle's position, \mathbf{v} is the velocity, a is the acceleration and b is the third time derivative of r . From Equation (2.7) we can calculate the position of a particle about a position $r(t)$ before and after a time step δt

$$r(t + \delta t) = r(t) + v(t)\delta t + \frac{1}{2}a(t)\delta t^2 + \frac{1}{6}b(t)\delta t^3 + \mathcal{O}(\delta t^4) \quad (2.18)$$

$$r(t - \delta t) = r(t) - v(t)\delta t + \frac{1}{2}a(t)\delta t^2 - \frac{1}{6}b(t)\delta t^3 + \mathcal{O}(\delta t^4) \quad (2.19)$$

where $\mathcal{O}(\delta t^4)$ is the order of accuracy. Now adding (2.8) and (2.9) gives

$$r(t + \delta t) + r(t - \delta t) = 2r(t) + a(t)\delta t^2 + \mathcal{O}(\delta t^4) \quad (2.20)$$

We notice that Verlet algorithm [64] is time-reversible (i.e. $r(t + \delta t)$ and $r(t - \delta t)$ are interchangeable). Also, the absence of velocities, since they are not required but are necessary for the calculation of the kinetic energy. They can be calculated by subtracting Equation (2.9) from (2.8) and obtain:

$$v(t) = \frac{r(t + \delta t) - r(t - \delta t)}{2\delta t} + \mathcal{O}(\delta t^2) \quad (2.21)$$

Equation (2.20) is accurate to δt^4 while Equation (2.21) is accurate to order δt^2 .

Ensembles

Statistical mechanics simulations are performed in different ensembles. The microcanonical or NVE ensemble, it's where the system is isolated from changes in particles (N), volume (V) and energy (E). A microcanonical molecular dynamics trajectory may be seen as an exchange of potential and kinetic energy, with total

energy being conserved. The other ensemble is canonical or NVT ensemble, its where the number of particles, the volume and temperature are the constant quantities. And isothermal-isobaric or NPT ensemble, where the number of particles, pressure and temperature are the constant quantities. Initially a NPT simulation is performed on the bulk simulation cell (analogous to a constant pressure simulation in energy minimization) to remove any lattice strains. Thereafter, for example when considering surfaces, constant volume ensembles such as the NVT ensemble are used.

Molecular Dynamics Simulation Properties

The molecular dynamics studies result in various quantities describing the temperature-dependent behaviour of the analyzed systems. In our case we looked at the radial distribution functions (RDFs), mean squared displacement (MSD), and diffusion coefficient. These quantities provide the structural information about the solid and liquid phases and about the melting phenomenon, meaning the temperatures of the solid-liquid transition can be estimated. However as stated by [65] the interpreted temperatures are not the real melting temperatures of the systems, but rather the temperatures of the mechanical instability of the infinite single crystal.

Radial Distribution Functions (RDFs)

The RDF is defined as the probability of finding an atom at a distance r from another atom compared to a homogeneous distribution [66] [67] and is given by

$$g(r) = \frac{V}{N_1 N_2} \frac{1}{4\pi r^2 \delta r} \left\langle \sum_i \sum_{j>i} \delta(r - r_{ij}) \right\rangle \quad (2.22)$$

where V is the volume, N_1 and N_2 are the atom types of the RDF. The delta function must give rise to a value of one for a range of $r(\delta r)$. The RDF tends to 1 at long distances with sharp peaks indicating a regular lattice structure. For amorphous or liquid systems the RDF shows characteristically a small number of broad peaks at short distance, indicating short range order, superimposed on an oscillating trace to 1, which indicates a loss of long range order [68]. The structural properties of our system were investigated by analysing the partial radial distribution functions (RDFs), $g_{CoS}(r)$, $g_{SS}(r)$. The partial RDFs $g_{\alpha\beta}(r)$ are defined in such a way that, by considering an atom of the species α , the probability of finding an atom of the species β in a spherical shell $(r, r + dr)$ is:

$$\rho_{\beta} 4\pi r^2 g_{\alpha\beta}(r) dr \quad (2.23)$$

where $\rho_{\beta} = \frac{x_{\beta}}{V}$, is the number density of the species β with mole fraction x_{β} , and V is the volume per atom.

RDFs give the probability of finding the centre of a particle or atom at a given distance from the centre of another particle. We calculated the partial distribution functions obtaining the nearest neighbour interatomic distances of $Co - S$ and $S - S$.

The light atom at the center is the reference atom, and the circles around it represent the other atoms. A ring centered on the reference is drawn with radius r and thickness dr . The radial distribution function can be an effective way of describing the structure of a system at different temperatures.

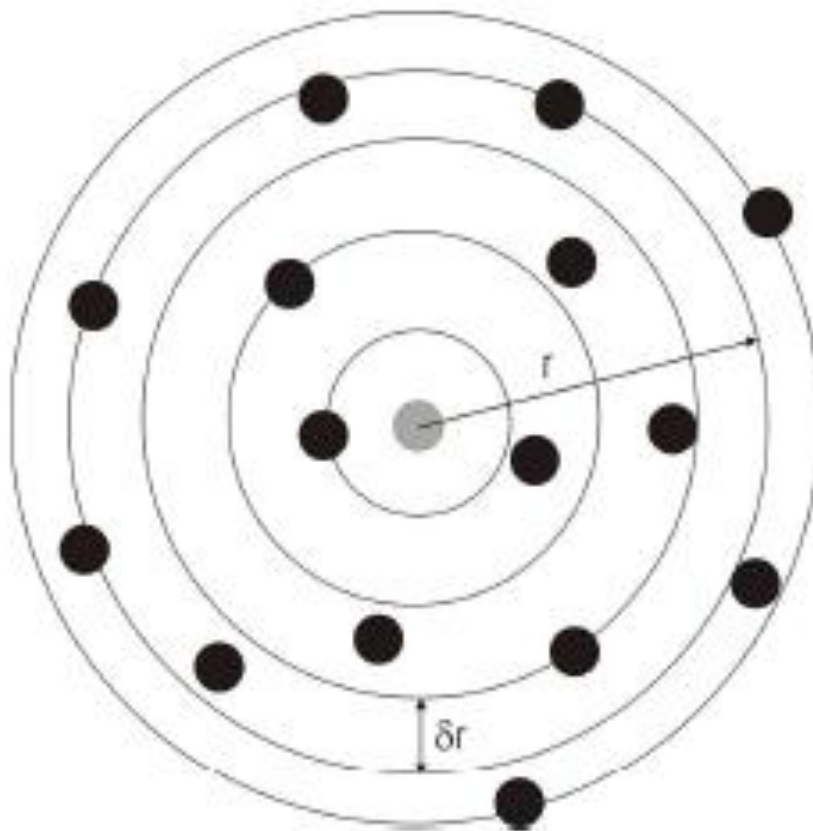


Figure 2.1: Schematic representation of the radial distribution function.

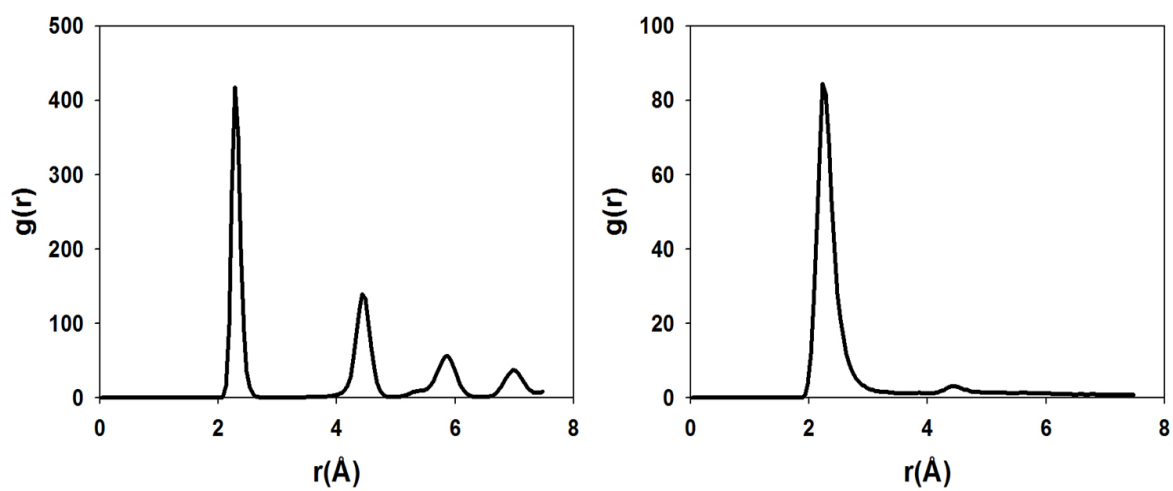


Figure 2.2: Example of a Cobalt-Sulphur RDF in a crystalline solid on the left and in a liquid phase on the right.

Differentiation between a solid and a liquid can be made using the rdfs by the number of peaks appearing in a particular RDF plot. In a crystal or solid, the radial distribution functions have a multiple number of sharp peaks and heights are characteristic of the lattice structure. The radial distribution function of a liquid has a small number of peaks at short distances and the height of the peaks decreases. The examples of cobalt-sulphur radial distribution functions are given in Figure 2.2. For the crystalline solid, the peaks are sharp and thin and show long-range order. In case of a liquid phase, the peaks are broad and the radial distribution function rapidly converges to one.

Mean Squared Displacement (MSD)

In this study, the behavior of the mean squared displacement (MSD) as a function of time is also used to discriminate between a solid and a liquid phase as suggested by [69]. The time dependence of the average mean squared displacement (MSD) is one of the tools to obtain the information on the atom mobility. It is calculated according to the following relationship:

$$6Dt = \langle |r_i(t) - r_i(0)|^2 \rangle \quad (2.24)$$

In a solid (i.e. at a lower temperature), the diffusion will be significantly smaller and the MSD is flat. In a liquid (i.e. at a higher temperature), the particles diffuse randomly and the gradient of the curve is proportional to the diffusion coefficient. The curve takes a parabolic shape at the start, this is due to the short time it takes an atom to feel the effect of the other atoms. If there is no increase in the MSD of an ion type with time, then the ions are vibrating about their mean lattice site. Also as the MSD is the distance squared a vibrational will add to the function rather than cancel itself out.

However such movements are small compared to atoms actually diffusing through the crystal. If the MSD's increases with time, then the ions are considered to be moving away from their initial positions [50].

Diffusion Coefficient

The diffusion is another measure to estimate relative mobilities of individual Co_9S_8 atoms. It is known that diffusion coefficient can be estimated from the slope of MSD plots using the Einstein relation as follows:

$$D = \frac{1}{6} \frac{d}{dt} \langle |r_i(t) - r_i(0)|^2 \rangle \quad (2.25)$$

The integral Equation 2.25 is the velocity autocorrelation function (VAF), which is related to the diffusion coefficient. The VAF decays to zero at long time; the function is integrated mathematically to calculate the diffusion coefficient as in Equation 2.26.

$$D = \frac{1}{3} \int_0^{\infty} \langle v_i(t) \cdot v_i(0) \rangle dt \quad (2.26)$$

The melting point of the simulated system can be located by increasing the temperature of a crystalline system until diffusion appears.

Periodic Boundary Conditions

Periodic boundary conditions are used in most of our simulations of molecular dynamics (and energy minimization). Implementing periodic boundary conditions means that the particles are usually enclosed in a cubic simulation box of a fixed side-length. The box is then replicated to infinity by rigid translations in the three Cartesian

directions, producing infinite images of each particle in the box. A particle in the box would not only interact with the rest of the particles in the same box, but with the images in the nearby boxes, provided that they lie within the range of interaction. When a particle leaves the simulation box, one image fills the void, shown in Figure 2.3.

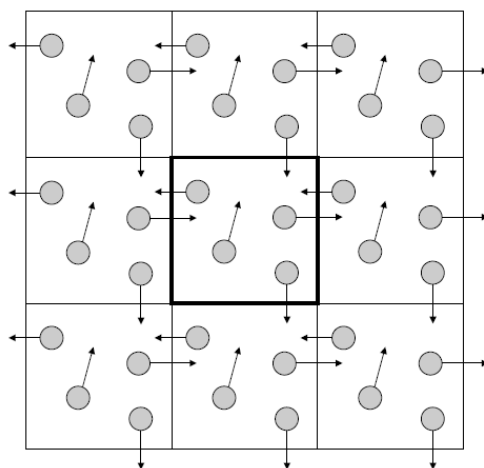


Figure 2.3: Schematic representation of the periodic boundary conditions where the simulation cell is highlighted in bold. [52].

The highlighted cell in Figure 2.3 indicates the simulation cell whereas the other cells indicate the images. The system no longer has a surface, which is necessary to simulate bulk crystals or in the case of liquids to prevent outer molecules from boiling off into space. Two strategies can be employed when simulating surfaces. The first is to use two-dimensional periodic boundary conditions, that is where the cell is periodic in only two directions and the other direction is used to create the surface. This method uses the Parry summation which is described in the next chapter. The second is to use three-dimensional periodicity but have the simulation cell to be large so that

the interactions between the interface and its images are negligible. This method use Ewald summation to model the electrostatic interactions.

2.1.3. Surface Energy Calculations

We calculated the surface energy from energy minimization and from molecular dynamics simulations. The surface energy is defined as the excess energy, per unit area of the surface compared to the bulk crystal. Thus any calculation of the surface energy also requires that we model a comparable amount of bulk crystal under identical conditions.

Energy Minimization Surface Energy Calculations

The energy minimization code employed was METADISE [51]. In METADISE calculations, the system is considered to consist of a series of charged planes parallel to the surface and periodic in two dimensions. A bulk crystal consists of two blocks (see Figure 2.4) and each block has two regions, namely region I and region II. The ions in region I are allowed to relax relative to region II, while the ions in region II are held fixed at their equilibrium position. When the two blocks are separated the surface will be created. Then the Energy of the crystal consists of two parts:

$$E_{total} = E_1 + E_2 \quad (2.27)$$

where E_1 is the energy of ions in region I and E_2 is the energy of ions in region II.

The energy of region I is given by Equation 2.30 below:

$$E_1 = \sum_{\substack{i \in I \\ j \in I}} \sum_l \Psi_{ij}(|r_{ij} - r_l|) + \frac{1}{2} \sum_{\substack{i \in I \\ j \in II}} \sum_l \Psi_{ij}(|r_{ij} - r_l|) \quad (2.30)$$

where the first term includes interactions between the ions in region I and the second term the interactions between the ions in region I and region II. The energy of region II consists of only the second term as the ions are kept fixed and hence the interactions between the ions in region II is unchanged. The energy contribution of region II is then represented as:

$$E_2 = \frac{1}{2} \sum_{\substack{i \in I \\ j \in II}} \Psi_{ij}(|r_{ij} - r_l|) \quad (2.31)$$

Two METADISE calculations are necessary when calculating the surface energy of a crystal, one for the surface block and one for a bulk block, as shown in Figure 2.4. The surface energy is described using the following method. If the energy of the surface block is E_S and the bulk block is E_B then this energies can be broken down into the following components:

$$E_S = E'_{I-II} + E'_{I-I} + E'_{II-I} + E'_{II-II} \quad (2.32)$$

$$E_B = E''_{I-II} + E''_{I-I} + E''_{II-I} + E''_{II-II} \quad (2.33)$$

where E_{I-I} is the interaction energy of the ions in region I with others in region I and E_{II-I} is the interaction energy of all the ions in region I with all the ions in region II, etc. The surface energy of a crystal face is defined as the excess in energy of a surface simulation over the energy of a bulk system containing the same number of atoms per unit area and is described by the following equation:

$$\gamma = \frac{(E_S - E_B)}{AREA} \quad (2.34)$$

Since the ions in region II do not relax, the total interaction energy, E_{II-II} , of all the ions in region II with the other ions in region II does not change, and will therefore cancel in the surface energy calculation.

The effect of water on the surfaces can also be modelled, and the surface energy of a hydrated surface is:

$$\gamma = \frac{E_h - E_b - nE_{H_2O}}{A} \quad (2.35)$$

where E_h is the energy of the hydrated surface, n the number of water molecules adsorbed on the surface and E_{H_2O} is the energy of a water molecule, i.e., the water self-energy plus the condensation energy.

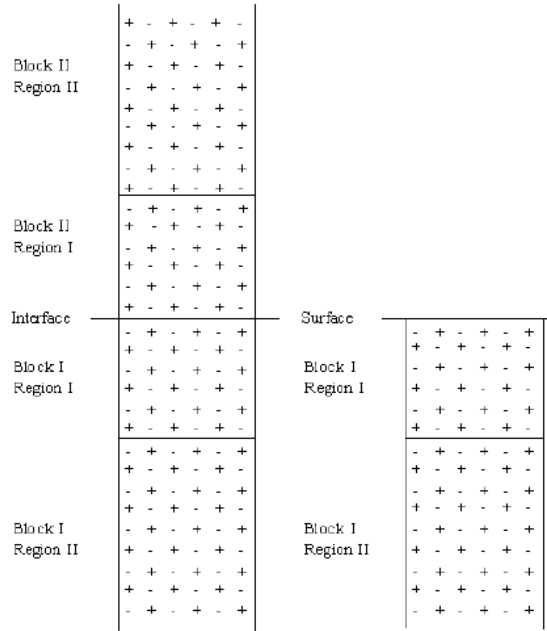


Figure 2.4: The two region approach used in METADISE, the left hand case for a complete crystal unit (BULK) and the right hand case a half crystal exposing a surface [56].

Molecular Dynamics Surface Energy Calculations

Molecular dynamics simulations yield the average energy per ion of the bulk block and surface slabs. The surface energy is calculated as:

$$\gamma = \left(\frac{E_s - \frac{n_s}{n_b} E_b}{2A} \right) \quad (2.36)$$

where n_s is the number of atoms in a surface and n_b is the number of atoms in a bulk. The surface energy with water can be calculated by:

$$\gamma = \left(\frac{E_{s+H_2O} - \left(\frac{n_s}{n_b} E_b + n_{H_2O} E_{H_2O} \right)}{2A} \right) \quad (2.37)$$

where E_{s+H_2O} is the energy of the slab with water and n_{H_2O} is the number of water molecules and other parameters are the same as those in previous section.

2.2. Types of Surfaces

In this section we discuss types of surfaces that are simulated. Surfaces are created when a crystal lattice is cleaved in different crystallographic directions according to Miller indices. Following the classification of Tasker [70], there are three types of surfaces (see Figure 2.5):

1. Type I surface has a repeat unit cell where all the anions and cations in the same plane are in stoichiometric ratio. Each plane has no net charge meaning there is no dipole moment perpendicular to the surface (example MgO (100)).
2. Type II surface has a stacking sequence of charged planes, but the repeat unit consists of several planes, which when considered together have no dipole moment perpendicular to the surface (example CaF (111)).
3. Type III surface are made up of a stack of alternately charged planes and produce a dipole moment perpendicular to the surface if cut between any planes. In nature these surfaces are stabilized by defects and/or adsorbed species (example CaF (111)).

To be able to simulate type III the dipole needs to be removed, hence the reconstructed type III surface by [71]. One way of doing this is to remove half ions at the top layer and transferring them to the bottom of the unit cell

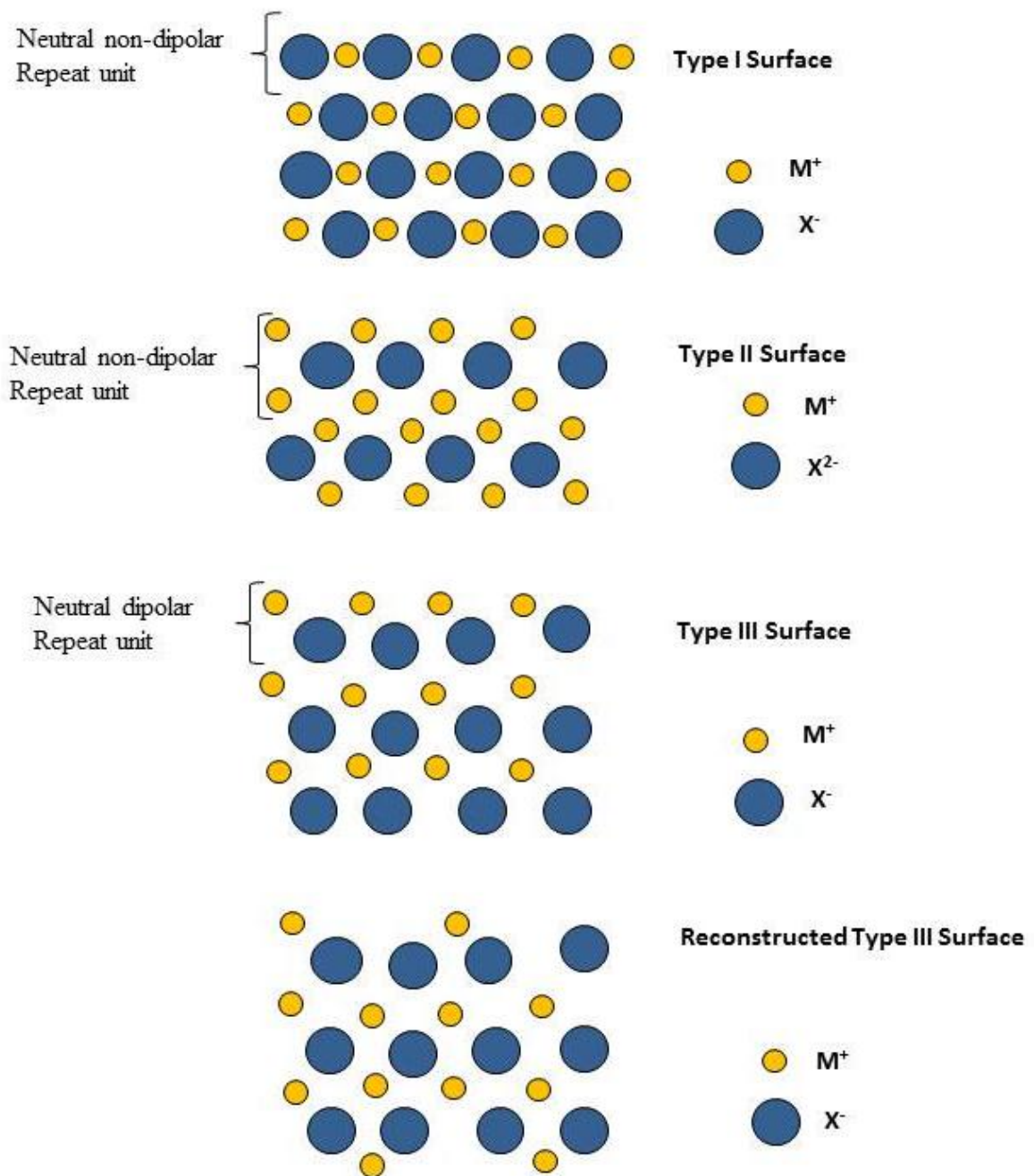


Figure 2.5: Three types of stacking sequences described by Tasker [70] and the reconstructed type III by Oliver et al, 1993 [71].

2.3. Crystal Morphology

From our calculated surface energies, we generated the equilibrium crystal morphology using METADISE. This technique was first introduced by Wulf [72] and Gibbs [73]. They proposed that the equilibrium form of a crystal should possess minimal surface energy for a given constant volume, which can be illustrated by the following equation:

$$\gamma = \sum_i \gamma_i A_i \quad (2.38)$$

where γ_i is the surface energy and A_i is the surface area of the i^{th} crystallographic face. They also suggested that the crystal morphology formed would be a result of h_i , the normal vector to the face from a point within a crystal, being proportional to the surface energy of the face, γ_i :

$$h_i = \lambda \gamma_i \quad (2.39)$$

where λ is a constant that depends on the absolute size of the crystal resulting in the crystal morphology. A schematic example of crystal morphology is shown in figure 2.4. The bold line indicates the equilibrium morphology for a case where the {100} and {110} surfaces have the same specific free energies and hence the same height, as the height of the face is directly proportional to its specific free energy [55]. In the final construction, high surface energies will not be present, because of the large growth rate resulting in a fast growing surface.

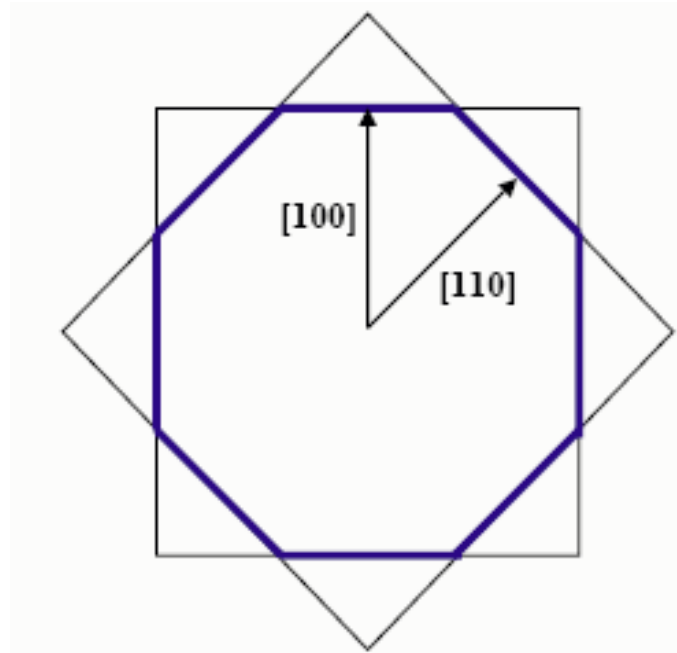


Figure 2.6: Schematic representation of equilibrium morphology due to two faces with equal specific free energy in two dimensions.

Chapter 3: Computational Models for Co₉S₈

In this chapter the description of quantum mechanical and atomistic simulation methods is given. Related approximations and derivation of potential models are discussed, together with their validation.

3.1. Quantum Mechanical Methods

Quantum mechanics calculations compared to other types of simulations are exceptional or outstanding, since it does not depend on any experimental data or other variable input but solely on the atomic number of the chemical species; hence it is by nature *ab initio* [74]. The last two decades have witnessed tremendous progress in the development of methods for *ab initio* calculations of materials properties and for simulations of processes in materials. The cornerstone of this development was laid by density-functional theory (DFT), which casts the intractable complexity of the electron–electron interactions in many-electron systems into an effective one-electron potential, which is a functional of the electron density only [75]. In this section we look at the theoretical background of *ab initio* methods.

3.1.1 Many-Body Schrödinger Equation

The aim of an *ab initio* method is to find the solution to the many-body Schrödinger equation for the system being studied. The quantum physics of electrons in materials is governed by the Schrödinger equation. The first simplification that we make is the

Born Oppenheimer approximation [76], whereby the electronic and nuclear degrees of freedom are separated. The justification for this is that the electrons are much less massive than the nuclei but experience similar forces and therefore the electrons will respond almost instantaneously to the movement of the nuclei. Thus, the energy for a given nuclear configuration will be that of the ground state of the electrons in that configuration. The equation we must solve is, therefore,

$$H\Psi = E\Psi \quad (3.1)$$

where Ψ is the many body wavefunction for the N electronic eigenstates, being an anti-symmetric function of the electronic coordinates $\{r_i : i=1\dots N\}$ and E is the total energy. The Hamilton H operator is given by

$$H = \sum_i -\frac{\hbar^2}{2m_e} \nabla_{r_i}^2 + V_{ext}(\{R_I\}) + V_{e-e}(\{r_i\}) \quad (3.2)$$

where V_{ext} is the external potential imposed by the nuclear configuration $\{R_I\}$ and V_{e-e} is the electron-electron coulombic interaction. In principle, this equation may be solved to arbitrary accuracy by representing Ψ as a direct product wavefunction and diagonalising the Hamiltonian. The total energy E can then be written as

$$E[\Psi] = \frac{\langle \Psi | H | \Psi \rangle}{\langle \Psi | \Psi \rangle} \quad (3.3)$$

where the variational principle states that the ground state is that given by minimisation of E over all possible $\Psi(\{r_i\})$. Quantum Monte Carlo techniques may then be used to evaluate $E[\Psi]$ [77] for a given wavefunction and perform the

minimisation over all possible wavefunction configurations [78] [79] [80] but these increases the computational cost still further.

3.1.2. Born-Oppenheimer Approximation

The Born-Oppenheimer approximation is used for electronic structure methods to separate the motion of the nuclei from that of the electrons, so that the problem is reduced to that of solving the equations of motion for an electron gas in a static potential [81]. Electrons are both faster and lighter than the nuclei; therefore the electronic wave functions depend upon the nuclear positions but not their velocities. This allows the nuclei to be described classically as fixed charges, becoming part of the external potential [82].

3.1.3. Density Functional Theory

Density functional theory (DFT) is a quantum mechanical modeling method used in physics and chemistry to investigate the electronic structure (principally the ground state) of many-body systems, in particular atoms, molecules, and the condensed phases. With this theory, the properties of a many-electron system can be determined by using functionals, i.e. functions of another function, which in this case is the spatially dependent electron density. Hence the name density functional theory comes from the use of functionals of the electron density. DFT is among the most popular and versatile methods available in condensed-matter physics, computational physics, and computational chemistry [83]. DFT is commonly used to calculate the many-body electronic interactions between atoms in molecules and in the solid state [84]. DFT is a quantum mechanical approach used in physics and chemistry, to investigate

the electronic structure of many-body systems. It is one of the most popular and versatile methods available in condensed matter physics, computational physics and computational chemistry. It is widely used to calculate the binding energy of molecules in chemistry and the band structure of solids in physics [85].

3.1.4. Approximation Exchange Correlation Functional

The drawback with the DFT is that the exact functional for exchange and correlation are only known for free electron gas. However, there are some approximations of this functional that are used and are known to allow the calculation of certain physical properties accurately.

Local Density Approximation (LDA)

Local density approximation (LDA) is the simplest form of approximating the exchange-correlation functional. With the LDA the exchange-correlation energy depends on the local electron density where the functional is evaluated:

$$E_{xc}^{LDA} = \int \rho(r) \varepsilon_{xc}[\rho(r)] dr \quad (3.4)$$

where $\varepsilon_{xc}[\rho(r)]$ is the exchange correlation energy per particle of an homogeneous electron gas at density $\rho(r)$.

Generalized Gradient Approximation (GGA)

However, for strongly correlated systems, such as semiconductors and metallic, the LDA is inadequate and is calculated to over bind [82]. So an alternative to LDA is the Generalised Gradient Approximation (GGA), which includes gradient correlations. GGA are still local but also take into account the gradient of the electron density at the same coordinate:

$$E_{xc}^{GGA} = \int \rho(r) \varepsilon_{xc} [\rho(r)] dr + \int F_{xc} [\rho(r), \nabla \rho(r)] dr \quad (3.5)$$

where ε_{xc} is the exchange correlation energy and $\nabla \rho(r)$ is the gradient term.

3.1.5. Convergence for Bulk Co₉S₈

In this section we study convergence of the of cobalt pentlandite (Co₉S₈) using the VASP code. The *ab-initio* code VASP was used for convergence of bulk Co₉S₈. Vienna *ab initio* Simulation Package (VASP) is a software package widely used by modelers to calculate the structure, energy and properties of molecule or a solid. It performs *ab-initio* quantum mechanical energy minimisation and molecular dynamics (MD) simulations using pseudopotentials or the projector-augmented wave method and a plane wave basis set [86]. The bulk Co₉S₈ was initially studied using DFT. We noted that the compound does not have a band gap. We use density functional theory to describe the electronic and magnetic structure of the Co₉S₈, which require the use of electronic structure techniques to determine. Initially, a standard DFT methodology was considered. Bulk Co₉S₈ was modelled in the *Fm3m* (225) space group. The first requirement was the selection of energy convergence parameters, the plane wave cut

off and the selection of a k-point. The calculations on different values of cut-off energy were determined until a constant energy is obtained. The plane wave cut-off energy for Co_9S_8 selected is 700 eV, which is suitably large as to ensure energy convergence. Figure 3.1 shows the graph of total energy against the k-points of the selected cut off. The quality of the approximation can then be assessed by further examination of the density of states and the band gap. We found that Co_9S_8 does not have band gap, which implies that the compound is predominantly metallic. The bulk structure of Co_9S_8 was optimized with 17 atoms. The theoretically optimized bulk cell constant using VASP is 9.811 Å, which compares well with the experimental values of 9.928 Å [37] and 9.930 Å [87].

We observed that the total energy for the unit cell is the same with or without spin-polarization, which shows that the bulk material is not magnetic. Figure 3.2 shows the graph of total energy as a function of plane wave cut-off energy for different k-points. Clearly, the total energy is the same for both the cut-off energy for different k-points (Table 3.1). These can also be observed from the density of states graph (Figure 3.2), of which the spin up and spin down graphs are the same. Sidik and Anderson [17] also found that the total energy for the bulk unit cell is the same with and without spin-polarization.

As explained in chapter 1, Co_9S_8 consists of two types of cobalt atoms: an octahedrally coordinated cobalt atom with six sulphur neighbours and a tetrahedrally coordinated cobalt atom forming a cubic array through coordination to three other cobalt neighbours.

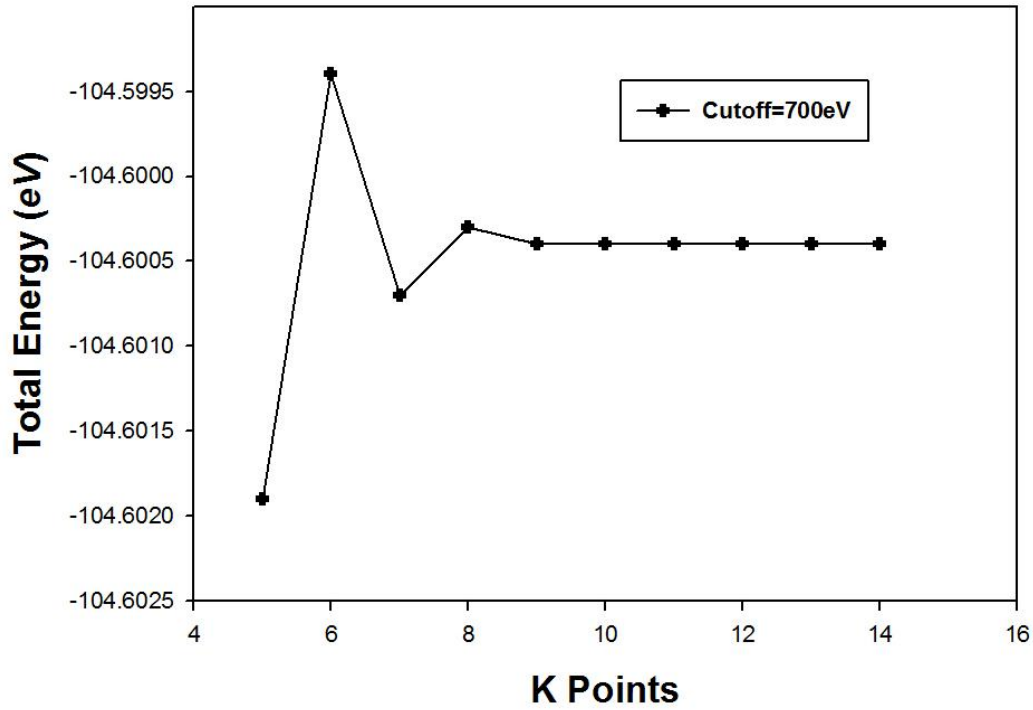


Figure 3.1: The graph of total energy against K points for the chosen cut off of 700 eV.

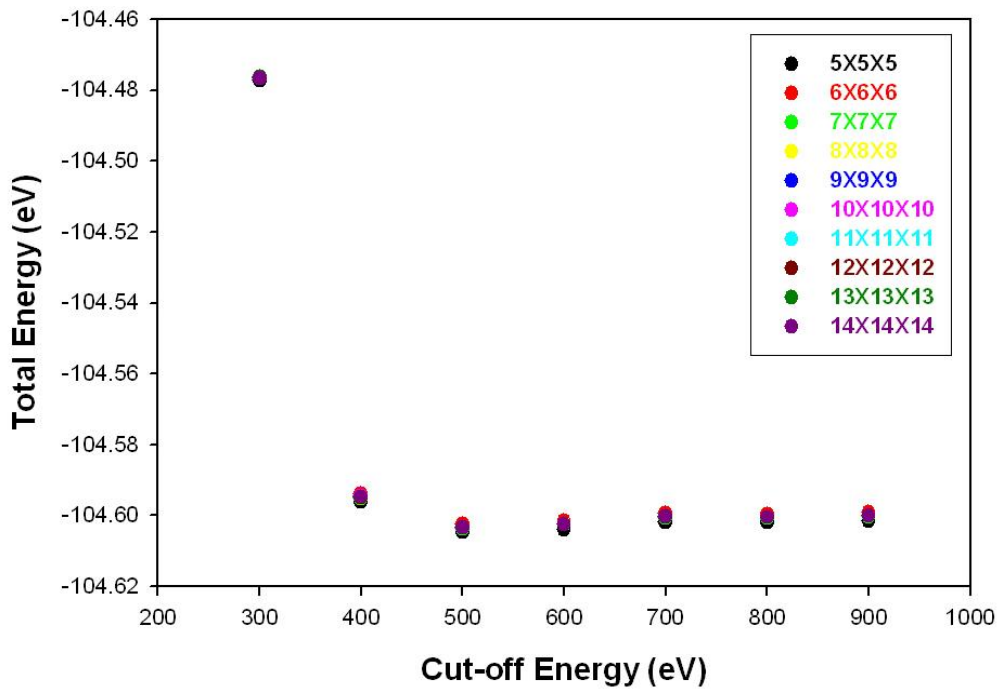


Figure 3.2: The graph of total energy against plane wave cut off energy for different k-points.

Table 3.1: Total energy of bulk Co_9S_8 as a function of plane-wave cut-off and density of k-point

Mesh	Etotal of bulk Co_9S_8						
	300eV	400eV	500eV	600eV	700eV	800eV	900eV
5x5x5	-104.4772	-104.5962	-104.6048	-104.6039	-104.6019	-104.6020	-104.6016
6x6x6	-104.4762	-104.5940	-104.6024	-104.6015	-104.5994	-104.5996	-104.5991
7x7x7	-104.4768	-104.5952	-104.6037	-104.6027	-104.6007	-104.6009	-104.6004
8x8x8	-104.4766	-104.5948	-104.6033	-104.6024	-104.6003	-104.6005	-104.6000
9x9x9	-104.4767	-104.5947	-104.6034	-104.6024	-104.6004	-104.6006	-104.6001
10x10x10	-104.4765	-104.5947	-104.6034	-104.6024	-104.6004	-104.6006	-104.6001
11x11x11	-104.4767	-104.5948	-104.6034	-104.6024	-104.6004	-104.6006	-104.6001
12x12x12	-104.4766	-104.5948	-104.6034	-104.6024	-104.6004	-104.6006	-104.6001
13x13x13	-104.4764	-104.5948	-104.6034	-104.6024	-104.6004	-104.6006	-104.6001
14x14x14	-104.4767	-104.5948	-104.6034	-104.6024	-104.6004	-104.6006	-104.6001

In the next section the atomistic potential functions and interatomic potential model used in this work are discussed.

3.2. Atomistic Potential Model

Atomistic potential models describe the variation in the energy of the molecule or solid as a function of atomic coordinates [43]. The reliability of the calculations depends on the quality and accuracy of the potential model. The potential model; describes the interactions between two or more species. The different Coulombic summation schemes that have been employed are described. Finally, the potential functions used in this study are presented and all the potential parameters are discussed.

3.2.1. The Born Model of Solids

The atomistic simulation techniques used in this study are based on the Born model of solids [49]. In this model, it is assumed that the energy and its derivatives can be defined as the summation of all interactions between the atoms in the system which gives rise to the total interaction and total net force acting on each atom due to others [73]. Furthermore, the atoms of a system are represented as point-charge particles that interact via long-range electrostatic forces and short-range interactions. Hence, the interaction energy between two ions is obtained by

$$\phi_{ij} = \frac{1}{4\pi \epsilon_0} \frac{q_i q_j}{r_{ij}} + \Phi(r_{ij}) \quad (3.6)$$

where the first term represents the long-range Coulombic interactions, ϵ_0 is the permittivity of vacuum, q_i and q_j are the ionic charges, and r_{ij} is the interatomic distance. The second term, $\Phi(r_{ij})$, describes the short-range interactions between ions, which include the repulsion between the electron charge clouds and the van der Waals attraction forces.

The interaction energy of a system is the sum of the pairwise interactions between all ions i and j . Where appropriate, many-body terms are also included to take into account, for example, deviations from equilibrium bond angles. Thus, the overall interaction energy of a system can be written in terms of the atomic positions

$$\phi_i = \sum_i^N \sum_{\substack{j \\ j \neq i}}^N \frac{1}{4\pi \epsilon_0} \frac{q_i q_j}{r_{ij}} + \sum_i^N \sum_{\substack{j \\ j \neq i}}^N \Phi(r_{ij}) + \sum_i^N \sum_{\substack{j \\ j \neq i}}^N \sum_{\substack{k \\ k \neq i \\ k \neq j}}^N \Phi_{ijk}(r_{ijk}) \quad (3.7)$$

The first term of the equation (3.7), the Coulombic energy of the system, cannot be obtained by simply summing all the pairwise electrostatic interactions. This is because

the contribution of the point-charges to the electrostatic potential decays as $1/r$, which causes the Coulombic term to converge very poorly. Therefore, the electrostatic interactions are calculated using summation methods, such as the Ewald sum for example, as described later in this chapter. The other terms of equation 2, the short-range interactions, converge much faster and thus can usually be calculated by a simple summation.

3.2.2. Long Range Interactions

Coulombic Simulation

The electrostatic interactions between charged particles are long-ranged and hence a particle i will interact with all other particles j in the simulation box and also, with the periodic images of these particles, including those of i . Therefore, the Coulombic contribution, ϕ_i to the interaction energy is

$$\phi_i = \frac{1}{2} \left(\frac{1}{4\pi \epsilon_0} \right) \sum_n \sum_{i=1}^N \sum_{j=1}^N \frac{q_i q_j}{|r_{ij} + nL|} \quad (3.8)$$

where q_i and q_j represent the charges on particles i and j , r_{ij} is the interatomic distance, ϵ_0 is the permittivity of free space, and L is the set of simulation cell vectors reflecting the periodicity of the simulation box. The sum over n is the sum of all the periodic images where n is the ordered triple of integers that define the periodic images, where n is the ordered triple of integers that define the periodic images of the simulation cell. The prime on the first summation indicates that $i = j$ is ignored for $n = 0$. The problem is that the sum in (Equation 3.3) is very slow to converge due

to the $1/r$ term. Therefore, one needs a quicker and more reliable summation scheme such as Ewald summation.

Ewald Summation

Ewald summation [88] is an excellent technique for calculating electrostatic interactions in periodic systems in three-dimension and is an efficient technique for summing the interaction between an ion and all its infinite periodic images. This method divides the Coulombic potential into three separate parts, i.e. a term in reciprocal space, ϕ_1 , a real space term, ϕ_2 , and a self-interaction term ϕ_3 , where:

$$\phi = \phi_1 + \phi_2 + \phi_3 \quad (3.10)$$

In the Ewald method, every particle, of charge q_i , is assumed to be surrounded by a spherically symmetric charge distribution of opposite sign, which exactly cancels q_i and is usually taken to be a Gaussian distribution such as

$$\rho_i(r) = -q_i \left(\frac{\alpha}{\pi} \right)^{3/2} \exp(-\alpha r^2) \quad (3.11)$$

where the arbitrary parameter α determines the width of the distribution, and r is the position relative to the centre of the distribution. Therefore, only the fraction of q_i that is not screened contributes to the electrostatic potential due to the particle i . At long distances, this fraction rapidly converges to zero and the screened interactions are thus short-ranged. Therefore, the electrostatic interactions between these screened charges can now be calculated by direct summation in real space.

The total contribution of the screened Coulombic interactions, ϕ_i to the interaction energy is then given by

$$\phi_2 = \frac{1}{2} \left(\frac{1}{4\pi \epsilon_0} \right) \sum_n \sum_{i=1}^N \sum_{j=1}^N \frac{q_i q_j}{|r_{ij} + nL|} \times \text{erfc}(\alpha |r_{ij} + nL|) \quad (3.12)$$

where erfc is the complementary error function

$$\text{erfc}(x) = 1 - \frac{2}{\sqrt{\pi}} \int_0^x \exp(-t^2) dt \quad (3.13)$$

The rate of convergence of Equation 3.12 is dependent on the width of the cancelling Gaussian distribution, defined by α ; the wider the Gaussians; the faster the series converges, as Equation 3.13 tends to zero with increasing x .

The contributions of the charge distributions to the electrostatic potential, ϕ_1 are calculated by summing their Fourier transforms in reciprocal space, further detail is given in Kittel (1963) [89]:

$$\phi_1 = \frac{1}{2} \sum_{k \neq 0} \sum_{i=1}^N \sum_{j=1}^N \frac{1}{\pi \lambda^3} \frac{q_i q_j}{4\pi \epsilon_0} \frac{4\pi^2}{k^2} \exp\left(-\frac{k^2}{4\alpha^2}\right) \cos(K \cdot r_{ij}) \quad (3.14)$$

where the vectors K are reciprocal vectors and given by $K = 2\pi n / \lambda$. This expression ignores the term when $k = 0$, which can be neglected provided the net charge on the unit cell is zero. Although this reciprocal sum converges much more rapidly than the original point charge sum, the number of terms that need to be included increases with the width of the Gaussians. The ϕ_1 summation includes the interaction between the continuous Gaussian charge cloud of charge q_i with itself. The self-interacting component, ϕ_3 , must be subtracted. The self-interaction term is defined as:

$$\phi_3 = -\frac{\alpha}{\sqrt{\pi}} \sum_{k=1}^N \frac{q_k^2}{4\pi \epsilon_0} \quad (3.15)$$

Three parts of the electrostatic interaction can then be summed to give the overall Coulombic interaction using Equation 3.4.

Parry Summation

The Parry summation [90] [91], which is a modification of the Ewald method was used in this study, in the simulations of surfaces, which are two dimensional periodic systems. In this method, the crystal is assumed to consist of a series of charged planes of infinite size rather than an infinite lattice. When summing the electrostatic interactions the vectors are now divided into in-plane vectors and vectors perpendicular to the plane. Hence the reciprocal space term needs to be modified to account for the fact that the overall charge of a plane of atoms can be different from zero. The detailed derivation of the reciprocal space term can be found in reference [92].

3.2.3. Short Range Interactions

The short range interactions consist of different contributions. At small distances electron charge clouds will start to interact strongly and therefore will repel each other. Also, at these distances, the dipole-dipole interactions, due to fluctuating dipoles on each ion, will result in attractive van der Waals forces. In addition, when considering covalent systems, the short-range interactions between three or more ions can also be included in the model to represent directionality in the bonding. In this work, the short-range attractive and repulsive interactions are described by simple parameterised potential functions. The potential parameters can be derived empirically by fitting to experimental data, such as crystallographic positions, elastic or dielectric properties, and infrared frequencies, or, by fitting to more accurate simulations such as electronic calculations.

One of the issues that will be addressed in this thesis is that of the transferability of potential parameters. Can potential parameters be employed to model systems that are significantly different from those they have been derived for? In Chapter 5, it will be shown that potential parameters derived will demonstrate the interactions between water and nanoparticle.

Lennard-Jones Potential

The Leonard-Jones potential is often used to describe the intermolecular interactions and takes the form:

$$U(r_{ij}) = \frac{A_{ij}}{r_{ij}^n} - \frac{B_{ij}}{r_{ij}^m} \quad (3.16)$$

where the most common values for n and m are 12 and 6, respectively. The first term represents the repulsion between electronic clouds, which dominates at very short distances. The second term is the attractive part of the potential and models the van der Waals dispersion forces, which dominate at larger distances.

To facilitate the parameters (n and m) fitting process, the Lennard-Jones potential can also be written as:

$$U(r_{ij}) = \frac{E_0}{(n-m)} \left[m \left(\frac{r_0}{r_{ij}} \right)^n - n \left(\frac{r_0}{r_{ij}} \right)^m \right] \quad (3.17)$$

Buckingham Potential

In the Buckingham potential, the repulsive term is replaced by an exponential term and potential takes the form

$$U(r_{ij}) = A_{ij} \times \exp\left(\frac{-r_{ij}}{\rho_{ij}}\right) - \frac{C_{ij}}{r_{ij}^6} \quad (3.18)$$

Where A_{ij} and ρ_{ij} are parameters that represent the ion size and hardness, respectively. The first term is known as the Born-Mayer potential and the attraction term was later added to form the Buckingham potential. Very often, for the cation-anion interactions, the attractive term is ignored due to the very small contribution of this term to the short-range potential, or, alternatively, the interaction is subsumed into the A and ρ parameters.

Morse Potential

The Morse potential is used to model the interactions between covalently bonded atoms and has the form

$$U(r_{ij}) = A_{ij} \times (1 - \exp(-B_{ij} \times (r_{ij} - r_0)))^2 - A_{ij} \quad (3.19)$$

where A_{ij} is the bond dissociation energy, r_0 is the equilibrium bond distance, and B_{ij} is a function of the slope of the potential energy well. The Coulombic interactions between covalently bonded atoms are often partially or totally ignored as the Morse potential already contains the attractive component of the interaction between neighbours.

Three-Body Potential

A further component of the interactions of covalent species is the bond-bending term, which is added to take into account the energy penalty for deviations from the equilibrium value. Hence, this potential describes the directionality of the bonds and has a simple harmonic form:

$$U(\theta_{ijk}) = \frac{1}{2} k_{ijk} (\theta_{ijk} - \theta_0)^2 \quad (3.20)$$

where k_{ijk} is the three-body force constant and θ_0 is equilibrium angle

Shell Model Potential

The shell model is different from previous models; it includes the electronic polarisation of the atoms. The shell model was developed by Dick and Overhauser in 1958 [93]. In this model the ion is described by a core and a shell. The core, which contains all the mass of the ion, is attached to the shell by harmonic spring. The shell has no mass and models the electronic charge cloud. The core has all the ion's mass and determines the position of the ion. The total charge of the ion is shared between the core and the shell. The core has the positive charge and the shell a negative charge; however there exist potentials for highly oxidised cations that have positive charges on the shell. Figure 3.3 shows a schematic representation of the shell model.

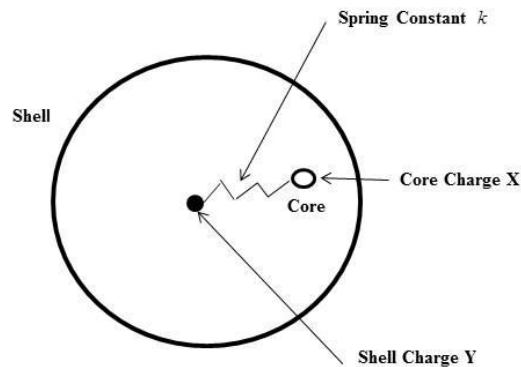


Figure 3.3: Schematic representation of the shell model.

The ion electronic polarisability, α , is related to the shell charge, Y , and the spring constant, k , by

$$\alpha = \frac{Y^2}{k} \quad (3.21)$$

The parameters Y and k are obtained by empirical fitting to dielectric constants, elastic constants or phonon dispersion curves. The disadvantage of shell model is that the number of species in the computer simulation is doubled; hence the calculations become computationally expensive.

The remainder of the chapter tackle the methods of deriving the potentials and the potentials used in this work.

3.3. Derivation of Interatomic Potentials

Deriving interatomic potentials or force fields is one of the challenges when using the force fields methods. The derivation of model parameters is critical to any successful simulation [94]. There are a number of potentials in the literature for other materials, i.e. TiO_2 [95], FeS_2 [96], MnO_2 [97], but to the best of my knowledge, they are no reported interatomic potentials for the Co_9S_8 .

There are two approaches of deriving force fields. The first approach is to adjust the parameters to fit experimental data. This approach depends on the availability of a range of experimental data. The second approach of fitting the potentials parameters is by adjusting the parameters to reproduce *ab-initio* electronic structure data; this is done by adjusting the energy with respect to atomic position. Nowadays with the advancement of computer technologies [98][99] and the development of good *ab-initio* softwares, such as VASP code [100], CASTEP code [25] and SIESTA code [101], this approach is being used more often. In the past the first approach was favoured, because the electronic structure calculations were time consuming and because of lack of powerful computers then, hence computationally expensive.

Nevertheless, both approaches use the same principle, which is to derive a model that can accurately reproduce the available data. Data can be elastic constants, bulk moduli, dielectric constants or phonon frequencies. In performing a fit, it is important to define a quantity that measures the quality of results known as the sum of squares F :

$$F = \sum_{i=1}^{N_{obs}} w (f_i^{obs} - f_i^{calc})^2 \quad (3.22)$$

where N_{obs} is the number of observables, f_i^{obs} and f_i^{calc} are the fitted and calculated values of the observable, respectively, and w_i is the weighting factor for the observable. There are several criteria of knowing how to choose an appropriate and sensible weighting factor. Firstly, the weighting factor should be inversely proportional to the uncertainty in the measured value, when fitting for experimental data. Secondly, to ensure that all the values are fitted on an equal footing, regardless of units, the weighting factor should be inversely proportional to the magnitude of the observable squared. The process of fitting involves minimising the value of F , through the variation of potential parameters. To do this, we use the default approach which is similar to that used in optimisation. A commonly used approach is a Newton-Raphson minimisation via the simulation package GULP (General Utility Lattice Package) [102].

3.4. The Atomistic Potentials Used In This Work

As with any atomistic simulation, the accuracy and reliability of the results depend, ultimately, on the quality of the interionic potentials [103]. In this section, a simple two-body potential function based on the Born model of ionic solids was used. As

with most of MD simulations, the shell model (used to approximate electronic polarization effects) was not incorporated because of the significant increase in computational time that would ensue; as such all particles were assumed to be rigid ions. We report on the derivation of interatomic potentials which were finally tested by comparison of structural results with experimental values. Furthermore, molecular dynamics (MD) calculations, based on such potentials, using the DLPOLY code, were carried out in particular to assess their reliability at high temperatures. The corresponding structural properties of our calculated parameters are in agreement with the experimental and other calculated results.

The experimental structural parameters were used as inputs for derivation of the potential model. Furthermore, charge density differences of Co_9S_8 calculated by Chauke [MSc Thesis] [104], guided us on the choice of models to represent the interactions of ions. The charge density differences of Co_9S_8 reflect much directional bonding between the metal cobalt and sulphur atoms and the charge difference maps show charge accumulation between the sulphur and metal ions which indicate a predominance of covalent bonding, hence the choice of Morse potential to model the interaction of cobalt and sulphur atoms. Elastic properties were calculated by *ab-initio* methods (shown in Table 3.2), in the current study, to assist in the fitting since no experimental results are available.

Table 3.2: Calculated elastic constants of Co_9S_8 .

Elastic Constants (GPa)	C_{11}	C_{12}	C_{44}
	223.8	71.3	80.3

In addition, the electronic density of states (DOS) were determined by ab initio methods and plotted on a scale of $E - E_f$, where, E is the energy and E_f the Fermi energy (the energy of the highest occupied electronic energy level). The DOS for Co_9S_8 , in Figure 3.4 has no bandgap and consequently demonstrates a metallic character, owing to the presence of Co-Co bonds. Ramos *et al* [24] also found that the DOS of Co_9S_8 presents a metallic character using the DFT code CASTEP.

A number of different potential models were derived and tested to determine their suitability for predicting properties of Co_9S_8 . Apart from the potential model used in the current study (see Table 3.3); there are other models which were able to reproduce the structure of Co_9S_8 , though to a lesser degree of accuracy. The two models are listed in Table B1 as Model 1 and Table B2 as Model 2 under Appendix B. Model 1 was able to reproduce the structure and elastic constants; however the shear modulus

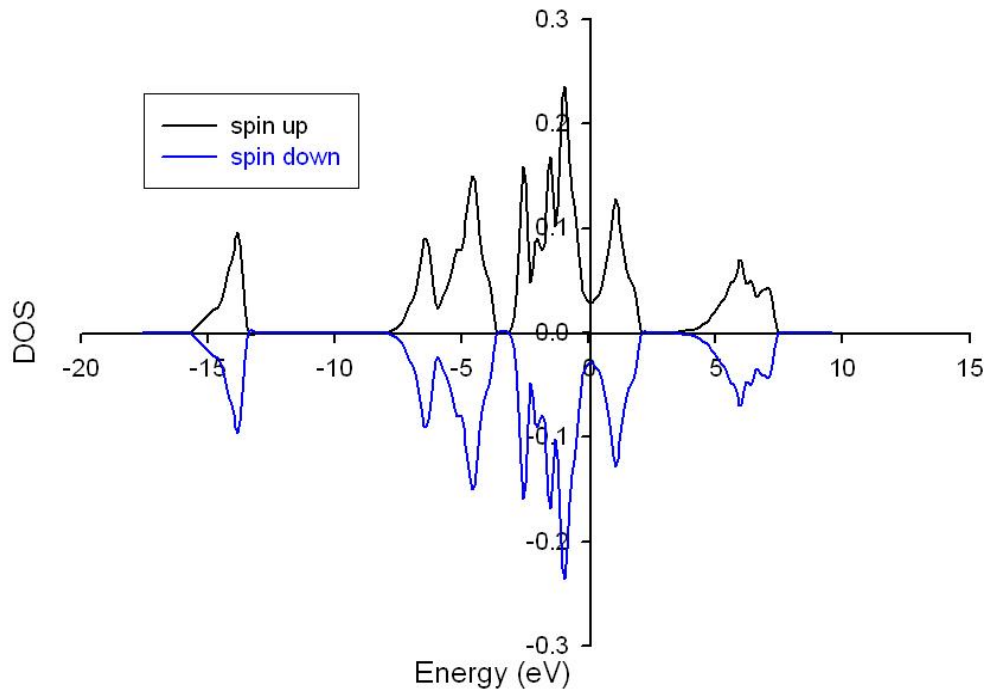


Figure 3.4: The total density of states of bulk Co_9S_8 .

was very low. In case of Model 2, the C_{11} and C_{12} were very low as compared to the observables; however the model was able to reproduce the structure. After a significant effort of fitting and optimization (which took about 2 years), we finally found a model that reproduced properties of Co_9S_8 reasonably well. It consisted of the Buckingham potential modelling the interaction between S-S ions and the Morse potential modelling the interaction between Co-S ions, together with two potential terms taking into account of the Co-S-S and S-Co-Co three-body bond-bending of the covalent bond. Such derived interatomic potentials of Co_9S_8 are given in Table 3.2, and these are, thus far, the best potentials after a considerable developmental effort. The water potential used in this work is a modified version of the de Leeuw and Parker potential. [105]. Table 3.4 shows the water potentials. This potential model uses the core-shell description for the oxygen atom (in our model it was not included, as such the model was modified to be a rigid ion model); and was used successfully to simulate the pyrite surfaces with the original potentials [96]. They were also employed to model surfaces of other structures, magnesium oxide surfaces [105] and α -quartz [106] and calcite, aragonite and vaterite [107]. Table 3.5 shows the potential parameters for the cobalt pentlandite (Co_9S_8) interaction with the water potentials.

Table 3.3: Interatomic potential parameters for the Cobalt pentlandite (Co₉S₈) as derived in the present study.

Species	Charge (e)			
Cobalt (Co)	+0.40			
Sulphur (S)	-0.45			
Buckingham potential	$A(eV)$	$\rho(\text{\AA})$	$C(eV/\text{\AA}^6)$	$Cut-off(\text{\AA})$
Co core – S core	1130.53064	0.184528	0.0	20.0
Morse Potential	$D(eV)$	$\alpha(eV)$	$r_0(\text{\AA})$	
S core – S core	3.0	1.47	2.6	
Three-body potential	$k(eV/rad^{-2})$		$\theta_0(^{\circ})$	
Co core – S core – S core	3.541/2.89		109.503	
S core – Co core – S	0.694/0.82		109.503	

Table 3.4: Water potential parameters [105].

WATER				
Ion	Charges (e)		Core-Shell	
	Core	Shell	Interactions ($eV \text{ \AA}^{-2}$)	
Water Oxygen (Ow)	+1.250	-2.050	209.449602	
Water Hydrogen (Hw)	+0.400	-	-	
BUCKINGHAM POTENTIALS				
Ion pair (ij)	$A_{ij}(eV)$	$\rho_{ij}(\text{\AA})$	$C_{ij}(eV\text{\AA}^6)$	
Hw-Ow	396.27	0.250	10.0	
LENNARD-JONES POTENTIALS				
Ion pair (ij)	$A(eV\text{\AA}^{12})$		$B(eV\text{\AA}^6)$	
Ow-Ow	39344.98/252446.059		42.15/25.80524056	
MORSE POTENTIALS				
Ion pair	$D_{ij}(eV)$	$\alpha_{ij}(eV)$	$r_0(\text{\AA})$	Coulombic Substraction (%)
Ow-Hw	6.203713	2.22003	0.92367	50
Hw-Hw	0.00000	2.8405	1.50000	50
THREE-BODY POTENTIALS				
Ions	$k(eVrad^{-2})$		$\theta_0(^{\circ})$	
Hw-Ow-Hw	4.19978		108.693195	

Table 3.5: Potential parameters for the cobalt pentlandite-water interactions.

BUCKINGHAM POTENTIALS			
Ion pair (ij)	$A_{ij}(eV)$	$\rho_{ij}(\text{\AA})$	$C_{ij}(eV\text{\AA}^6)$
Co-Ow	483.04	0.30840	0.0
S-Hw	495.38	0.25000	0.0
S-Ow	1421.67	0.3308	64.1040

3.5. Validation of the Atomistic Potentials Model

3.5.1. Structural and Elastic Properties

In this section we consider the validation of our derived interatomic potential model for Co_9S_8 . The bulk Co_9S_8 is cubic and has a space group of $Fm\bar{3}m$ (225) with the lattice parameter $a = 9.923 \text{ \AA}$ [42]. In a unit cell, cobalt atoms occupy $1/8^{\text{th}}$ of the available octahedral and half ($1/2$) of the tetrahedral sites. One out of every nine cobalt atoms one is in an octahedral position, with the rest occupying pseudo-tetrahedral site [23]. Figure 3.3 shows the cubic unit cell of bulk Co_9S_8 .

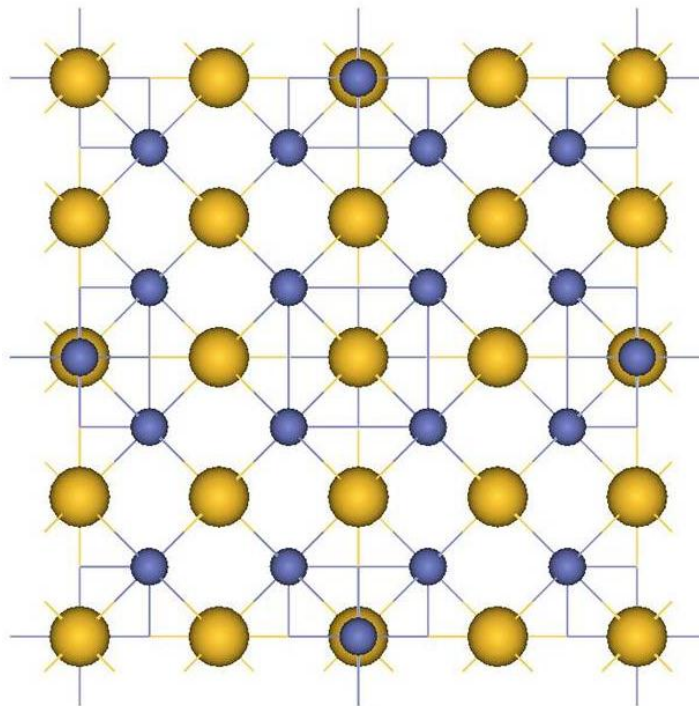


Figure 3.3: Cubic unit cell of bulk Co_9S_8 .

The potential models are developed to simplify the complexity of the quantum mechanical computations. For example, even a semi-qualitative force field or

potential model can be used to identify the most probable surfaces, and hence reduce the number of surfaces that need to be examined using quantum mechanical methods. The elastic constants, calculated by quantum mechanics, were used as input data for the development of potentials models. The accuracy of the derived interatomic potentials was first checked by comparing the known experimental and calculated data. To validate our potential models we start by showing the properties that were obtained from our derived potentials i.e., lattice parameters, interatomic distances, and elastic properties.

Table 3.5 shows the calculated lattice parameters obtained from different methods. The lattice parameters obtained using energy minimisation codes GULP and METADISE are smaller than those from the literature, but still within the acceptable range of 2%.

Table 3.5: Comparison of the lattice parameter of Co_9S_8 , obtained from the derived interatomic potentials, with the other calculated and experimental values.

Method	Parameter $a(\text{\AA})$
Potential Model (This Work)	9.806
VASP (PW-GGA) (This Work)	9.811
*TB-LMTO ^a	9.918
VASP ^b (US-PP) **	9.865
Extended Huckel Type Band Calculations ^c	9.927
EXPERIMENTAL ^d	9.977

^a[23], ^b [22], ^c[39], ^d[40]

**Tight-binding linear-muffin-tin-orbital*

***Ultra-soft pseudo potentials*

Table 3.6 shows the interatomic distances calculated from the derived model as compared with the other calculated as well as the experimental interatomic distances. Our calculated interatomic distances are smaller than other calculated and experimental values by less than 1% while the S-S interatomic distance is larger by acceptable difference of less than 4%. The experimental interatomic distances by Geller [37] are discussed below. There are two kinds of cobalt atoms in the structure: one is surrounded by a regular octahedron of sulphur atoms with Co-S distance, 2.39 Å; the other is surrounded by a tetrahedron of S atoms, one Co-S distance being 2.13 Å, and the other three being 2.21 Å. Each of the cobalt atoms with tetrahedral sulphur coordination is also linked to three similarly coordinated cobalt atoms at a distance of 2.50 Å which is essentially the Co-Co distance in the elementary cobalts.

Table 3.6: Comparison of the interatomic distances (Å) calculated from the derived model with other calculated and experimental results.

	GULP	VASP	Calculated [22]	Experimental [37]
	(This Work)	(This Work)		
Co-S2 (O)*	2.363	2.350	2.389	2.392
Co-S1 (T)*	2.094	2.130	2.130	2.132
Co-S2 (T)	2.184	2.230	2.206	2.208
Co-Co (T)	2.485	2.500	2.499	2.501
S-S	3.497	3.330	3.379	3.362

* (O) denotes the octahedral site and (T) denotes the tetrahedral sites

Table 3.7 shows a comparison of the elastic properties of Co₉S₈ we calculated using DFT methods (VASP code) and those calculated from our derived interatomic potentials employing the GULP and METADISE codes; experimental elastic constants are currently not available for Co₉S₈. The elastic constants from the

interatomic potentials are in good agreement with those from DFT calculations, together with the various moduli of elasticity, i.e. the bulk, shear, elasticity moduli and Poisson's ratio. In addition, the Co₉S₈ phase has elastic constants that satisfy the generalized elastic stability criteria for cubic crystals [108] [109]:

$$\begin{aligned} (C_{11} - C_{12})/3 &> 0, \\ C_{11} + 2C_{12} &> 0, \\ C_{44} &> 0 \end{aligned} \quad (3.23)$$

Table 3.7: Calculated elastic constants and moduli of the Co₉S₈ phase.

	Observables (VASP)	GULP (Fitted)	METADISE
C ₁₁	223.8	214.3	203.7
C ₁₂	80.3	82.3	83.9
C ₄₄	71.3	70.0	58.9
Bulk Modulus, <i>B</i> (GPa)	128.1	126.3	123.9
Shear Modulus, <i>G</i> (GPa)	71.5	68.4	59.3
Elastic Modulus, <i>E</i> (GPa)	180.8	173.8	153.4
Poisson Ratio, <i>v</i>	0.26	0.27	0.29
Volume (Å ³) *		947.6	940.2

*Experimental Volume is 978.56 Å³ [36]

The bulk modulus *B*, shear modulus *G* and elastic modulus *E* of the cubic Co₉S₈ phase were deduced according to the following formulae [110] [111] [112] [113].

$$B = \frac{1}{3}(C_{11} + 2C_{12}) \quad (3.24)$$

$$G = \frac{1}{5}(C_{11} - C_{12} + 3C_{44}) \quad (3.25)$$

$$E = \frac{(C_{11} - C_{12} + 3C_{44})(C_{11} + 2C_{12})}{2C_{11} + 3C_{12} + C_{44}} \quad (3.26)$$

Poisson ratio ν is obtained from:

$$\nu = \frac{3B - E}{6B} \quad (3.27)$$

3.5.2. Phonon Calculations of Co₉S₈

Phonons play a major role in many of the physical properties of solids, including a material's thermal and electrical conductivities. They are a quantum mechanical description of a special type of vibrational motion, in which a lattice uniformly oscillates at the same frequency. In classical mechanics this is known as normal mode [114]. Phonon calculations are exact at the zone centre for a single unit cell and for a supercell composed of more unit cells at the wave vectors commensurate with the supercell. In practice, a phonon calculation is converged if the force constants between an atom at the centre of the supercell and those at the cell boundaries are effectively zero [115].

The phonon calculations of Co₉S₈ cubic phase were executed using the VASP code [86] [116] [117] [118]. This density functional calculation uses the Perdew-Burke-Emzerhot (PBE) Generalized Gradient Approximation (GGA) [119] for the exchange correlation functional. All atoms were described with pseudopotentials taken from the VASP library and developed on plane waves basis sets using the Projector Augmented Wave (PAW) method [120] [121]. The recommended energy cutoff (410 eV) for the plane wave basis set and the K-point mesh [122] of 5x5x5 was used; which corresponds to a k-point spacing of 0.219 per Å. For the optimisation of atom

positions, we used a supercell of 17 atoms. The first order Methfessel-Paxton smearing scheme [123] with a smearing width of 0.2 eV was used to help smooth the Fermi surface and accelerate total energy convergence.

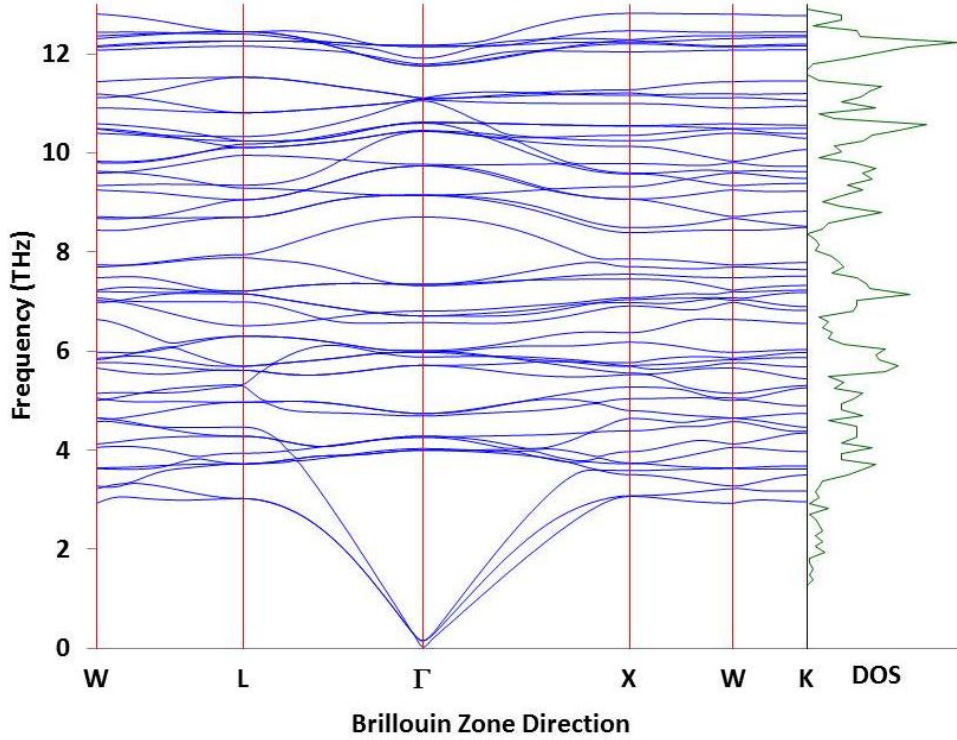


Figure 3.4: Phonon DOS and dispersion curve of Co₉S₈ phase.

Figure 3.4 shows the phonon dispersion curve and the total density of states (DOS) of the Co₉S₈ phase which allude to the stability of the system. This is deduced from all phonon branches lying above 0 THz, implying that there are no soft modes encountered along high symmetry directions. This is an indication that the Co₉S₈ phase is stable. Co₉S₈ contains 17 atoms ($N = 17$) per unit cell and Figure 3.4 shows that there are 3 acoustical branches (1 longitudinal and 2 transverse) occurring at the lower part of the phonon dispersion curve, and $3N - 3 = 48$ optical branches ($N - 1 = 16$ longitudinal and $2N - 2 = 32$ transverse). The phonon density of states for Co₉S₈ phase for both the partial DOS and total DOS are shown in Figure 3.6.

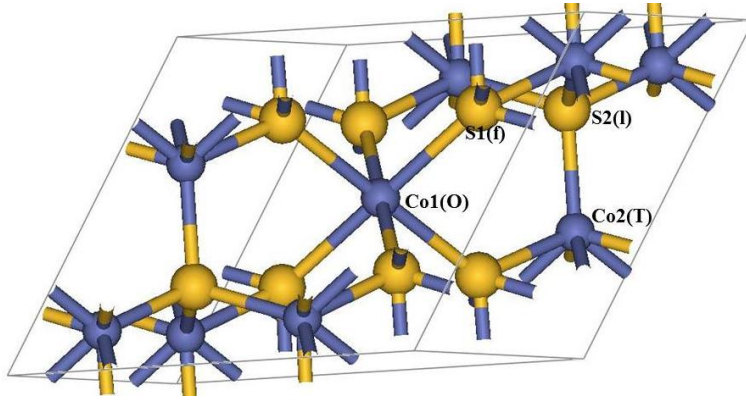


Figure 3.5: The primitive unit cell of Co_9S_8 . Co1 (O) is octahedral type 1 cobalt; Co2 (T) is tetrahedral type 2 cobalt; S1 (l) is linking type 1 sulphurs; S2 (f) is face-capping type sulphurs.

The Co and S atoms vibrate at different frequencies for various types of atoms. The primitive unit cell of Co_9S_8 illustrating the different types of cobalt and sulphur atoms are shown in Figure 3.5. As mentioned earlier in the thesis, in terms of the bonding properties of Co_9S_8 , the S atoms are held together mainly through bonding with Co, the octahedrally coordinated Co1 (O) atoms are held together through bonding with S, while tetrahedrally coordinated Co2 (T) atoms are held together through bonding with S as well as through bonding between the special Co2 (T)-Co2 (T) pair [40].

The total phonon density of states of Co_9S_8 , calculated quantum mechanically by the VASP code, is given in Figure 3.6 a) and is compared with that determined by the GULP code (Figure 3.6 b) using our derived interatomic potentials. Although not all finer details are reproduced, some features such as distinct peaks of the densities of states from the two methods, marked A to H can be correlated. Some differences are noted especially with intensities of DOS peaks. Larger K point grids in GULP calculations could not improve the correspondence of the DOS from the two codes. Hence the differences can be ascribed to the simulation of our potential model. The quantum mechanical partial phonon density of states, given in Figure 3.7, can assist in ascribing the peaks to vibrations of specific types of atoms.

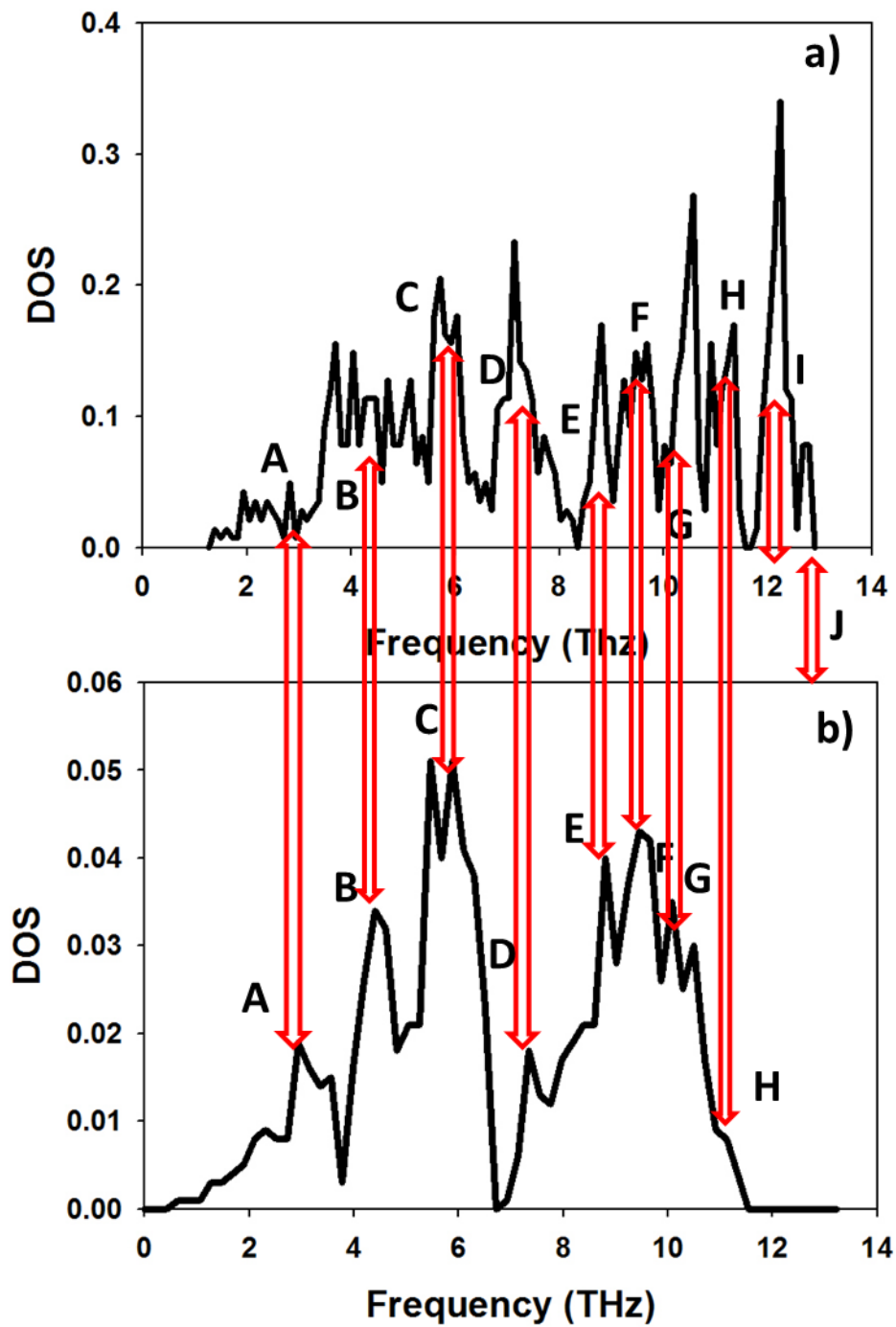


Figure 3.6: A comparison of the total phonon densities of states (DOS) of Co_9S_8 calculated using a) ab initio method with the VASP code and b) our derived interatomic potentials using the GULP program.

The lower frequency peak below A (2-3 THz) is mainly attributable to the vibration of the Co2 and slightly that of the S2 atoms. The peaks ranging from B to C (3-6 THz) are dominantly associated with the vibration of the Co1 atom and with smaller contributions related to Co2, S1 and the y component of the S2 atoms. The peaks spanning C-D (6-7.4 THz) are ascribed to the Co2 and to a lesser degree the z component of vibration of the S2 atoms.

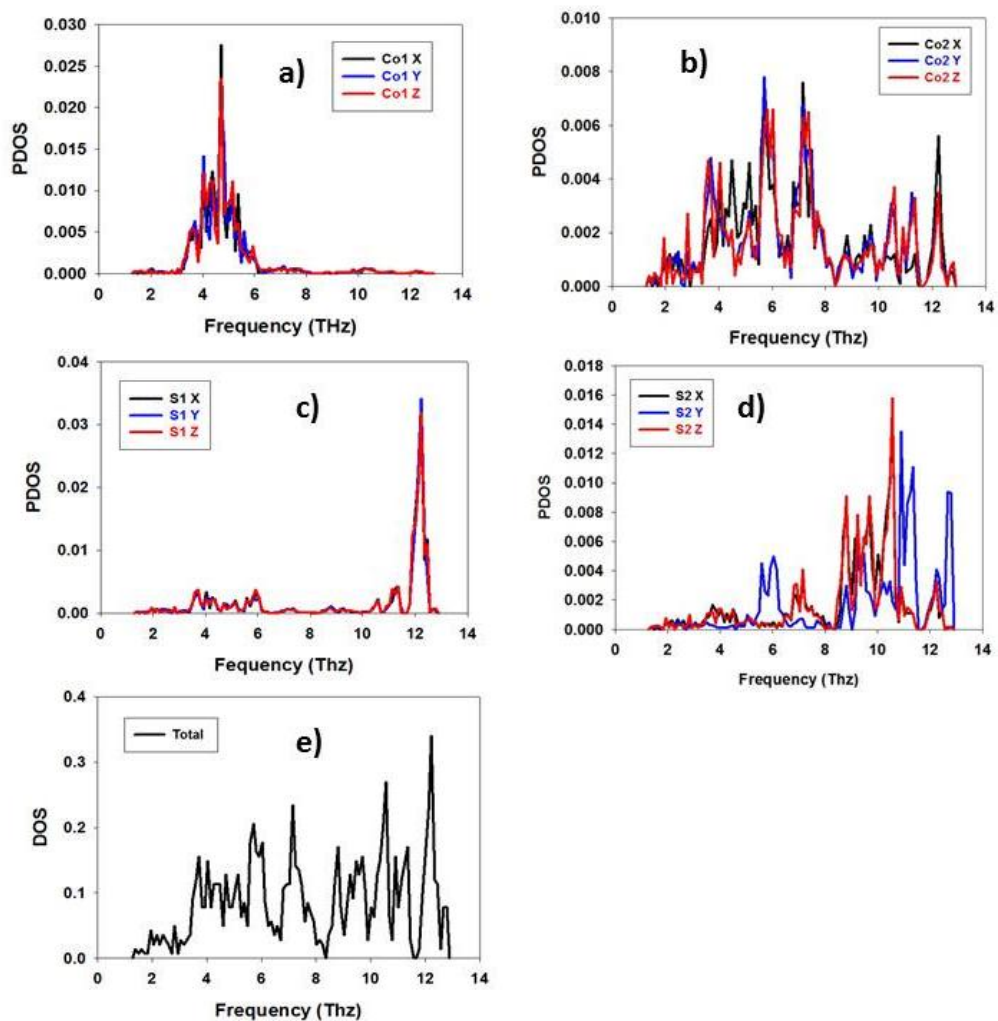


Figure 3.7: Phonon density of states for different types of cobalt and sulphur in a Co₉S₈ phase and the total DOS.

The peaks covering E through F (8.7-10 THz) are predominantly linked to the S2 atoms particularly its z component of vibration with smaller contributions from Co2. The peak G, located close to 10.5 THz, is mainly ascribed to the y component of

vibration of the S2 atom, whereas its x and y components of vibration contribute predominantly to peak H at 11 THz, and with a lesser contribution from the S1 atom. The next peak I at 12 THz is overwhelmingly contributed by the S1 atom which is an order of magnitude larger in intensity than that of the S2 atom and from Co2 atom. The peak J observed at 12.7 THz is associated with the y component of vibration of the S2 atom. The settings of the GULP calculations excluded the appearance of the last two peaks, however, since a good correlation exists with the quantum mechanical phonon results, such peaks could have been observed. It may be generally concluded that the interatomic potential model of Co_9S_8 reproduces general features of the lattice dynamics reasonably and with the aid of ab initio calculations, in the frequency range of interest, vibrational contributions of Co1 are concentrated at lower frequencies, those of Co2 are distributed over the frequency range, those of S2 occur mid-range and at higher frequencies and lastly vibrations of S1 have very high intensities and occur at the highest frequencies.

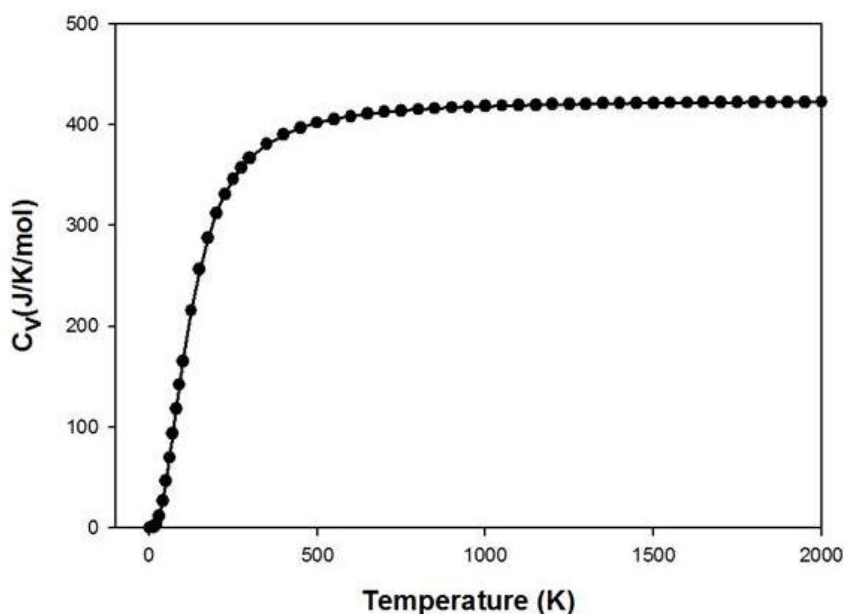


Figure 3.8: Heat capacity C_v as a function of temperature for Co_9S_8 phase using VASP code.

A variation of the heat capacity with temperature at constant volume is shown in Figure 3.8 and was determined using the VASP code. It is clear that when $T < 400$ K, the heat capacity C_v increases steeply with temperature. The change in C_v is slow at higher temperatures. The harmonic approximation gives reasonable values for the specific heat up to the room temperature. The heat capacity of the Co_9S_8 at a temperature of 298 K is 366.2 J.K/mol. This heat capacity is in good agreement with our calculated heat capacity of 378.4 J.K/mol, using interatomic potentials code GULP, at a temperature of 300K. Experimentally the heat capacity of the synthetic pentlandite $\text{Fe}_{4.60}\text{Ni}_{4.54}\text{S}_8$ was determined as 442.7 J.K/mol at a temperature of 298.15 K [124].

3.5.3. X-Ray Diffraction Pattern

The consistency of our potential model was also demonstrated by the X-ray Diffraction (XRD) patterns compared with the experimental findings. Figure 3.9 shows XRD patterns of Co_9S_8 for this work a) and X-Ray Diffraction patterns from the literature b). The XRD pattern for this work is consistent with the experimental data by Bezverkhy *et al* [11]. From both XRDs the first main peak is observed at around 30 deg followed by a lower peak at 40 deg and the second main peak is observed just above 50 deg. Recently, Ramos *et al* [24] on their work on High-resolution transmission electron microscopy (HRTEM) simulation reported the diffraction peaks of Co_9S_8 phase, which are observed at 30.4 deg, 48.2 deg and 52.7 deg. The diffraction peak at around 48 deg is also observed from our calculations, depicting good consistency of our results with the experimental data.

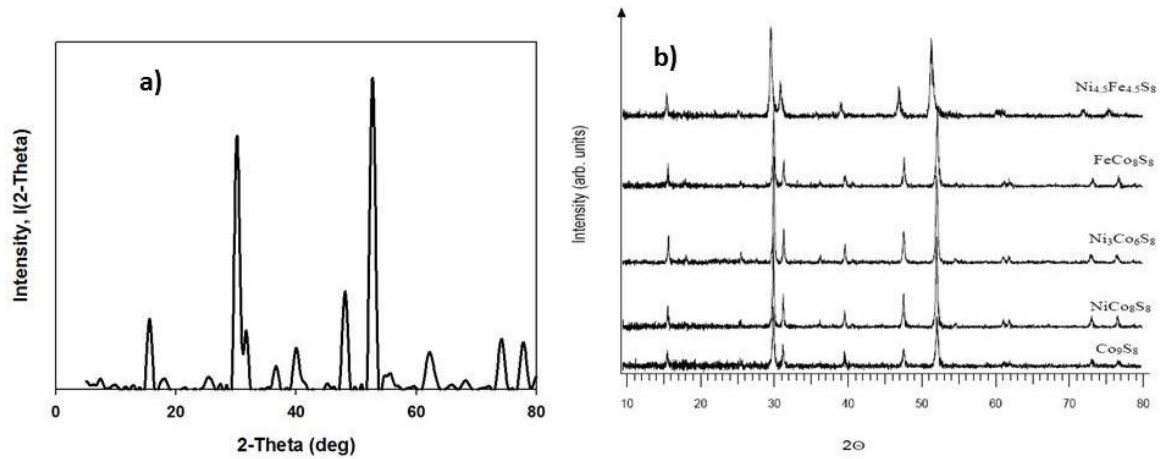


Figure 3.9: X-Ray diffraction patterns of Co_9S_8 bulk structure for a) this work and b) experimental [11].

In summary, our new derived interatomic potential model is able to simulate and reproduce the structure and elastic properties of Co_9S_8 phase, to within smaller percentage of other calculated and the available experimental results. Furthermore, the potential model reasonably reproduces some phonon DOS peaks by DFT calculations, although it predicts fairly low intensities. Notwithstanding this limitation, the potential is good, as the calculation of DOS is a stringent test. Its strength has been mainly demonstrated by its good performance on structural and mechanical properties, and as will be shown in the next chapter using two MD codes, i.e. GULP [102] and DLPOLY [63], its accurate reproduction of high temperature bulk properties and predication of surface effects. This far exceeds what is normally required of models in literature

Chapter 4: Structure and Stability of Bulk and Surfaces of Co_9S_8

In this chapter we study the structure, ion transport and stability of the Co_9S_8 using molecular dynamics computational methods. Both bulk and surfaces of Co_9S_8 structure are studied.

4.1. MD study of bulk Co_9S_8

Molecular dynamics (MD) is a key theoretical tool in understanding microstructural, dynamic and thermal effects in various systems at the atomistic level. Modern simulations with millions of atoms can investigate collective phenomena, such as melting and phase transitions. The key factors in atomistic molecular dynamics are the interatomic potentials, which determine the forces on the atom [125]. Atomistic MD calculations form an effective simulation method for investigating systems consisting of a large number of atoms and it provides dynamical information on atomic positions and velocities at the various simulation time steps [126]. In addition, molecular dynamics (MD) method is a powerful and effective tool to study the physical characteristics of micro/nanostructure [127]. Hence we will use MD to study the nanostructures later in the thesis. In this chapter we use the derived interatomic potentials of cobalt pentlandite, Co_9S_8 , to study the temperature effects on both the surfaces and bulk structures using molecular dynamics technique. The bulk properties

such as lattice parameter, interatomic distances, and elastic constants are calculated using energy minimisation technique. The following properties; radial distribution functions (RDFs), diffusion coefficients and mean squared displacements (MSD); will depict changes induced by temperature. The influence of water permeates virtually all areas of biochemical, chemical and physical importance, and is especially evident in phenomena occurring at the interfaces solid surfaces [128]. We will also study the effect of water on the surfaces of Co_9S_8 , by comparing the surface energies of pure and hydrated surfaces using both molecular dynamics and energy minimisation methods. Most of the MD calculations in this thesis use the NVT ensemble. The NVT MD method was introduced by Nosé in 1984 [129], and subsequently developed by Hoover in 1985 [130], and is presently called the standard Nosé–Hoover (NH) thermostat method [131].

Firstly we report the results of molecular dynamics calculations using the GULP program, which is incorporated in the Materials Studio. Materials Studio is software for simulating and modeling materials developed and distributed by Accelrys a company specializing in research software for computational chemistry, bioinformatics, cheminformatics, molecular simulation, and quantum mechanics [132]. For our simulations we used 3x3x3 supercell of Co_9S_8 bulk structure shown in Figure 4.1. In our simulations we used NVT ensemble (constant number of particles, volume, and temperature). The equilibration time was set at 100 picoseconds and the production time was set at 200 picoseconds. The 3x3x3 supercell simulation system contained 459 cobalt and sulphur atoms. The simulation cell volume was approximately $(21 \times 21 \times 21) \text{ \AA}^3$.

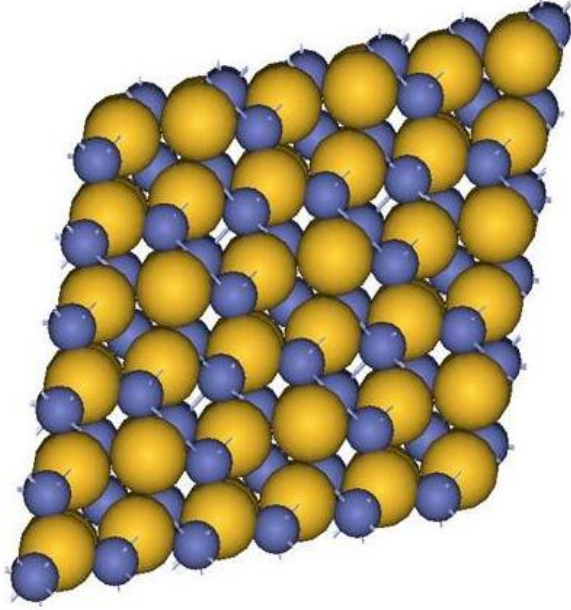


Figure 4.1: The 3x3x3 supercell of Co_9S_8 bulk structure used in the MD calculations.

The thermal expansion coefficient is a thermodynamic property of a substance. It connects the change of temperature with linear dimensions of a material [133].

A thermal expansion coefficient in MD simulation was computed directly from the temperature derivative of the lattice parameter:

$$\beta = \frac{\partial V}{(V_0 \partial(T_1 - T_0))} \quad (4.1)$$

where β is the volumetric temperature expansion coefficient, $\partial V = V_1 - V_0$, is change in volume and T_1 and T_0 is the final and initial temperatures, respectively.

Figure 4.2(a) shows the temperature variation of the bulk lattice parameter (or the expansion of the lattice with respect to temperature). The lattice parameter initially increases near linear, and non-linearly at higher temperatures. Sugaki and Kitakaze [15] also found that the $a/2$ increases as the temperature increases, as shown in Figure 4.2(b). From the graph we calculated the thermal coefficient of expansion to be

$0.9 \times 10^{-5} \text{ } ^\circ\text{C}^{-1}$ for temperatures of $27 - 1227 \text{ } ^\circ\text{C}$. Experimentally, Rajamani and Prewitt [134] got different values of thermal coefficient of expansion. With Frood pentlandite they obtained $20.6 \times 10^{-5} \text{ } ^\circ\text{C}^{-1}$ for temperatures of $24 - 200 \text{ } ^\circ\text{C}$ and with Outokumpu pentlandite they obtained $3.9 \times 10^{-5} \text{ } ^\circ\text{C}^{-1}$ for temperatures of $24 - 235 \text{ } ^\circ\text{C}$ and $11.1 \times 10^{-5} \text{ } ^\circ\text{C}^{-1}$ for temperatures of $24 - 350 \text{ } ^\circ\text{C}$. Morimoto and Kullerud in 1965 [135] obtained $15.1 \times 10^{-5} \text{ } ^\circ\text{C}^{-1}$ for temperatures of $25 - 220 \text{ } ^\circ\text{C}$ with the synthetic pentlandite.

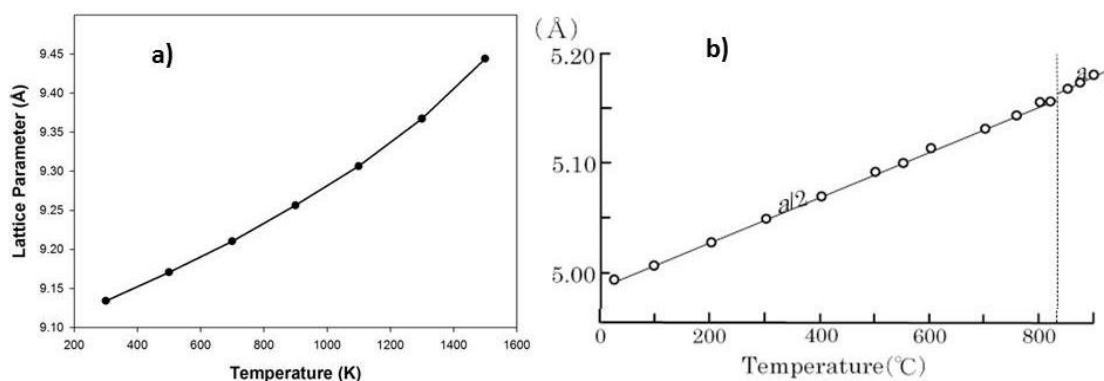


Figure 4.2: Lattice parameter as a function of temperature for Co_9S_8 bulk structure for a) this work and b) experimental [15].

One of the mechanisms of checking the melting temperature of bulk structures is the variation energy with respect to temperature using molecular dynamics method. Figure 4.3 shows the graph of total energy against the temperature and the energy change between 300 K and 1100 K is near linear; however, after 1100 K there is a slight deviation from linearity. This could be attributed to the phase change of Co_9S_8 . We notice a further very significant change in energy at 1300 K. This indicates that there is a phase transition from solid phase to a liquid phase from 1300 K.

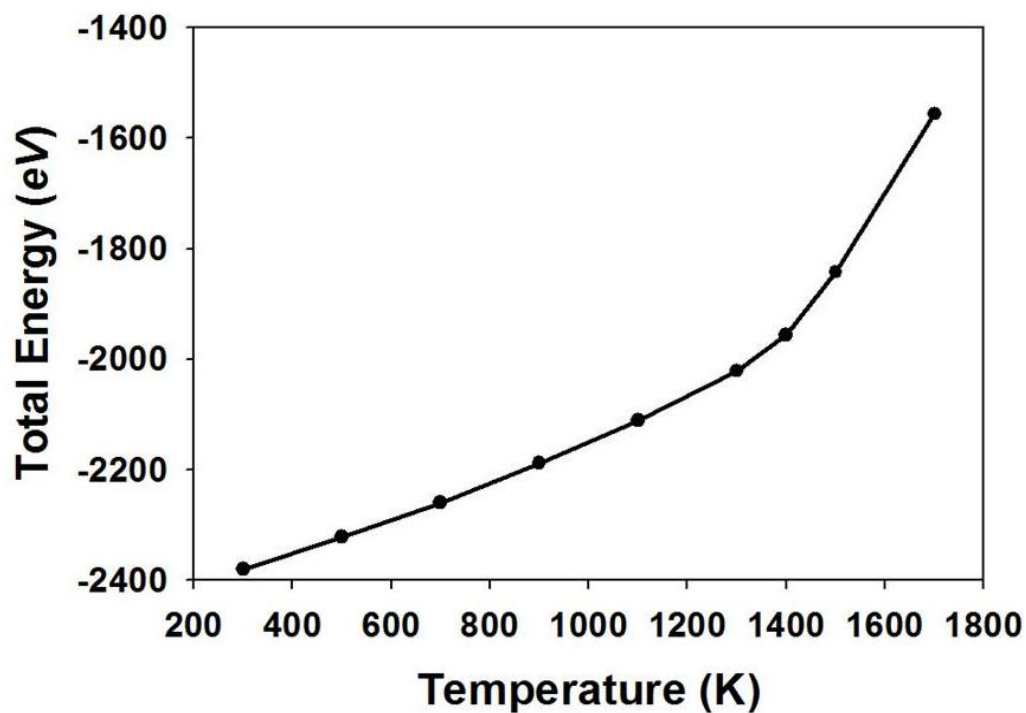


Figure 4.3: The total energy variation with temperature for Co_9S_8 bulk structure.

Figure 4.4 shows the radial distribution functions (RDFs) at different temperatures, from 300 K to 1900 K with the increment of 200 K. From the radial distribution function plots we observe that at lower temperatures of 300 K there are several sharp peaks, implying a well-defined structure. However, as we increase the temperature the peaks become broader and their number decreases, showing that the structure is experiencing the phase transition from a solid phase to a liquid phase.

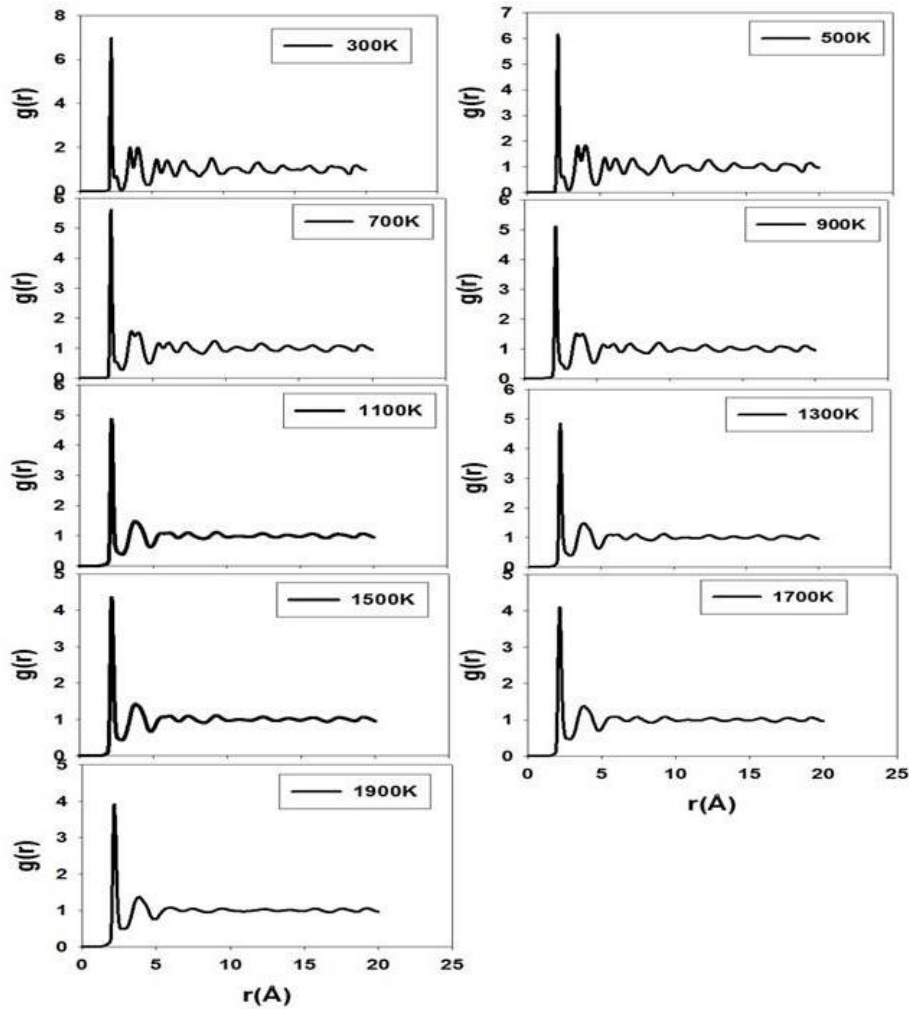


Figure 4.4: Radial distribution functions of the Co_9S_8 bulk structure at different temperatures.

In order to demonstrate the phase changes of the Co_9S_8 structure, we superimposed the total radial distribution functions of Co_9S_8 bulk at different temperatures in Figure 4.5. The total magnified RDFs indicate that as the temperature increases, the peaks become broader and the number of peaks decreased. Furthermore, the total RDFs show that between 300 and 900 K, the second and third peaks (denoted by B and C, respectively) are well-defined and approach each other. However, at 1100 K the peaks coalesce, and the combined peak (denoted by D) remains in the same position at 1300 K. This is the temperature range where Co_9S_8 undergoes phase change from normal to high form pentlandite according to experimental work of Kitakaze &

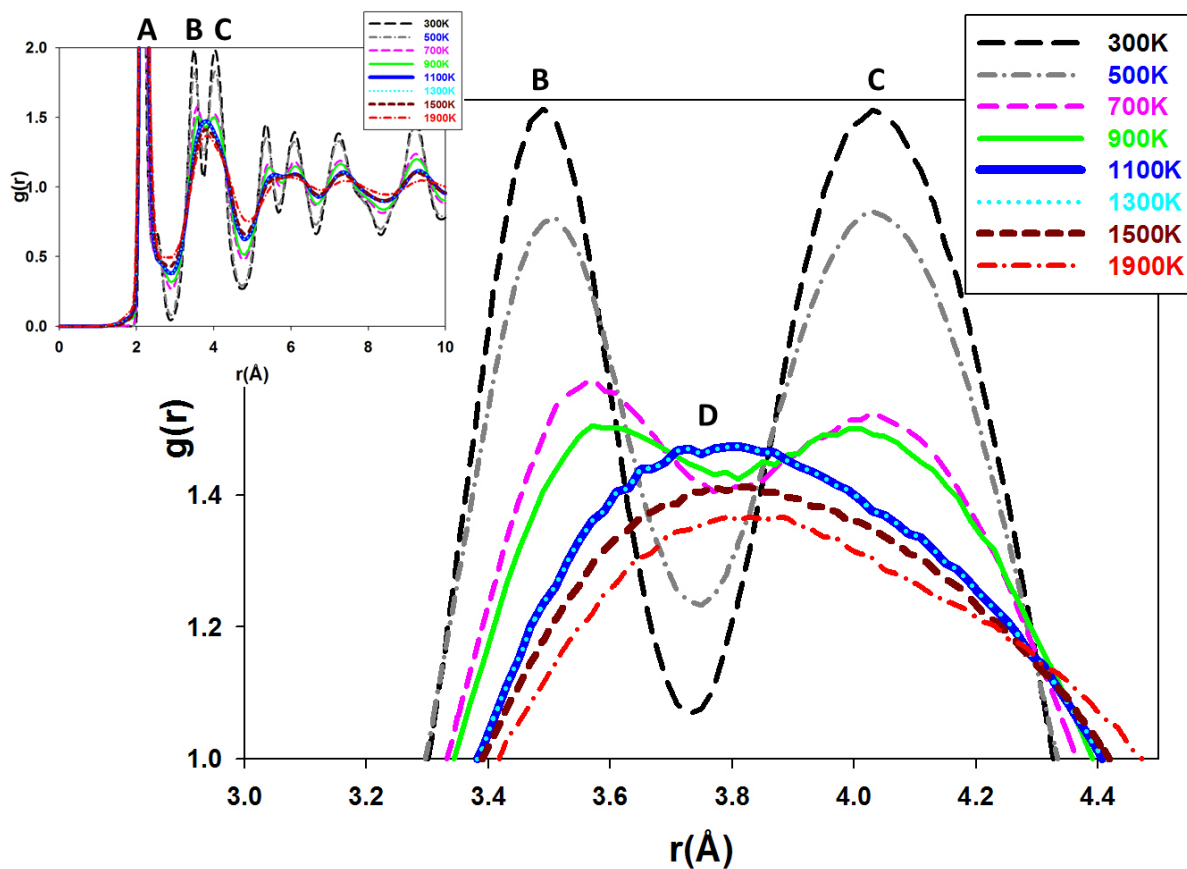


Figure 4.5: The total radial distribution functions of the Co_9S_8 bulk structure at different temperatures.

Sugaki [15]. They reckoned that the high form of cobalt pentlandite is stable up to $930^\circ \pm 3^\circ \text{C}$ ($1203 \text{ K} \pm 3 \text{ K}$), where it breaks down to a mixture of cobalt monosulfide (Fe- and Ni-free end-member of monosulfide solid-solution) and liquid in an incongruent melting reaction. They finally observed that, remnant cobalt monosulfide melts completely at $1069^\circ \pm 5^\circ \text{C}$ ($1342 \pm 5 \text{ K}$). Indeed our simulations (Figure 4.5) confirm the molten phase at 1500 K, since the height of the coalesced peak is reduced, which is further in agreement with the total energy versus temperature (Figure 4.4) anomalous enhancement above 1400 K. At a higher temperature of 1900 K the height of the coalesced peak is further reduced showing a completely molten

structure. The first peak of the RDF gives a radial distance of approximately 2.15 Å at 300 up to 900 K and 2.17 Å at 1100 K up to 1500 K.

According to the calculated and experimental data in Table 3.5, the radial distance is close to the experimental interatomic distance of Co-S on the tetrahedral site which is 2.13 Å. The second and third peaks give approximately 3.45 Å and 3.97 Å, respectively at 300 K up to 900 K. At 1100 K up to 1500 K the second and third peaks combine to give one peak of approximately 3.61 Å. The radial distance is close to the EXAFS measurement interatomic distance of Co-Co on the tetrahedral site which is 3.54 Å [136]. Hence it may be deduced that the phase change from the normal to high form pentlandite is associated with the movement of Co on the tetrahedral sites. The ability of the interatomic potentials to reproduce the complex high temperature phase change of pentlandite and to elucidate atoms participating in such change demonstrates the robustness of the potentials.

In addition, Figure 4.6 shows the snapshots for the 3x3x3 primitive structure of Co₉S₈ simulated at different temperatures. From the pictures we observe that there is a phase transition from a lower temperature to a higher temperature. At 300 K the structure is still intact and crystalline. However, as we increase the temperature in steps of 200K up to 1900 K, we observe that the structure loses its crystallinity, from 1100 K, as the regular arrangement of atoms disappears.

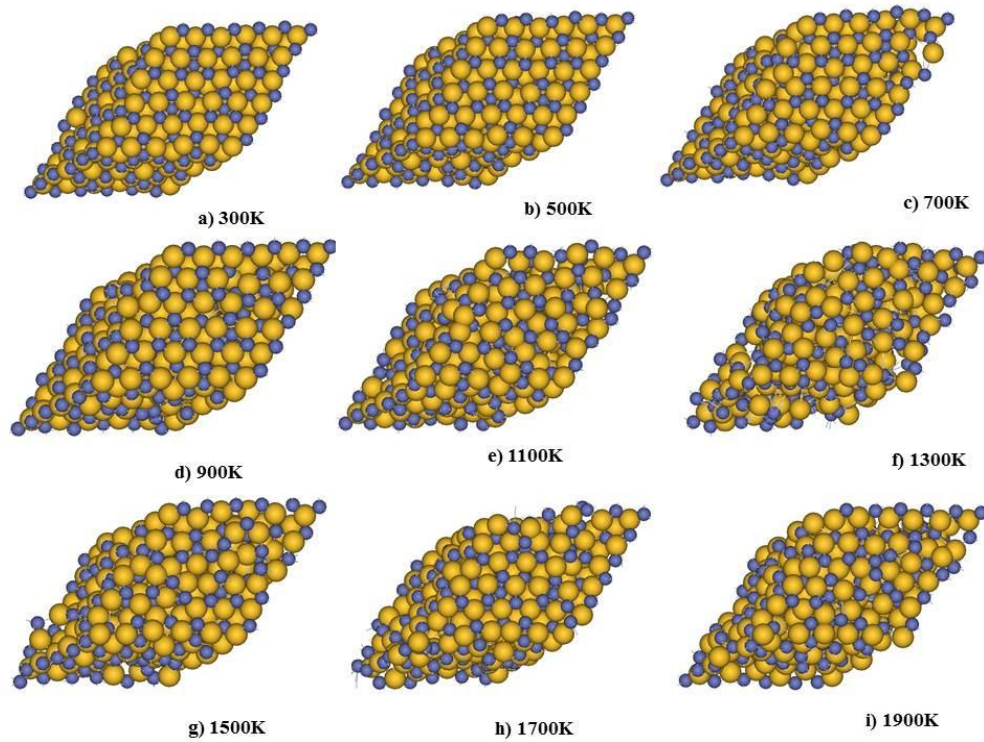


Figure 4.6: Snapshots of MD simulation at different temperatures for Co_9S_8 bulk structure.

At 1300 K the arrangement of atoms has completely disappeared. This is in further support of the high temperature proposition put forward by the results of the radial distribution functions and the total energy. Another indicator on the melting of systems is through the mean square displacements (MSD) of ions. Figure 4.7 shows the total MSD as a function of time at different temperatures. It is apparent that ions do not diffuse up to 900 K, except at 700 K which could be attributed to other phenomena not yet observed. This is due to the existence of complex transitions in pentlandite structures and it cannot be concluded with certainty that what is observed is melting. The movement at 1300 K could be associated with structural breakdown mentioned experimentally [15]. The continuous increase of MSDs above 1500 K for species at each temperature indicates that the system has attained its molten phase.

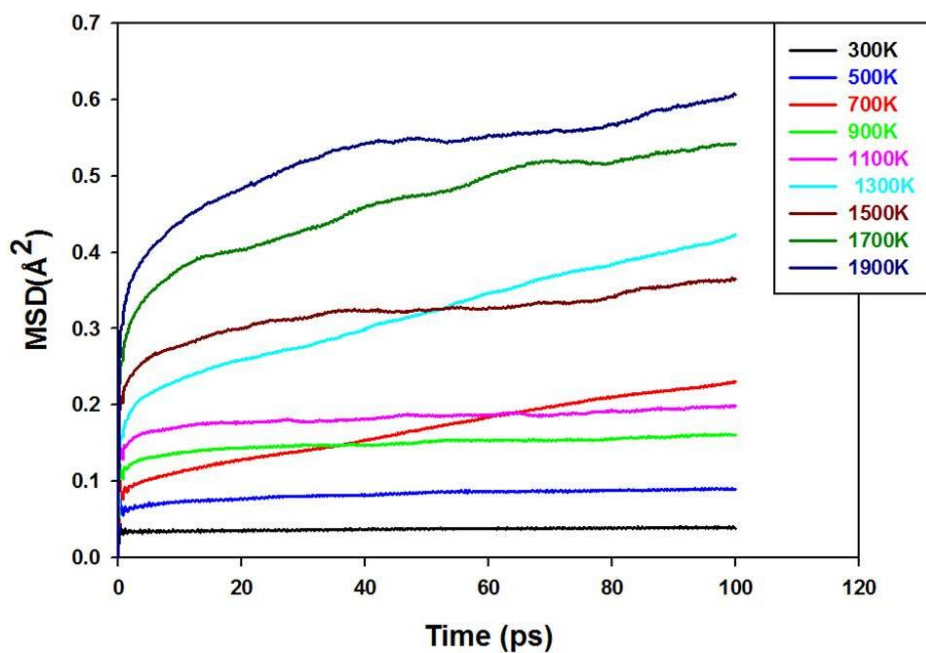


Figure 4.7: Total Mean square displacements (MSD) as a function of time for the Co_9S_8 bulk structure at different temperatures.

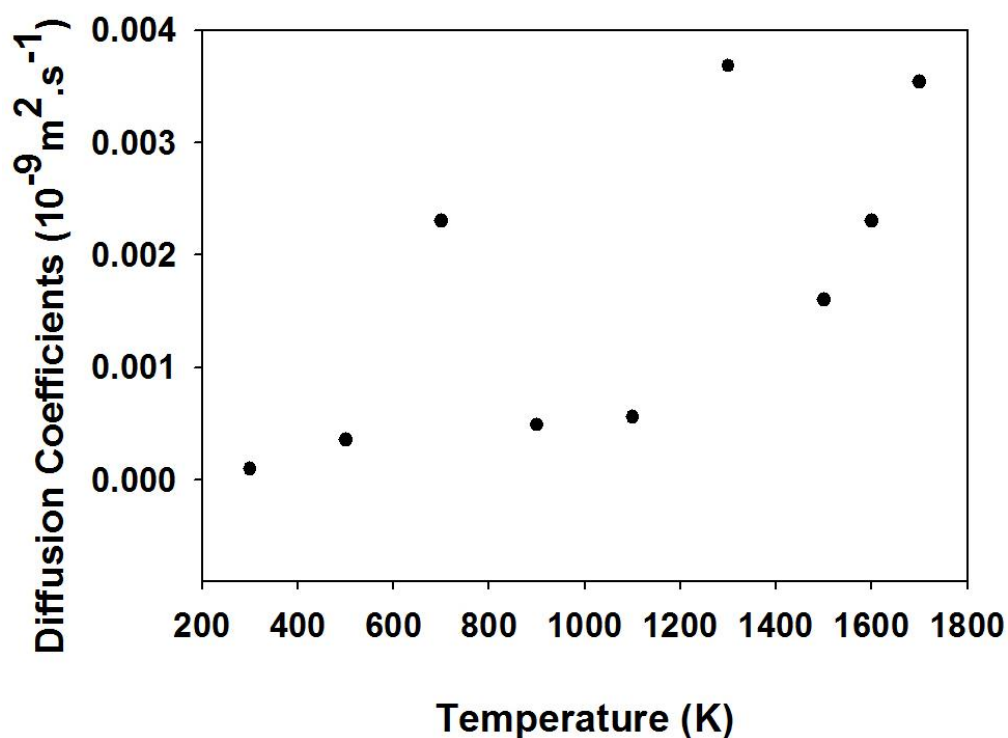


Figure 4.8: Diffusion coefficient as a function of temperature for Co_9S_8 bulk structure.

The total diffusion coefficients of the bulk Co_9S_8 was deduced from the mean square displacement and Figure 4.8 shows the variation of the diffusion coefficient with temperature for the bulk Co_9S_8 . The total diffusion coefficients show that there is a minimal movement of atoms from 300 up to 700 K. However, at 700 K, the atoms appear mobile and beyond 700 K the diffusion reverts to almost zero, until 1300 K is reached, where melting of the bulk Co_9S_8 is expected. The 1300K is very close to the melting temperature of 1342 K and diffusion could be commencing at a lower temperature of 1300 K. The average slopes of curves for 1300, 1700 and 1900 K appear equivalent, as expected since they are all in the molten state. That of 1500 K is also equivalent up to 30 ps, and declines above this temperature, which could be owing to a different diffusion regime at this temperature. This can also be explored fully in the future, together with the anomaly at 700 K.

Different properties and mechanisms calculated by the molecular dynamics methods, based on the derived interatomic potentials have demonstrated the phase changes and melting temperature of Co_9S_8 bulk structure. Such thermodynamic properties are mostly in agreement with another in their predictions and consistent with observed experimental results. Chen et al [137] mentioned that the melting of solids is one of the most common observations of a phase transition; the mechanism of melting is still an outstanding problem in condensed matter physics.

4.2. Surfaces of Co_9S_8

In this section we study the molecular dynamics simulation of the three high symmetry surfaces of Co_9S_8 i.e. $\{111\}$, $\{100\}$ and $\{101\}$. We constructed the surfaces by generating slabs, which were periodic and perpendicular to the surface plane in question. The block energy for both surfaces was calculated using a cell of 544 ions.

First we start by presenting the surface energies calculations and morphology of the three surfaces.

4.2.1 Surface Energy Calculations

Surface energy quantifies the disruption of intermolecular bonds that occur when a surface is created. In the physics of solids, surfaces must be intrinsically less energetically favorable than the bulk of a material (the molecules on the surface have more energy compared with the molecules in the bulk of the material), otherwise there would be a driving force for surfaces to be created, removing the bulk of the material. The surface energy may therefore be defined as the excess energy at the surface of a material compared to the bulk [69]. Relative surface energies can be used to predict particle and crystal morphologies, pore shapes, interface cohesion, fracture behavior and crystal growth rates, while a detailed knowledge of the surface structure can aid the design of advanced materials and the interfaces between them [89]. The surface energy of solids are important physical properties which play a role in determining the behaviour of solids surfaces when used in various applications, as examples, heterogeneous catalysis, electrochemistry, corrosion, etc. Furthermore, the surface energy of various crystallographic facets determines the equilibrium shape of crystals [138]. In this section we will consider the calculated surface energies of Co_9S_8 using both energy minimisation code METADISE and the DFT code, VASP. To the best of my knowledge there are no reported experimental and calculated surface energies of Co_9S_8 . It has been said that the direct experimental measurements of the surface energy are difficult to perform and subject to various uncertainties, e.g. presence of impurities [139]. This could be the reason of the unavailability of the experimental surface energies of most of the materials including the cobalt pentlandite (Co_9S_8)

structures. Most of the available experimental surface-energy data of materials are said to be obtained from surface tension measurements in the liquid phase and extrapolated to zero temperature [140]. With the difficulties of obtaining experimental surface energies, most authors rely on the modern first-principles methods. We will also study the hydrated surfaces. Table 4.1 gives the calculated surface energies using derived potential model and the calculated surface energies by DFT methods.

Table 4.1: Calculated surface energies of Co_9S_8 using atomistic energy minimisation compared with surface energies using DFT.

Surface	Potential Model (METADISE Code) ($\text{J}\cdot\text{m}^{-2}$)	DFT (VASP Code) ($\text{J}\cdot\text{m}^{-2}$)
{111}	2.213	2.452
{101}	3.980	4.682
{100}	6.098	2.452

The {111} surface is the most stable according to both the derived potential model and DFT methods. The {100} is the least stable surface, as predicted by the potential model. The DFT method suggests the {100} surface to have equivalent stability to the {111} surface, which is not in agreement with experiments, as will be shown by crystal morphologies in section 4.2.2. The surface energies of the {100} and {111} surfaces have been carefully verified, in all respects of terminations and convergence. We next investigated the adsorption of water on Co_9S_8 surfaces using the energy minimisation code METADISE. Figure 4.9 shows the structures of the hydrated {111}, {100} and {101} surfaces.

Table 4.2: Calculated hydrated surface energies of Co₉S₈.

Surface	Potential Model (METADISE Code) (J.m ⁻²)	DFT (VASP Code) (J.m ⁻²)
{111}	1.761	2.379
{101}	2.835	2.384
{100}	4.412	2.382

Table 4.2 shows the hydrated surface energies of low index surfaces of Co₉S₈. A comparison with the dry surfaces (Table 4.1) clearly depicts that hydration lowers surface energies; consequently the surfaces are more stable when hydrated. The {111} surface is still the most stable for both methods after hydration. De Leeuw and Parker [106] have also found that hydration of the surfaces has a stabilizing effect on the following minerals: calcite, aragonite and vaterite. Furthermore, de Leeuw et al [96] studied the effect of water on the surface structure and stability of FeS₂ which confirms this supposition.

The adsorption energies (E_{ads}) were obtained by comparing the energy of the hydrated surface (E_H) directly with the sum of the energies of the pure surface (E_s) and the self-energy of a water molecule (E_{H_2O}), as follows:

$$E_{ads} = E_H - (E_s + E_{H_2O}) \quad (4.1)$$

The hydration energies for the adsorption of water molecules onto the solid surfaces of Co₉S₈ were calculated with equation 4.1 by the potential model using the METADISE code. The adsorption energies of {111}, {101} and {100} surfaces were calculated to be -16.40 kJ/mol, -14.00 kJ/mol and -24.90 kJ/mol, respectively. The

calculation of adsorption energies using the potential model shows that water stabilises the {100} surface more. The hydrated surface energies in Table 4.2 also suggest that water stabilizes {100} surface more, since the decrease in surface energy is very high.

These suggest that the potential model and the method of calculating adsorption energies are sufficiently accurate to reproduce the relative surface stabilities of the hydrated mineral [141].

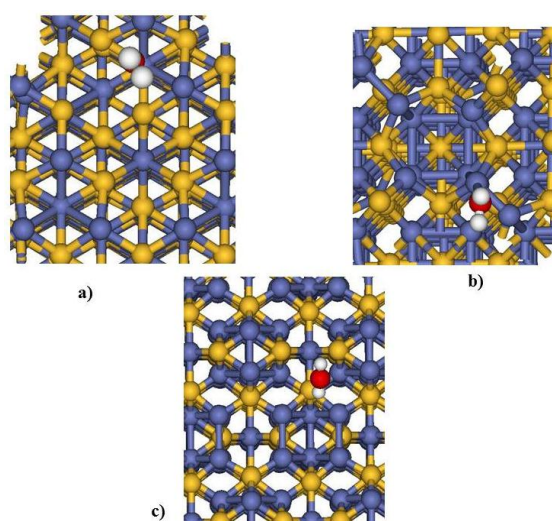


Figure 4.9: Top view of the adsorption site of adsorbed water on a) {111}, b) {100} and c) {101} Co_9S_8 surfaces. Purple, yellow, red, white spheres are cobalt, sulphur, oxygen, and hydrogen atoms, respectively.

4.2.2. Crystal Morphology

With the calculated surface energies we can use METADISE to construct 3-dimensional nanoparticles. The surface energy is different for various facets. For a crystal consisting of a given number of atoms, the equilibrium shape is the shape which minimizes the surface energy. We used the surface energy of {111} surface, since is the most stable surface, with the lowest surface energy. A surface with high surface energy will not be present in the final construction of morphology. The

constructions in 3-dimensions are in principle the same except a spherical coordinate system is used and at the end of the vectors a tangent plane is drawn [142]. Figure 4.10 shows the surface morphologies of the $\{111\}$, $\{100\}$ and $\{101\}$ surfaces of Co_9S_8 and the experimental surface morphology of the $\{111\}$ surface which was done by Kitakaze and Sugaki [15], is shown in Figure 4.11.

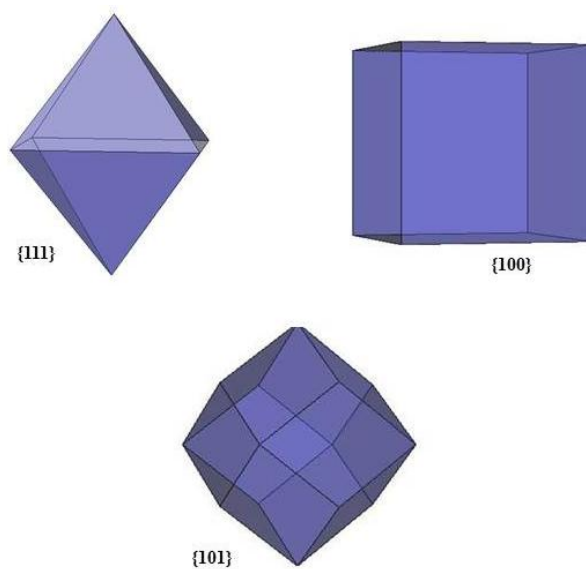


Figure 4.10: Morphology of Co_9S_8 showing a) $\{111\}$, b) $\{100\}$ and c) $\{101\}$ surfaces.

They also found that the surface of Co_9S_8 , with morphology, consists of a facet $\{111\}$. From our calculations of surface energies, we found that the $\{111\}$ surface is the most stable surface, since it gave the smallest surface energy value. Hence, the correspondence of the morphology calculated with our derived interatomic potentials and the experiments indicates a reliable prediction of surface properties by potentials.

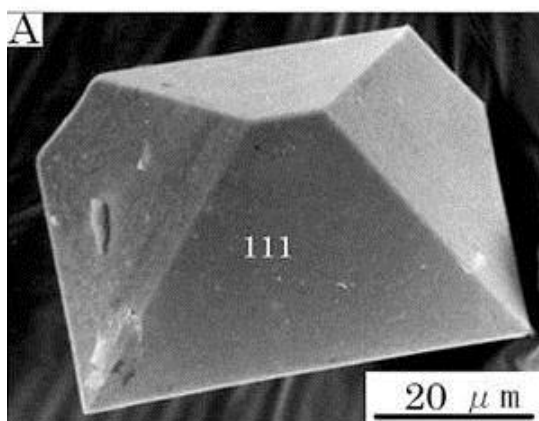


Figure 4.11: The experimental morphology of the {111} facet [15].

4.2.3. MD study of Co₉S₈ Surfaces

The surfaces of ionic solids are of increasing technological importance, not least because of their role in catalysis, gas sensing, and electrolysis [103]. We now look at the effect of temperature on the three pure surfaces of Co₉S₈ through molecular dynamics studies. Molecular dynamics simulations were performed on the three surfaces i.e. {111}, {101} and {100}, where the simulation box of the surfaces contained 544 atoms of both cobalt and sulphur atoms. Since the interatomic potentials of Co₉S₈ reproduced the high temperature bulk properties well, we presume they will predict valuable high temperature surface properties.

4.2.3.1. {111} Surface

We commence by studying the {111} surface of Co₉S₈. The surface is terminated by the cobalt atoms. Figure 4.12 shows the top view and the side view of the {111} surface. The arrangement of atoms on the {111} surface is shown in Figure C1 under Appendix C. Figure 4.13 shows the variation of the average diffusion coefficients of Co and S with temperature for the slab constituting the {111} surface of Co₉S₈.

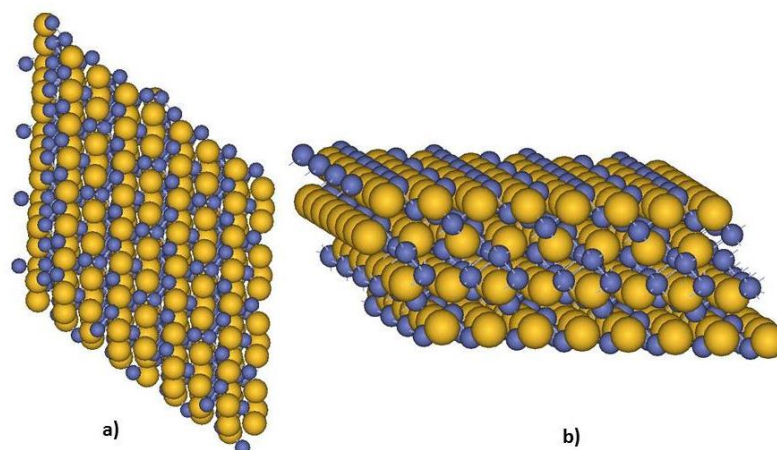


Figure 4.12: The different views of the {111} surface of Co_9S_8 a) side view and b) top view. The cobalt and sulphur atoms are represented by purple and yellow balls respectively.

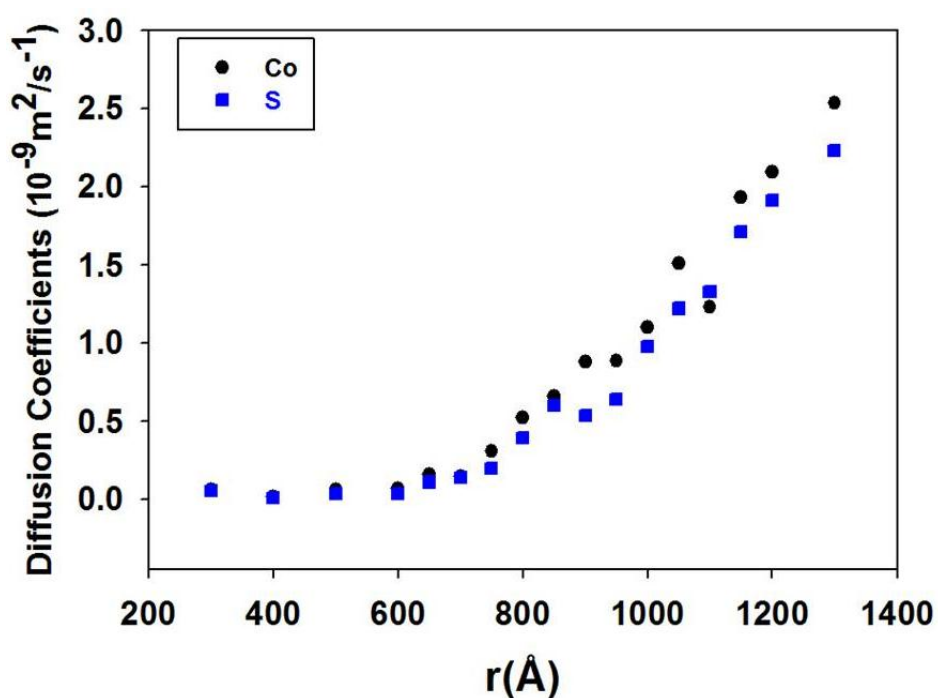


Figure 4.13: Average diffusion coefficients of Co and S as a function of temperature for the slab constituting the {111} surface of Co_9S_8 .

It is quite explicit that a significant increase in the average diffusion coefficient commences near 650K. The observed phase transition is where it is expected that the surface is in a stable liquid or amorphous phase.

Figure 4.14 shows the RDFs of the Co-Co, Co-S, and S-S pairs for {111} surface at different temperatures. The radial distances of the pairs change as the temperature is increased. The first peaks of the Co-Co, Co-S and S-S pairs at 300 K correspond to radial distances 2.68, 2.18 and 3.53 Å, respectively; however at 800 K, they change to 2.78, 2.28 and 3.73 Å, respectively. This is indicative of the broadening of the peaks at increased temperatures. At 300 K we have a well-ordered structure, implying the structure is crystalline. We observe that at 300 K the RDFs have many peaks, but at 800 and 1000 K the peaks are broader. At 750 K the peaks start to fade and the height of the peaks decreases. Furthermore, at 800 and 1000 K most of the peaks are not well defined, which could imply surface melting.

Another property which depicts the melting of the surfaces is the atomic density profile. It is a measure of the probability of finding an atom of certain type along the specific direction. Hence, it provides the basic understanding of how the structure of Co_9S_8 is affected by the increasing of temperature. Figure 4.15 shows atomic density profiles of the {111} surface for cobalt (Co) and sulphur (S) across the simulation box at different temperatures. In these plots, we observe that at 300 K the surface is denser, having many peaks than at temperatures from 650 to 1000 K. At such higher temperatures, the decrease of peak heights as well as broadened peaks, compared to those at 300 K, is indicative of the atom displacements. The peaks disappear or are combined into one peak at higher temperatures.

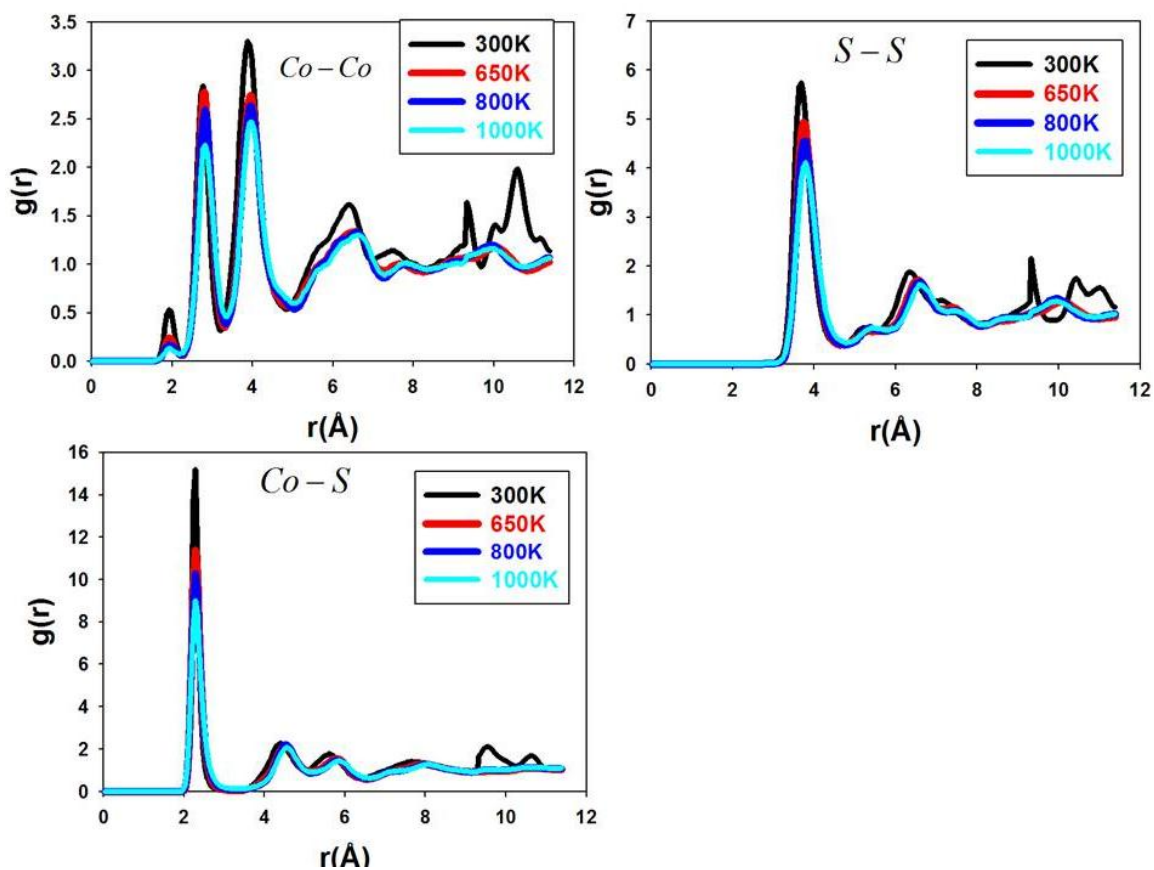


Figure 4.14: RDFs of the Co-Co, Co-S and S-S pairs for the {111} surface of Co_9S_8 at various temperatures.

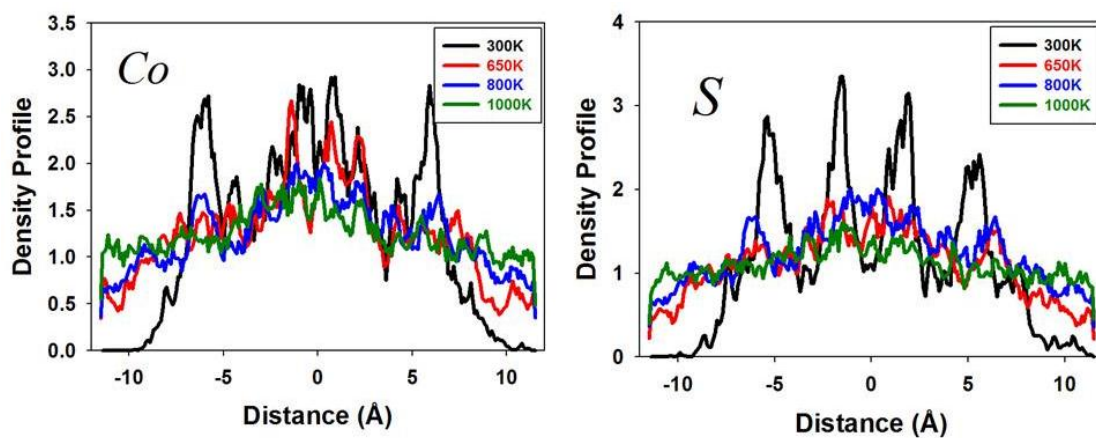


Figure 4.15: Density profiles of {111} Co_9S_8 surface for cobalt (Co) and sulphur (S) at various temperatures.

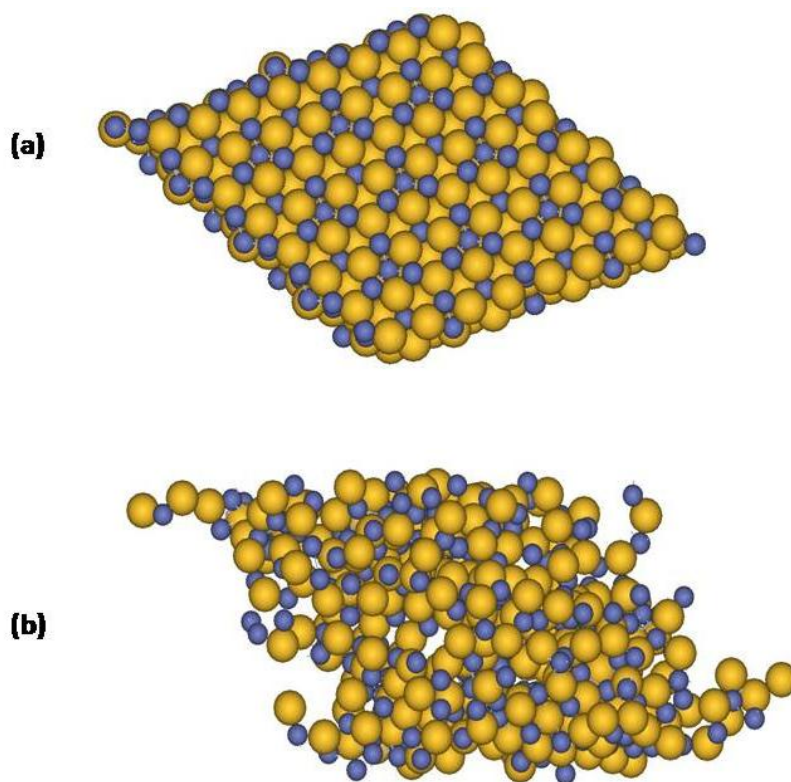


Figure 4.16: Snapshots of MD simulation at a) 300 and b) 800K for the {111} surface of Co₉S₈.

Figure 4.16 shows the snapshots of MD simulation at 300 and 800 K of the {111} surface. From the figure (Figure 4.16a), an ordered structure is observed at 300 K. On the increasing temperature to 800 K (Figure 4.16b), a disordered structure is noted, as the order is completely lost, depicting a melted or amorphous surface at 800 K.

4.2.3.2. {101} Surface

Now we consider the temperature effect on the Co₉S₈ {101} surface. The surface is terminated by both cobalt and sulphur atoms and Figure 4.17 shows the side and the top view of the {101} surface. The arrangement of atoms in the {101} surface is depicted in Figure C2 under Appendix C.

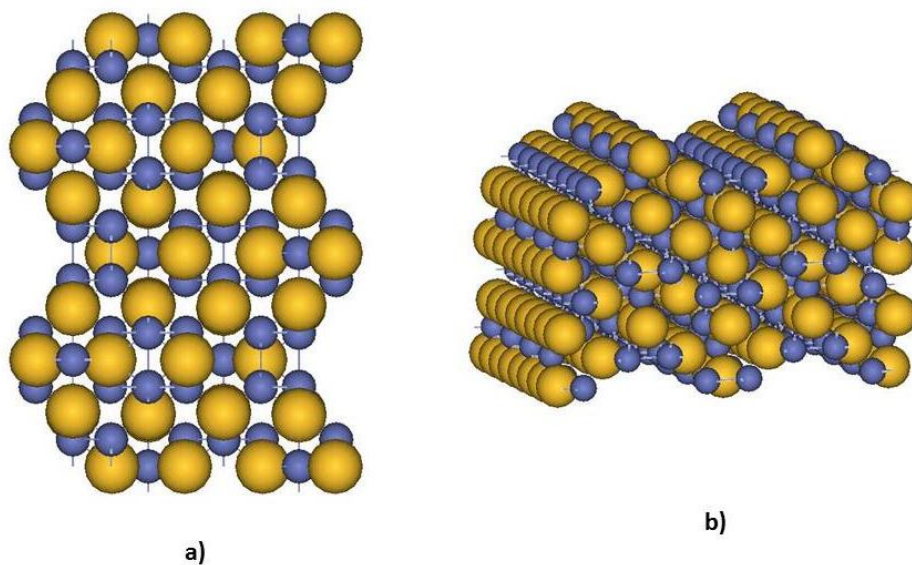


Figure 4.17: The different views of the {101} surface of Co_9S_8 a) side view and b) top view. The cobalt and sulphur atoms are represented by purple and yellow balls respectively.

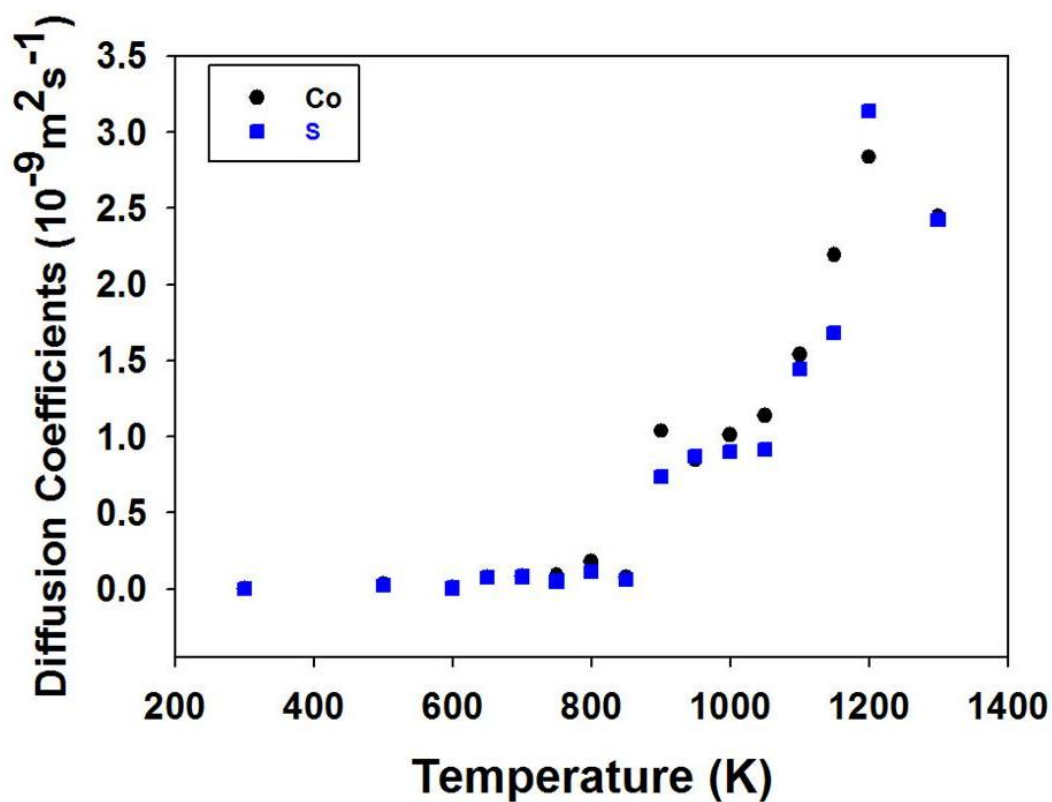


Figure 4.18: Average diffusion coefficients of Co and S as a function of temperature for the slab constituting the {101} surface of Co_9S_8 .

Figure 4.18 shows the graph of average diffusion coefficients on the slab constituting the {101} surface of Co and S as a function of temperature for Co_9S_8 . Diffusion is almost zero or minimal from the temperature of 300 up to 850 K for both the cobalt and sulphur ions. This is an indication that the surface is in the solid state at such temperatures. Our calculations suggest a significant increase in diffusion at 900 K for both ions. The two ions have different average diffusion coefficients on the slab constituting the {101} surface, with cobalt diffusing at $1.04 \times 10^{-9} \text{ m}^2 \cdot \text{s}^{-1}$ and sulphur diffusing at $0.74 \times 10^{-9} \text{ m}^2 \cdot \text{s}^{-1}$.

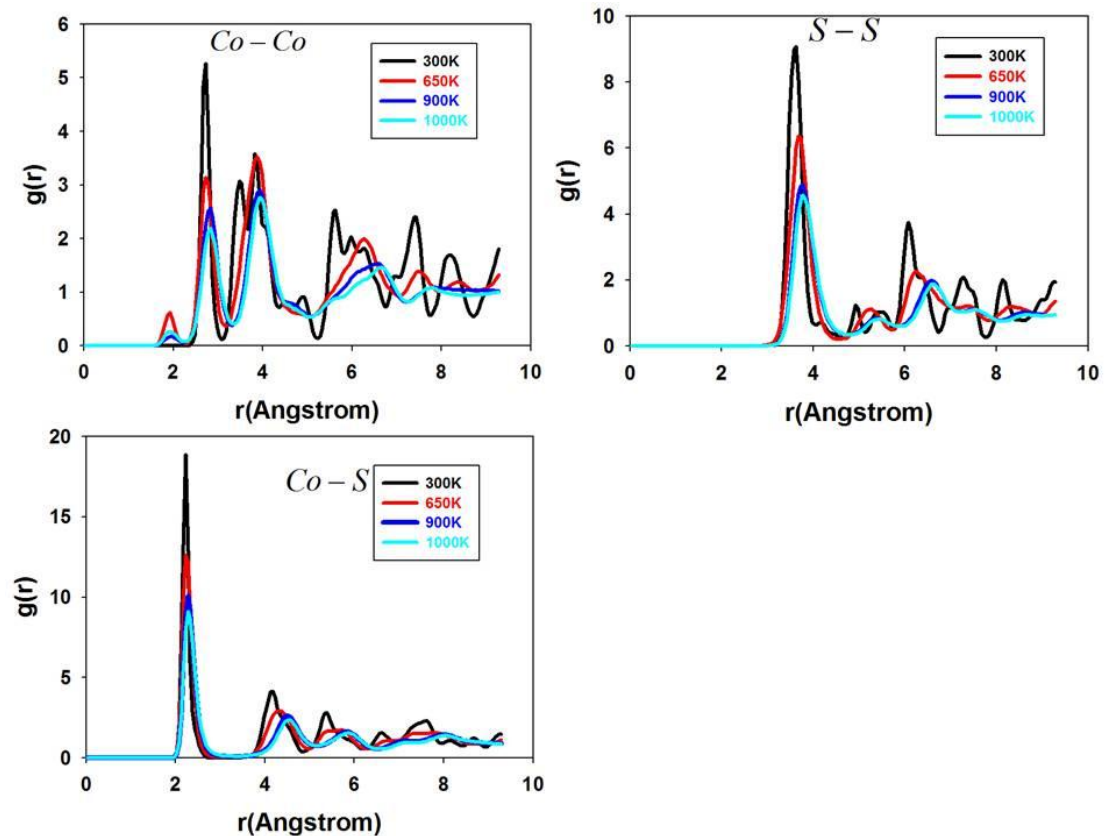


Figure 4.19: RDFs of the Co-Co, Co-S and S-S pairs for the {101} surface of Co_9S_8 at various temperatures.

Figure 4.19 shows the RDFs of the Co-Co, Co-S, and S-S pairs for {101} surface at different temperatures. The RDFs for all pairs have defined peaks at 300 and 650 K,

which is an indication that the surface is still crystalline. However, at 900 and 1000 K, both the number of peaks and the height of peaks are reduced. Furthermore, at 900 K and 1000 K most of the peaks are not well defined, which could imply that the surface melts or amorphises. It is interesting to note that the second and third Co-Co peaks coalesce and form a single peak at high temperatures, and generally radial distances increase.

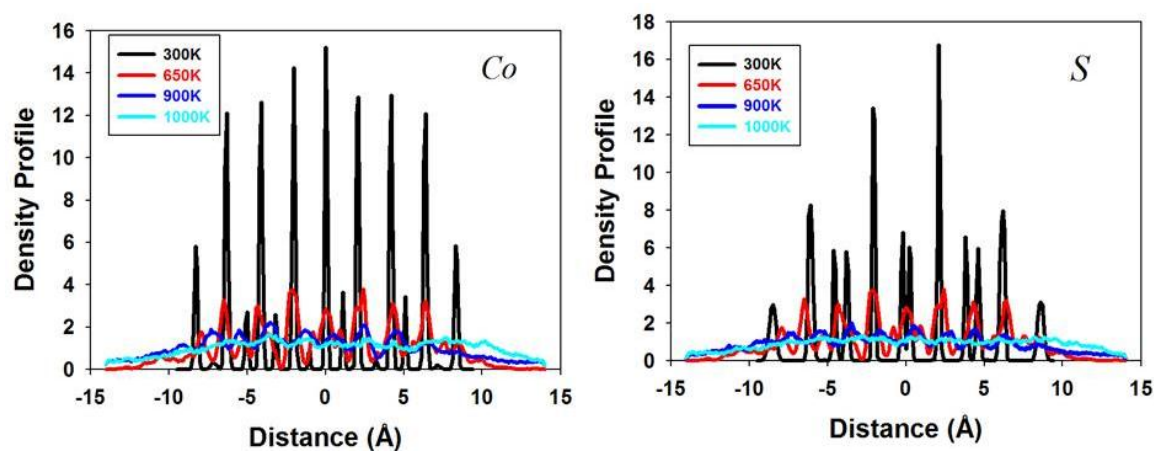


Figure 4.20: Density profiles of Co_9S_8 {101} surface for cobalt (Co) and sulphur (S) at various temperatures.

Figure 4.20 shows atomic density profiles of the {101} surface for cobalt (Co) and sulphur (S) across the simulation box at different temperatures. In the range 300-650K, the density profiles exhibit well-defined peaks for both cobalt and sulphur atoms. However, at 900 and 1000 K, the density profiles exhibit a broad profile, which is an indication of melting or disorder of the {101} surface.

We now show structural changes of MD simulations at lower and melted temperatures. Figure 4.21 shows the snapshots of the MD simulation for the {101} surface at different temperatures of 300 and 900 K. In the case of 300 K (Figure

4.22a), an orderly and intact structure is observed. However, at 900 K (Figure 4.22b), the order is completely lost, indicative of a molten or disordered surface.

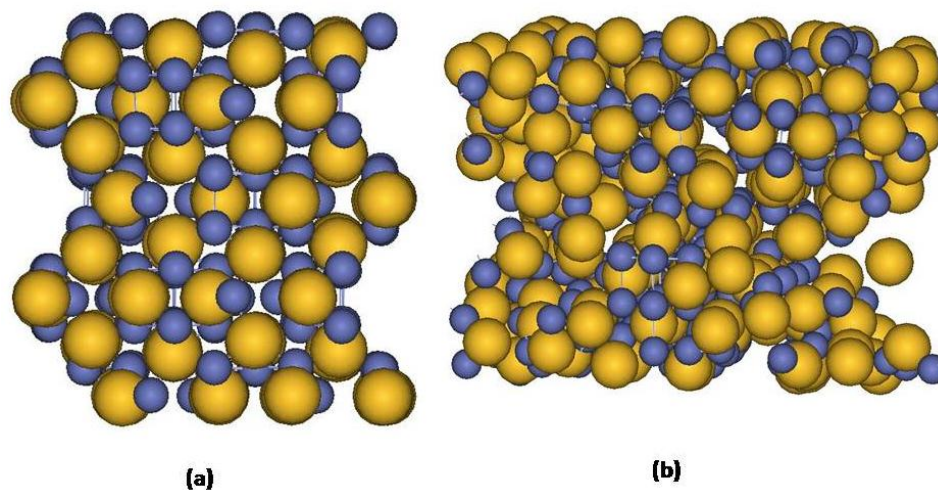


Figure 4.21: Snapshots of MD simulation at a) 300K and b) 900K for the {101} surface of Co_9S_8 .

4.2.3.3. {100} Surface

We now consider temperature effects on the Co_9S_8 {100} surface. The surface is terminated by both the cobalt and sulphur atoms. Figure 4.22 shows the side view of the {100} surface of Co_9S_8 . The arrangement of atoms in the Co_9S_8 {100} surface is shown in Figure C3 under Appendix C.

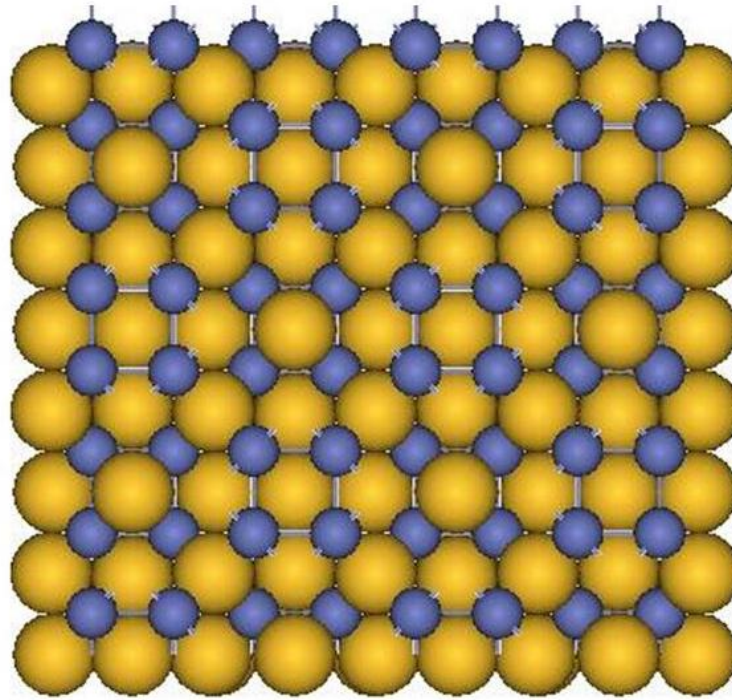


Figure 4.22: The side view of the {100} surface of Co_9S_8 . The cobalt and sulphur atoms are represented by purple and yellow balls respectively.

The mechanism of identifying the transition temperature from solid to liquid or disordered phase is by the variation of the average diffusion coefficients on the slab constituting the {100} surface as a function of temperature. Figure 4.23 shows the graph of average diffusion coefficients on the slab constituting the {100} surface as a function of temperature. Our calculations indicate that there is a movement of both ions, i.e. Co and S, at 900 K. Above 900 K the diffusion is enhanced and the cobalt ion has a average diffusion coefficient of $0.99 \times 10^{-9} \text{ m}^2 \cdot \text{s}^{-1}$ and sulphur of $0.81 \times 10^{-9} \text{ m}^2 \cdot \text{s}^{-1}$ at 900 K.

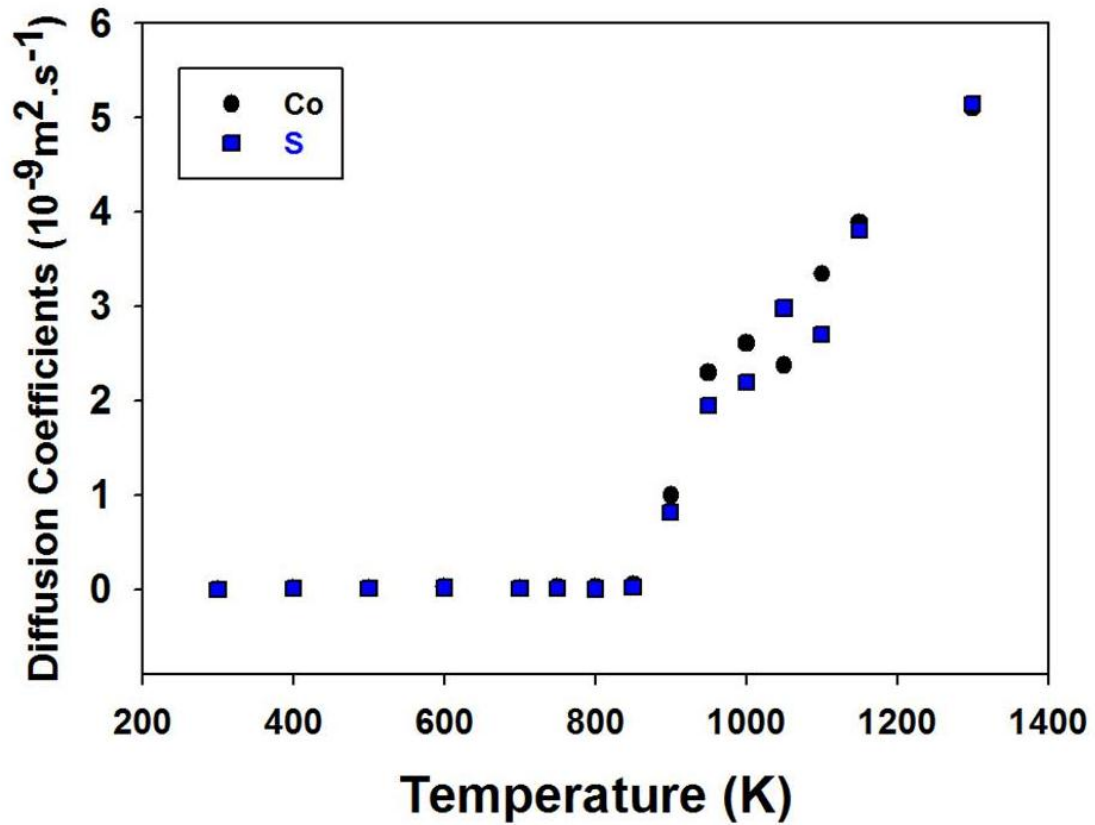


Figure 4.23: Average diffusion coefficients of Co and S as a function of temperature for the slab constituting the {100} surface of Co_9S_8 .

Figure 4.24 shows the RDFs of the Co-Co, Co-S and S-S pairs for {100} surface at different temperatures and it is clear that the surface has a well-ordered structure at 300 K, since the RDFs have many sharp peaks. We notice the disorder of the surface at 900 and 1000 K. The peaks decrease in height and broaden at 900 and 1000 K. The radial distances of the pairs are the same as those found on the {111} and {101} surfaces.

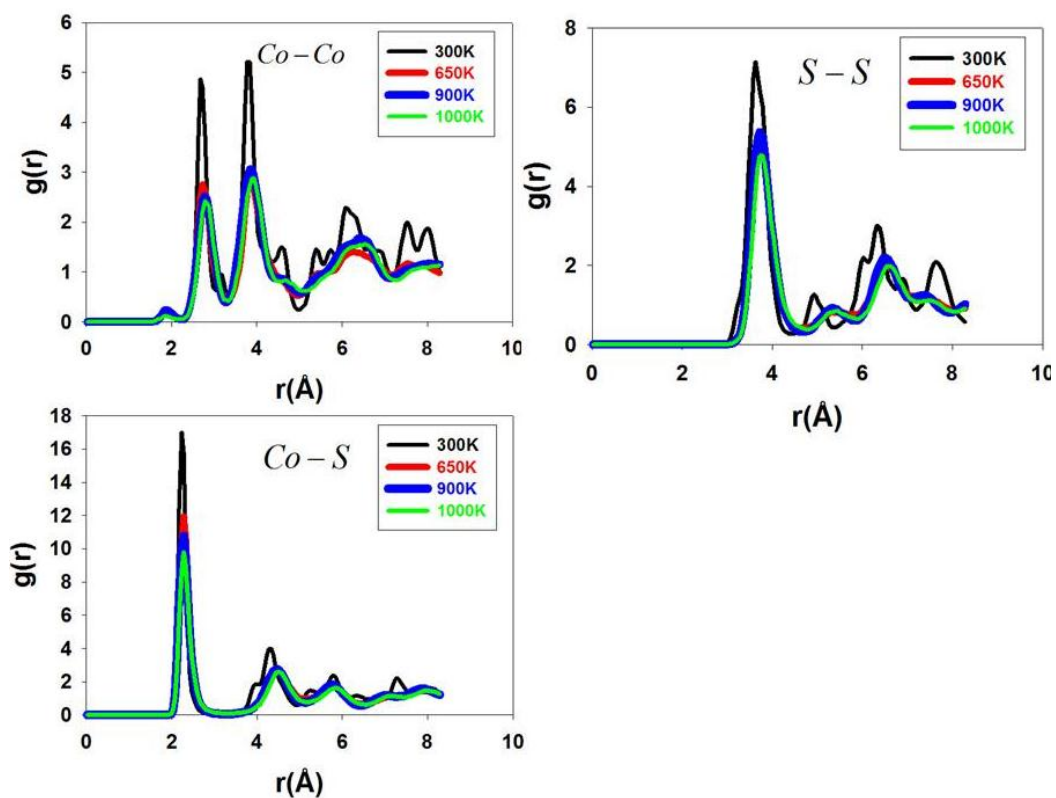


Figure 4.24: RDFs of the Co-Co, Co-S and S-S pairs for the {100} surface of Co_9S_8 at various temperatures.

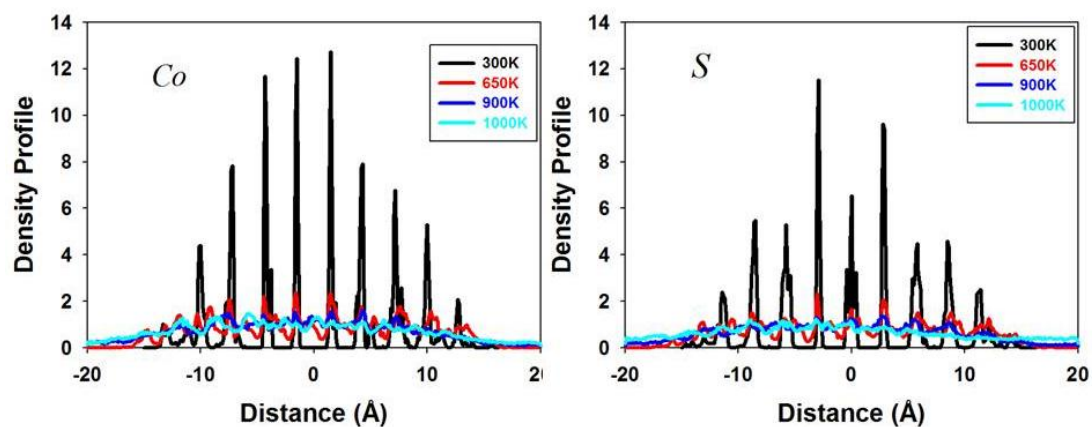


Figure 4.25: Density profiles of the Co_9S_8 {100} surface for cobalt (Co) and sulphur (S) at various temperatures.

Figure 4.25 shows atomic density profiles of Co_9S_8 {100} surface for cobalt (Co) and sulphur (S) across the simulation box with different temperatures. In these figures, we observe that the density profiles exhibit well-defined peaks in the 300-650 K range according to crystalline solid for both the cobalt (Co) and sulphur (S) ions. Upon increasing temperatures of 900 K and 1000 K, the density profiles broaden, reflecting the appearance of surface disorder. At these temperatures the profiles are flat, and could suggest a molten surface.

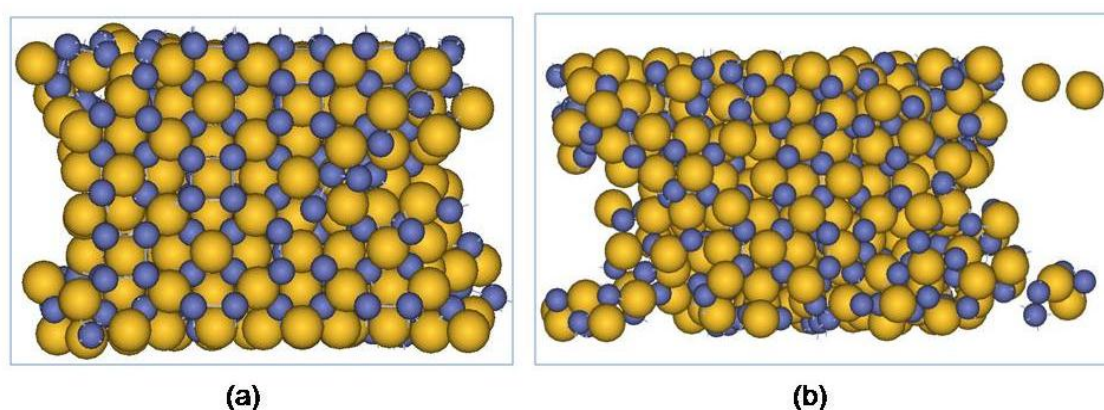


Figure 4.26: Snapshots of MD simulation at a) 300K and b) 900K for a {100} surface of Co_9S_8 .

Figure 4.26 shows the snapshots of MD simulation of the Co_9S_8 {100} surface at temperatures of 300 K and 900 K. In the case of 300 K (Figure 4.26a), an orderly structure still observed, however, at 900 K (Figure 4.26b), the order is completely lost, indicative of the molten surface at this temperature.

The prediction of the melting behaviour of the three low index pure surfaces of Co_9S_8 was illustrated by means of the diffusion coefficients, radial distribution functions, and density profiles. Furthermore, the changes in the structure at corresponding temperatures, as in the RDFs and density profiles, were shown. The predicted melting temperatures of surfaces; as observed and expected; are lower than that of bulk. In the

next section we will predict the melting behaviour of the same surfaces when in contact with water.

4.2.4. Interaction of Water with the Surfaces of Co_9S_8

In this section we use molecular dynamics simulations to model the interaction of water with the surfaces of Co_9S_8 . Liquid-surface interactions are of central importance in a number of fields such as electrochemistry, the physics and chemistry of corrosion, heterogeneous catalysis of materials, solar energy conversion, or liquid transport of geological materials such as clays or rocks [143] [144]]. Water adsorption on solid surfaces plays an important role in many natural and technological processes including mineral weathering, corrosion, water behaviour in soils, pollutant transport in the environment, and heterogeneous ice nucleation. Thus, it has long been of widespread interest in many scientific fields from meteorology and geochemistry to heterogeneous catalysis and materials chemistry. The adsorption of water can change the properties of mineral surfaces, including the protonation state, surface structure and charge, surface energy, and surface reactivity [145].

Three Co_9S_8 surfaces were considered in this work, namely, {111}, {101} and {100} surfaces. For each surface, the Co_9S_8 slab was generated with the computer program METADISE and put in contact with water. The DL_POLY 2.20 code was used to perform MD simulations using the NVT (constant number of particles, volume, and temperature) ensemble. The surfaces had 544 cobalt and sulphur atoms and the simulations contained more than 230 water molecules for both surfaces. The water model used is the modified version rigid ion by de Leeuw and Parker [105].

4.2.4.1 {111} Co₉S₈ Surface

We start by considering the {111} surface of Co₉S₈, since from our calculations of surface energies, it is the most stable surface. Figure 4.27 shows the initial configuration of the {111} surface in contact with water. The slab has approximately 231 water molecules on both sides.

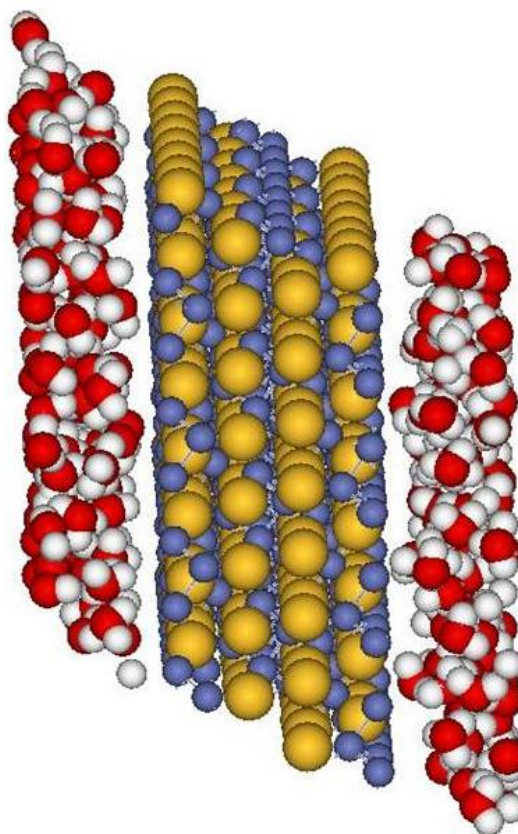


Figure 4.27: Snapshot of the initial configuration of interaction of water with {111} surface of Co₉S₈.

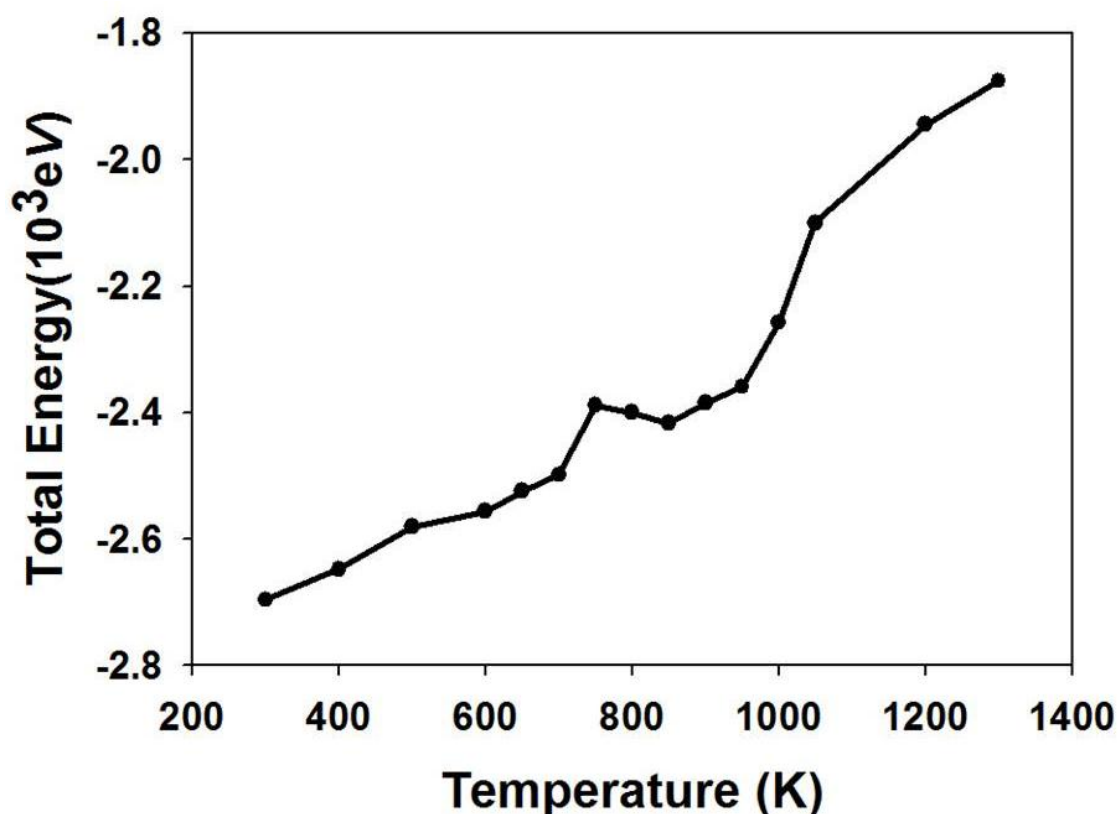


Figure 4.28: Total energy variation as a function of temperature for {111} surface Co_9S_8 in water.

Figure 4.28 shows the variation of total energy with the temperature for Co_9S_8 {111} surface. The energy increases linearly with temperature up to 700 K. A small jump at 750 K can be attributed to some transition; it could also be ascribed to the reaction of water with the surface at that temperature. Indeed the diffusion coefficients of Co and S atoms show a similar pattern around 750 and 800 K. In addition Co and S begin to have different diffusion coefficients in this temperature range. Hence the anomaly in energy could be ascribed to dissociation of Co and S from the surface. It is interesting that {100} and {101} surfaces, in later sections, depict a similar behaviour. The energy subsequently drops at 850 K, until there is an abrupt change of slope at approximately 1000 K. In the temperature range of 300-950 K, where energy just

slightly increases with temperature, the surface is still in the solid phase. At 1000 K there is a significant modification of the {111} surface in contact with water and this corresponds to the observed change in the slope of the energy vs. temperature graph.

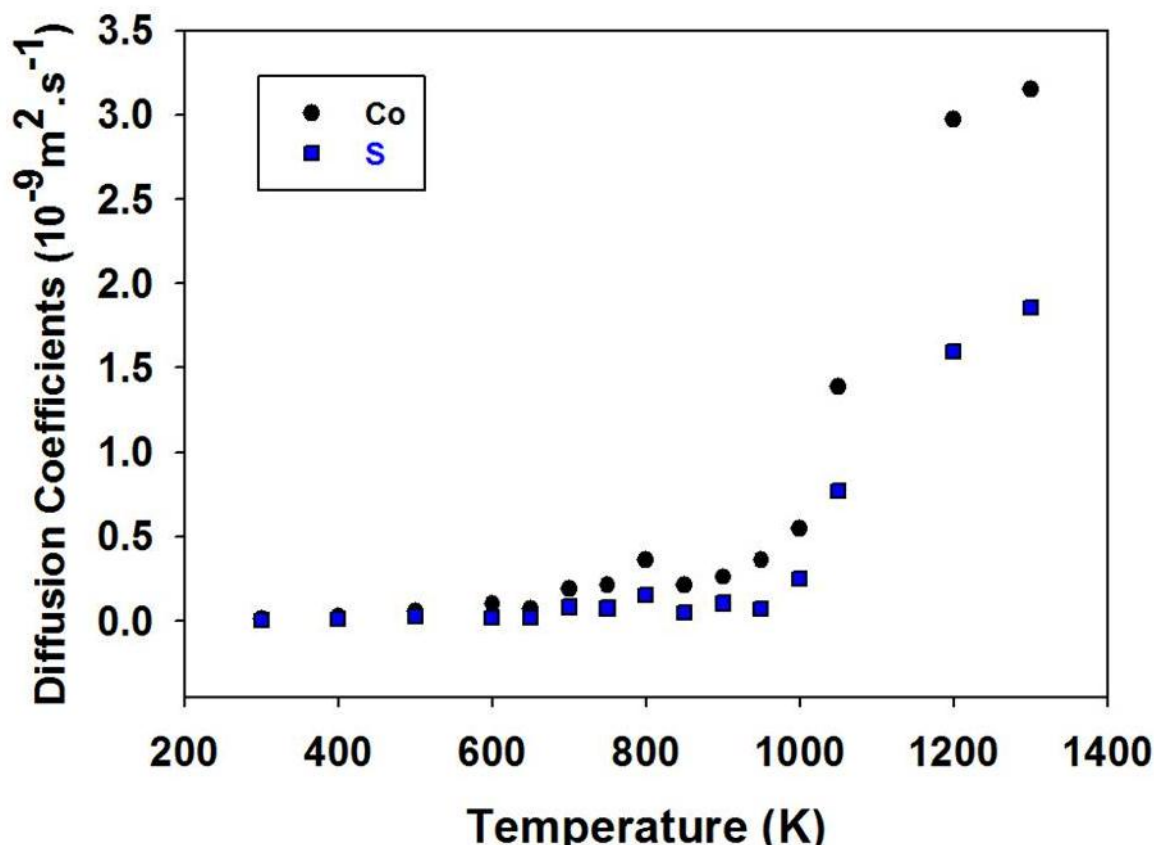


Figure 4.29: A temperature dependence of ion average diffusion coefficients on the slab constituting the {111} surface in contact with water.

Figure 4.29 shows the average diffusion coefficients for slab constituting the {111} surface of Co and S as a function of temperature. There is no movement of both cobalt and sulphur ions between 300 and 650 K, since the diffusion is almost zero. However, at 700 K there is minimal mobility of both ions with average diffusion coefficients on the slab constituting the {111} surface of $0.19 \times 10^{-9} \text{ m}^2 \text{ s}^{-1}$ for cobalt and $0.08 \times 10^{-9} \text{ m}^2 \text{ s}^{-1}$ for sulphur. The onset of ion mobility, particularly on cobalt, accords well with the sudden change of the total energy in Figure 4.28. Significant diffusion of both ions is noted above 1000 K with that of cobalt being higher.

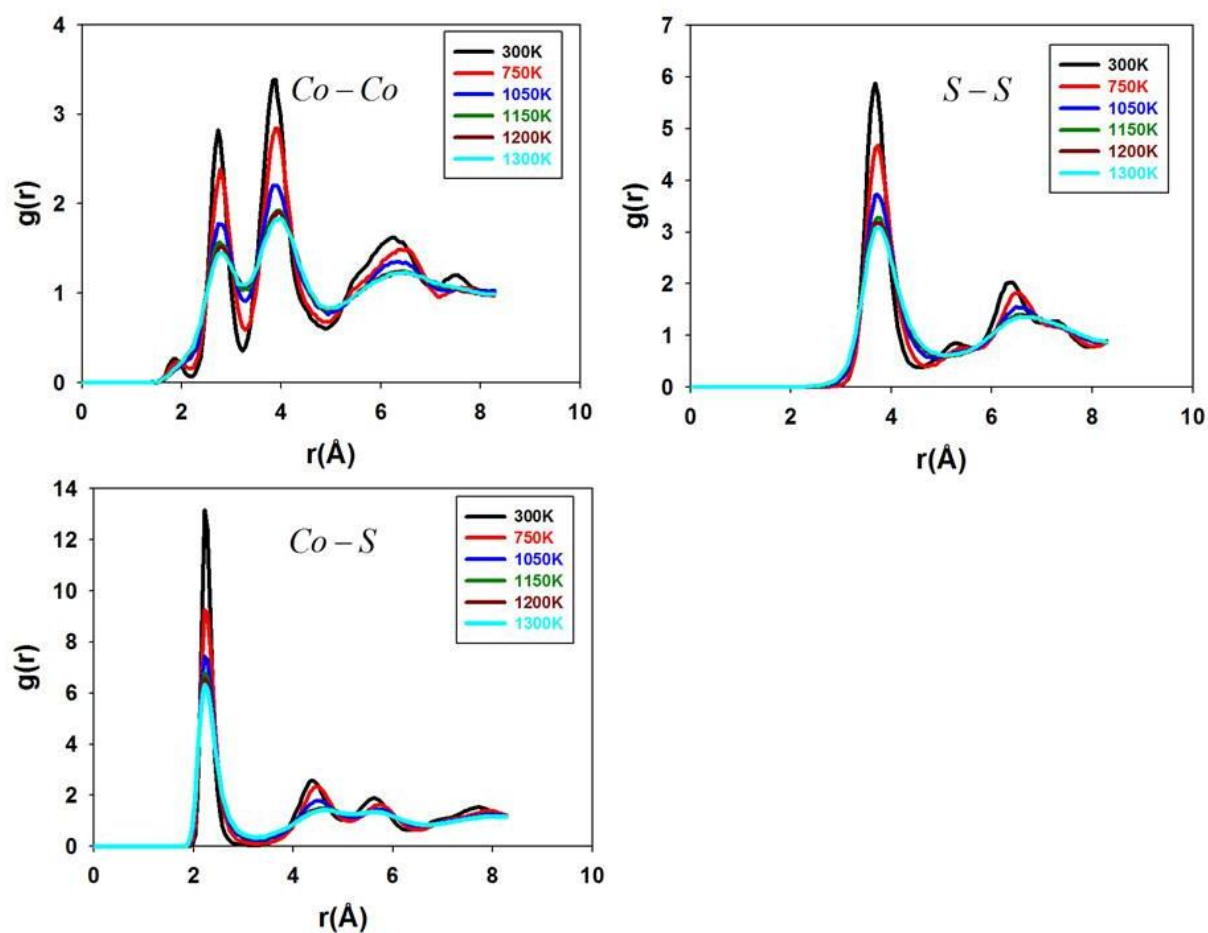


Figure 4.30: The radial distribution functions (RDFs) of Co-Co, Co-S and S-S pairs for the {111} surface of Co_9S_8 in the presence of water for different temperatures.

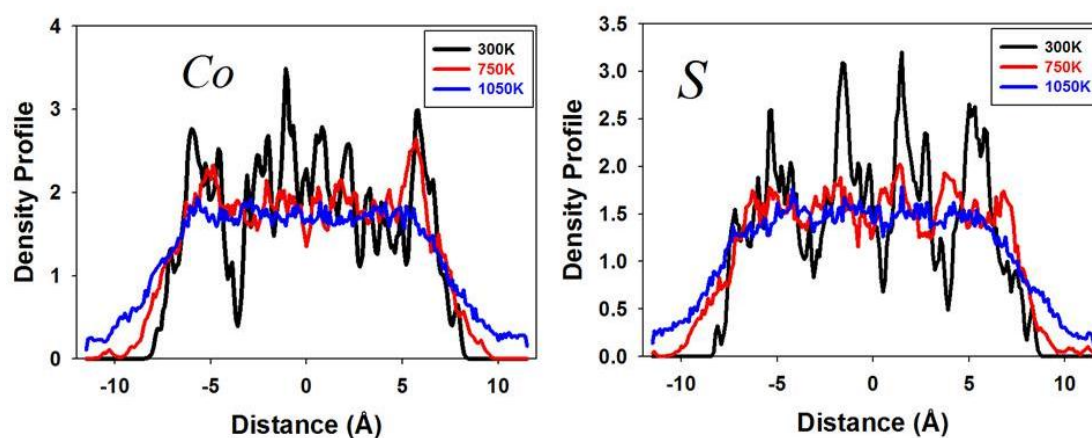


Figure 4.31: Density profile of cobalt (Co) and sulphur (S) atoms at indicated temperatures for the {111} surface of Co_9S_8 .

Figure 4.30 shows the RDFs of Co-Co, Co-S and S-S pairs for the {111} surface of Co_9S_8 in the presence of water for different temperatures. Comparing these RDFs with {111} surface without water in the previous section, we notice that the presence of water does not affect the RDF peak positions. However, the inclusion of water notably affects the height. The height of the first RDF peaks for Co-Co, Co-S and S-S pairs for the surface without water are 3.3, 15.2 and 5.7 \AA , respectively; whereas the height of the first RDF peaks for Co-Co, Co-S and S-S pairs for the surface with water are 3.4, 13.2 and 5.9 \AA , respectively. Furthermore, at temperatures 1050 K to 1150 K; the peaks are broader than those without water (discussed in previous section of the thesis). As an approach for investigating the melting behaviour of the surface in contact with water, we constructed the plots of density profiles as a function of distance. Figure 4.31 shows the density profiles of ions, i.e. cobalt and sulphur at several temperatures. At 300 K, the peaks are relatively sharp; however at higher

temperatures those peaks are broadened and reduced. The pattern of the peaks levels off at 1050 K.

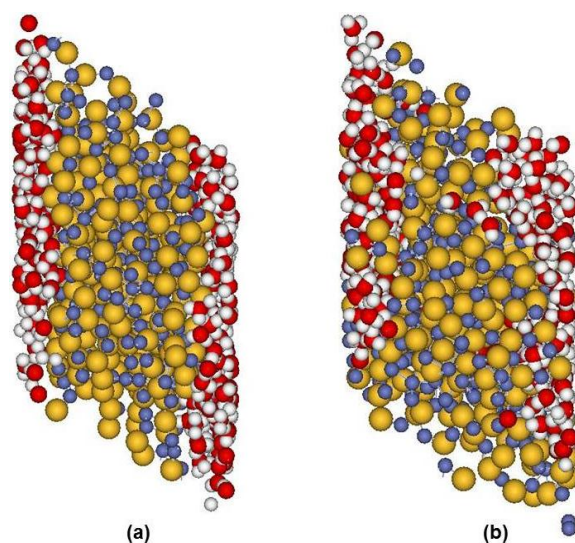


Figure 4.32: Snapshots of the MD simulation for interaction of water with {111} surface of Co_9S_8 at a) 300K and b) 1050K.

In order to depict general features of the system configuration, snapshots of the final configurations of MD simulations of slab in contact with water at 300 and 1050 K are shown in Figure 4.32. The snapshot of MD simulation at 300 K (Figure 4.32a) reveals the presence of a well-defined adsorption layer. However, the snapshot of MD simulation at 1050 K (Figure 4.32b), depicts disorder of the adsorption layers and it is mixed with water.

4.2.4.2. {101} Co_9S_8 Surface

We now consider the {101} surface of Co_9S_8 , and Figure 4.34 shows the initial configuration of the {101} surface in contact with water. The slab has about 235 water molecules on both sides. Figure 4.35 shows the graph of total energy as a function of temperature for the {101} surface of Co_9S_8 . It is noted that the slope of the curve changes sharply over the entire temperature range. The energy changes linearly

with temperature up to 950 K, and an almost stepwise change in slope occurs above 1000K.

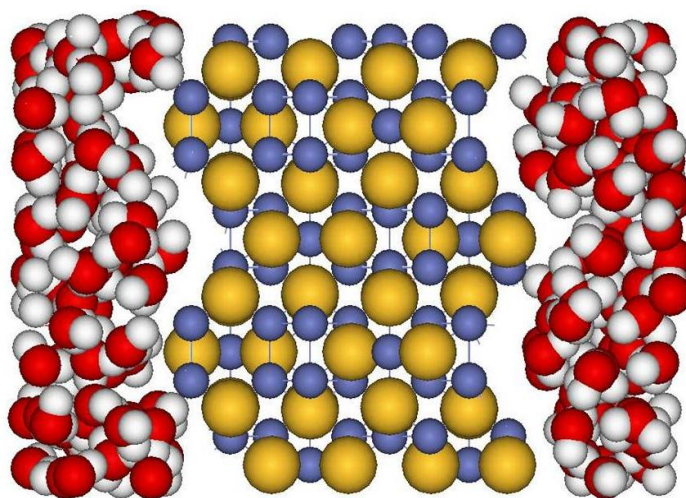


Figure 4.34: Initial structure of interaction of water with {101} surface of Co_9S_8 .

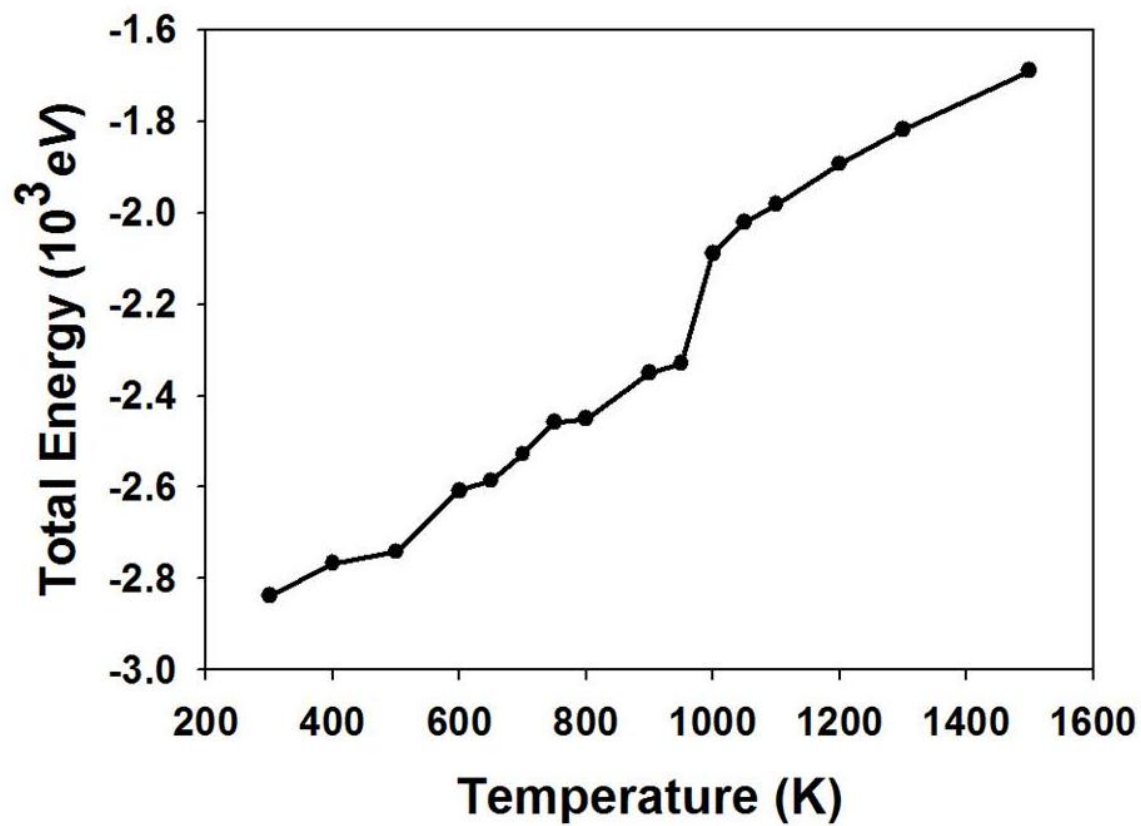


Figure 4.35: Total energy as a function of temperature for {101} surface.

In the temperature range of 300-950 K, where the total energy just slightly increases with temperature, the surface is still in the solid phase. The starting point of the deviation from linearity can be considered as a transition to a disordered phase, and in this case it 950 K. Above 1000 K, the slope of the curve changes and adopts the same value as that before 950 K. This could suggest that equilibrium has been established between the {101} surface and the water in contact.

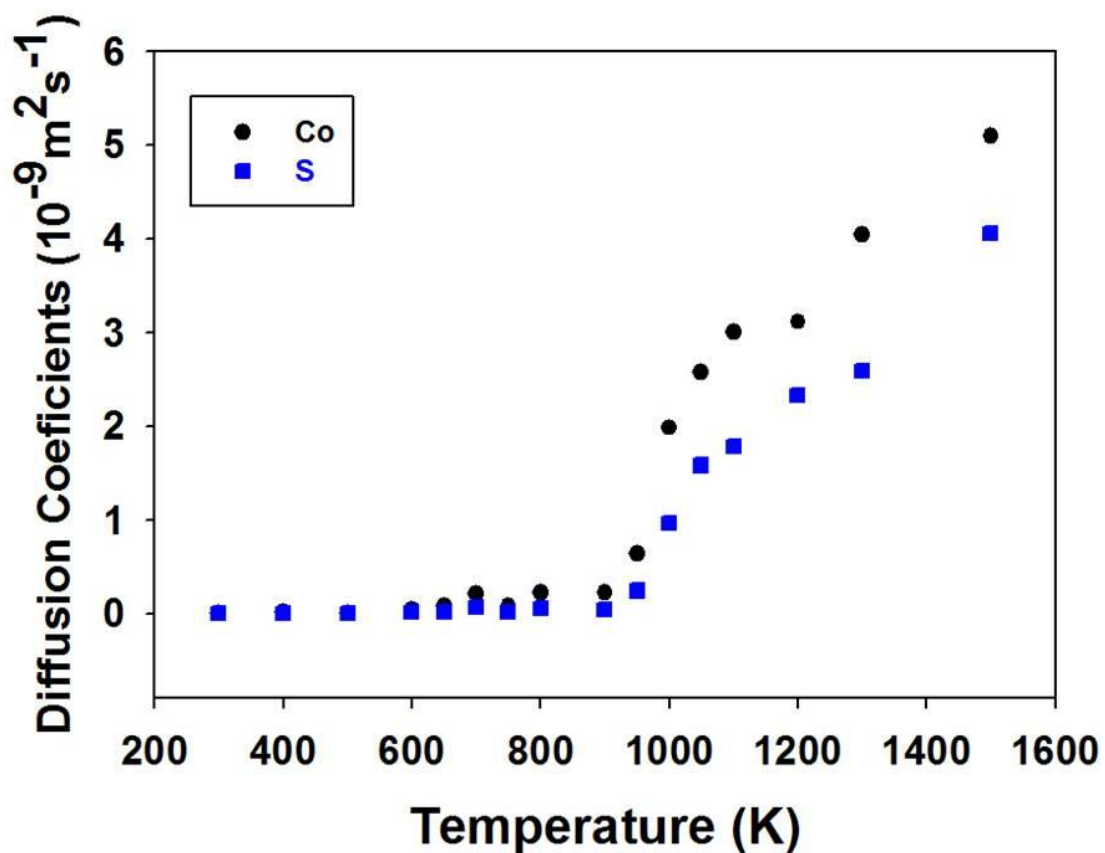


Figure 4.36: Temperature dependence of the average diffusion coefficients of Co and S on the slab constituting the {101} surface with water, for Co_9S_8 .

The other mechanism to check the melting or disorder of the surface is through the diffusion of ions. Figure 4.36 shows the average diffusion coefficients on the slab constituting the {101} surface of Co and S as a function of temperature, for {101} surface. The diffusion of both ions is almost zero or minimal in the temperature range

300-900K. The movement of both ions is noticeable at 950 K, where the diffusion of cobalt is higher. This mechanism seems to agree with the energy variation as function of temperature on the melting temperature of the {101} surface in Figure 4.35.

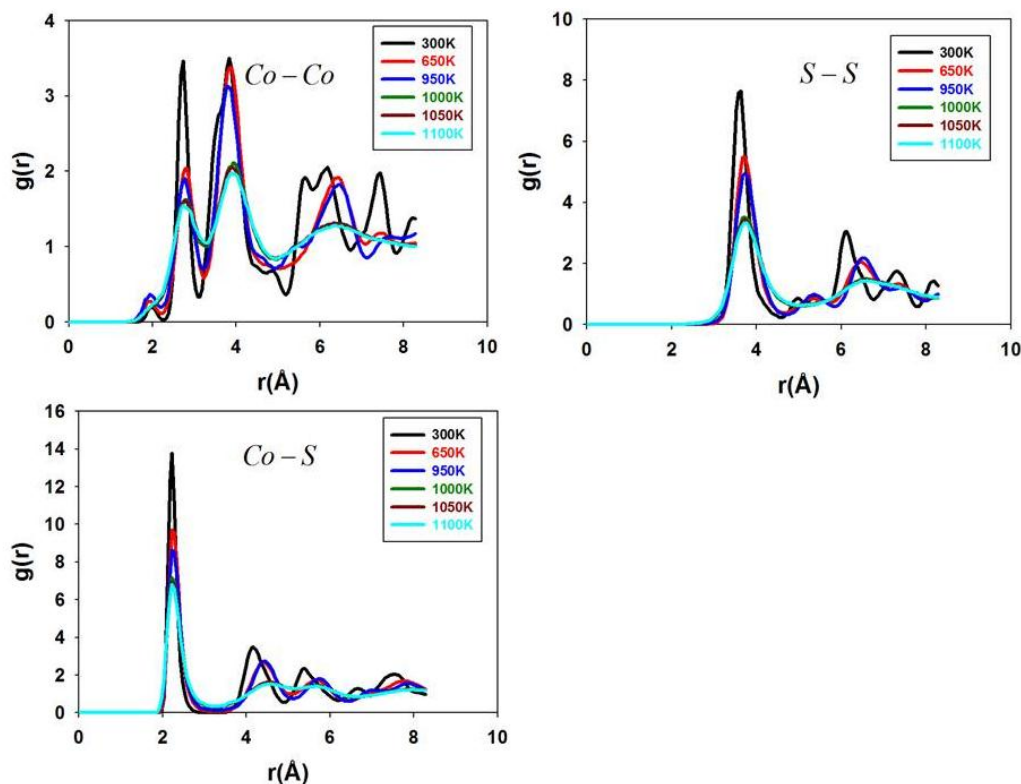


Figure 4.37: Radial distribution functions (RDFs) of Co-Co, Co-S and S-S pairs for {101} surface of Co_9S_8 in contact with water at different temperatures.

Figure 4.37 shows the RDFs of the {101} surface at different temperatures. At 300 K the peaks are well-defined, which is an indication of crystallinity at low temperatures. However, the height of the peaks decreases rapidly as the temperature increases. And also some peaks disappear as the temperature increases, indicating the phase transition from a solid to a liquid phase. At 1000 K the only noticeable peak is the first for Co-S and S-S interactions. However, for the Co-Co interaction the first and the second peaks are still noticeable, which could be the associated with the metal-metal interaction in the cubic cluster of tetrahedral Co (II) in the Co_9S_8 structure.

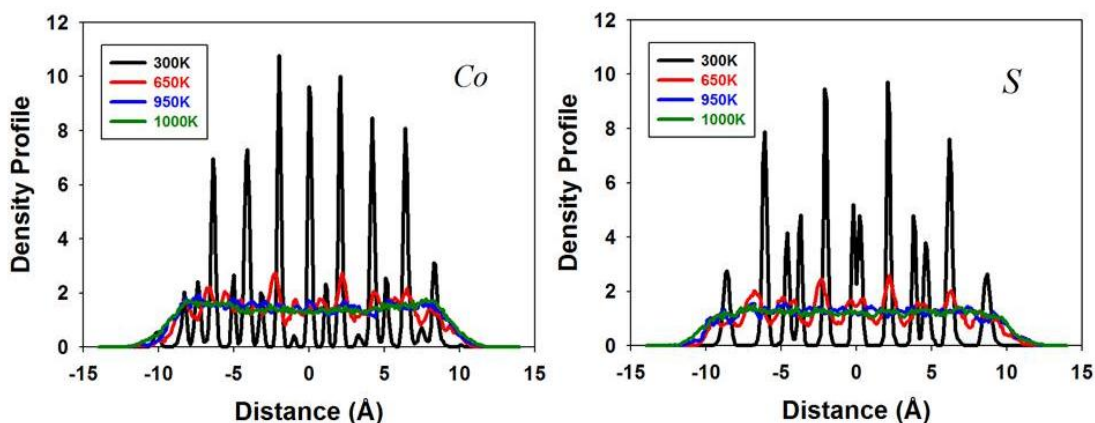


Figure 4.38: Density profile of cobalt (Co) and sulphur (S) atoms of Co_9S_8 at indicated temperatures for the $\{101\}$ surface.

The melting behaviour of the $\{101\}$ surface in contact with water was further elucidated by constructing the plots of density profiles as a function of distance. Figure 4.38 shows the density profiles of ions, i.e. cobalt and sulphur at several temperatures. At the temperature of 300 K, the peaks are relative sharp; however at increased temperatures those peaks are broadened. This implies the mobility of the ions at high temperatures.

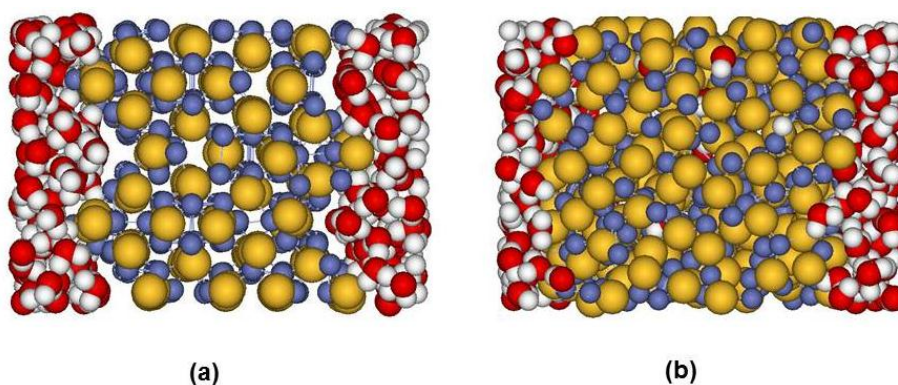


Figure 4.39: Snapshots of the MD simulation of interaction of water with $\{101\}$ surface of Co_9S_8 at a) 300K and b) 1000K.

In order to give general features of the system configuration, snapshots of the final configurations of MD simulations of slab in contact with water at temperatures of 300 K and 1000 K are shown in Figure 4.39. It can be noted that at 300 K (Figure 4.39a) the surface is still crystalline; however at 1000K, the surface is no longer crystalline when compared to the initial configuration in Figure 4.34 and it is mixed with water.

4.2.4.3. {100} Co₉S₈ Surface

We now consider the {100} surface in contact with water. From our surface energy calculations the {100} surface is the least stable surface, among the surfaces considered. The slab has approximately 264 water molecules on both sides and the initial configuration is shown in Figure 4.40.

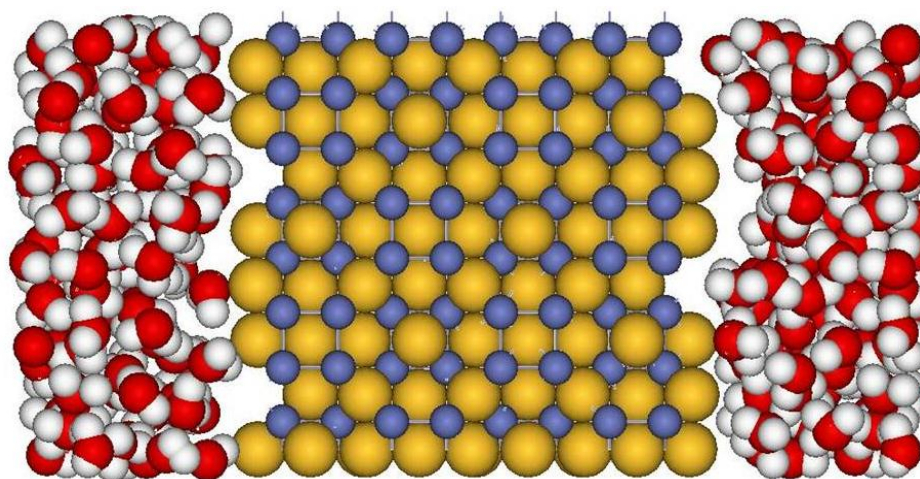


Figure 4.40: Initial configuration of slab in contact with water of {100} surface for Co₉S₈.

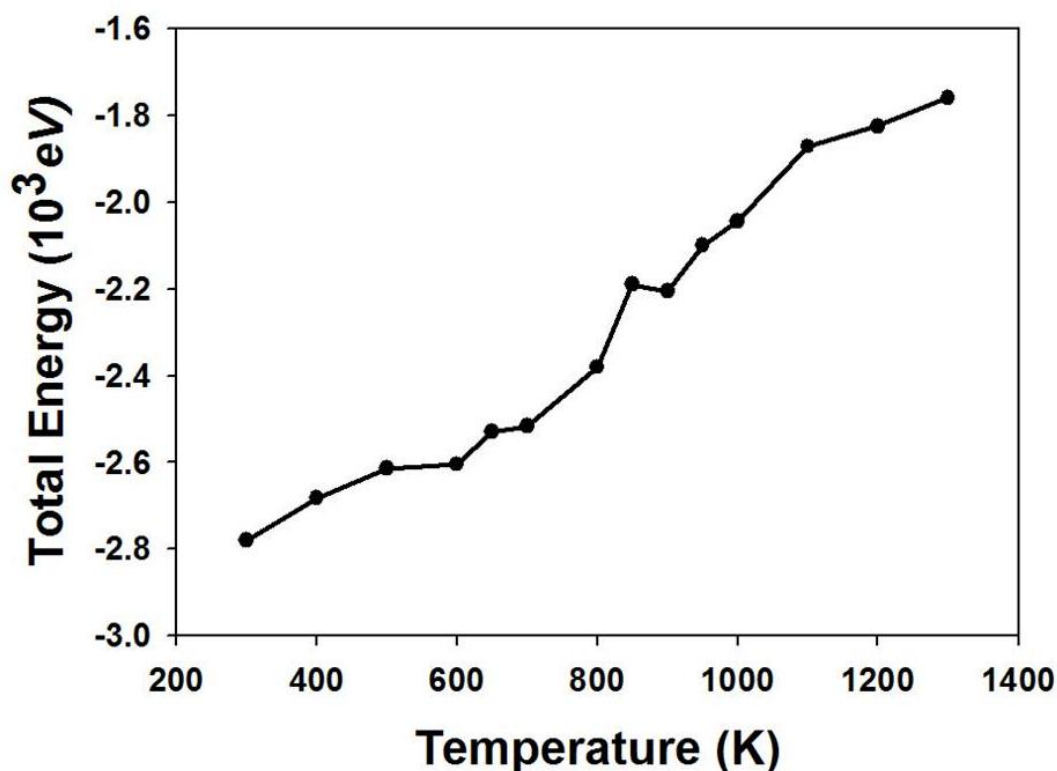


Figure 4.41: Total energy as a function of temperature for {100} surface of Co_9S_8 in contact with water.

Figure 4.41 shows the total energy as a function of temperature for the {100} surface of Co_9S_8 in contact with water. The energy seems to be increasing almost linearly as the temperature increases up to 800 K. However, there is a slight change of slope around the temperature of 850K. This suggests that the enhanced interaction of water on the {100} surface occurs from at approximately 850 K.

Another mechanism to check the melting or disorder of the surface is through the diffusion of ions. Figure 4.42 shows the average diffusion coefficients on the slab constituting the {100} surface of Co and S as a function of temperature, for the {100} surface in contact with water in Co_9S_8 . The movement of ions is almost zero in the 300-700 K range, and it is noticeable above 800K for both ions. This mechanism

appears to be aligned with the manner in which energy changes with temperature in Figure 4.41.

Figure 4.43 shows the RDFs of the {100} surface in contact with water at different temperatures. The same trend was observed for the {101} surface, where at 300 K, the peaks are well-defined, which could be an indication of a strong correlation at low temperatures. However, the heights of the peaks reduce rapidly as the temperature increases. Furthermore, most peaks disappear as the temperature increases, indicating the phase transition from a solid to a liquid or disordered phase. At 1100 K only the first peak is noticeable for the Co-S and S-S interactions, whereas the first two are visible for the Co-Co interactions.

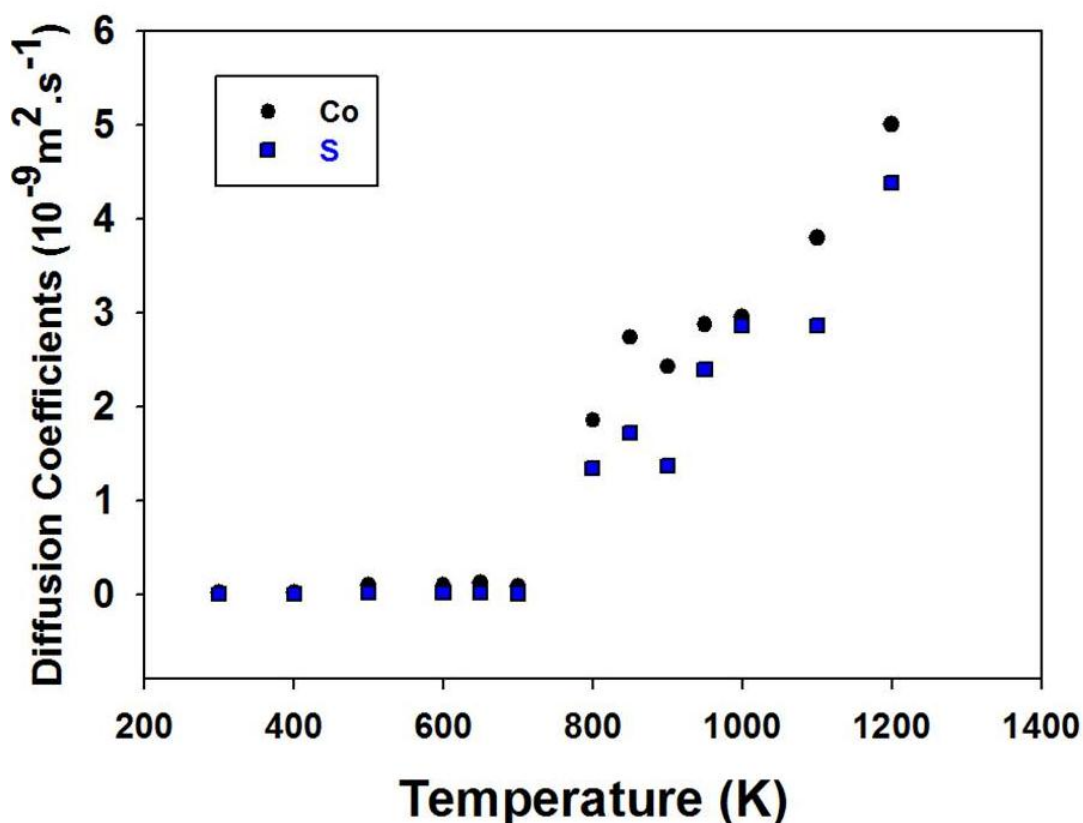


Figure 4.42: Temperature dependence of the average diffusion coefficients of Co and S on the slab constituting the {100} surface of Co_9S_8 in contact with water.

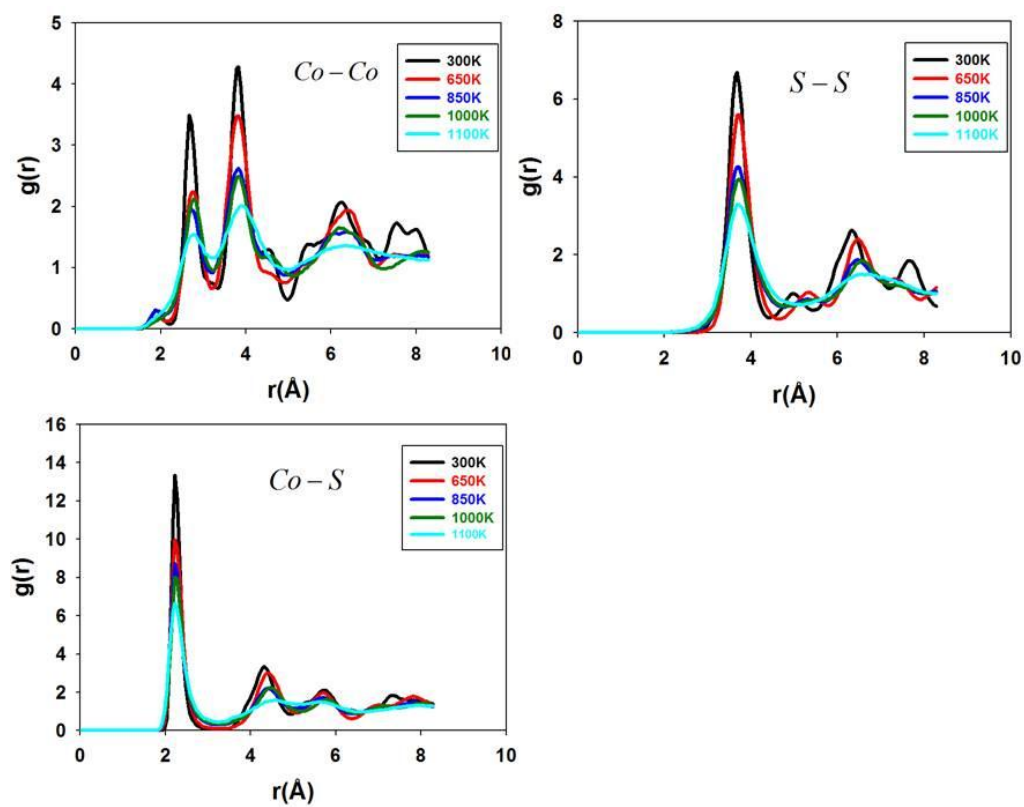


Figure 4.43: Radial Distribution functions of Co-Co, Co-S and S-S pairs of the {100} surface of Co_9S_8 in contact with water at different temperatures.

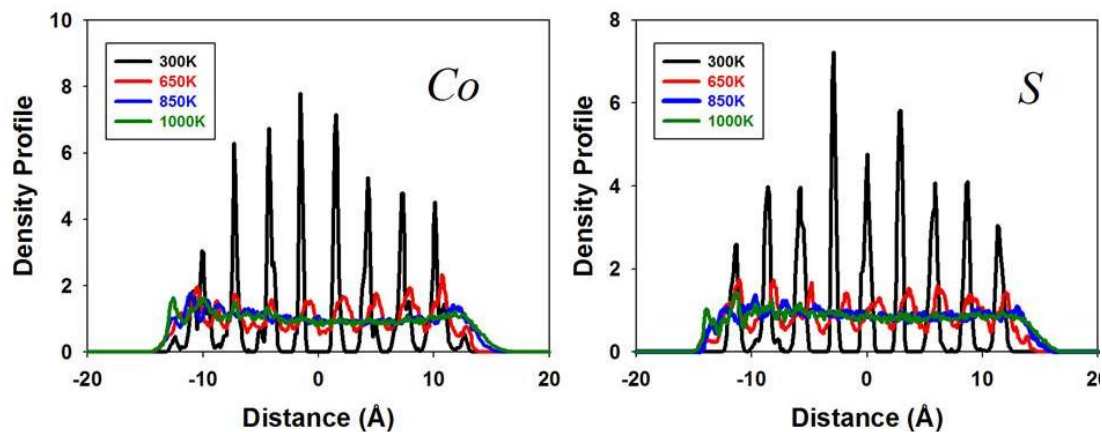


Figure 4.44: Density profile of cobalt (Co) and sulphur (S) atoms of Co_9S_8 in contact with water at indicated temperatures for the $\{100\}$ surface.

Similarly to the other two surfaces, the investigation of the melting behaviour of the $\{100\}$ surface in contact with water was produced by constructing the plots of density profiles as a function of distance. Figure 4.44 shows the density profiles of ions, i.e. cobalt and sulphur at several temperatures. At the temperature of 300 K, the peaks are relative sharp; however at increased temperatures those peaks are broadened. This implies the mobility of the ions at high temperatures.

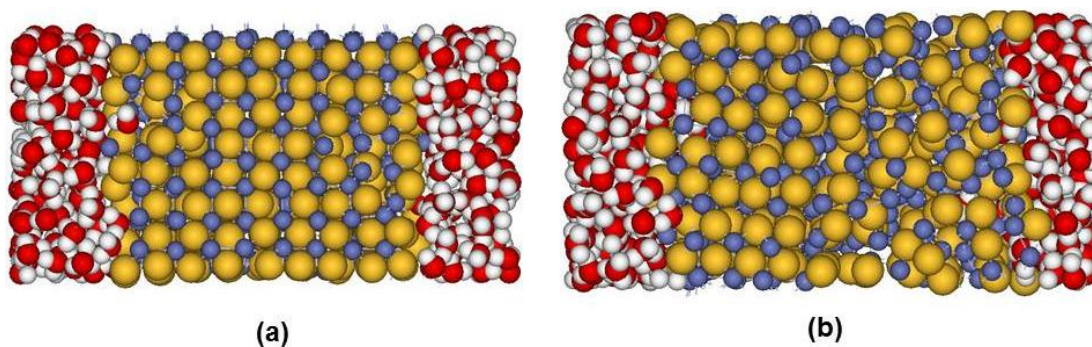


Figure 4.45: Snapshots of the MD simulation of interaction of water with $\{100\}$ surface of Co_9S_8 at 300K and 850K.

In order to reflect general features of the system configuration, snapshots of the final configurations of the MD simulations of a slab in contact with water at temperatures of 300 and 850 K are shown in Figure 4.45. It can be observed that, at 300 K the structure is crystalline, which implies that is still at solid phase. However, at 850 K the structure is disordered, which implies that the surface is no longer crystalline as compared to the initial configuration shown in Figure 4.40. The water does not, however, permeate through the slab to the same extent as it does on the {111} and {101} surfaces.

Chapter 5: The Structure and Stability of Co_9S_8 Nanoparticles

Nanoscience and nanotechnology collectively represent one of the fastest growing interdisciplinary scientific areas, spanning interests from physics, through chemistry and geoscience, to biology [146]. Nanostructured materials and nanophase systems are words used to describe particles of between 1 and 100 nm in size. One of the features of these very small particles is that, they often have unique physical and chemical properties [147]. Hence, nanoscaled systems have been extensively investigated by both experiments and computer simulations in recent years not only due to their enormous technological importance, but also due to scientific interests [148]. Akbarzadeh *et al* [149] mentioned that particles with diameter of 1-10 nm exhibit properties that are often intermediate between those of the molecular and crystalline states. Furthermore, they mentioned that nanoscience and nanomaterials have been identified worldwide as key to unlocking a new generation of devices with revolutionary properties and functionalities. The study of nanoparticles with new properties has become an emerging interdisciplinary field based on solid state physics, chemistry, biology and materials science [150]. Bulk solid and liquid phases of materials are in equilibrium at a specific temperature and pressure, the melting point: however, the melting of nanoparticles is more complex. The nature of the melting process and the temperature at which a particle melts depends on its size, as

mentioned by Alavi and Thompson [151]. They further mentioned that, as the size of the particle increases, the melting behavior and the melting point will approach that of the bulk. Researchers have paid more attention to the melting of nanosolids (nanosolids can be nanoparticles, nanowires or nanofilms), since their melting temperatures are lower than those of corresponding bulk materials [152]. Gilbert *et al* [153] mentioned that nanoparticles may contain unusual forms of structural disorder that can substantially modify materials properties and thus cannot solely be considered as small pieces of bulk material. It has long been known that the particle-size-dependent melting point (T_m) depression occurs when the particle size is on the order of nanometers since it was first reported by Pawlow in 1909 [154] and recently by Zhao *et al* in 2001 [155]. The melting temperature of any nanoparticle basically depends on the ratio of the number of surface atoms to the total number of atoms. Significant melting temperature suppression is observed when the particle size approaches the sub-20 nm range as mentioned by Gupta *et al* [156]. They further mentioned that, the behavior of melting temperature is similar for the larger nanoparticles of all considered shapes but differs significantly for small nanoparticles. Fluctuations and deviations from the bulk are shown to produce a considerable effect on the melting of small particles [157]. In this chapter we will study the effect of size and shape of the Co_9S_8 nanoparticles on melting. The effect of water on the Co_9S_8 nanoparticles will also be studied. As intermediates between the molecular and the solid state inorganic, nanoparticles combine chemical accessibility in solution with physical properties of the bulk phase. This makes them ideal elements for the construction of nanostructured materials with adjustable physical and chemical properties [158].

Mineral particles with diameters on the scale of nanometers (nanoparticles) are important constituents of natural environments. The small size of such particles has a host of consequences for biogeochemical systems. One consequence is that, nanoparticles have the potential for a long lifetime in the environment, and widespread transport under certain circumstances [159]. Mineral nanoparticles have variety of important geological and technological properties, which includes removal of toxins from the environment [160] and as a key abrasive material for chemical-mechanical planarization of advanced integrated circuits [161]. In addition to mineral growth or weathering, nanoparticles can be generated by mechanical grinding associated with earthquake-generating faults in Earth's crust [162]. Studies of nanoparticles connect with several other important scientific areas dealing with lower dimensional materials, especially the study of mineral and other solid surfaces and the investigation of the nucleation and initial growth of precipitates [163]. There is an immediate synergy between the study of nanoscale particles in natural systems and the disciplines of mineralogy, chemistry, physics and materials science, because nanoscale processes are intrinsically molecular [164]. Metal sulphide nanostructures are important nanomaterials due to their extensively promising applications in electronic, optical, optoelectronic and magnetic devices [165]. Along with many other metal sulfides, cobalt sulphides are considered as promising electrodes for lithium batteries for their low cost and high theoretical capacity [32]. Wang et al [34] examined the possibility of using cobalt sulphide nanopowders as cathode materials for lithium-rechargeable batteries.

This chapter describes the investigation of Co_9S_8 nanoparticles using molecular dynamics. It concentrates on Co_9S_8 nanoparticles bounded by the {111}, {101} and {100} surfaces. We start by considering how the nanoparticles are constructed.

5.1. Construction of nanoparticles

Spagnoli and co-workers [166] developed a simple and robust approach for generating mineral nanoparticles, which involves the use of Wulff construction [72] based on the surface energies calculated from the different two-dimensional surfaces. The Wulff construction states that, the equilibrium shape is that which minimizes the surface energy. Wulff construction is one of the classic models to describe particle shape, whether small, large, free-standing, or as precipitates and it dictates a particle shape given its orientation-dependent surface free energy [167]. The equilibrium morphology of Co_9S_8 is similar to that of the $\{101\}$ surface most stable surface.

We constructed three different morphologies of Co_9S_8 nanoparticles using the surface energies of the $\{111\}$, $\{100\}$ and $\{101\}$ Miller indices for a comparative study. The surface energies of two-dimensional static lattice calculations were calculated using energy minimisation code, METADISE. The generated nanoparticles of Co_9S_8 consisted of only one surface and the resulting crystal morphologies together with the surface energies of the $\{111\}$, $\{100\}$ and $\{101\}$ Miller indices are shown in Figure 5.1. Since the Co_9S_8 was modelled using an $Fm\bar{3}m$ space group, the $\{111\}$ equilibrium morphology is octahedral, the $\{100\}$ is cubic and $\{101\}$ is rhombic dodecahedral. To the best of my knowledge this method was never used for the Co_9S_8 , however has been applied successfully to simulate MgO structure by Spagnoli *et al* [166], which has the same space group as Co_9S_8 . In addition, it was also successful in simulating the calcite nanoparticles by Kerisit *et al* [168], Cooke and Elliott [169] and Martin *et al* [170] and again simulating the hematite nanoparticles by Spagnoli *et al* [171].


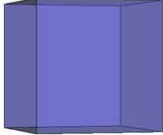
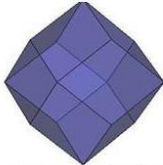
Miller Indices	Surface energy (J/m ²)	Crystal Morphology
{111}	2.213	
{100}	6.098	
{101}	3.098	

Figure 5.1: The predicted crystal morphologies together with the surface energies of {111}, {100} and {101} Miller indices.

5.2. Effect of Size on Melting Temperature of Co₉S₈ Nanoparticles

In this section we present the results of the MD study on the melting of Co₉S₈ nanoparticles. The physics of melting, particularly the relationship between melting and intrinsic instabilities of crystals and liquids, has remained a subject of great interest for most of the century beginning at least as early as Lindemann (1910) paper relating melting to a threshold for atom displacements from their equilibrium positions [172]. It is well known that the bulk solid and liquid phases of materials are in equilibrium at a specific temperature and pressure, the melting point; however, the melting of nanoparticles is more complex. The nature of the melting process and the temperature at which a particle melts depends on its size. Of course, as the size of the particle increases the melting behaviour and the melting point approach that of the bulk [152].

The melting properties of size-selected Co_9S_8 nanoparticles of the surfaces $\{111\}$, $\{101\}$ and $\{100\}$ with different number of atoms are studied using molecular dynamics simulations. Some of the distinctive melting mechanisms are identified. The melting of Co_9S_8 nanoparticles may be explained by the radial distribution functions (RDFs), where at the low temperatures, the RDFs have many peaks and at the high temperatures the peaks are broadened. The other distinctive melting mechanism is diffusion coefficients as a function of temperature, where the mobility of the ions, i.e. cobalt and sulphur is noted as the temperature increases. Furthermore, the melting of nanoparticles may be described as a transition from a low-energy solid-like structure at low temperatures to a higher-energy liquid-like structure at high temperature [163]. The arrangement of atoms on a nanoparticle structure after simulation is the other way to identify the melting of nanoparticles.

5.2.1. Surface $\{111\}$ Co_9S_8 nanoparticle

We start by investigating the equilibrium morphology $\{111\}$ terminated Co_9S_8 nanoparticles of different sizes. According to our energy minimisation surface energy calculations, $\{111\}$ is the most stable surface, with the lowest surface energy. We performed the simulations of $\{111\}$ Co_9S_8 terminated nanoparticles containing different numbers of identical atoms, i.e., it contains 342, 708, 1394, 2422, which corresponds to 2.9 nm, 3.3 nm, 4.4 nm and 5.3 nm in diameter, respectively. The MD simulation box sizes of the different number of atoms are shown in Table 5.1. All calculations were performed using an NVT ensemble for 200 picoseconds. The MD simulation box sizes of different number of atoms of the $\{111\}$ terminated Co_9S_8 nanoparticles are shown in Table 5.1. Periodic boundary conditions are used in the simulations.

Table 5.1: Simulation box sizes of different number of atoms for {111} terminated Co₉S₈ nanoparticles.

No. of Atoms	Particle dimension (nm)	Simulation Box Size (Å ³)
342	2.9	49.61×49.61×90
708	3.3	54.29×54.29×98
1394	4.4	64.47×64.47×120
2422	5.3	73.83×73.83×137

Thermodynamically, the melting of bulk crystalline solids is characterized by a sudden increase in the free energy [173]. Figure 5.2 shows the variation of total energy as a function of temperature for a {111} terminated Co₉S₈ nanoparticle with different number of atoms. It can be seen that as the temperature increases, the energy first increases almost linearly up to a certain temperature (say point A), where a sudden change in slope occurs which extends to the other temperature (say point B) after which energy again increases near linearly with temperature. Point A may be considered to be where the melting starts and point B where it ends. For a nanoparticle with 342 atoms in Figure 5.2a the melting seems to be happening between the temperature of 930 and 950 K, and there is an abrupt increase in energy. In the case of a nanoparticle with 708 atoms in Figure 5.2b, the energy change occurs between the 800 and 950 K and is more gradual than for 342 atoms. For a nanoparticle with 1394 atoms in Figure 5.2c the sudden increase in energy is observed between 900 and 1050 K.

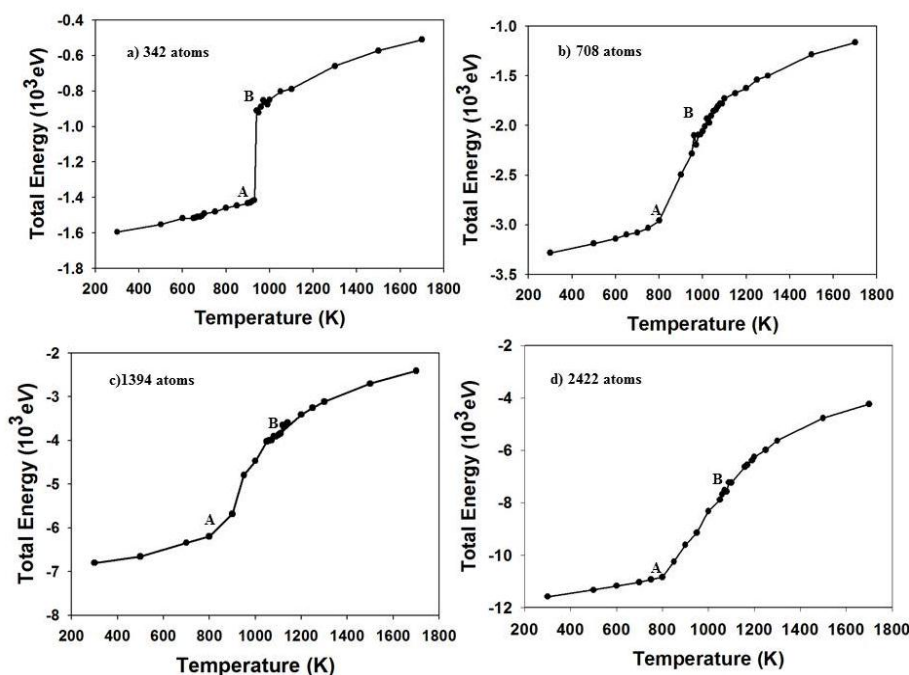


Figure 5.2: Total energy variation with temperature for the {111} terminated Co_9S_8 nanoparticle with a) 342 atoms, b) 708 atoms, c) 1394 atoms and d) 2422 atoms.

As for a nanoparticle with 2422 atoms, we note the sudden increase in energy from 800 to 1000 K. The energy plots, particularly for 708, 1394 and 2422 atoms, do not give the exact melting temperature of the nanoparticles; consequently we further demonstrate the melting of the nanoparticles from diffusion of ions. Figure 5.3 shows the diffusion coefficients of Co and S as a function of temperature for different sizes of {111} terminated Co_9S_8 nanoparticles. We note that between certain temperatures, for all sizes of nanoparticles, there is no movement of both the cobalt and sulphur ions, since the diffusion is almost zero. For a nanoparticle with 342 atoms, there is no movement of both the cobalt and sulphur ions between 300 and 930 K, as depicted in Figure 5.3a. The noticeable movement of both ions is at 940 K, where an abrupt increase of diffusion to a value of $42.24 \times 10^{-9} \text{ m}^2 \cdot \text{s}^{-1}$ occurs. This temperature falls within the range of the melting temperature depicted by the energy against temperature curve in Figure 5.2a. In the case of a nanoparticle with 708 atoms, shown

in Figure 5.3b, we observe the mobility of both cobalt and sulphur ions at 800 K, with the diffusion coefficient of $21.77 \times 10^{-9} \text{ m}^2 \cdot \text{s}^{-1}$ and it increases gradually with temperature. Figure 5.3c features the nanoparticle with 1394 atoms, where both cobalt and sulphur ions start to move at 900 K with the diffusion coefficient of $14.91 \times 10^{-9} \text{ m}^2 \cdot \text{s}^{-1}$. For a nanoparticle with 2422 atoms, in Figure 5.3d, the mobility of both cobalt and sulphur ions is observed at 850 K with the diffusion coefficient of $3.55 \times 10^{-9} \text{ m}^2 \cdot \text{s}^{-1}$. The temperature at which the onset of ions mobility occurs for a nanoparticle with 1394 atoms is higher than that of a nanoparticle with 2422 atoms; however the ion diffusion of a nanoparticle with 2422 atoms is less as compared to the one with 1394 atoms. The most abrupt change in the diffusion coefficient is observed on the nanoparticle with 342 atoms, and it appears like a first order transition.

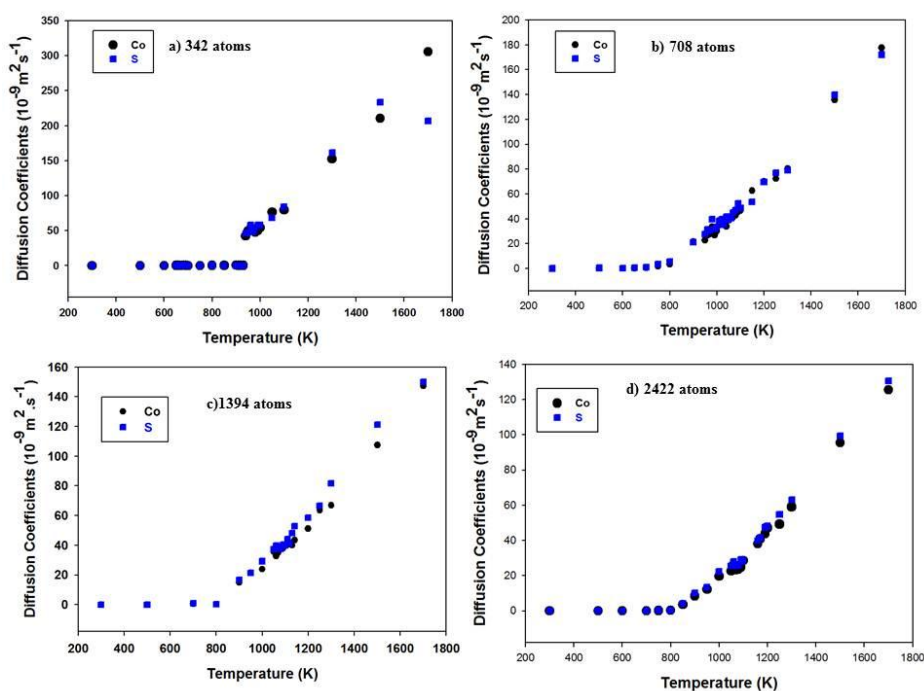


Figure 5.3: Diffusion coefficients as a function of temperature for $\{111\}$ terminated Co_9S_8 nanoparticle with a) 342 atoms, b) 708 atoms, c) 1394 atoms and d) 2422 atoms.

The other mechanism of detecting the melting temperature of the structure is through the radial distribution functions (RDFs), which also provide specific information on local structures in Co_9S_8 . We calculated the RDFs for all pairs of ions for various sizes of the surface $\{111\}$ Co_9S_8 nanoparticle. Co-Co, Co-S and S-S RDFs pairs for different temperatures of nanoparticles with 342 atoms, 708 atoms, 1394 atoms and 2422 atoms are shown in Figures (5.4, 5.5, 5.6, 5.7) respectively. It can be deduced that the RDFs show structural changes at different temperatures for different sizes of nanoparticles.

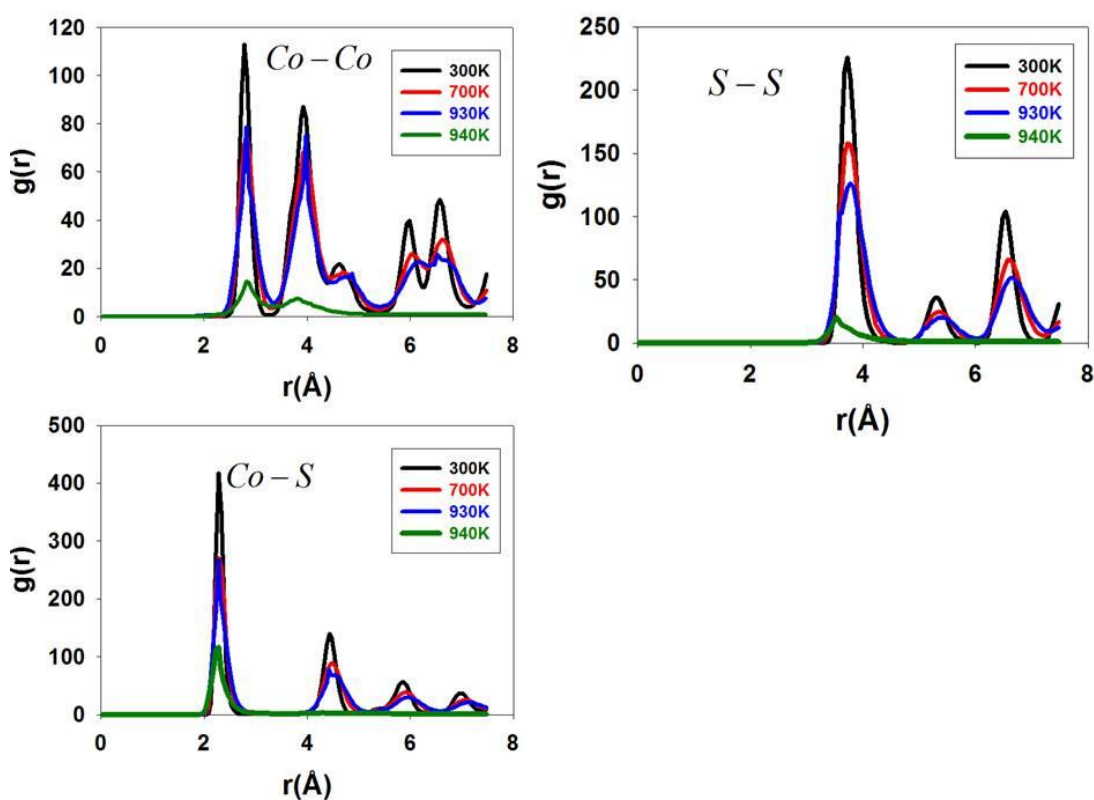


Figure 5.4: The RDFs of Co-Co, Co-S and S-S pairs for a $\{111\}$ terminated Co_9S_8 nanoparticle with 342 atoms at the indicated temperatures.

The nanoparticle with 342 atoms, in Figure 5.4, has a well-defined structure, as observed by many peaks of the RDFs, from 300 to 930 K. The height of the peaks is also reduced as the temperature increases. The significant peak height reduction for

the Co-Co, Co-S and S-S pairs is observed at 940 K; in particular the second Co-Co peak almost collapses, suggestive of the liquid phase of the nanoparticle with 342 atoms. This is the same temperature observed for the energy against temperature graph in Figure 5.2a and for the diffusion of ions in Figure 5.3a. For a nanoparticle with 708 atoms, in Figure 5.5, the structure is well-ordered between the temperatures of 300 K and 950 K. At the temperature of 950 K the peaks start to be broader; however, at 960 K the peaks have disappeared completely, suggestive of the melting of the nanoparticle with 708 atoms.

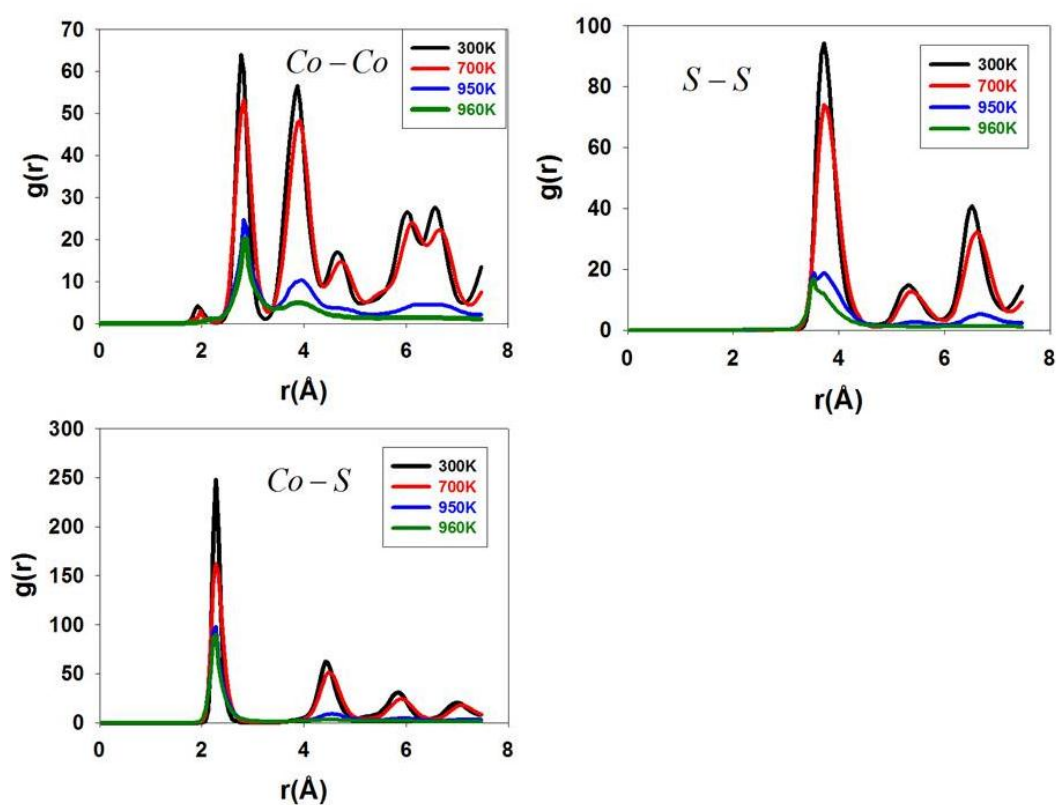


Figure 5.5: The RDFs of Co-Co, Co-S and S-S pairs for a {111} terminated Co_9S_8 nanoparticle with 708 atoms at the indicated temperatures.

Figure 5.6 shows the Co-Co, Co-S and S-S RDFs pairs of the nanoparticle with 1394 atoms at the temperatures leading to the melting. It can be deduced from the many peaks of the RDFs that from 300 to 1000 K, the nanoparticle has a well-defined

structure. At 1000 K the peaks start to broaden and the height of the peaks has decreased substantially as compared to those at lower temperatures; however at 1040K the peaks beyond the first have almost disappeared, indicative of the liquid phase of the nanoparticle with 1394 atoms. Figure 5.7 shows the RDFs pairs Co-Co, Co-S, S-S of the nanoparticle with 2422 atoms. At the temperatures between 300 and

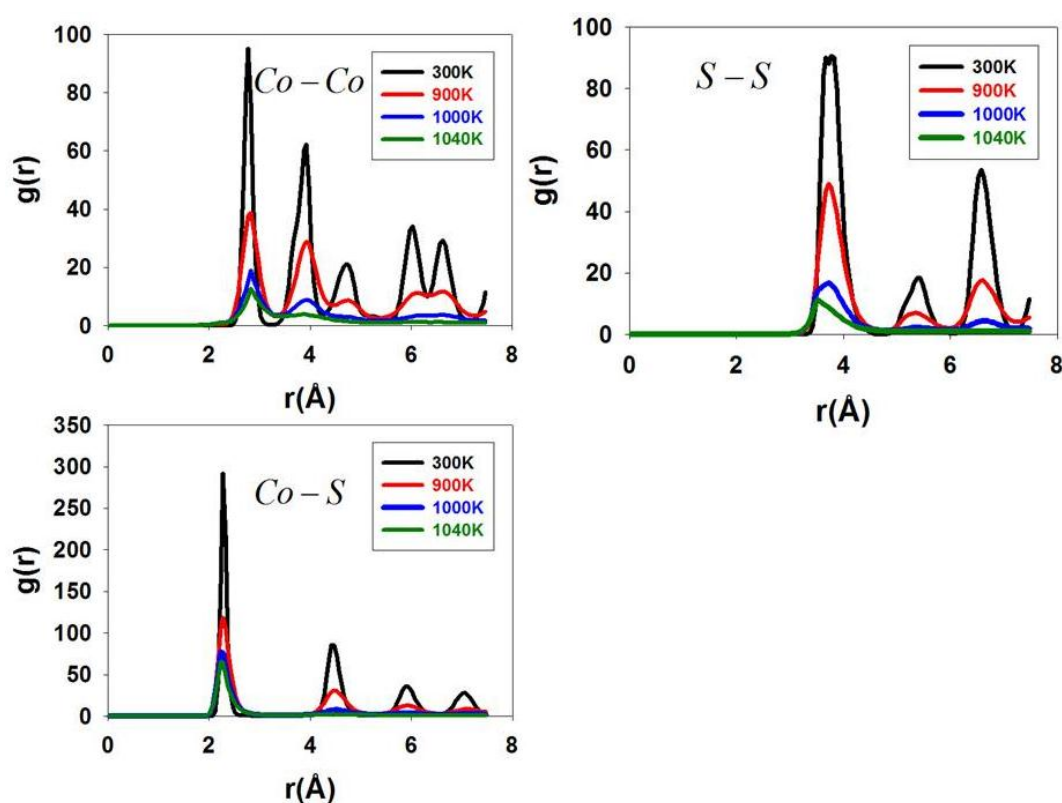


Figure 5.6: The RDFs of Co-Co, Co-S and S-S pairs for a {111} terminated Co_9S_8 nanoparticle with 1394 atoms at the indicated temperatures.

1050 K, a nanoparticle has a well-ordered structure, as observed by the many and sharp peaks. At 1050 K, the peaks are broader; however, it is at 1090 K where most peaks have almost disappeared, indicative of the melting of the 2422 atoms nanoparticle. The RDFs demonstrate that the melting temperature of the nanoparticles is enhanced with the increase in the number of atoms in a nanoparticle.

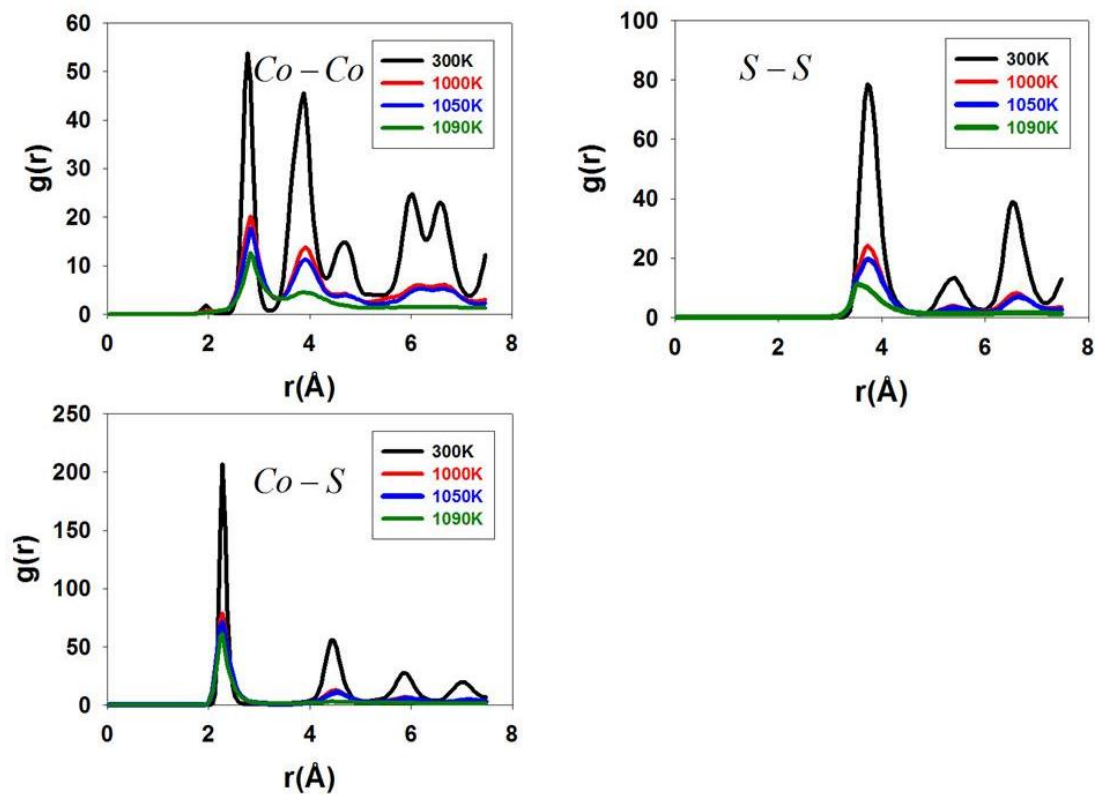


Figure 5.7: The RDFs of Co-Co, Co-S and S-S pairs for a {111} terminated Co_9S_8 nanoparticle with 2422 atoms at the indicated temperatures.

A further approach of probing the melting of nanoparticles of different sizes is through the atomic density profiles. Figures (5.8, 5.9, 5.10 and 5.11) present the atomic density distribution of cobalt (Co) and sulphur (S) atoms in the {111} surface Co_9S_8 nanoparticles along the nanoparticle axis during the melting process. The direction corresponds to the axis of the octahedral. At lower temperatures the solid like features are apparent, which are indicated by distinct peaks. These suggest that there is less movement of atoms along the nanoparticles axes in the specified temperature range. At the melting temperature of nanoparticles of different sizes the atomic distribution becomes smooth, indicating the liquid phase. From the atomic density profiles of cobalt and sulphur for a nanoparticle with 342 atoms in Figure 5.8

at the temperatures of 300 K, 700 K, 930 K we still have the solid like features, which is indicated by the sharp peaks.

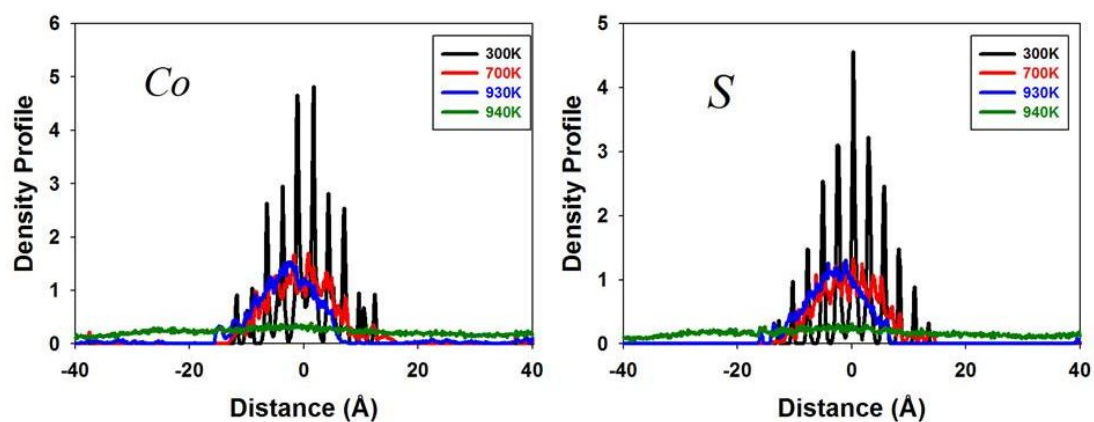


Figure 5.8: Atomic density profiles of {111} terminated Co_9S_8 nanoparticle with 342 atoms for cobalt (Co) and sulphur (S) at various temperatures.

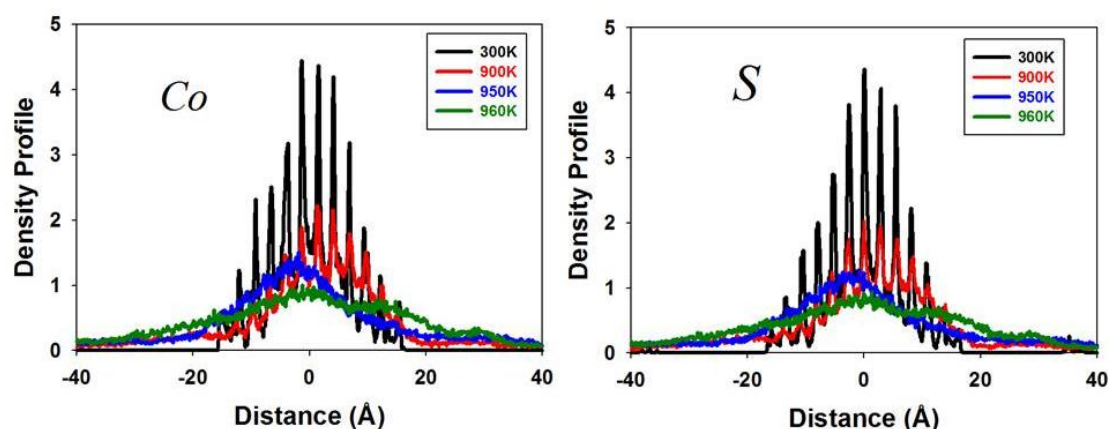


Figure 5.9: Atomic density profiles of {111} terminated Co_9S_8 nanoparticle with 708 atoms for cobalt (Co) and sulphur (S) at various temperatures.

However, at 940 K the atomic distribution for both the cobalt and sulphur atoms becomes smooth, indicating the liquid phase. For a nanoparticle with 708 atoms the atomic density profiles in Figure 5.9 at the temperatures of 300 K, 900 K, 950 K, we observe the solid like features of the nanoparticle, which is depicted by the many peaks. However at 960 K the atomic distribution for both the cobalt and sulphur atoms becomes smooth, suggestive of the melting of the nanoparticle with 708 atoms. We

now present the atomic density profiles of a nanoparticle with 1394 atoms shown in Figure 5.10 and a nanoparticle with 2422 atoms shown in Figure 5.11. It can be seen that at lower temperatures, we still have the solid like features, which is indicated by the many peaks. At a higher temperature of 1100 K, the atomic density profiles exhibit broadened peaks with lower intensities, which is evidence that the nanoparticles are in a liquid or amorphous phase.

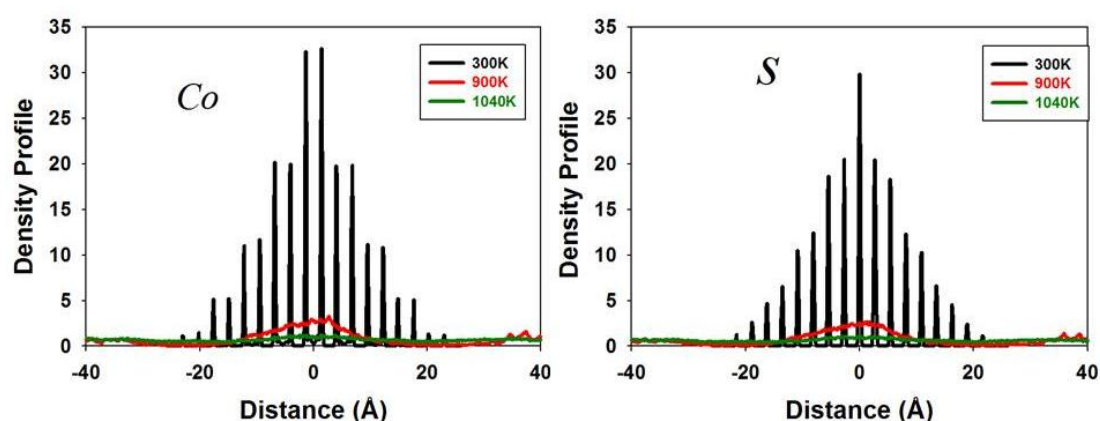


Figure 5.10: Atomic density profiles of {111} terminated Co_9S_8 nanoparticle with 1394 atoms for cobalt (Co) and sulphur (S) at various temperatures.

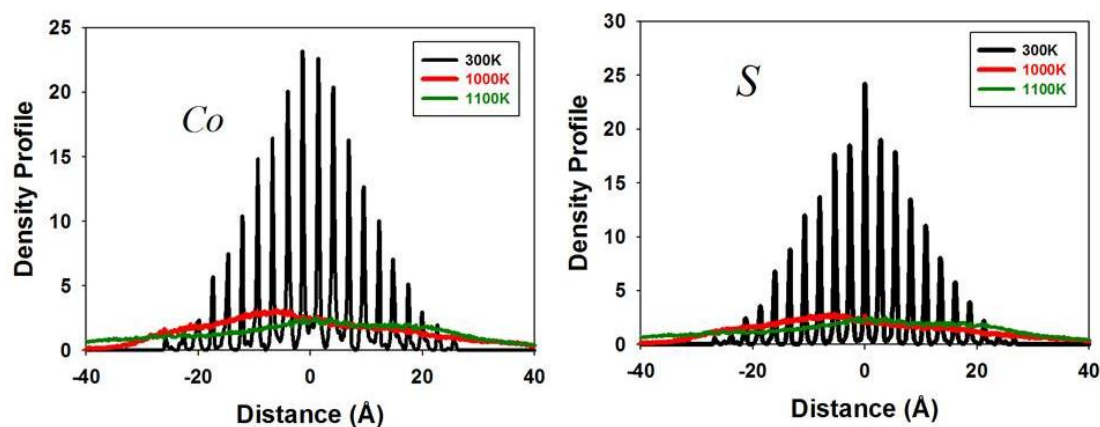


Figure 5.11: Atomic density profiles of {111} terminated Co_9S_8 nanoparticle with 2422 atoms for cobalt (Co) and sulphur (S) at various temperatures.

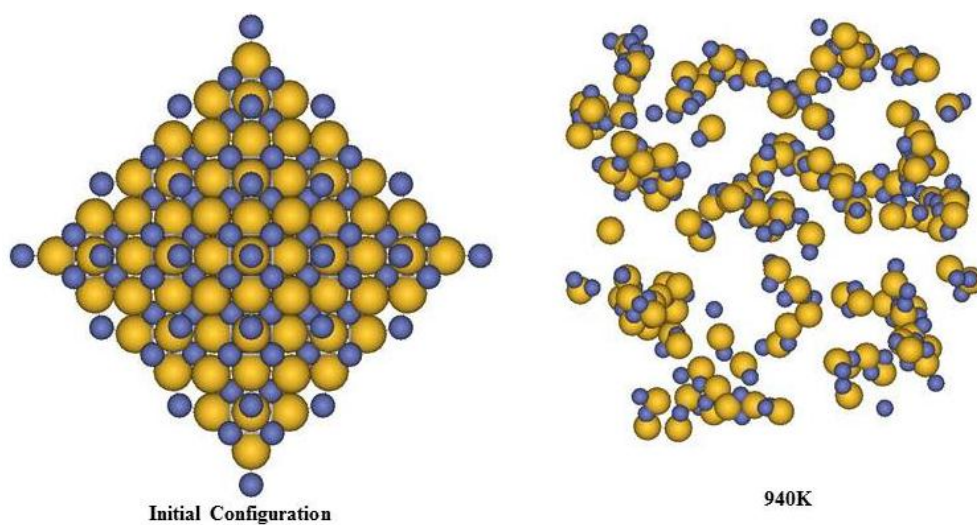


Figure 5.12: The initial configuration on the left and the structure at melting point on the right of the Co_9S_8 nanoparticle of $\{111\}$ surface with 342 atoms. Purple, yellow spheres represent cobalt (Co), sulphur (S) atoms respectively.

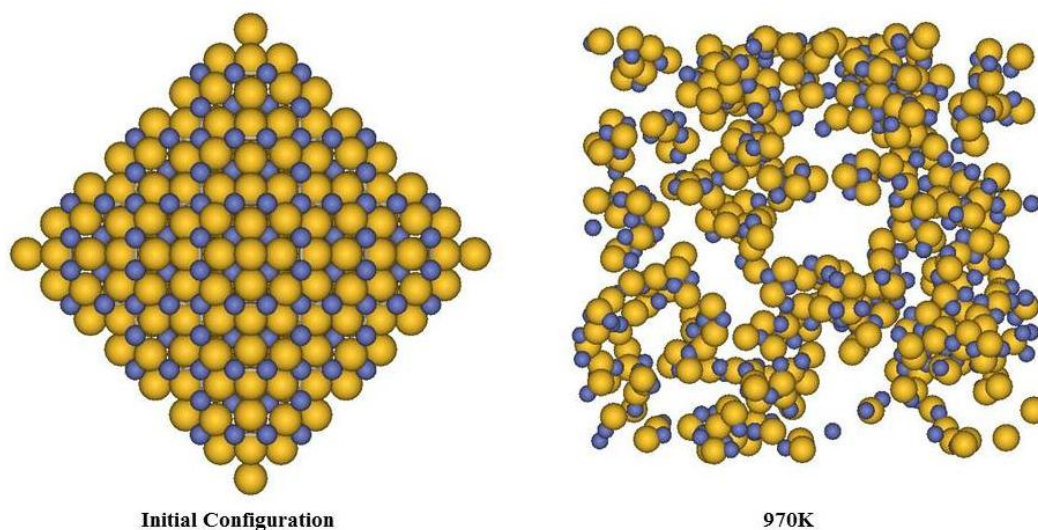


Figure 5.13: The initial configuration on the left and the structure at melting point on the right of the Co_9S_8 nanoparticle of $\{111\}$ surface with 708 atoms. Purple, yellow spheres represent cobalt (Co), sulphur (S) atoms respectively.

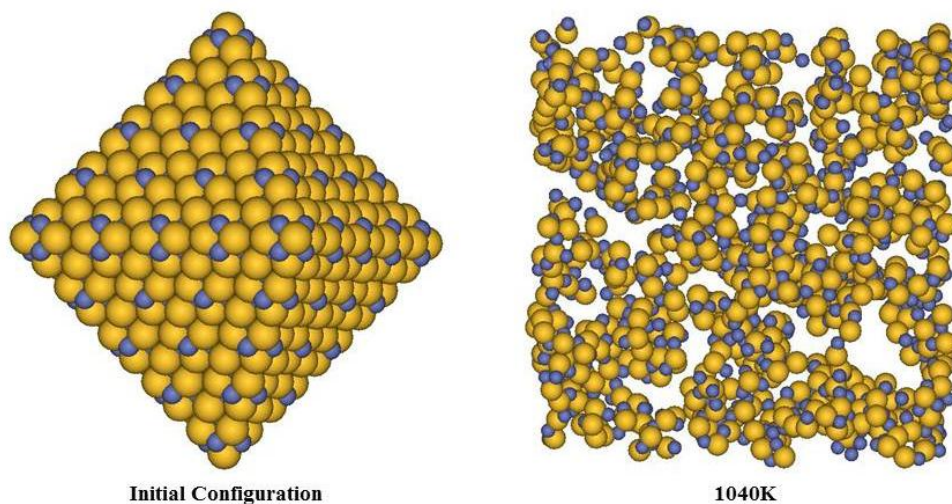


Figure 5.14: The initial configuration on the left and the structure at melting point on the right of the Co_9S_8 nanoparticle of $\{111\}$ surface with 1394 atoms. Purple, yellow spheres represent cobalt (Co), sulphur (S) atoms respectively.

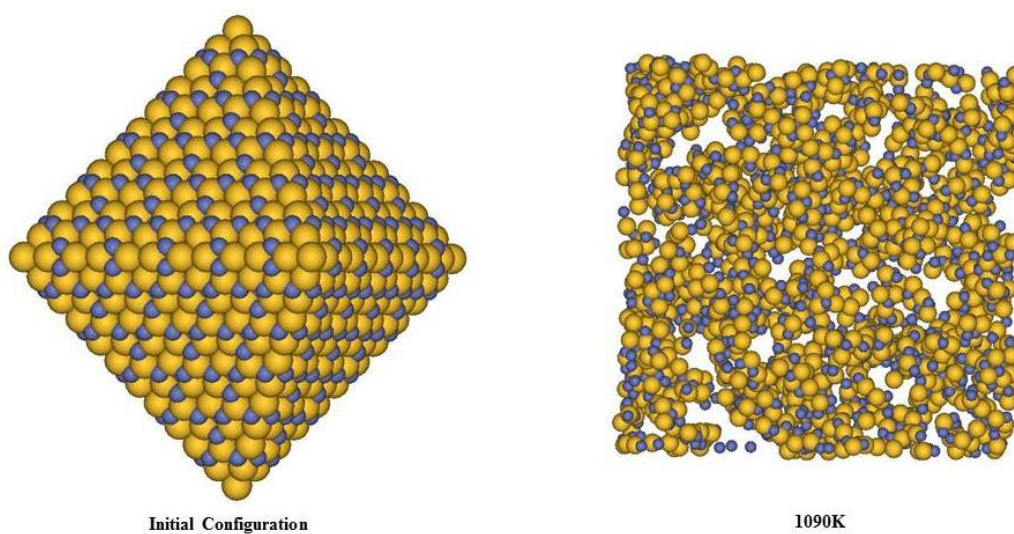


Figure 5.15: The initial configuration on the left and the structure at melting point on the right of the Co_9S_8 nanoparticle of $\{111\}$ surface with 2422 atoms. Purple, yellow spheres represent cobalt (Co), sulphur (S) atoms respectively.

The initial configuration structures and the structures at melting points of the surface {111} Co_9S_8 nanoparticles with 342 atoms, 708 atoms, 1394 atoms and 2422 atoms are shown in Figures (5.12, 5.13, 5.14 and 5.15), respectively. It can be seen that the nanoparticles assumes a well-ordered octahedral shapes at the initial configuration, and at the indicated melting points the atom packing is disordered, with hollow portions, suggestive of the melting or amorphous nature of the nanoparticles.

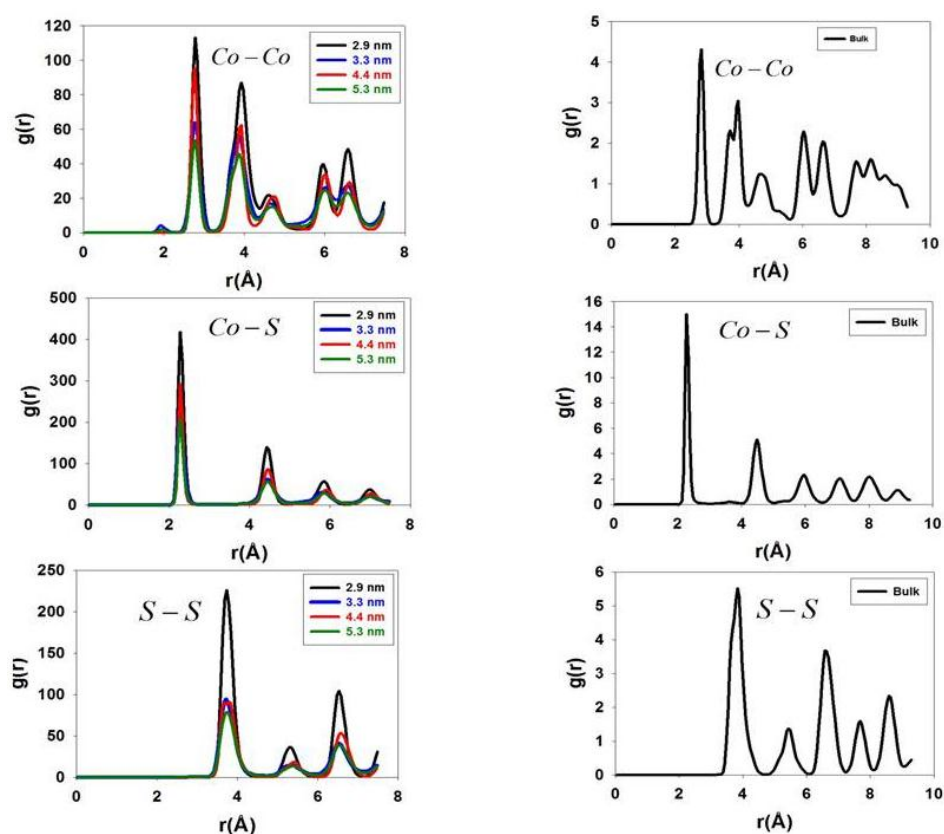


Figure 5.16: Radial distribution functions of Co_9S_8 {111} nanoparticle at 300K for the Co-Co, Co-S and S-S pairs for different number of atoms and bulk pairs.

The radial distribution functions (RDFs) for different atomic pairs are shown in Figure 5.16. Table 5.2 shows the positions of the peaks in RDFs. It can be seen that position of the peaks for Co-S, Co-Co and S-S pairs does not change with the particle size.

Table 5.2: Interatomic distances of different materials of Co₉S₈.

Materials	Co-S	Co-Co (I)*	Co-Co (II)*	S-S
2.9nm	2.28	2.78	3.83	3.73
3.3nm	2.28	2.78	3.83	3.73
4.4nm	2.28	2.78	3.83	3.73
5.3nm	2.28	2.78	3.83	3.73
Bulk	2.28	2.78	3.98	3.78
^a Crystallographic data Bulk	2.227/ 2.127 (T) 2.359(O)	2.505	3.474/3.543	
^b Exp. Bulk (EXAFS)	2.21	2.51	3.54	

* denotes the two types of Cobalt. I is in the tetrahedral site and II is in the octahedral site
^a Ref. [136], ^b Ref. [174]

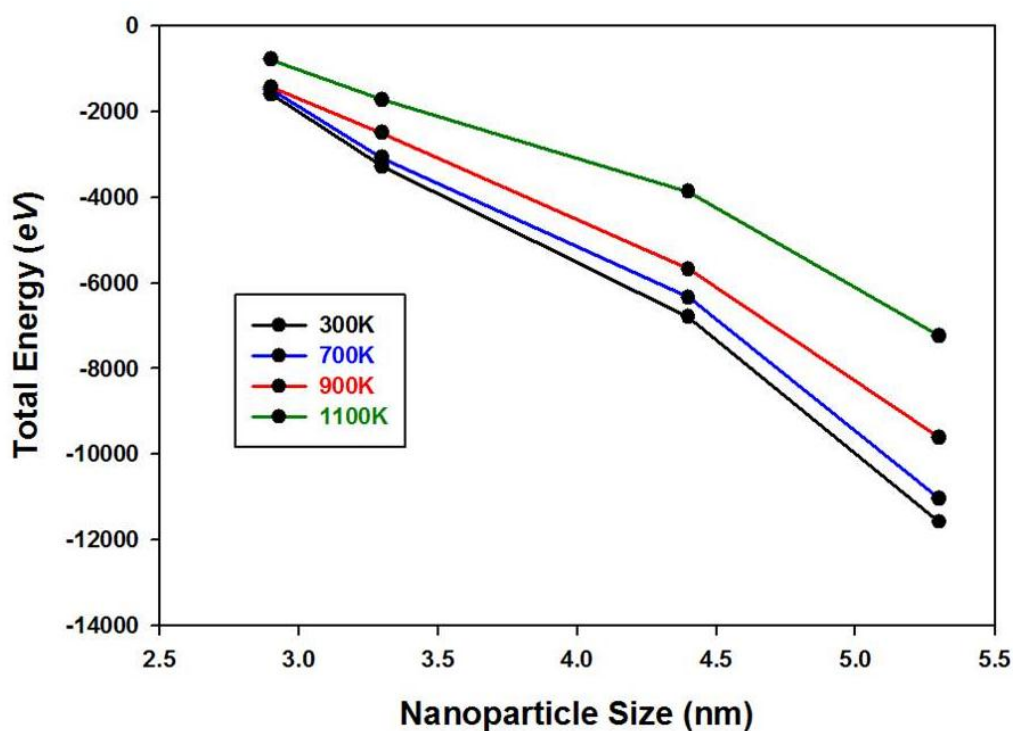


Figure 5.17: Total energy as a function of nanoparticle size for surface {111} Co₉S₈ nanoparticle at 300 K, 700 K, 900 K and 1100 K.

Figure 5.17 shows the approximate change in total energy versus nanoparticle size in nanometres. From the figure it is evident that as the nanoparticle size decreases the energy becomes more positive. As expected, the stability of nanoparticle is enhanced as the number of atoms increase.

5.2.2. Surface {101} Co₉S₈ nanoparticle

We now consider the {101} terminated Co₉S₈ nanoparticle. According to our surface energy calculations using energy minimisation, {101} surface is the second most stable surface. We performed the simulations of {101} nanoparticles containing different numbers of atoms, i.e., 360, 748, 1324, 2480, which correspond to sizes of approximately 2.5 nm, 3.3 nm, 3.7 nm and 4.7 nm in diameter, respectively. All calculations were performed on an NVT ensemble for 200 picoseconds. The MD simulation box sizes of different number of atoms are shown in Table 5.2. The periodic boundary conditions are used in the simulations.

Table 5.3: Simulation box sizes of different number of atoms for {101} terminated Co₉S₈ nanoparticles.

No. of Atoms	Particle dimension (nm)	Simulation Box Size (Å ³)
360	2.5	44.93×44.93×81
748	3.3	54.29×54.29×98
1324	3.7	56.91×56.91×106
2480	4.7	69.15×69.15×129

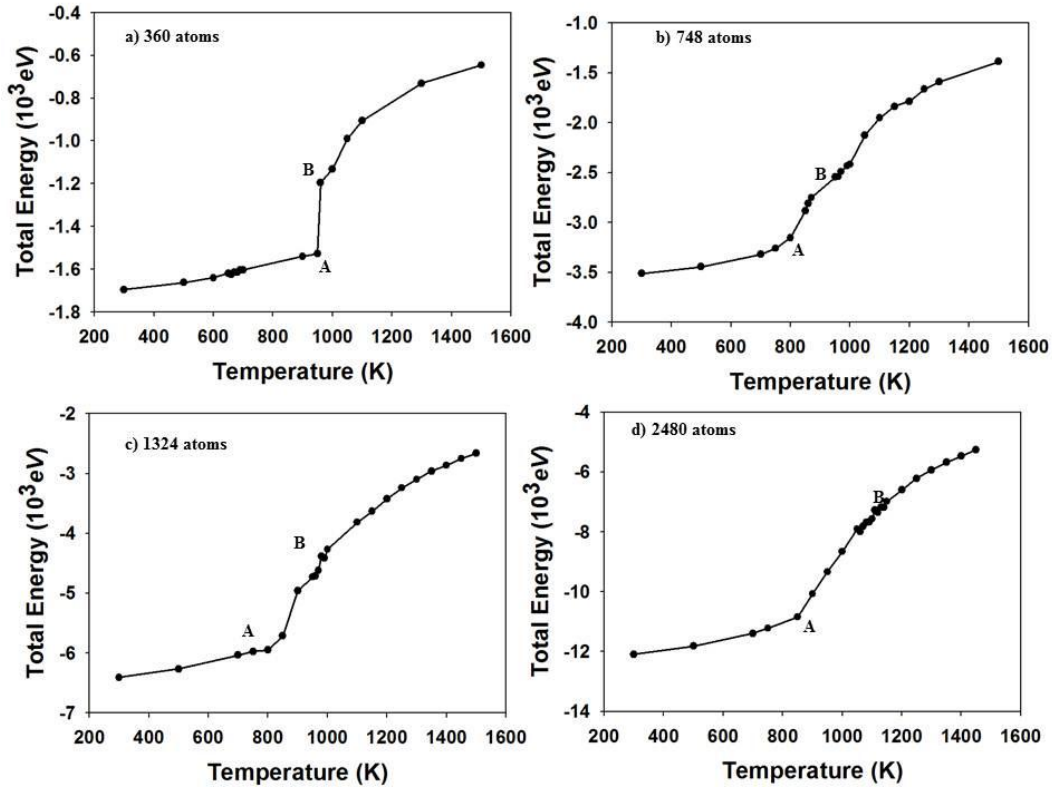


Figure 5.18: Total energy variation with temperature for the $\{101\}$ terminated Co_9S_8 nanoparticle with a) 360 atoms, b) 748 atoms, c) 1324 atoms and d) 2480 atoms.

Figure 5.18 shows the temperature dependence of the energy for the surface $\{101\}$ Co_9S_8 nanoparticle with different numbers of atoms. The transition from solid to liquid phase can be identified by a jump in the energy curve. It can be noted that there is a change of slope at a certain temperature for different sizes of nanoparticles. For the nanoparticle with 360 atoms (Figure 5.18a), an abrupt energy change occurs at a temperature of 960 K. In the case of a nanoparticle with 748 atoms in Figure 5.18b, the change, even though it is not clear, is observed between the 800 and 1000 K. For a nanoparticle with 1324 atoms in Figure 5.18c, the change is between 900 and 1000 K and for nanoparticle with 2480 atoms in Figure 5.18d the change of energy is noticed between 850 and 1050 K. Except for the nanoparticle with 360 atoms the energy variations with temperature plots do not give the exact melting temperature of nanoparticles.

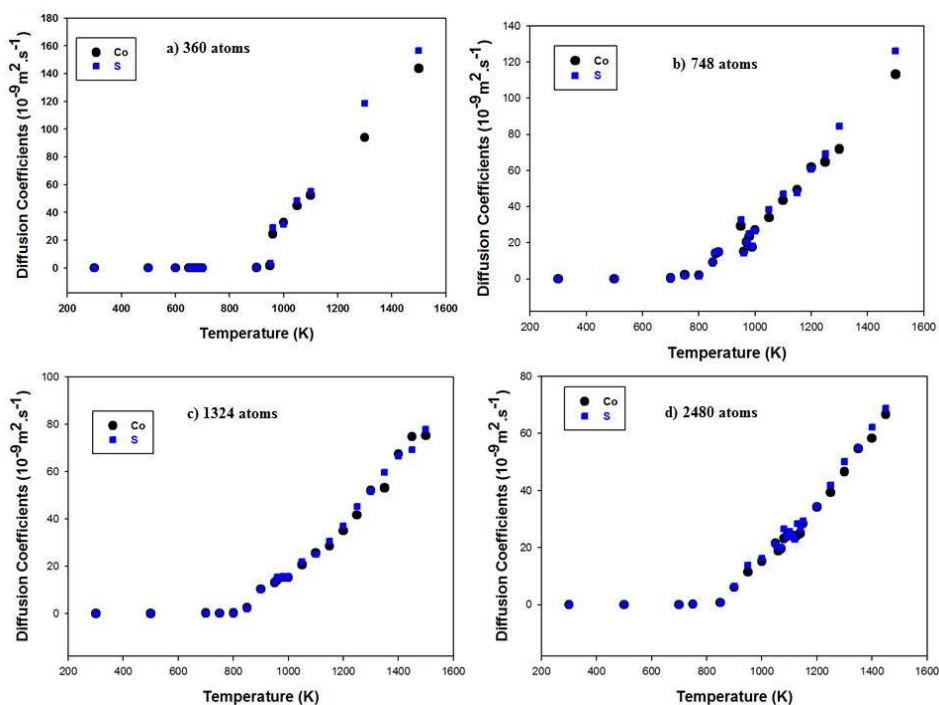


Figure 5.19: Diffusion Coefficients as a function of temperature for {101} terminated Co_9S_8 nanoparticle with a) 360 atoms, b) 748 atoms, c) 1324 atoms and d) 2480 atoms.

We further demonstrate the melting of the nanoparticles by the diffusion of ions. Figure 5.19 shows the diffusion coefficients as a function of temperature for different sizes of {101} terminated Co_9S_8 nanoparticles. Clearly, for all nanoparticles, there is no movement of both the cobalt and sulphur ions at lower temperatures, since the diffusion is almost zero. In case of the nanoparticle with 360 atoms, in Figure 5.19a, there is no movement of both the cobalt and sulphur ions between 300 and 950 K. The noticeable movement of both ions occurs at 960 K, with diffusion coefficient of between $24.47 - 29.21 \times 10^{-9} \text{ m}^2 \cdot \text{s}^{-1}$. For other nanoparticle sizes we notice the mobility of ions at 900 K for the nanoparticle with 748 atoms, with a diffusion coefficient of approximately $11.38 \times 10^{-9} \text{ m}^2 \cdot \text{s}^{-1}$ (Figure 5.19b). In the case of nanoparticles with 1324 atoms and 2480 atoms, in Figures 5.19c and Figure 5.19d

respectively, the mobility of ions is noticed from 850 K with diffusion coefficients of $2.41 \times 10^{-9} \text{ m}^2 \cdot \text{s}^{-1}$ and $0.73 \times 10^{-9} \text{ m}^2 \cdot \text{s}^{-1}$ respectively.

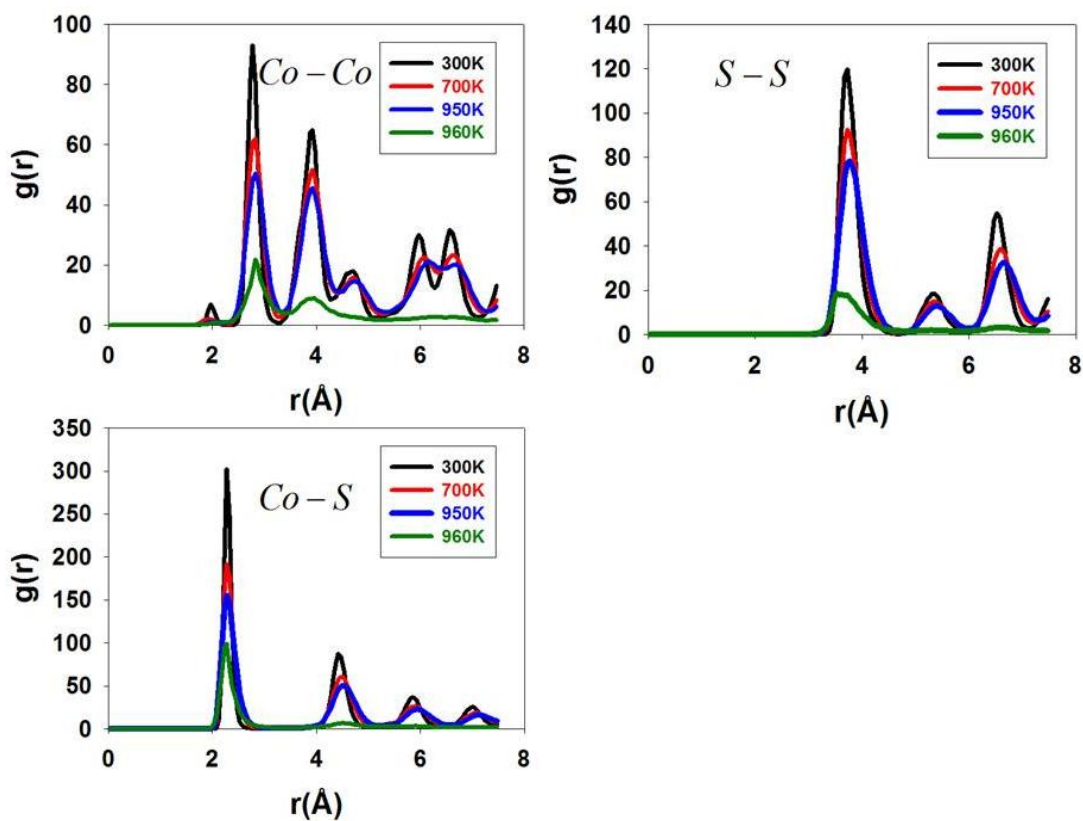


Figure 5.20: The RDFs of Co-Co, Co-S and S-S pairs for a {101} terminated Co_9S_8 nanoparticle with 360 atoms at the indicated temperatures.

The values of diffusion coefficients suggest that the ions of the nanoparticle with fewer atoms move more rapidly as compared to those with many atoms. In order to obtain specific information on the local structures in Co_9S_8 , the radial distribution functions (RDFs) for all pairs of ions of different sizes were calculated. Co-Co, Co-S and S-S RDFs pairs for different temperatures of nanoparticles with 360, 748, 1324 and 2480 atoms are shown in Figures (5.20, 5.21, 5.22 and 5.23) respectively.

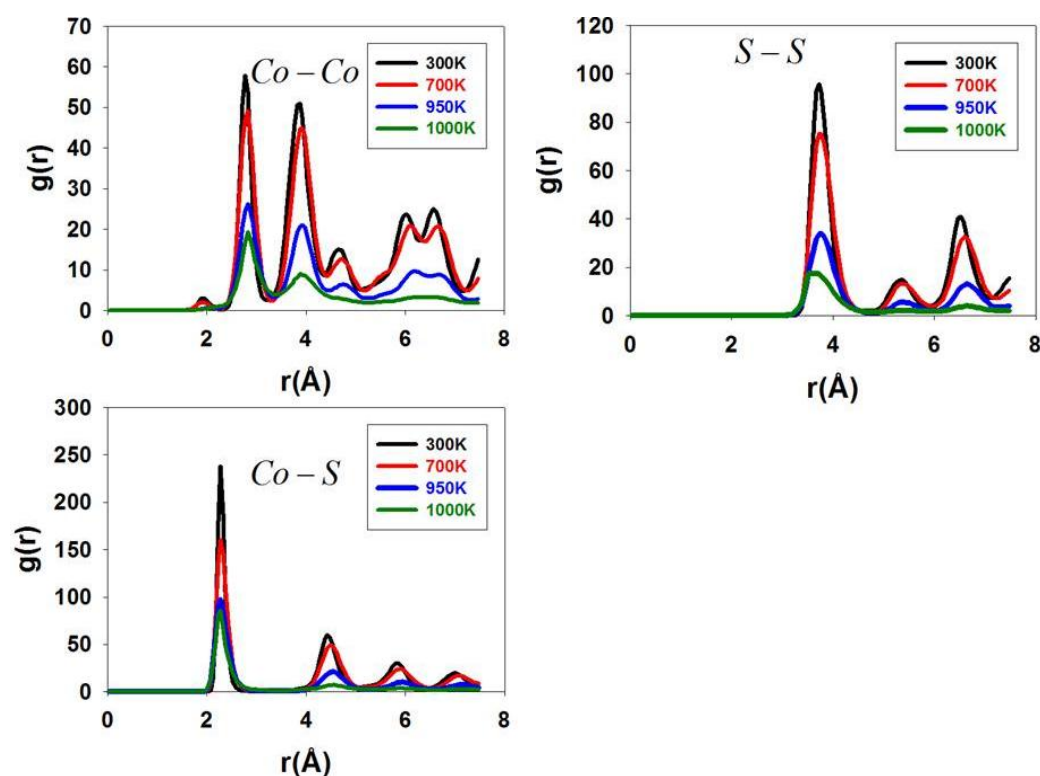


Figure 5.21: The RDFs of Co-Co, Co-S and S-S pairs for a {101} terminated Co_9S_8 nanoparticle with 748 atoms at the indicated temperatures.

It is observed from the figures that the RDFs show the structural changes at different temperatures for different sizes of nanoparticles. For a nanoparticle with 360 atoms (Figure 5.20), at the temperatures from 300 to 950 K, the nanoparticle has a well-defined structure, as evidenced by many peaks of the RDFs. However at 960K, the peaks have disappeared, as an indication of a change to a liquid phase. This corresponds to the melting of the nanoparticle, which was observed from the energy against temperature and diffusion against temperature graphs. These imply that the melting of the nanoparticle with 360 atoms is observed at 960 K.

The RDFs of nanoparticle with 748 atoms, shown in Figure 5.21, suggest that the melting occurs at 1050 K. It can be noted that from 300 to 1000 K, the nanoparticle has a well-ordered structure, since the RDFs have many peaks. However, at 1050 K,

the peaks have disappeared, which is a sign of melting. Figure 5.22 shows the RDFs of the nanoparticle with 1324 atoms, and it is observed that from 300 to 1050K, the nanoparticle has a well-defined structure. At 1000 K the peaks start to be broader, however, at 1060 K the peaks have completely disappeared, which is an indication of melting.

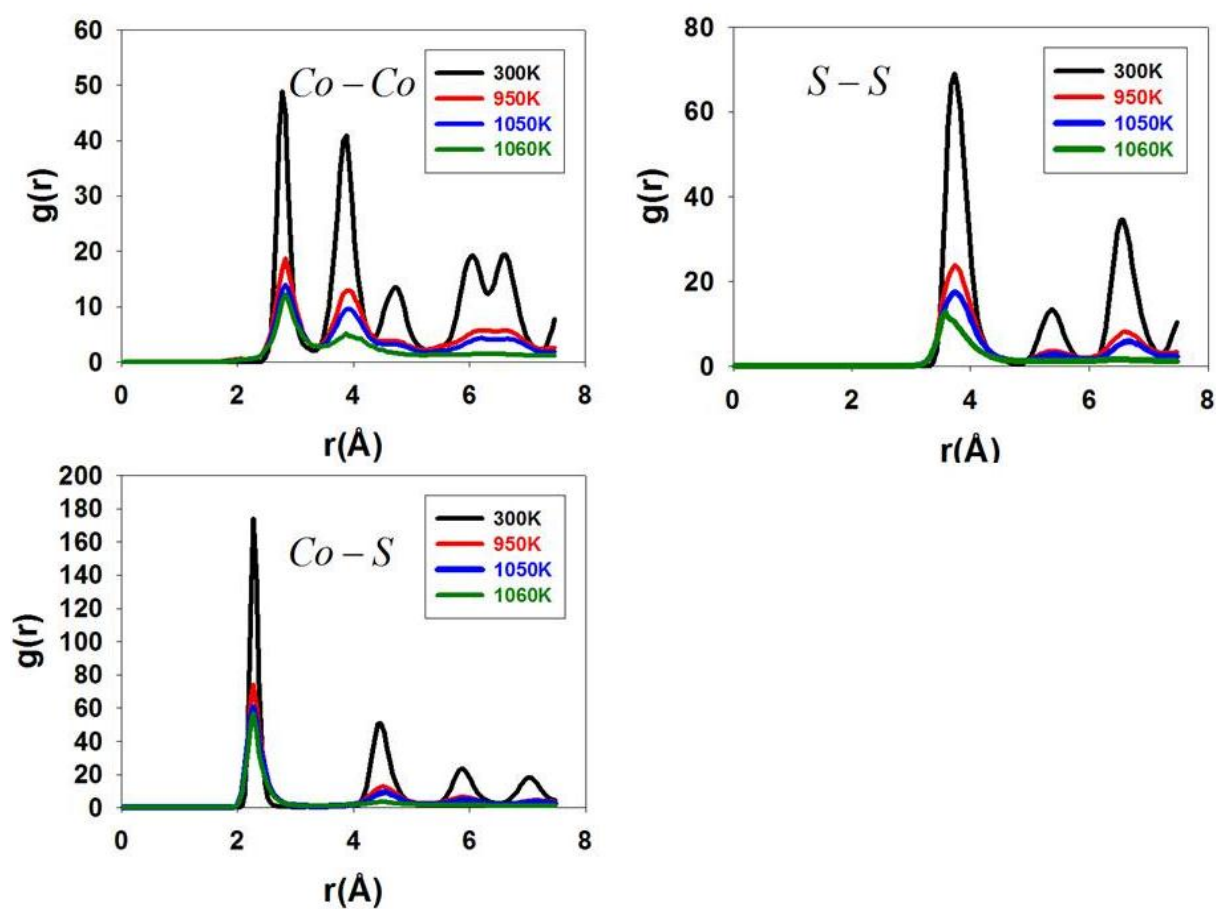


Figure 5.22: The RDFs of Co-Co, Co-S and S-S pairs for a {101} terminated Co_9S_8 nanoparticle with 1324 atoms at the indicated temperatures.

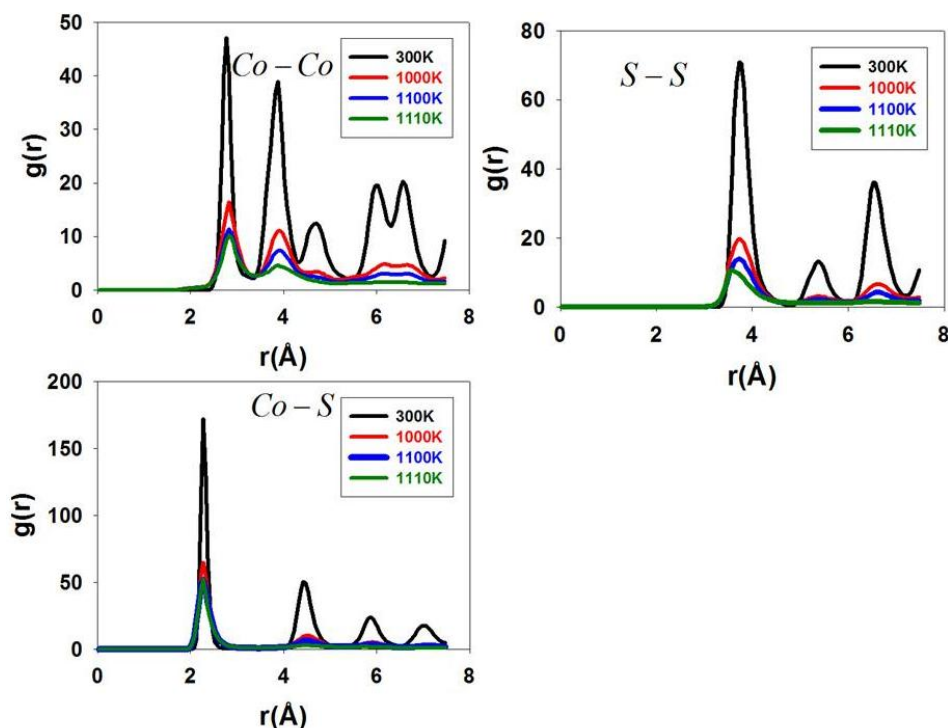


Figure 5.23: The RDFs of Co-Co, Co-S and S-S pairs for a {101} terminated Co_9S_8 nanoparticle with 2480 atoms at the indicated temperatures.

Figure 5.23 shows the RDFs of the nanoparticle with 2480 atoms. It can be noted, from the RDFs, that from 300 to 1100K the nanoparticle has a well-defined structure, and the onset of the disorder is observed at 1000 K. At this temperature the peaks are broader, but at 1110 K the peaks have disappeared completely, indicative of the liquid phase of the nanoparticle with 2480 atoms.

We now study the melting of the nanoparticles of different sizes is from the atomic density profiles. Figures (5.24, 5.25, 5.26 and 5.27) show the atomic distribution of cobalt (Co) and sulphur (S) atoms in surface {101} Co_9S_8 nanoparticle along the nanoparticle axis during the melting process. At lower temperatures we still have the solid like features, which is indicated by distinct peaks. These suggest that there is less movement of atoms along the nanoparticles axis in the specified temperature range. At the melting temperature of nanoparticles of different sizes the atomic distribution becomes smooth, indicating the liquid phase.

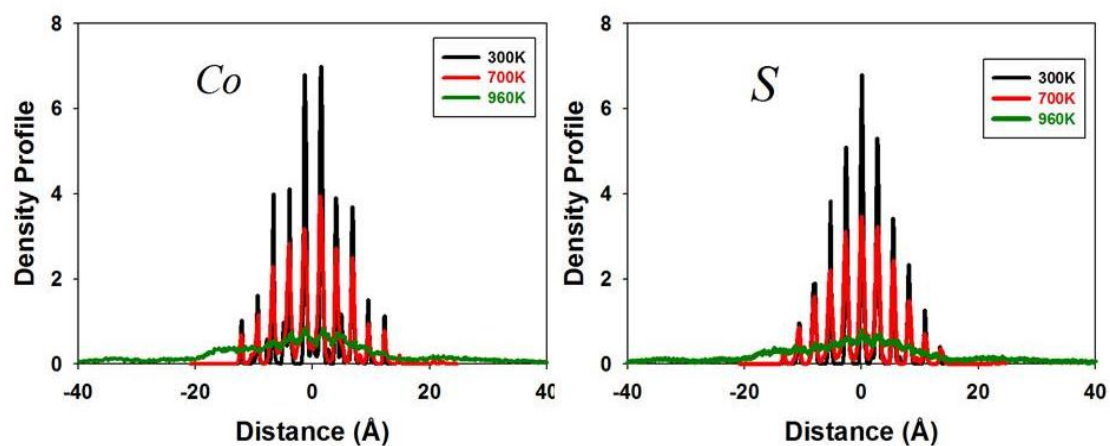


Figure 5.24: Density profiles of the {101} terminated Co_9S_8 nanoparticle with 360 atoms for cobalt (Co) and sulphur (S) at various temperatures.

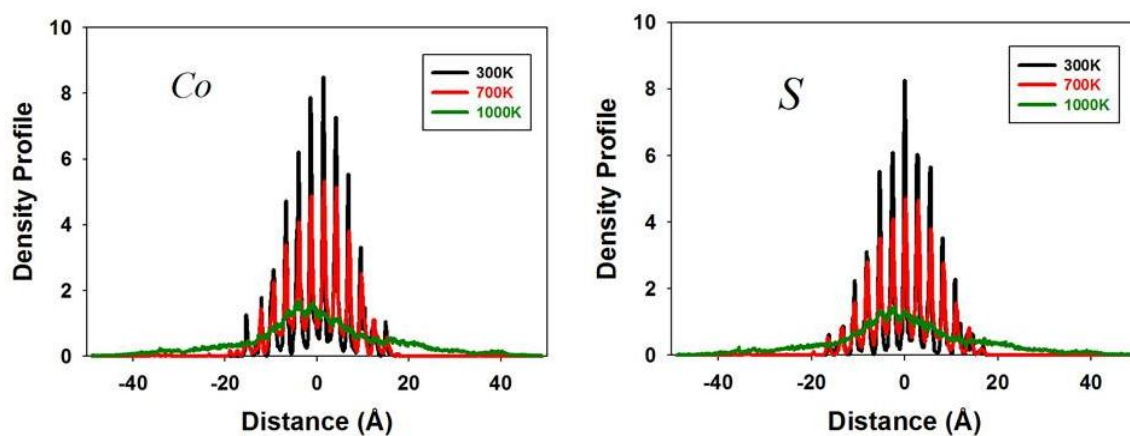


Figure 5.25: Density profiles of the {101} terminated Co_9S_8 nanoparticle with 748 atoms for cobalt (Co) and sulphur (S) at various temperatures.

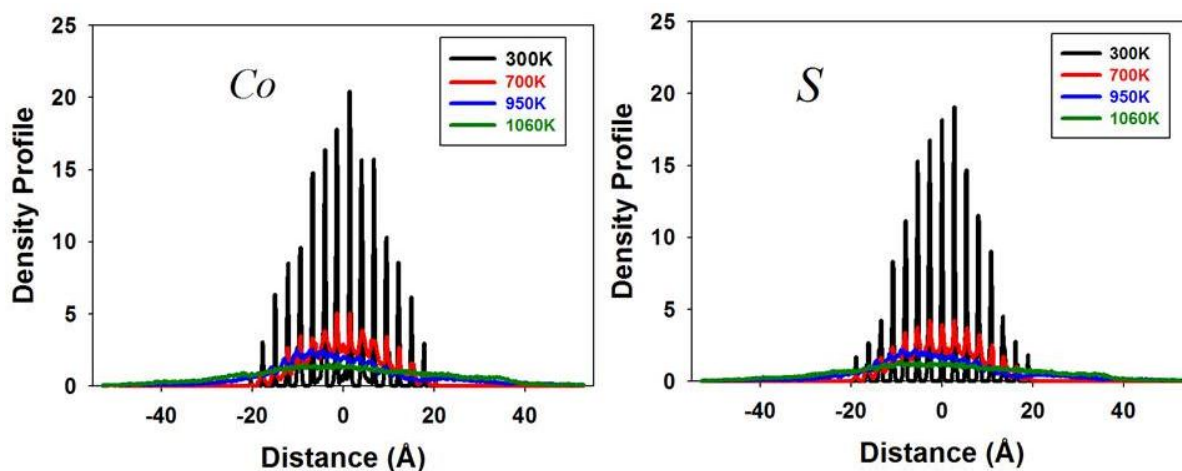


Figure 5.26: Density profiles of the {101} terminated Co_9S_8 nanoparticle with 1324 atoms for cobalt (Co) and sulphur (S) at various temperatures.

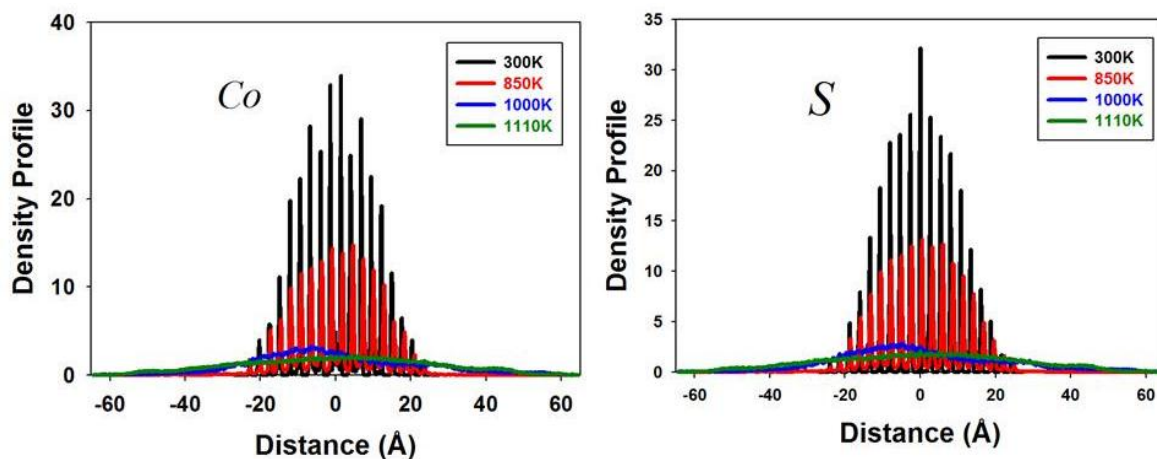


Figure 5.27: Density profiles of the {101} terminated Co_9S_8 nanoparticle with 2480 atoms for cobalt (Co) and sulphur (S) at various temperatures.

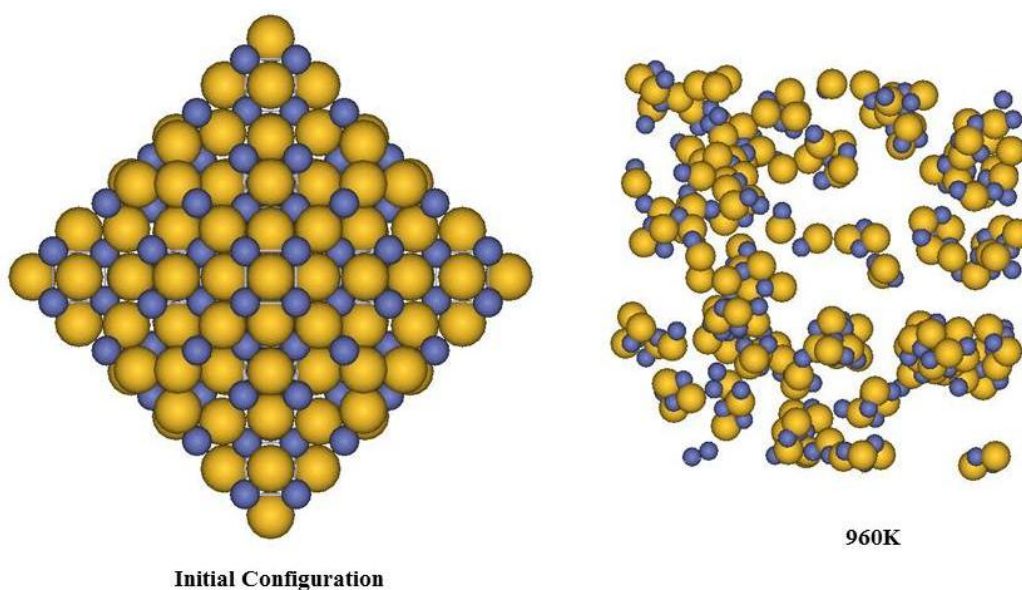


Figure 5.28: The initial configuration on the left and the structure at melting on the right of the Co_9S_8 nanoparticle of $\{101\}$ surface with 360 atoms. Purple, yellow spheres represent cobalt (Co), sulphur (S) atoms respectively.

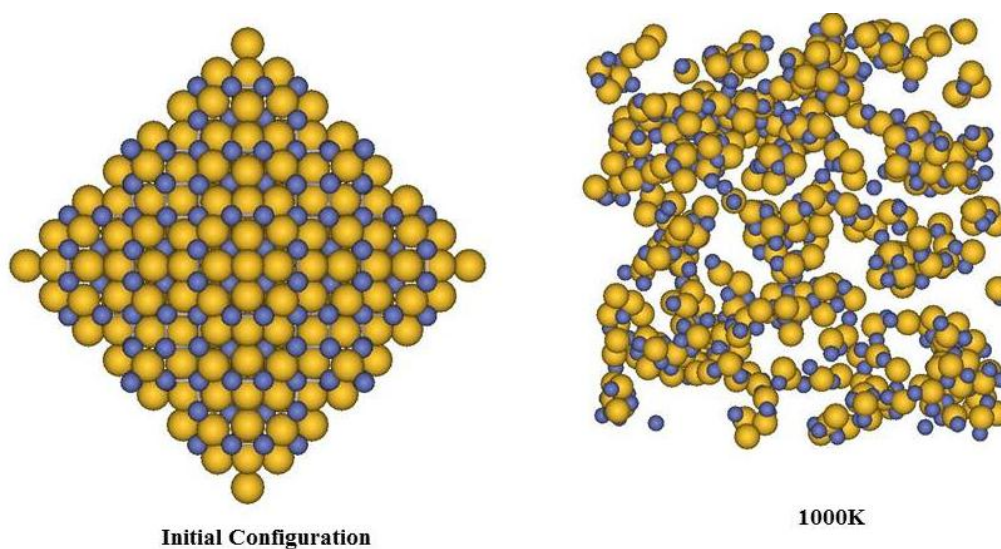


Figure 5.29: The initial configuration on the left and the structure at melting on the right of the Co_9S_8 nanoparticle of $\{101\}$ surface with 748 atoms. Purple, yellow spheres represent cobalt (Co), sulphur (S) atoms respectively.

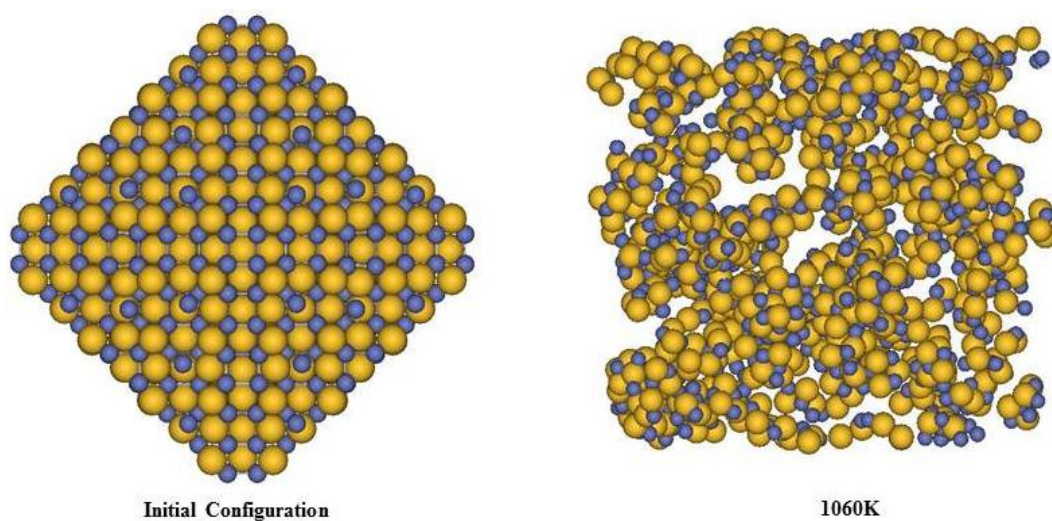


Figure 5.30: The initial configuration on the left and the structure at melting on the right of the Co_9S_8 nanoparticle of $\{101\}$ surface with 1324 atoms. Purple, yellow spheres represent cobalt (Co), sulphur (S) atoms respectively.

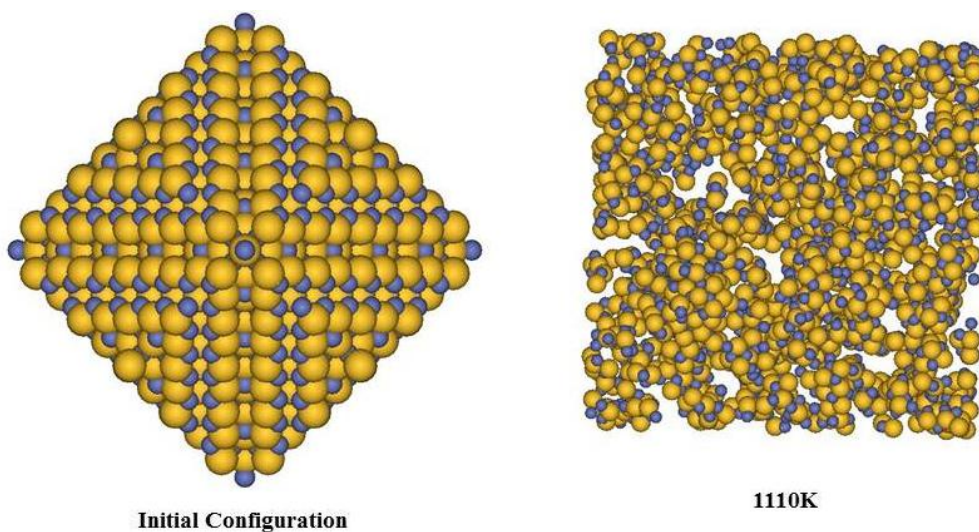


Figure 5.31: The initial configuration on the left and the structure at melting on the right of the Co_9S_8 nanoparticle of $\{101\}$ surface with 2480 atoms. Purple, yellow spheres represent cobalt (Co), sulphur (S) atoms respectively.

The initial configuration structures and the structures at melting points of the surface {101} Co_9S_8 nanoparticles with 360, 748, 1324 and 2480 atoms are shown in Figures (5.28, 5.29, 5.30 and 5.31), respectively. It can be seen that the nanoparticles assume a well-ordered rhombic dodecahedral shapes at the initial configuration, and at the indicated melting points the atom packing is disordered, suggestive of the melting of the nanoparticles.

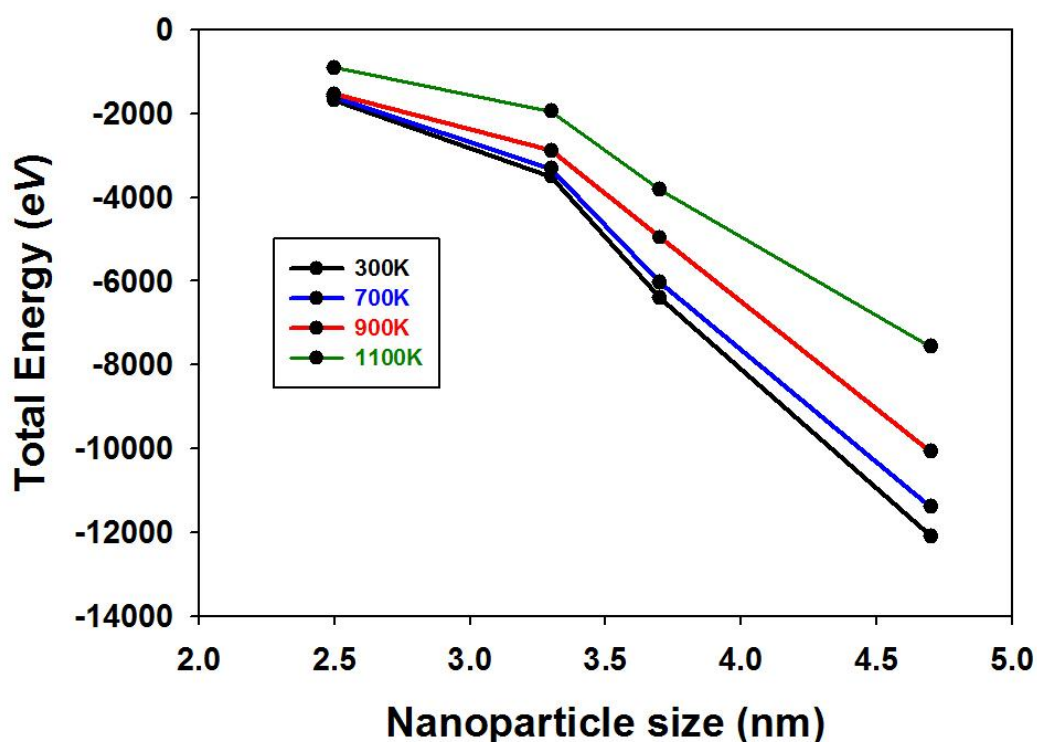


Figure 5.32: Total energy as a function of nanoparticle size for surface {101} Co_9S_8 nanoparticle at 300K, 700K, 900K and 1100K.

Figure 5.32 shows the approximate change in energy versus nanoparticle size in nanometres. It is evident that as the nanoparticle size decreases the energy becomes more positive. As expected, the stability of nanoparticle increases as the number of atoms increases.

5.2.3. Surface {100} Co₉S₈ nanoparticle

We now consider the surface {100} Co₉S₈ nanoparticle. According to our surface energy calculations using energy minimisation, {100} surface is the least stable surface, with the highest surface energy. We performed the simulations of {100} nanoparticles containing different numbers of identical atoms, i.e., it contains 442, 682, 1592, 2638, which corresponds to approximately 1.7 nm, 2.0 nm, 2.7 nm and 3.3 nm in diameter, respectively. All calculations were performed on an NVT ensemble for 200 picoseconds. The MD simulation box sizes of different number of atoms are shown in Table 5.4.

Table 5.4: Simulation box sizes of different number of atoms for surface {100} Co₉S₈ nanoparticles.

No. of Atoms	Particle dimension (nm)	Simulation Box Size (Å ³)
442	1.7	37.37 × 37.37 × 68
682	2.0	39.84 × 39.84 × 71
1592	2.7	47.14 × 47.14 × 88
2638	3.3	52.08 × 52.08 × 97

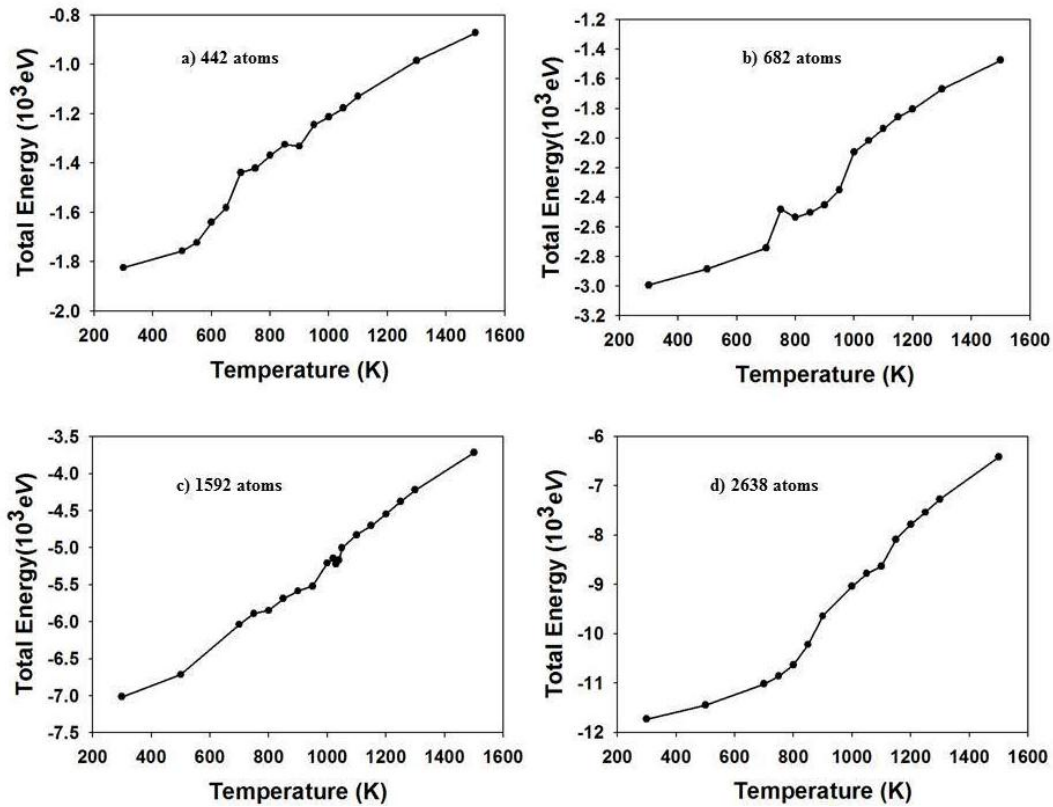


Figure 5.33: Total energy variation with temperature for {100} surface Co_9S_8 nanoparticle with a) 442 atoms, b) 682 atoms, c) 1592 atoms and d) 2638 atoms.

Figure 5.33 shows the temperature dependence of the energy for the surface {100} Co_9S_8 nanoparticle with different number of atoms. Unlike the {111} and {101} Co_9S_8 nanoparticles discussed in previous sections; where the transition from solid to liquid was clearly identified by a distinct change in the energy curve, in this case the plots do not show the exact change of slope at a specific temperature especially the nanoparticle with 442 atoms. In regard to the nanoparticle with 442 atoms (Figure 5.33a), there is a small change of energy between the temperatures of 650 and 700 K. For a nanoparticle with 682 atoms in Figure 5.33b, there is a jump on the energy curve at approximately 750 K, which is followed by a slight reduction. The energy subsequently increases and tends linear near 1000K. Pertaining to the nanoparticle with 1592 atoms, in Figure 5.33c, the energy almost changes linearly with temperature and slight fluctuations are observed between 950 and 1050 K. For the

nanoparticle with 2638 atoms in Figure 5.33d, there is noticeable change of slope above 750 K. However, there is a small energy fluctuation between the temperature 1100 and 1150 K.

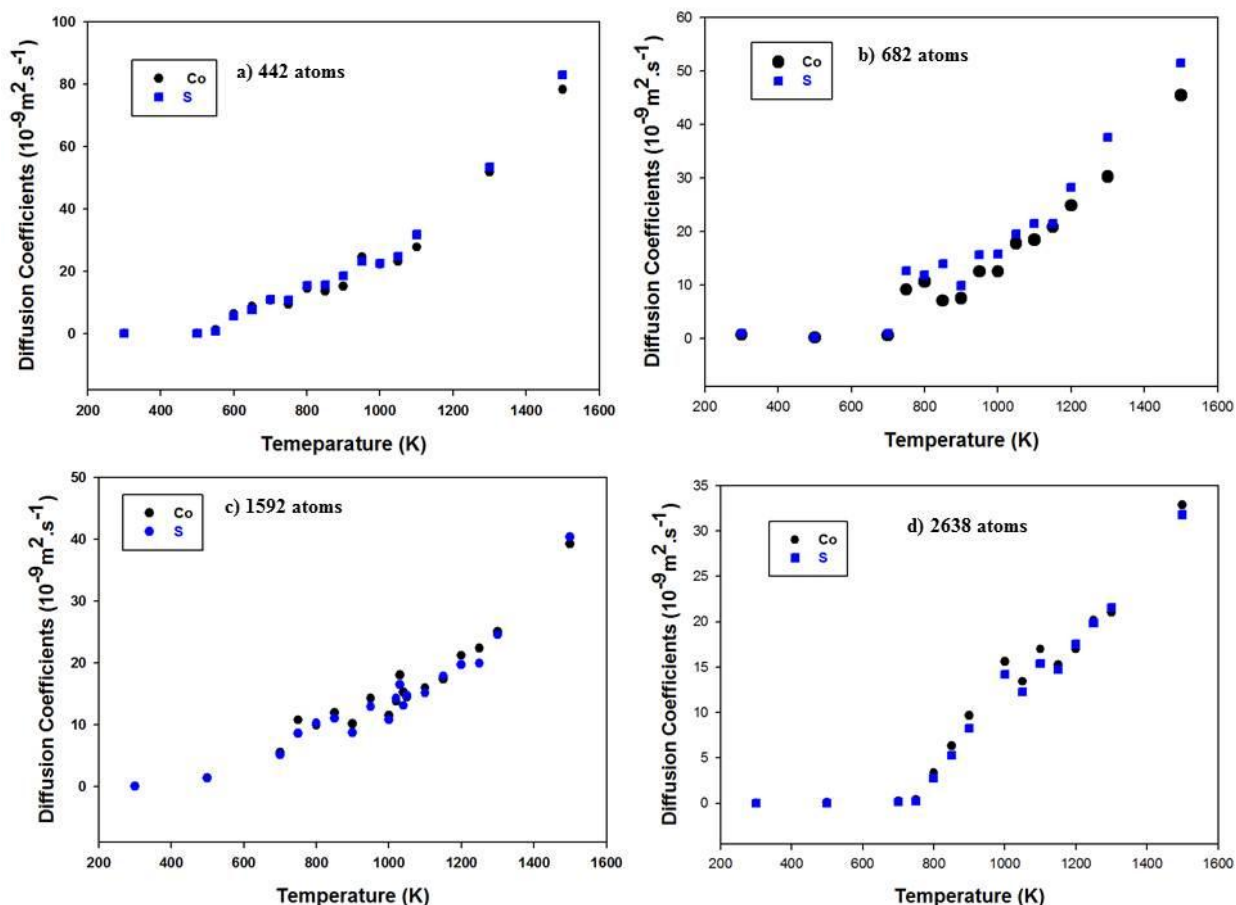


Figure 5.34: Diffusion coefficients as a function of temperature for {100} surface Co₉S₈ nanoparticle with a) 442 atoms, b) 682 atoms, c) 1592 atoms and d) 2638 atoms.

Since the energy variation plots do not give the exact melting temperature of the surface {100} Co₉S₈ nanoparticles of both different number of atoms, we checked melting of the nanoparticles from the diffusion of ions. Figure 5.34 shows the diffusion coefficients as a function of temperature for different sizes of surface {100} Co₉S₈ nanoparticles. It can be seen that the diffusion is almost zero at low

temperatures, since there is little or no movement of both cobalt and sulphur ions. For the nanoparticle with 442 atoms (Figure 5.34a) there is no movement of both ions between 300 and 550 K. The noticeable diffusion occurs at 600 K, with the diffusion coefficient of about $6.39 \times 10^{-9} \text{ m}^2 \cdot \text{s}^{-1}$. In regard to the nanoparticle with 682 atoms (Figure 5.34b), we notice the motion of both ions from 750 K, but diffusion coefficients of different magnitudes. The cobalt ions move with the diffusion coefficient of approximately $9.13 \times 10^{-9} \text{ m}^2 \cdot \text{s}^{-1}$ while the sulphur ions with the diffusion of $12.69 \times 10^{-9} \text{ m}^2 \cdot \text{s}^{-1}$. The temperature of 750 K is where the energy anomaly was observed from the energy against temperature plot, in Figure 5.33. In regard to a nanoparticle with 1592 atoms (Figure 5.34c) both cobalt and sulphur ions move at the temperature of 700K with the diffusion of $5.51 \times 10^{-9} \text{ m}^2 \cdot \text{s}^{-1}$. For the nanoparticle with 2638 atoms (Figure 5.34d) the mobility of ions is noticed at 800 K with the diffusion coefficient of $3.35 \times 10^{-9} \text{ m}^2 \cdot \text{s}^{-1}$ for the cobalt ions and $2.73 \times 10^{-9} \text{ m}^2 \cdot \text{s}^{-1}$ for the sulphur ions. The change in the slope of the diffusion coefficient against temperature plot is well defined as compared to nanoparticles with smaller number of atoms.

In order to obtain specific details on the local structures of the {100} Co_9S_8 nanoparticles, we calculated the radial distribution functions (RDFs) for all pairs of ions of different sizes. Co-Co, Co-S and S-S RDFs pairs at different temperatures of nanoparticles with 442, 682, 1592 and 2638 atoms are shown in Figures (5.35, 5.36, 5.37 and 5.38) respectively. The RDFs show the structural changes at varying temperatures for different sizes of nanoparticles. The nanoparticle with 442 atoms, in Figure 5.33, at temperatures 300 to 660 K has a well-defined structure, as evidenced by many RDFs peaks.

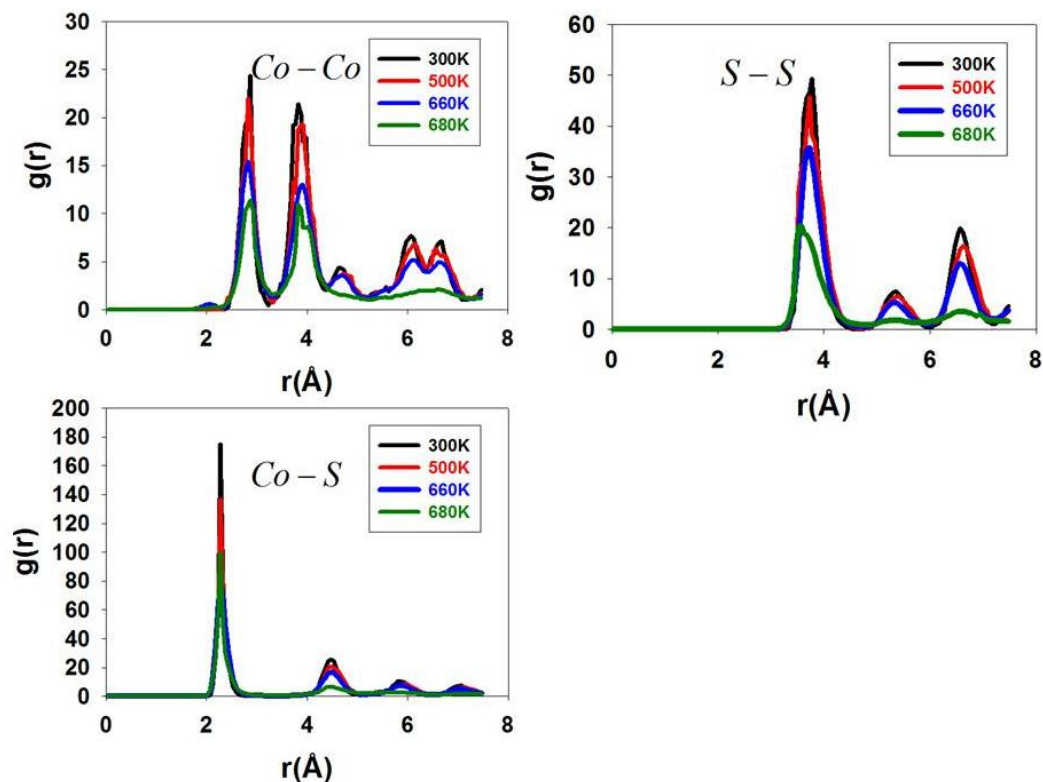


Figure 5.35: : The RDFs of Co-Co, Co-S and S-S pairs for a {100} terminated Co_9S_8 nanoparticle with 442 atoms at the indicated temperatures.

However at 680K, for both Co-S and S-S RDFs pairs, the peaks have disappeared, and those of Co-Co have been substantially reduced, suggesting a liquid phase of the nanoparticle with 442 atoms. This temperature falls within the temperature range where anomalies were observed in the energy against temperature plot of Figure 5.33a. The Co-Co, Co-S and S-S RDFs pairs of a nanoparticle with 682 atoms shown in Figure 5.36, suggest that the melting occurs at 960 K. Between 300 K and 950 K, the RDFs have many peaks, implying that the nanoparticle has a well-ordered structure, unlike at 960 K, where the peaks have disappeared. Figure 5.37 shows the Co-Co, Co-S and S-S RDFs pairs of the nanoparticle with 1592 atoms at the temperatures leading to the melting. In the temperature range 300 to 1040 K, the nanoparticle has a well-defined structure, as depicted by the number of peaks.

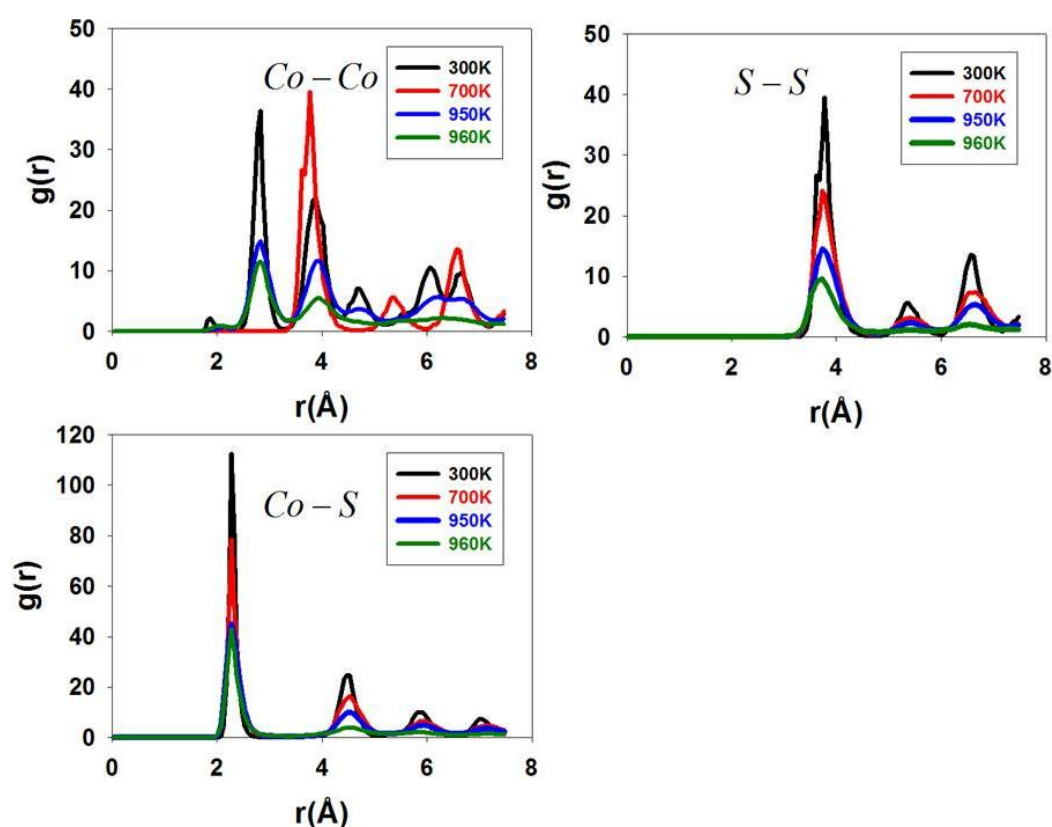


Figure 5.36: The RDFs of Co-Co, Co-S and S-S pairs for a {100} terminated Co_9S_8 nanoparticle with 682 atoms at the indicated temperatures.

Above 1000 K, the peaks start to be broader; however at 1050 K the peaks have completely disappeared, hence suggesting the melting of the nanoparticle with 1592 atoms. Figure 5.38 shows the Co-Co, Co-S and S-S RDFs pairs of the nanoparticle with 2638 atoms at the temperatures leading to melting. It can be observed from several peaks of the RDFs that the nanoparticle has a well-defined structure in the range 300 to 1140 K. However, at 1150 K the peaks have disappeared completely, suggesting a liquid phase of the nanoparticle with 2638 atoms. In the energy curve of Figure 5.33d, we noted a small change of energy in the temperature range of 1100 to 1150 K, which corresponds to the melting temperature noted from the RDFs.

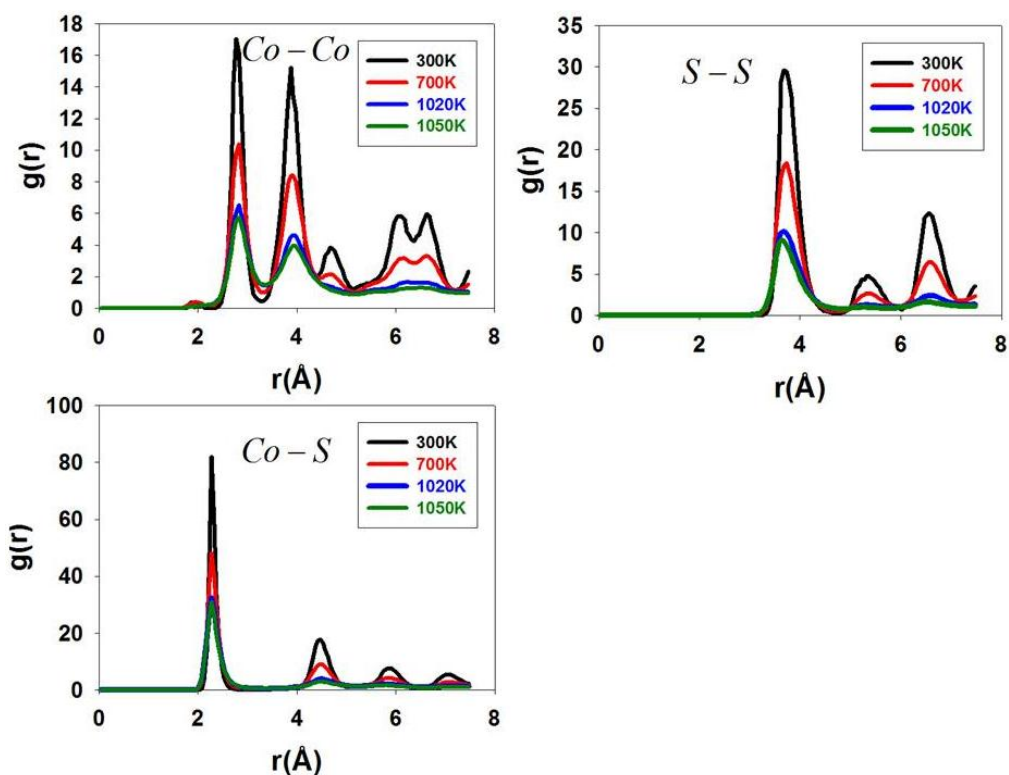


Figure 5.37: The RDFs of Co-Co, Co-S and S-S pairs for a {100} terminated Co_9S_8 nanoparticle with 1592 atoms at the indicated temperatures.

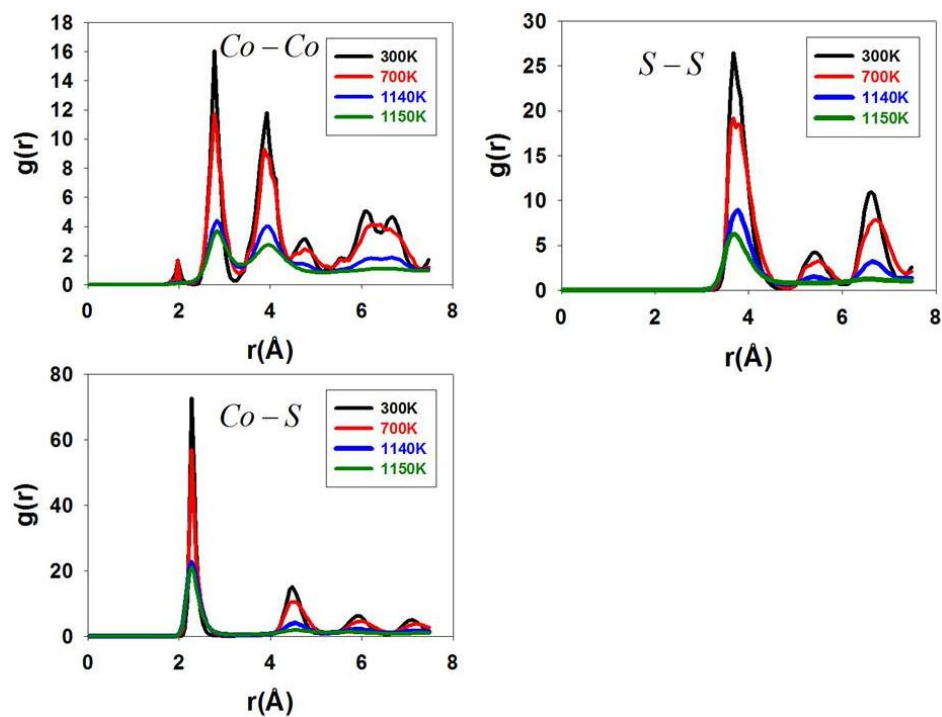


Figure 5.38: The RDFs of Co-Co, Co-S and S-S pairs for a {100} terminated Co_9S_8 nanoparticle with 2638 atoms at the indicated temperatures.

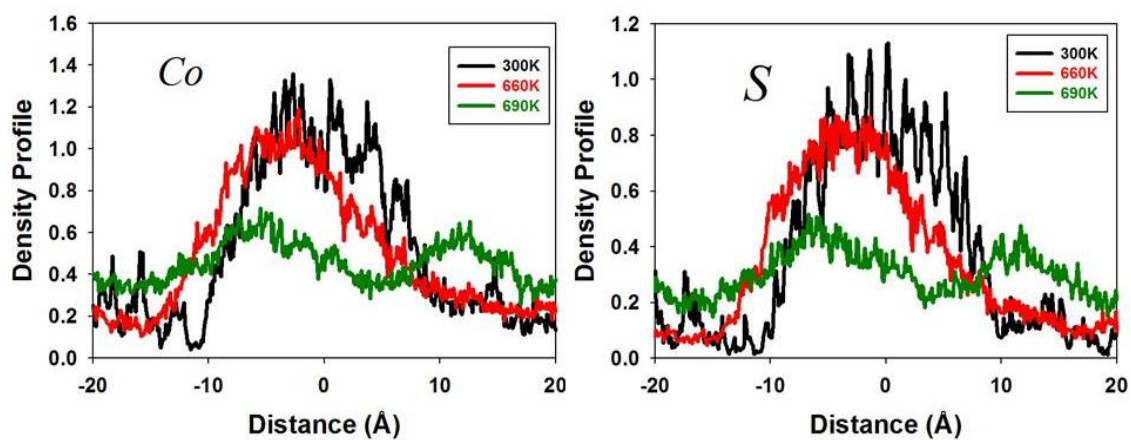


Figure 5.39: Atomic density profiles along the nanoparticle axis for Co and S atoms in {100} terminated Co_9S_8 nanoparticle with 442 atoms at temperatures leading up to melting.

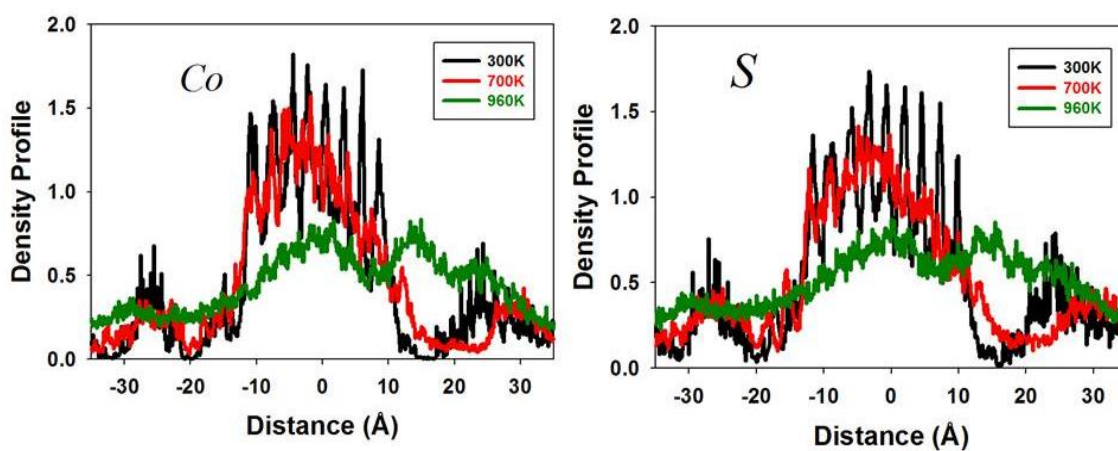


Figure 5.40: Atomic density profiles along the nanoparticle axis for Co and S atoms in {100} terminated Co_9S_8 nanoparticle with 682 atoms at temperatures leading up to melting.

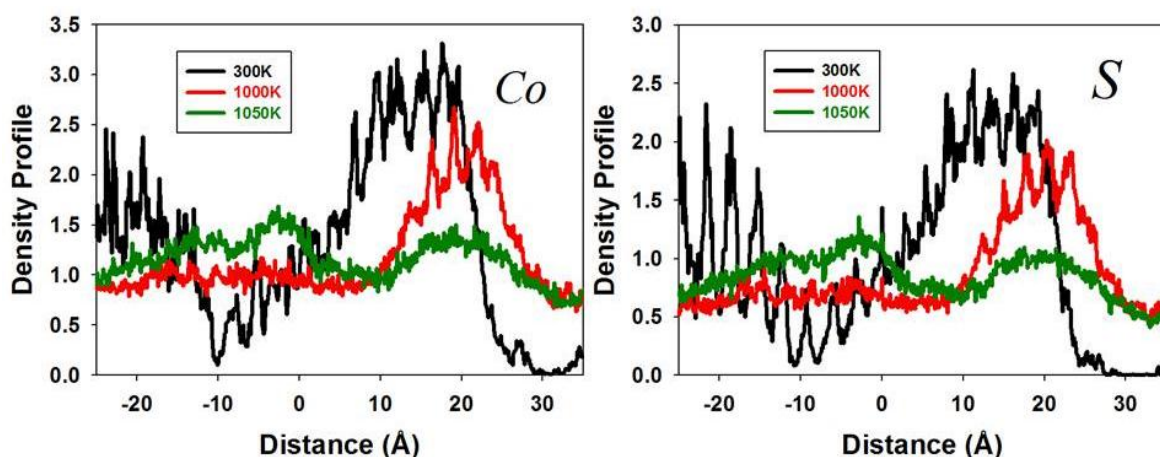


Figure 5.41: Atomic density profiles along the nanoparticle axis for Co and S atoms in {100} terminated Co_9S_8 nanoparticle with 1592 atoms at temperatures leading up to melting.

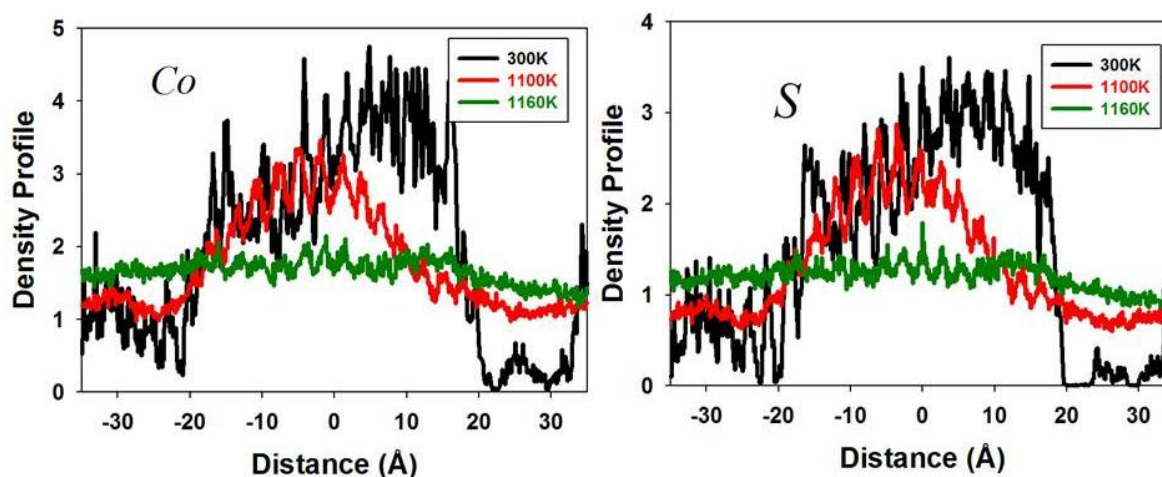


Figure 5.42: Atomic density profiles along the nanoparticle axis for Co and S atoms in {100} terminated Co_9S_8 nanoparticle with 2638 atoms at temperatures leading up to melting.

The nanoparticle melting process is associated with the redistribution of atoms owing to their increased motion, especially at high temperatures [175]. Figures (5.39, 5.40, 5.41, 5.42) shows the atomic distribution of Co and S atoms in surface {100} Co₉S₈ nanoparticle with 442, 682, 1592 and 2638 atoms along the nanoparticle axis during the melting process. At lower temperatures, the solid like features are indicated by the distinct peaks. For a nanoparticle with 442 atoms, in Figure 5.39, the peaks are noticeable between 300 and 660 K. At 690 K, the peaks become broader, which suggests the motion of both Co and S atoms. At the melting point (680 K), the atomic distribution becomes smooth which alludes to a liquid phase. The melting of nanoparticle with 442 atoms at 680K agrees with RDFs results in Figure 5.35. For a nanoparticle with 682 atoms, in Figure 5.40, the peaks are well-defined from 300K to 950 K. However, at 960 K the peaks are broader, suggesting the melting of the nanoparticle. This is in concurrence with the RDFs in Figure 5.36. In regard to a nanoparticle with 1592 atoms, in Figure 5.41, the sharp and well-defined peaks are observed from 300 to 1000 K for both the Co and S atoms. However, at 1050 K the atomic distribution becomes smooth indicating a liquid phase. For a nanoparticle with 2638 atoms, in Figure 5.42, the peaks remain distinct between 300 and 1100 K. At 1160 K the atomic distribution is smooth, which is associated with the melting of the nanoparticle. The melting temperatures of the nanoparticles with different sizes are not the same. Furthermore, the melting temperatures of the nanoparticles increase with the number of atoms.

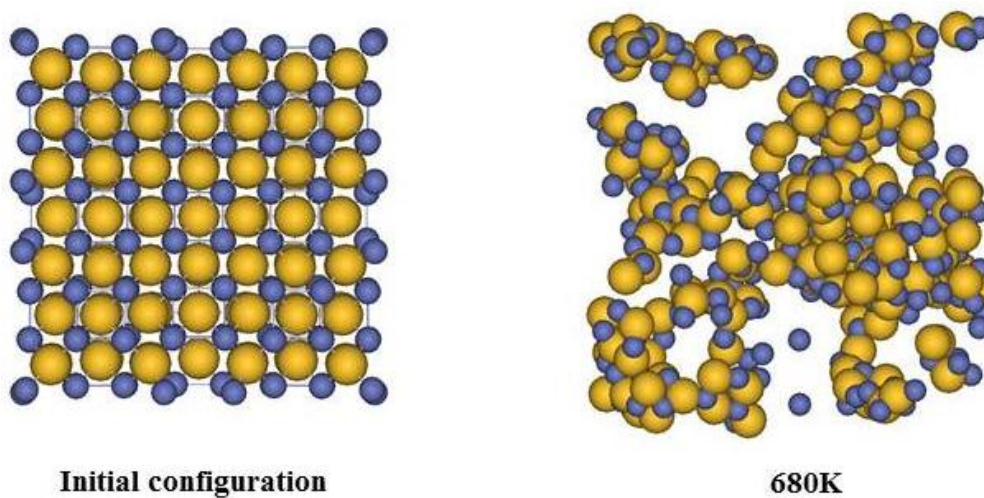


Figure 5.43: The initial configuration on the left and the structure at melting on the right of the Co_9S_8 nanoparticle of $\{100\}$ surface with 442 atoms. Purple, yellow spheres represent cobalt (Co), sulphur (S) atoms respectively.

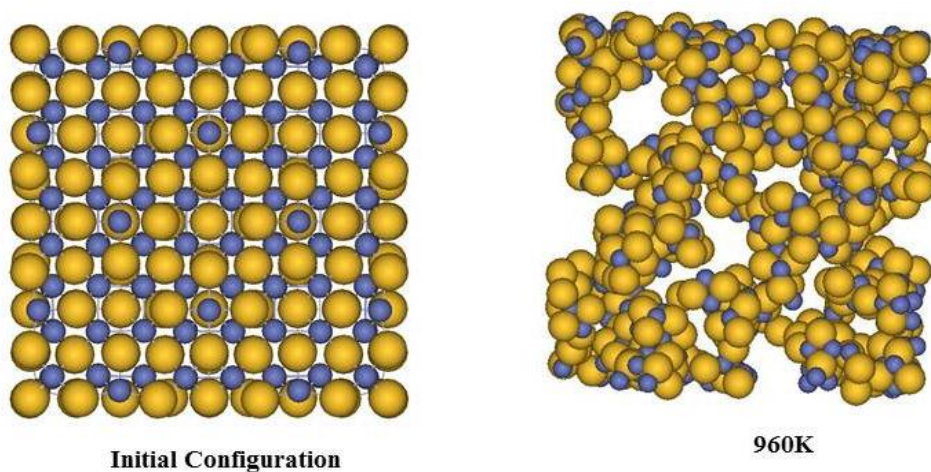


Figure 5.44: The initial configuration on the left and the structure at melting on the right of the Co_9S_8 nanoparticle of $\{100\}$ surface with 682 atoms. Purple, yellow spheres represent cobalt (Co), sulphur (S) atoms respectively.

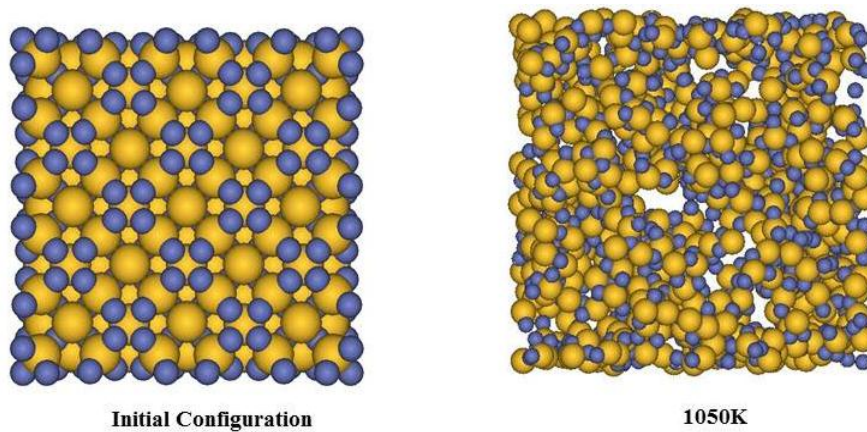


Figure 5.45: The initial configuration on the left and the structure at melting on the right of the Co_9S_8 nanoparticle of $\{100\}$ surface with 1592 atoms. Purple, yellow spheres represent cobalt (Co), sulphur (S) atoms respectively.

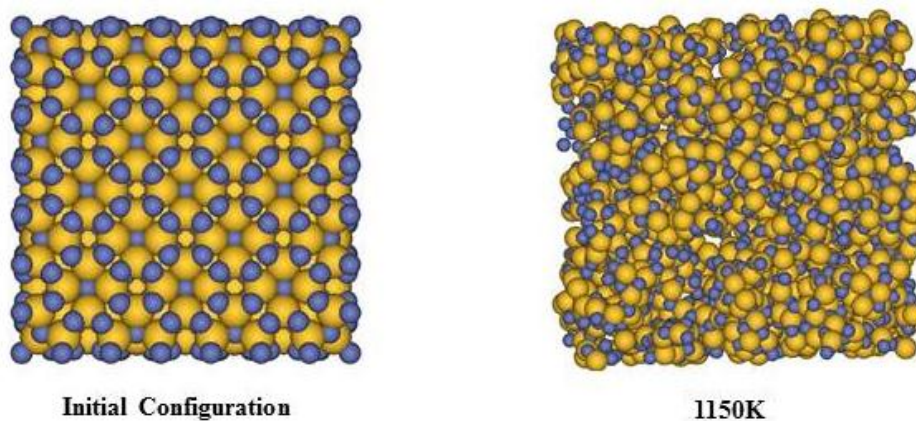


Figure 5.46: The initial configuration on the left and the structure at melting on the right of the Co_9S_8 nanoparticle of $\{100\}$ surface with 2638 atoms. Purple, yellow spheres represent cobalt (Co), sulphur (S) atoms respectively.

The initial structures and those at melting points of the {100} surface Co_9S_8 nanoparticles with 442, 682, 1592 and 2638 atoms are shown in Figures (5.43, 5.44, 5.45 and 5.46), respectively. It is noted that the nanoparticles assume well-ordered cubic shapes at initial configurations, which are significantly disordered at high temperatures as the nanoparticles melt. Figure 5.47 shows the approximate change in total energy versus nanoparticle size in nanometres. It is evident that as the nanoparticle size decreases the energy becomes more positive, and as expected the stability of the {100} surface nanoparticle increases as the number of atoms increases.

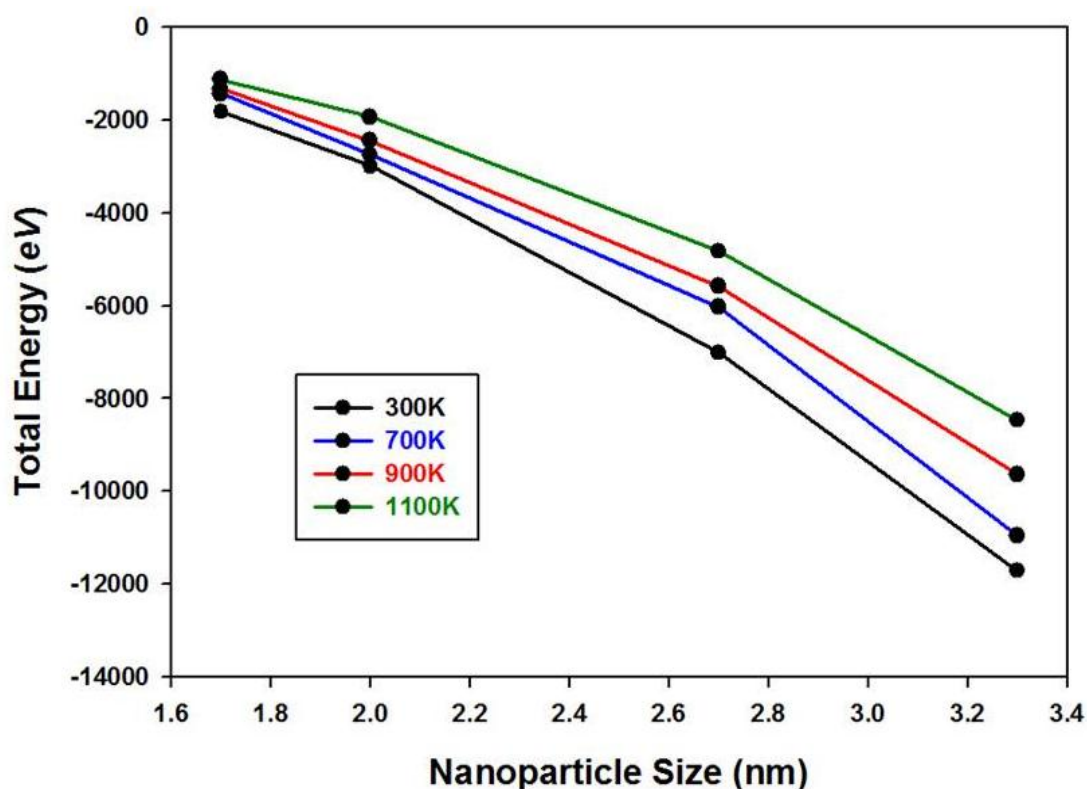


Figure 5.47: Total energy as a function of nanoparticle size for {100} terminated Co_9S_8 nanoparticle at 300, 700, 900 and 1100 K.

To summarise the section, the effect of size on the melting of the Co_9S_8 nanoparticles bounded by {111}, {101} and {100} surfaces showed that the melting temperature of the nanoparticles increases with the increase of the nanoparticle size. In the case of {111} and {101} Co_9S_8 nanoparticles, the abrupt changes in properties are observed around 940 K for the nanoparticles of the smallest size. Larger nanoparticles show gradual changes of thermodynamic properties with temperature. However, structural diagrams suggest that the smaller nanoparticles disintegrate at 940 K; whereas the larger nanoparticles contain this phenomenon by formation of voids. In the case of surface {100} Co_9S_8 nanoparticle (with the larger surface energy), properties do not change as abruptly as those of {111} and {101} surfaces. The disintegration is not as violent; and larger systems are more compact with fewer voids. The largest nanoparticles for all surfaces appear to have the same change in properties, distinct from the rest, especially with energy and diffusion coefficient change with temperature. Furthermore, the rdfs of the Co_9S_8 nanoparticles bounded by both surfaces showed that at higher temperatures the peaks are broader and the height decreases, suggesting that at higher temperatures the surfaces are molten. The different sizes of nanoparticles melt at different temperatures. The melting temperature increases with the increasing nanoparticle size. Table 5.5 shows the predicted melting temperatures of the three nanoparticles of different sizes.

Table 5.5: The predicted melting temperatures of the three nanoparticles of different sizes.

Surface {111} nanoparticle	
Number of Atoms	Temperature (K)
342	940
708	960
1394	1040
2422	1090
Surface {101} nanoparticle	
Number of Atoms	Temperature (K)
360	960
748	1000
1324	1060
2480	1110
Surface {100} nanoparticle	
Number of Atoms	Temperature (K)
442	680
682	960
1592	1050
2638	1150

5.3. Co₉S₈ Nanoparticle in Pure water

The intention of this section is to ascertain whether immersing the particles in water would modify their structure. Molecular dynamics simulation was performed on the 2.9 nm (in diameter) Co₉S₈ nanoparticle which is immersed in water, in the NVT ensemble at 300 K, and zero pressure. The simulation was run for 200ps and the cubic simulation box contained 9082 water molecules and 342 of both cobalt and sulphur atoms. The cubic simulation cell had a side length of 49.6 Å and contained 36670 species. The water model used is the rigid ion by de Leeuw and Parker [105]. The stable {111} surface was used to create the octahedral morphology. Figure 5.48a shows the initial configuration of Co₉S₈ nanoparticle immersed in water and Figure 5.48b depicts the generated surface {111} Co₉S₈ nanoparticle before immersion.

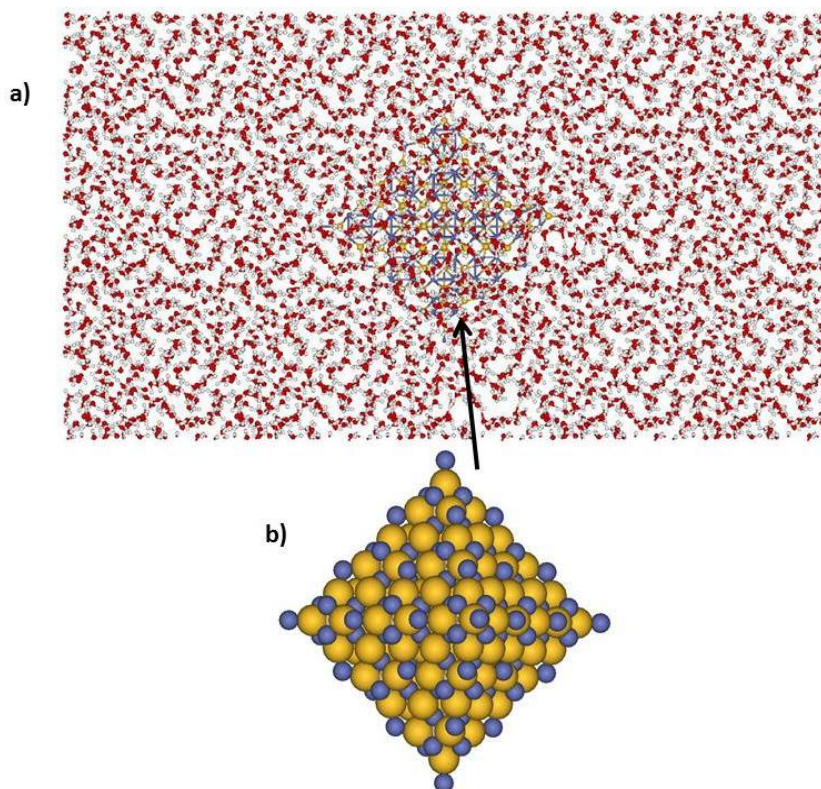


Figure 5.48: The initial configuration of a) the $\{111\}$ Co_9S_8 nanoparticle immersed in water and b) the initial configuration without water.

The cobalt-cobalt (Co-Co), cobalt-sulphur (Co-S) and sulphur-sulphur (S-S) RDFs pairs from MD simulation are shown in Figure 5.49a. For comparison, we use the Co-Co, Co-S, S-S RDFs pairs of the bulk Co_9S_8 , which is given in Figure 5.49c. Figure 5.49a depicts that the nanoparticle in water has lost the crystallinity when compared to the bulk crystal (Figure 5.49c) and the nanoparticle in vacuum (Figure 5.49b) which show well-ordered structures. The radial distances of the nanoparticles in water and vacuum and the bulk are shown in Table 5.6. On considering the first peaks of the RDFs, the Co-Co radial distances of the nanoparticles in water and in a vacuum are the same. The corresponding change of the Co-S interaction is 0.01 \AA at most, and for S-S interaction it is 0.13 \AA .

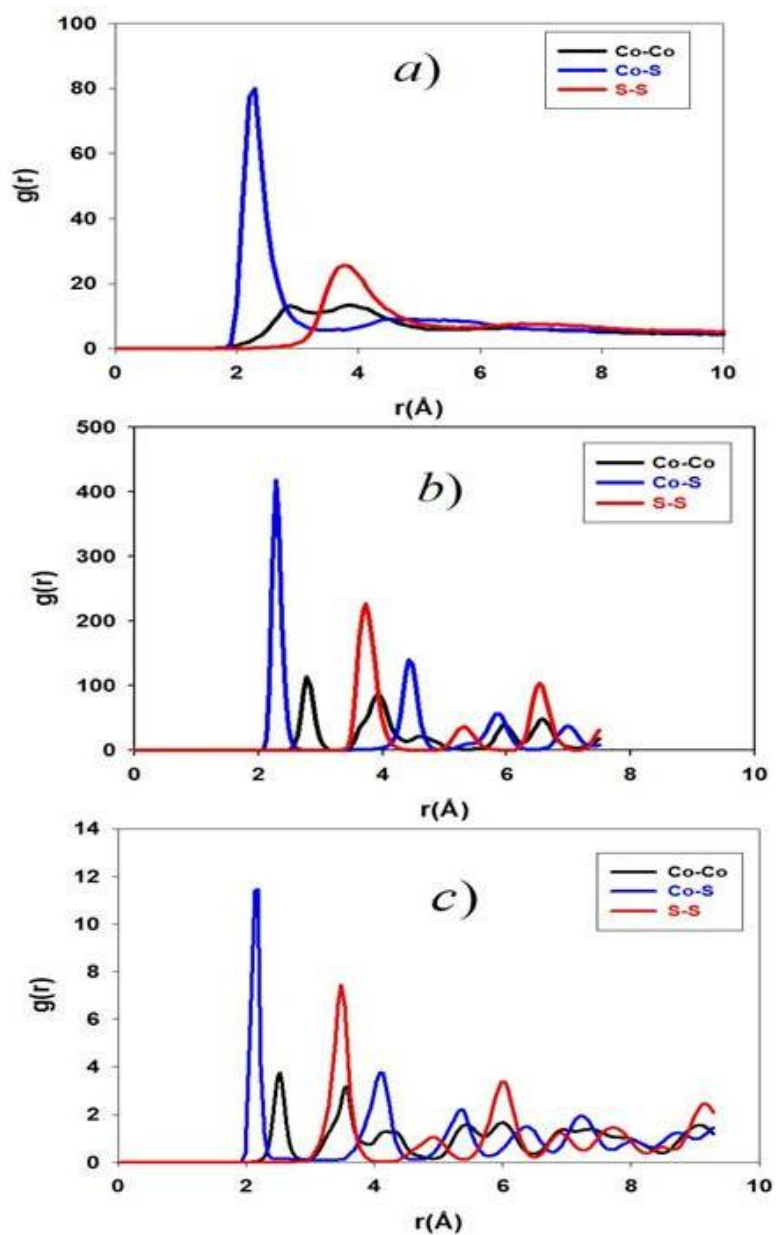


Figure 5.49: Cobalt-cobalt (Co-Co), Cobalt-sulphur (Co-S) and Sulphur-sulphur(S-S) RDFs of a) nanoparticle in water, b) bulk and c) nanoparticle in vacuum.

The second peak of the nanoparticle in water has disappeared completely as compared to the one in vacuum, which is well-defined. These suggest that the nanoparticle in water is more amorphous than in a vacuum. There is a significant difference of the radial distances of the bulk and that of nanoparticles. This difference emanates from the fact that as the size of a material reduces to the nanometre scale the properties change uniquely in comparison with the bulk characteristics of the parent.

Table 5.6: The radial distance of nanoparticles in water and in a vacuum and bulk.

Interaction	Water (Å)	Vacuum (Å)	Bulk (Å)
Co-Co	2.78	2.78	2.53
Co-S	2.29	2.28	2.18
S-S	3.86	3.73	3.48

Figure 5.50 show the snapshots of the nanoparticle in vacuum and in water after the simulation. In regard to the nanoparticle in vacuum (Figure 5.50a), the octahedral shape of the surface {111} Co_9S_8 nanoparticle is maintained. However, for the nanoparticle in water (Figure 5.50b), the nanoparticle has lost its shape and adopts an amorphous structure. Indeed, the nanoparticle in water is more amorphous than the one in vacuum.

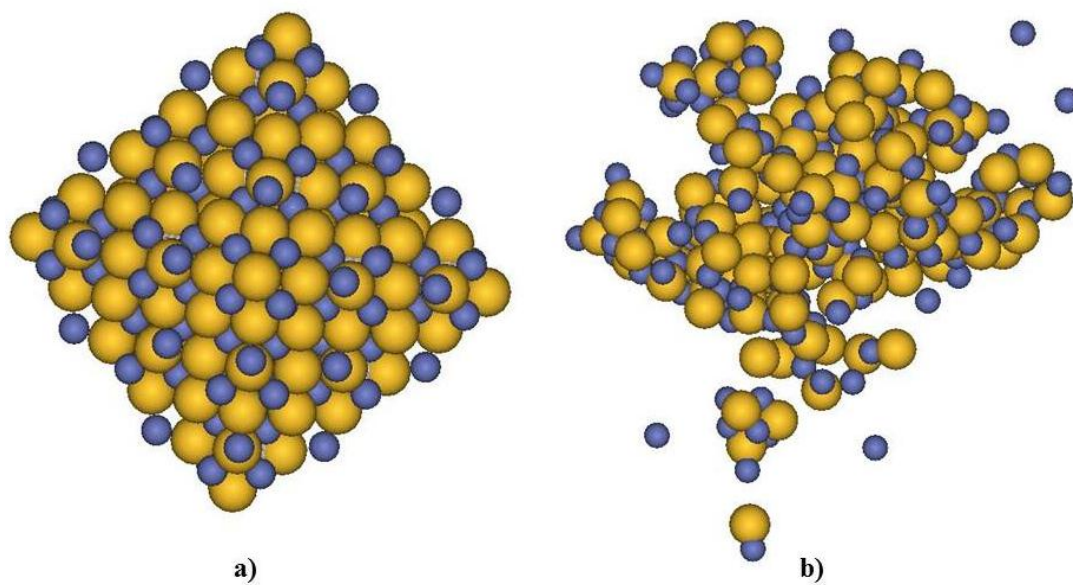


Figure 5.50: Snapshots of the {111} nanoparticle in a) vacuum and b) water (removed water for clarity) after simulation.

Chapter 6: Conclusions and Recommendations

6.1. Conclusions

Pentlandites are the most important nickel and cobalt sulphide minerals in economic deposits where it occurs with pyrrhotite, chalcopyrite and pyrite in mafic and ultramafic igneous rocks. They also occur as intergrowths and solid solutions with precious metals hence their understanding is crucial for extraction of the latter. Pentlandite minerals also play an important role in the production of cleaner fuels with low or ultra-low sulphur content that requires a continuous improvement of the catalytic materials used in the refinement industry. Mineral nanoparticles have a variety of important geological and technological properties, which include removal of toxins from the environment and as a key abrasive material for chemical-mechanical planarization of advanced integrated circuits. Nanomineral particles in ore deposits may be used to reveal the thermal history of the geological set-up.

Currently, most pentlandite computational modelling studies are based on *ab initio* methods, which whilst more accurate tend to be limited to smaller systems and do not adequately accommodate thermal effects. In order to address such concerns, the first empirical interatomic potentials for the pentlandite structures were derived in the present study. The attention is initially focussed on the binary cobalt pentlandite, Co_9S_8 , since it is more amenable to computational methods than the well-known ternary $(\text{Fe,Ni})_9\text{S}_8$ pentlandites. Several experimental structural, elastic and lattice

dynamics properties, which are key for fitting potentials, were scarce or not available, hence they were calculated, in the present study, by *ab initio* methods. The derived interatomic potentials of Co_9S_8 were adequately validated, in the bulk form, as evidenced by their accurate determination of structure, elastic constants and moduli and phonon density of states; which indeed compare well with those obtained by experiment or *ab initio* methods. The robustness of the interatomic potentials was further illustrated by their ability to reproduce complex high temperature transitions of the bulk Co_9S_8 which were observed experimentally. The change of radial distribution functions (especially the coalescing of the adjacent Co-Co tetrahedral peaks) and the total energy with temperature, deduced from molecular dynamics studies, clearly depicted the phase change from the normal to the high form Co pentlandite above 1100K. Furthermore, the potentials of the bulk Co_9S_8 show melting above 1300K, as demonstrated by the calculated rdfs and energy; all consistent with the experimental results. The rdfs of the bulk Co_9S_8 confirm the molten phase at 1500K, since the height of the coalesced peak is reduced and at higher temperature of 1900K the height of the coalesced peak is further reduced showing a completely molten structure.

The reliability of the interatomic potentials demonstrated in the bulk pentlandite provides a good basis for considering studies of three high symmetry surfaces of Co_9S_8 , i.e. {111}, {101}, and {100}. The {111} surface was found to be the most stable of the three, with the smallest surface energy, from energy minimisation methods, which is in agreement with the experimental morphologies of Co_9S_8 . Molecular dynamics method was used to predict the melting temperatures of the surfaces, which, as expected, were below that of the bulk structure. The melting was deduced from the anomalous temperature variation of the total energy, ion diffusion coefficients, and the commencement of smooth radial distribution functions and loss

of structure of Co_9S_8 . Changes of such properties were more abrupt for the {111} and {101} surfaces, than for the {100} surface. The adsorption energies of water on the surfaces were calculated using the derived potentials. The behaviour of the melting of the pure surfaces was found to be different from the melting of the surfaces in contact with water. Generally hydration of surfaces rendered them more stable, as the surface energies are reduced.

The structures and stability of the mineral Co_9S_8 nanoparticles, bound by the three surfaces, i.e. {111}, {101} and {100} were also investigated. The effect of size on the melting of the nanoparticles was clearly illustrated, where the melting temperature increased with the nanoparticle size. This has demonstrated that the particle size significantly modifies the crystallinity and structure of the nanoparticles. In regard to the {111} and {101} Co_9S_8 nanoparticles, abrupt thermodynamic property changes are observed for nanoparticles of smaller sizes; whereas the larger nanoparticles show gradual changes. The structural snapshots suggest that the smaller nanoparticles disintegrate at higher temperatures; whereas larger nanoparticles contain this phenomenon by the formation of voids. In the case of {100} Co_9S_8 nanoparticle (with the larger surface energy), properties do not change as abruptly as those of {111} and {101} Co_9S_8 nanoparticles. In addition, the disintegration is not as violent; and larger systems are more compact with fewer voids. The largest nanoparticles (with close to 2500 atoms) for all surface orientations appear to have the same change in properties, distinct from the rest, especially with energy and diffusion coefficient variation with temperature. Furthermore, the rdfs of the Co_9S_8 nanoparticles bounded by both surfaces showed that at higher temperatures the peaks are broader and the height decreases, suggesting that at higher temperatures the surfaces are molten. The

different sizes of nanoparticles melt at different temperatures. The melting temperature increases with the increasing nanoparticle size.

The 2.9 nm radius {111} Co_9S_8 nanoparticle in water was studied, and was compared with the one in vacuum. The presence of water renders the nanoparticle amorphous.

Experimental information on the atomic scale is scarce for the pentlandites, particularly in regard to surface and nanoparticle properties. Hence the derived interatomic potentials in the current work have shed valuable insights on these, particularly when heated to high temperatures and when hydrated.

6.2. Recommendations

In light of the findings of this thesis, several recommendations for future research are listed below:

- Use molecular-dynamics calculations to study the structural transformation of a Co_9S_8 in its melting process within the framework of the embedded-atom method (EAM).
- Use density functional theory to study the nanoparticles of Co_9S_8 .
- Study molecular dynamics using *ab initio* methods to validate the atomistic molecular dynamics findings.
- The refitting or refinement of our potential model used in this thesis, to be able to handle the bulk structure of Co_9S_8 very “well”. Incorporate the shell model on the potentials.
- To further study diffusion anomalies in the bulk Co_9S_8 at 700 K and 1300 K.
- The discrepancy in surface energies of the {100} surface, as determined by VASP and METADISE codes needs to be further investigated.

- To determine if the diffusion is parallel to the surface or perpendicular to it and if it differs as you move from the surface to the middle of the slab.
- More analysis on the coordination number of water – Co or water – S and the associated residence times.

References

- [1] H.M. Sithole, D. Nguyen-Manh, D.G. Pettifor and P.E. Ngoepe, Internal relaxations, band gaps and elastic constant calculations of FeS₂. *Molecular Simulation*, 22: 31–37, 1999.
- [2] J. Muscat, A. Hung, S. Russo, and I. Yarovsky, First-principles studies of the structural and electronic properties of pyrite FeS₂. *Physical Review B*, 65:54107-54119, 2002.
- [3] P. Raybaud, G. Kresse, J. Hafner and H. Toulhoat, *Ab initio* density functional studies of transition-metal sulphides: I. Crystal structure and cohesive properties. *Journal of Physics: Condensed Matter*, 9:11085–11106, 1997.
- [4] R. Oviedo-Roa, J-M. Martinez-Magadan and F. Illas, Correlation between electronic eroperties and hydrodesulphurization activity of 4d-transition-metal sulphides. *Journal of Physical Chemistry B*, 110:7951-7966, 2006.
- [5] P. Waldner and W. Sitte, Thermodynamic modeling of Fe-Ni pentlandite. *Journal of Physics and Chemistry of Solids*, 69:923-927, 2008.
- [6] Y.S. Borodaev, I.A. Bryzgalov, N.N. Mozgova, and T.Y. Uspenskaya; Pentlandite and co-enriched pentlandite as characteristic minerals of modern hydrothermal sulphide mounds hosted by serpentized ultramafic rocks (Mid-Atlantic Ridge), *Moscow University Geology Bulletin*, , 62:85–97, 2007.
- [7] Z. Johan, M. Ohnenstetter, E. Slansky, L.M. Barron, and D. Suppel, Platinum mineralization in the Alaskan-type intrusive complexes near

- fifield, New South Wales, Australia Part 1. Platinum-group minerals in clinopyroxenites of the kelvin grove prospect, Owendale intrusion. *Mineralogy and Petrology*, 40: 289-309, 1989.
- [8] <http://www.periodictable.com/Items/Pentlandite/index.html>
- [9] X. F Qian, X.M Zhang, C.Wang, Y. Xie and Y.T. Qian, The preparation and phase transformation of nanocrystalline cobalt sulphides via a toluene thermal process. *Inorganic Chemistry*, 38:2621-2623, 1999.
- [10] T.A. Pecoraro and R.R. Chianelli, Hydrodesulphurization catalysis by transition metal sulfides. *Journal of Catalysis* 67:430-45, 1981.
- [11] I. Bezverkhyy, M. Danot, and P. Afanasiev, New low-temperature preparations of some simple and mixed Co and Ni dispersed sulphides and their chemical behaviour in reducing atmosphere. *Inorganic Chemistry*. 42:1764-1768, 2003.
- [12] R.C. Hoodless, R.B. Moyes and P.B. Wells, D-tracer study of butadiene hydrogenation and tetrahydrothiophen hydrodesulphurisation catalysed by Co_9S_8 . *Catalysis Today*, 114:377–382, 2006.
- [13] R.J. Angelici. An overview of modeling studies in HDS, HDN and HDO catalysis. *Polyhedron*, 16:3073-3088, 1997.
- [14] S.P. Farrell and M.E. Fleet. Phase separation in $(\text{FeCo})_{1-x}\text{S}$ monosulfide solid solution below 450 °C with consequences for coexisting pyrrhotite and pentlandite in magmatic sulfide deposits. *Canadian Mineral* 40:33-46, 2002.
- [15] A. Kitakaze and A. Sugaki. The phase relations between $\text{Fe}_{4.5}\text{Ni}_{4.5}\text{S}_8$ and Co_9S_8 in the system Fe-Ni-Co-S at temperatures from 400 °C to 1100 °C. *Canadian Mineral*, 42:17-42, 2004.

- [16] L. Cemic and O.J. Kleppa. High temperature calorimetry of sulphide systems. III Standard enthalpies of formation of phases in the systems Fe-Cu-S and Co-S. *Physics and Chemistry of Minerals*, 16:172-179, 1988.
- [17] Z. Grzesik. On the defect diffusivity in $\text{Co}_{9-x}\text{S}_8$. *Solid State Ionics*, 141-142:295-299, 2001.
- [18] Z. Grzesik, S. Mrowec. Microthermogravimetry in studying the defect and transport phenomena in transition metal sulphides. *Solid State Ionics*, 154-155:93-100, 2002.
- [19] G. Huang, T. Chen, Z. Wang, K. Chang, W. Chen. Synthesis and electrochemical performances of cobalt sulfides/grapheme nanocomposite as anode material of Li-ion battery. *Journal of Power Sources*, In Press.
- [20] G. Chen, W. Ma, D. Zhang, J. Zhu, X. Liu. Shape evolution and electrochemical properties of cobalt sulfide via a biomolecule-assisted solvothermal route. *Solid State Sciences*, 17:102-106, 2013.
- [21] Q. Wang, L. Jiao, H. Du, W. Peng, D. Song, Y. Wang, H. Yuan. Facile synthesis and electrochemical properties of Co-S composites as negative materials for alkaline rechargeable batteries. *Electrochimica Acta*, 56:1106-1110, 2011.
- [22] H.R. Chauke, D. Nguyen-Manh, P.E. Ngoepe, D.G. Pettifor and S.G. Fries, Electronic structure and stability of the pentlandites Co_9S_8 and $(\text{Fe,Ni})_9\text{S}_8$. *Physical Review B*, 66:155105, 2002.

- [23] R.A. Sidik, and A.B. Anderson. Co₉S₈ as a catalyst for electroreduction of O₂: quantum chemistry. *Journal of Physical Chemistry B*, 110:936-941, 2006.
- [24] M. Ramos, G. Berhault, D.A. Ferrer, B. Torres and R.R. Chianelli. HRTEM and molecular modeling of the MoS₂-Co₉S₈ interface: understanding the promotion effect in bulk HDS catalysts. *Catalysis Science and Technology*, 2:164-178, 2012.
- [25] M.D. Segall, P. J.D. Lindan, M.J. Probert, C.J. Pickard, P.J. Hasnip, S.J. Clark and M.C. Payne. First-principles simulation: ideas, illustrations and the CASTEP code. *Journal of Physics: Condensed Matter*, 14:2717-2744, 2002.
- [26] P. Yin, L. Sun, Y. Gao and S. Wang, Preparation and characterization of Co₉S₈ nanocrystalline and nanorods. *Bulletin Materials Science*, 31:593-596, 2008.
- [27] C. Wang, X.M. Zhang, X.F. Qian, Y. Xie and Y.T. Qian, A low temperature route to nanocrystalline Co₉S₈. *Journal of Physics and Chemistry of Solids*, 60:2005-2008, 1999.
- [28] Z. Wang, L. Pan, H. Hu and S. Zhao, Co₉S₈ nanotubes synthesized on the basis of nanoscale Kirkendall effect and their magnetic and electrochemical properties. *The Royal Chemistry of Society: CrystEngComm*, 12:1899-1904, 2010.
- [29] J.H. Zhan, X.G. Xie, D.W. Wang, Y.T. Qian, and X.M. Liu, Hydrazine-controlled hydrothermal synthesis of Co₉S₈ from a homogeneous solution. *Journal of Materials Research*, 14:4418-4420, 1999.

- [30] X.C. Sun, K. Parvin, J. Ly and D.E. Nikles, Magnetic properties of a mixture of two nanosized Co-S powders produced by hydrothermal reduction. *IEEE Transactions on Magnetics*, 39:5, 2003.
- [31] G. Du, W. Li and Y. Liu, Filling Carbon nanotubes with Co_9S_8 nanowires through in situ catalyst transition and extrusion. *Journal of Physical Chemistry C*, 112:1890-1895, 2008.
- [32] W. Maneprakorn, M.A. Malik and P. O'Brien, The preparation of cobalt phosphide and cobalt chalcogenide (CoX , $\text{X} = \text{S}, \text{Se}$) nanoparticles from single source precursors. *Journal of Materials Chemistry*, 20:2329–2335, 2010.
- [33] Q. Wang, L. Jiao, Y. Han, H. Du, W. Peng, Q. Huan, D. Song, Y. Si, Y. Wang, and H. Yuan, CoS_2 Hollow spheres: fabrication and their application in Lithium-ion batteries. *Journal of Physical Chemistry C*, 115:8300–8304, 2011.
- [34] Y. Wang, J. Wu, Y. Tang, X. Lü, C. Yang, M. Qin, F. Huang, X. Li, and X. Zhang, Phase-controlled synthesis of cobalt sulphides for Lithium ion batteries. *Applied Material and Interfaces*, 4:4246–4250, 2012.
- [35] J. Wang, S.H. Nga, G.X. Wang, J. Chen, L. Zhaoa, Y. Chena, H.K. Liu, Synthesis and characterization of nanosize cobalt sulphide for rechargeable lithium batteries. *Journal of Power Sources*, 159:287–290, 2006.
- [36] W. Shi, J. Zhu, X. Rui, X. Cao, C. Chen, H. Zhang, H.H. Hng, and Q. Yan, Controlled synthesis of carbon-coated cobalt sulphide Nanostructures

- in oil phase with enhanced Li storage performances. *Applied Materials and Interfaces*, 4:2999–3006, 2012.
- [37] S. Geller, Refinement of the crystal structure of Co_9S_8 . *Acta Crystallographica*, 15:1195, 1962.
- [38] R. W. G. Wyckoff, *Crystal Structures*; John Wiley & Sons: New York, 2:222, 1964.
- [39] J. K. Burdett and G.J. Miller, Polyhedral clusters in solids: The electronic structure of pentlandite. *Journal of American Chemical Society*, 109:4081-4091, 1987.
- [40] A. Wold and K. Dwight, Low temperature synthesis of transition metal sulfides. *Journal of Solid State Chemistry*, 96:53-58, 1992.
- [41] R. Chen, Q. Xin and J. Hu, Quantum chemical study of hydrodesulphurization catalysts Part II. DV- $X\alpha$ calculation on clusters of Co_9S_8 and RuS_2 . *Journal of Molecular Catalysis*, 75:253-276, 1992.
- [42] V. Rajamani and C.T. Prewitt. Refinement of Co_9S_8 . *Canadian Mineralogists*, 13:75-78, 1975.
- [43] C.R.A. Catlow, J.D. Gale and R.W.Grimes, Recent computational studies in solid state chemistry. *Journal of Solid State Chemistry*, 106:13-26, 1993.
- [44] M.R. Levy, *Crystal structure and defect property predictions in ceramic materials*, University Of London, PhD Thesis, 2005.
- [45] E. Wimmer, The growing importance of computations in materials science: Current capabilities and perspectives. *Materials Science, Poland*, 23:325-345, 2005.

- [46] C.R.A Catlow, Computer modelling as a technique in solid state chemistry, *Faraday Discussion*, 106:1-40, 1997.
- [47] N.H. de Leeuw and S.C. Parker. Molecular-dynamics simulation of MgO surfaces in liquid water using a shell-model potential for water. *Physical Review B*, 58:13901-13908, 1998.
- [48] S.C. Parker, N.H. de Leeuw and S.E. Redfern. Atomistic simulation of oxide surfaces and their reactivity with water. *Faraday Discussion*, 114: 381-393, 1999.
- [49] M. Born and K. Huang, *Dynamical Theory of Crystal Lattices 1st edition*, University Press: Oxford, 1954.
- [50] D.K. Fisler, J.D. Gale and R.T.A. Cygan, Shell model for the simulation of rhombohedral carbonate minerals and their point defects. *American Mineralogist*, 85, 217-224, 2000.
- [51] G.W. Watson, E. T. Kelsey, N. H. de Leeuw, D. J. Harris and S. C. Parker, Atomistic simulation of dislocations, surfaces and interfaces in MgO. *Journal of the Chemical Society-Faraday Transactions*, 92:433-438, 1996.
- [52] S. Kerisit, *Atomistic simulation of calcite surfaces*. PhD Thesis, University of Bath, 2004.
- [53] M.J. Norgett, and R Fletcher. Fast matrix methods for calculating relaxation about defects in crystals. *Journal of Physics Part C: Solid State Physics*, 3:L190-L192, 1970.
- [54] R. Fletcher and M.J.D. Powell. A rapidly convergent descent method for minimization. *Computer Journal*, 6:163-168, 1963.

- [55] D. Mkhonto. *Computer simulation of apatite mineral surfaces and interfaces with silicates*. PhD Thesis, University of Limpopo, 2005.
- [56] D.J. Cooke. *Atomistic simulation of segregation to the surfaces of hematite and goethite*. PhD Thesis, University of Bath, 2003.
- [57] C.G. Broyden. The convergence of a class of double-rank minimization algorithms. *Journal of the Institute of Mathematics and its Applications*, 6, 76-90, 1970.
- [58] R. Fletcher. A new approach to variable metric algorithms. *Computer Journal*, 13:317-322, 1970.
- [59] D. Goldfarb. A family of variable-metric methods derived by variational means. *Mathematics of Computation*, 24:23-26, 1970.
- [60] D.F. Shanno, Conditioning of quasi-Newton methods for function minimization. *Mathematics of Computation*, 24:647-656, 1970.
- [61] H.Z. Zhang and J.F. Banfield, Aggregation, coarsening, and phase transformation in ZnS nanoparticles studied by molecular dynamics simulations. *Nano Letters*, 4:713-718. 2004.
- [62] D. Frenkel and B. Smit, *Understanding molecular simulations: from Algorithms to Applications* Academic Press; San Diego, 1996.
- [63] W. Smith and T.R. Forester. DL_POLY_2.0: A general-purpose parallel molecular dynamics simulation package. *Journal of Molecular Graphics*, 14:136-341, 1996.

- [64] L. Verlet. Computer "Experiments" on Classical Fluids. I. Thermodynamical properties of Lennard-Jones molecules. *Physical Review*, 159:98-103. 1967.
- [65] J.M. Holender. Molecular-dynamics studies of the thermal properties of the solid and liquid fcc metals Ag, Au, Cu, and Ni using many-body interactions. *Physical Review B*, 41: 8054-8061, 1990.
- [66] M.P. Allen and D.J. Tildesley, *Computer simulation of liquids*, Oxford Scientific Publishing, Oxford, UK, 1987.
- [67] D.C. Sayle, J.A. Doig, S.A. Maicananu and G.W. Watson, The atomistic structure of oxide nanoparticles supported on an oxide substrate. *Physical Review B*, 65: 245414, 2002.
- [68] W. Kob, Computer simulations of supercooled liquids and glasses. *Journal Physics: Condensed Matter*, 11:85, 1999.
- [69] P.M. Oliver, G.W. Watson and S.C. Parker, Molecular dynamics simulations of nickel oxide surfaces. *Physical Review B*, 52:5323-5329, 1995.
- [70] P.W. Tasker. The stability of ionic crystal surfaces. *Journal of Physics C: Solid State Physics*, 12:4977-4984, 1979.
- [71] P.M. Oliver, S.C. Parker and W.C. Mackrodt, Computer-simulation of the crystal morphology of NiO. *Modelling and Simulation in Materials Science and Engineering*, 1:755-760, 1993.
- [72] G. Wulff, On the question of the rate of growth and dissolution of crystal surfaces. *Zeitschrift fuer Kristallographie und Mineralogie*, 34:449-530, 1901.

- [73] J.W. Gibbs, The collected works, volume 1, Thermodynamics. Longmans & Green, New York, 1928.
- [74] P. Hellstrom, *Ab-Initio* Modelling of Xanthates; Adsorbed on Ge and ZnS surfaces. PhD Thesis, Luleå University of Technology, 2007
- [75] J. Hafner, *Ab-initio* simulations of materials using VASP: Density-functional theory and beyond. *Journal of Computational Chemistry*, 29:2044-2078, 2008.
- [76] M. Born and R. Oppenheimer, On the quantum theory of molecules. *Annalen der Physik*, 84:457, 1927.
- [77] S. Fahy, X.W. Wang and S.G. Louie, Variational quantum Monte Carlo nonlocal pseudopotential approach to solids: Formulation and application to diamond, graphite, and silicon. *Physical Review B*, 42:3503, 1990.
- [78] C.J. Umrigar, K.G. Wilson and J.W. Wilkins, Optimized trial wave functions for quantum Monte Carlo calculations. *Physical Review Letters*, 60:1719-1722, 1988.
- [79] D. Wei and K. Osseo-Asare, Semiconductor electrochemistry of particulate pyrite: dissolution via hole and electron pathways. *Journal of Electrochemical Society*, 143:3192-3198, 1996.
- [80] D. Ceperly, and M. KalosIn and K. Binder, editor Monte Carlo methods in statistical physics. *Springer*, Berlin, 1979.
- [81] P.D. Haynes, *Linear-scaling methods in ab-initio quantum-mechanical calculations*, PhD Thesis, University of Cambridge, 1998.
- [82] J.A. Allen, *Computational Study of the adsorption of water and carbon dioxide at oxide surfaces*. PhD Thesis, University of Bath, 2009.

- [83] Wikipedia website June 21, 2011.
- [84] W. Tang, E. Sanville and G. Henkelman, A grid-based Bader analysis algorithm without lattice bias. *Journal of Physics: Condensed Matter*, 21:084204, 2009.
- [85] K. Capelle, *A bird's-eye view of density-functional theory*. 2006.
- [86] <http://cms.mpi.univie.ac.at/vasp/vasp/>
- [87] D. M. Pasquariello, R. Kershaw, J. D. Passaretti, K. Dwight and A. Wold, Low-temperature synthesis and properties of Co_9S_8 , Ni_3S_2 , and Fe_7S_8 . *Inorganic Chemistry*, 23:872-814, 1984.
- [88] P.P. Ewald, Die Berechnung optischer und elektrostatischer Gitterpotentiale. *Annalen der Physik*, 64:253-440, 1921.
- [89] C. Kittel. Introduction to solid state physics, 2nd Edition, John Wiley & Sons, New York, USA, 1963.
- [90] D.E. Parry, The electrostatic potential in the surface region of an ionic crystal. *Surface Science*, 49:433-440, 1975.
- [91] D.E. Parry. Erratum. *Surface Science*, 54:195-195, 1976.
- [92] D.M. Heyes, M. Barber and J.H.R. Clarke. Molecular dynamics computer simulation of surface properties of crystalline potassium chloride. *Journal of the Chemical Society - Faraday Transactions II*, 73:1485-1496, 1977.
- [93] A.W Dick, and B.G. Overhauser, Theory of dielectric constants of alkali halide crystals. *Physical Review*, 112:90-103, 1958.
- [94] K.J. W. Atkinson, *Atomic scale simulation of defects in bulk materials and monolayer surfaces*, PhD Thesis, University of London, 2002.

- [95] M. Matsui and M. Akaogi; Molecular dynamics simulation of the structural and physical properties of the four polymorphs of TiO₂. *Molecular Simulation*, 6:239-244, 1991.
- [96] N. H. de Leeuw, S. C. Parker, H. M. Sithole, and P. E. Ngoepe; Modeling the surface structure and reactivity of pyrite: Introducing a Potential Model for FeS₂. *Journal of Physical Chemistry B*, 104:7969–7976, 2000.
- [97] S.D. Fleming, J.R. Morton, A.L. Rohl and C.B. Ward, Interatomic potentials for simulating MnO₂ polymorphs. *Molecular Simulation*, 31:25-32, 2005.
- [98] C.R.A. Catlow, New science from high-performance computing: an introduction. *Philosophical Transactions of the Royal Society: London A*, 360: 1075-1078, 2002.
- [99] S.M. Woodley and C.R.A. Catlow, High-performance computing in the chemistry and physics of materials. *Proceedings of the Royal Society A*, 2011.
- [100] G. Kresse and J. Furthmuller, Efficient iterative schemes for *ab initio* total-energy calculations using a plane-wave basis set. *Physical Review B*, 54: 11169–11186, 1996.
- [101] J.M. Soler, E. Artacho, J.D Gale, A Garcia, J. Junquera, P. Ordejon and D. Sanchez-Portal, The SIESTA method for *ab initio* order-*N* materials simulation. *Journal of Physics: Condensed Matter*, 14: 2745–2779, 2002.
- [102] J. D. Gale and A. L. Rohl "The General Utility Lattice Program (GULP)". *Molecular Simulation*, 5:291-341, 2003.

- [103] C.A.J. Fisher, Molecular dynamics simulations of reconstructed NiO surfaces. *Scripta Materialia*, 50:1045-1049, 2004.
- [104] H.R. Chauke, *Computer simulation studies of pentlandite structures*. MSc Thesis, University of the North, 2000.
- [105] N. H. de Leeuw and S. C. Parker, Molecular-dynamics simulation of MgO surfaces in liquid water using a shell-model potential for water. *Physical Review B*, 58:13901-13908, 1998.
- [106] N.H. De Leeuw, F.M. Higgins and S.C. Parker, Modeling the surface structure and stability of α -quartz. *Journal of Physical Chemistry B*, 103:1270-1277, 1998.
- [107] N.H. de Leeuw and S.C. Parker, Surface structure and morphology of calcium carbonate polymorphs calcite, aragonite, and vaterite: An atomistic approach; *Journal of Physical. Chemistry B*, 102:2914-2922, 1998.
- [108] W. Yu, N. Wang, X. Xiao, B. Tang, L. Peng and W. Ding, First-principles investigation of the binary AB₂ type laves phase in Mg–Al–Ca alloy: Electronic structure and elastic properties. *Solid State Sciences*, 11:1400–1407, 2009.
- [109] Z. Dian-wu, L. Jin-shui and P. Ping, A first-principles study on electronic structure and elastic properties of Al₄Sr, Mg₂Sr and Mg₂₃Sr₆ phases. *Transactions of Nonferrous Metals Society of China*, 21:2677–2683, 2011.
- [110] M. J. Mehl, J. E. Osburn, D. A. Papaconstantopoulos and B.M. Klein, Structural properties of ordered high-melting-temperature intermetallic alloys from first-principles total-energy calculations. *Physical Review B: Condensed Matter*, 41:10311–10323, 1990.

- [111] T. Wang, P. Chen, Y. Deng and B. Tang, First-principles calculation of structural and elastic properties of $\text{Pd}_{3-x}\text{Rh}_x\text{V}$ alloys. *Transactions of Nonferrous Metals Society of China*, 21: 388–394, 2011
- [112] E. Screiber, O.L. Anderson and N. Soga, Elastic constants and their measurement, McGraw-Hill, New York, 1973.
- [113] F. Benkabou , H. Aourag and M. Certier, Atomistic study of zinc-blende CdS, CdSe, ZnS, and ZnSe from molecular dynamics. *Materials Chemistry and Physics*, 66:10–16, 2000.
- [114] Wikipedia website, 21 April 2012.
- [115] M.R. Johnson , K. Parlinski , I. Natkaniec and B.S. Hudson, Ab initio calculations and INS measurements of phonons and molecular vibrations in a model peptide compound – urea. *Chemical Physics*, 291:53–60:2003.
- [116] G. Kresse and J. Hafner, VASP the guide (University of Vienna, 2012), <http://cms.mpi.univie.ac.at/vasp/>;
- [117] G. Kresse and J. Furthmüller, Efficiency of ab-initio total energy calculations for metals and semiconductors using a plane-wave basis set *Computer Materials Science*, 6:15, 1996.
- [118] G. Kresse and J. Hafner, Ab initio molecular dynamics for liquid metals, *Physical Review B*, 47:RC558, 1993.
- [119] J.P. Perdew, K. Burke and M. Ernzerhof, Generalized gradient approximation made simple. *Physical Review Letters*, 77:3865–3868, 1996.
- [120] P. E. Blöchl, Projector augmented-wave method. *Physical Review B*, 50:17953-17979, 1994.

- [121] G. Kresse and D. Joubert, From ultra-soft pseudopotentials to the projector augmented-wave method. *Physical Review B*, 59:1758-1775, 1999.
- [122] H.J. Monkhorst and J.D. Pack, Special points for Brillouin-zone integrations. *Physical Review B*, 13:5188–5192, 1976.
- [123] M. Methfessel and A. T. Paxton, High-precision sampling for Brillouin-zone integration in metals. *Physical Review B*, 40:3616-3621, 1989.
- [124] G.A. Berezovskii, V.A. Drebuschak, and T.A. Kravchenko, Low-temperature heat capacity of pentlandite. *American Mineralogist*, 86:1312–1313, 2001.
- [125] M.I. Mendeleev and G.J. Ackland, Development of an interatomic potential for the simulation of phase transformations in zirconium. *Philosophical Magazine Letters*, 87:349-359, 2007.
- [126] H. Chiba, K. Nishidate, M. Baba, N. Kumagai, T. Sato and K. Nishikawa; Molecular dynamics study of a V₂O₅ crystal. *Solid State Communications*, 110:497–502, 1999.
- [127] W. Chen, C. Wua and H. Cheng, Modified Nosé–Hoover thermostat for solid state for constant temperature molecular dynamics simulation. *Journal of Computational Physics*, 230:6354–6366, 2011.
- [128] M.A. Henderson, The interaction of water with solid surfaces: fundamental aspects revisited *Surface Science Reports*, 46:1-308, 2002.
- [129] S. Nose', A unified formulation of the constant temperature molecular dynamics methods. *Journal Chemical Physics*, 81:511, 1984.

- [130] W.G. Hoover. Canonical dynamics-equilibrium phase space distributions. *Physical Review A*, 31:1695, 1985.
- [131] D. J. Evans and B. L. Holian, The Nose–Hoover thermostat. *Journal of Chemical Physics*, 83: 4069-4074, 1985.
- [132] Accelrys website, 2011.
- [133] B.K. Benazzouz and A. Zaoui, Thermal behaviour and superheating temperature of kaolinite from molecular dynamics. *Applied Clay Science*, 58:44-51, 2012.
- [134] V. Rajamani and C.T. Prewitt, Thermal expansion of the pentlandite structure. *American Mineralogist*, 60:39-48, 1975
- [135] N. Morimoto and G. Kullerud, Pentlandite-thermal expansion. *Carnegie Inst. Wash. Year Book*, 64, 204-207, 1964
- [136] S. M. A. M. Bouwens, J. A. R. van Veen, D. C. Koningsberger, V. H. J. de Beer, and R. Prins, Extended X-RAY absorption fine structure determination of the structure of cobalt in carbon-supported Co and Co-Mo sulfide hydrodesulphurization catalysts. *Journal of Physical Chemistry*, 95:134-139, 1991
- [137] E.T. Chen, R.N. Barnett and U. Landman, Surface melting of nickel (110). *Physical Review B*, 41:439, 1990.
- [138] N.H. de Leeuw, S.C. Parker, C.R.A. Catlow and G.D. Price, Modelling the effect of water on the surface structure and stability of forsterite. *Physical and Chemistry of Minerals*. 27:332–341, 2000.
- [139] J.L.F. Silva, C. Stampfl, and M. Scheffler. Converged properties of clean metal surfaces by all-electron first-principles calculations, *Surface Science*, 600:703-715, 2006.

- [140] W.R. Tyson and W.A. Miller, Surface free energies of solid metals: Estimation from liquid surface tension measurements, *Surface Science*, 62:267-276, 1977.
- [141] J. Marti, G. Nagy, E. Guardia, and M.C. Gordillo, Molecular dynamics simulation of liquid water confined inside graphite channels: Dielectric and dynamical properties. *Journal of Physical Chemistry B*, 110:23987-23994, 2006.
- [142] D. Spagnoli, Atomistic simulations of the mineral water interface. University of Bath, PhD Thesis, 2006.
- [143] M.C. Gordillo and J. Marti, Water on graphene surfaces. *Journal of Physics: Condensed Matter*, 22:284111, 2010.
- [144] A.K. Soper and M.G. Phillips, A new determination of the structure of liquid water at 25 degree. *Chemical Physics*, 107:47-60, 1986.
- [145] J. Wang, A.G. Kalinichev, R. J. Kirkpatrick, and R.T. Cygan, Structure, energetics, and dynamics of water adsorbed on the muscovite (001) surface: A molecular dynamics simulation. *Journal of Physical Chemistry B*, 109:15893-15905, 2005.
- [146] D. Spagnoli and J.G. Gale, Atomistic theory and simulation of the morphology and structure of ionic nanoparticles. *Nanoscale*, 4:1051-1067, 2012.
- [147] A.V. Chadwick and G.E. Rush, Characterization of nanocrystalline oxides by EXAFS Spectroscopy. *Nanocrystalline Metals and Oxides*, eds, P Knauth and J Schoonman; Kluwer, Boston, 2002.

- [148] V. van Hoang and T. Odagaki, Molecular dynamics simulations of simple monoatomic amorphous nanoparticles. *Physical Review B*, 77:125434, 2008.
- [149] H. Akbarzadeh, H. Abroshan and G.A. Parsafar, Surface free energy of platinum nanoparticles at zero pressure: A molecular dynamic study. *Solid State Communication*, 150: 254-157, 2010.
- [150] H. Gleiter. Nanostructured materials: basic concepts and microstructure. *Acta Materialia*. 48:1-29, 2000.
- [151] S. Alavi and D.L. Thompson, Molecular dynamics simulations of the melting of aluminum nanoparticles. *Journal Physical Chemistry A*, 110:1518-1523, 2006.
- [152] W.H. Qi, Size effect on melting temperature of nanosolids. *Physica B*, 368:46-50, 2005.
- [153] B. Gilbert, F. Huang, H. Zhang, G.A. Waychunas, J.F. Banfield, Nanoparticles: strained and stiff. *Science*, 305:651, 2004.
- [154] P. Pawlow, Melting point dependence on the surface energy of a solid body. *Zeitschrift fuer Physikalische Chemie, Stoechiometrie und Verwandtschaftslehre*, 65:1-35, 1909.
- [155] S. J. Zhao, S. Q. Wang, D. Y. Cheng and H. Q. Ye, Three distinctive melting mechanisms in isolated nanoparticles. *Journal of Physical Chemistry B*, 105:12857-12860, 2001.
- [156] S.K. Gupta, M. Talati and P. K. Jha, Shape and size dependent melting point temperature of nanoparticles. *Materials Science Forum*, 570:132-137, 2008.

- [157] V. P. Skripov, V. P. Koverda and V. N. Skokov, Size effect on melting of small particles. *Physica Status Solidi*, 66:109–118, 1981.
- [158] F.E. Osterloh, Directional superparamagnetism and photoluminescence in clusters of magnetite and cadmium selenide nanoparticles. *Comments on Inorganic Chemistry*, 27: 41–59, 2006.
- [159] B. Gilbert and J.F. Banfield, Molecular-scale processes involving nanoparticulate minerals in biogeochemical systems. *Reviews in Mineralogy & Geochemistry*, 59:109-155, 2005.
- [160] G.A. Waychunas, C.S. Kim and J.F. Banfield, Nanoparticulate iron oxide minerals in soils and sediments: unique properties and contaminant scavenging mechanisms. *Journal of Nanoparticle Research*, 7:409–433, 2005.
- [161] X. Feng, D.C. Sayle, Z.L. Wang, M. S. Paras, B. Santora, A.C. Sutorik, T.X.T. Sayle, Y. Yang, Y. Ding, X. Wang, and Y. Her, Converting ceria polyhedral nanoparticles into single-crystal nanospheres. *Science* 312:1504-1507, 2006.
- [162] M.F. Hochella Jr., S.K. Lower, P.A. Maurice, R.L. Penn, N. Sahai, D.L. Sparks and B.S. Twining, nanominerals, mineral nanoparticles, and earth systems. *Science*, 319:1631-1635, 2008.
- [163] G.A. Waychunas and H. Zhang, Structure, chemistry, and properties of mineral nanoparticles. *Elements*, 4:381–387, 2008.

- [164] U. Becker, M. Reich, and S. Biswas, “Nanoparticle host interactions in natural systems” in *Nanoscopic approaches in Earth and planetary sciences*, F. Brenker and G. Jordan, Eds. EMU Notes in Mineralogy 8: 2010.
- [165] C. Lai, M. Lu and L. Chen, Metal sulfide nanostructures: synthesis, properties and applications in energy conversion and storage. *Journal of Materials Chemistry*, 22, 19–30, 2012.
- [166] D. Spagnoli, J.P. Allen, and S.C. Parker, The structure and dynamics of hydrated and hydroxylated magnesium oxide nanoparticles. *Langmuir*, 27:1821–1829, 2011.
- [167] E. Ringe, R.P. Van Duyne and L.D. Marks, Wulff construction for alloy nanoparticles, *Nano letter*, 11:3399-3403, 2011.
- [168] S. Kerisit, D.J. Cooke, D. Spagnoli and S.C. Parker, Molecular dynamics simulations of the interactions between water and inorganic solids. *Journal of Materials Chemistry*, 15:1454-1462, 2005.
- [169] D.J. Cooke and J.A. Elliott. Atomistic simulations of calcite nanoparticles and their interaction with water. *Journal of Chemical Physics*, 127:104706, 2007.
- [170] P. Martin, D. Spagnoli, A. Marmier, S. C. Parker, D. C. Sayle and G. Watson, Application of molecular dynamics DL_POLY codes to interfaces of inorganic materials. *Molecular Simulation*, 32:1079–1093, 2006.
- [171] D. Spagnoli, B. Gilbert, G. A. Waychunas and J. F. Banfield, Prediction of the effects of size and morphology on the structure of water

around hematite nanoparticles. *Geochemica et Cosmochimica Acta*, 73: 4023-4033, 2009.

[172] R.E. Cohen and Z. Gong, Melting and melt structure of MgO at high pressure. *Physical Review B*, 17:12301-12311, 1994.

[173] A. Adnan and C.T. Sun, Effect of surface morphology and temperature on the structural stability of nanoscale wavy films. *Nanotechnology*, 19:315702, 2008.

[174] Z. Li, Y. Fua, J. Baob, M. Jiang, T. Huc, T. Liu and Y. Xie, Effect of cobalt promoter on Co–Mo–K/C catalysts used for mixed alcohol synthesis. *Applied Catalysis A: General*, 220:21–30, 2001.

[175] S.K.R.S. Sankaranarayanan, V.R. Bhethanabotla, and B. Joseph. Molecular dynamics simulation study of the melting and structural evolution of bimetallic Pd-Pt nanowires. *Physical Review B* 74:155441, 2006.

Appendix A

Papers Presented at Local and International Conferences

1. Computer Simulation of Pentlandite Compounds: Molecular Dynamics Study, South African Institute of Physics (54th), University of KwaZulu Natal, (July 2009).
2. Computer Simulation of Mineral Sulphide Co_9S_8 , Royal Society of Chemistry Solid State Group 30th Anniversary Christmas Meeting, University College London, UK, (December 2010).
3. Computer Modelling Studies of Pentlandites, Perspectives in Computational Materials Science and Physics, 60th Birthday Conference in Honour of Professor P.E. Ngoepe, University of Limpopo (Turfloop Campus) (January 2013).
4. Atomistic simulations studies of the bulk cobalt pentlandite (Co_9S_8): Validation of the potential model. American Physical Society (APS) Meeting, Baltimore, Maryland, USA, (March 2013).

Papers to be submitted

1. Mehlape M.A., Parker S.C and Ngoepe P.E. "Density Functional Theory and Interatomic Potential Study of the Bulk and Surface Structure and Properties of the cobalt pentlandite (Co_9S_8): Validation of Potential model"
2. Mehlape M.A., Parker S.C and Ngoepe P.E. "The Effect of Size on Melting of Co_9S_8 nanoparticles"
3. Mehlape M.A., Parker S.C and Ngoepe P.E. "Structure and Reactivity of cobalt pentlandite (Co_9S_8) surfaces: Molecular Dynamics Study"

Appendix B

Table B1: Interatomic potential parameters for Co₉S₈. Model 1

Species	Charge (e)			
Cobalt, Co core	+0.40			
Sulphur, S core	-0.45			
Buckingham potential	$A(eV)$	$\rho(\text{\AA})$	$C(eV/\text{\AA}^6)$	Cut-off(\AA)
Co core – S core	1130.5331	0.1845	0.0	20.0
Morse Potential	$D(eV)$	$\alpha(eV)$	$r_0(\text{\AA})$	
S core – S core	3.0	1.420177	2.198531	
Three-body potential	$k(eV/\text{rad}^{-2})$		$\theta_0(^{\circ})$	
Co core – S core – S core	4.084		109.4666667	
S core – Co core – S	3.5		109.4666667	

Table B2: Interatomic potential parameters for Co₉S₈. Model 2

Species	Charge (e)			
Cobalt, Co core	+0.40			
Sulphur, S core	-0.45			
Buckingham potential	$A(eV)$	$\rho(\text{\AA})$	$C(eV/\text{\AA}^6)$	Cut-off(\AA)
Co core – S core	1130.5331	0.1845	0.0	20.0
Morse Potential	$D(eV)$	$\alpha(eV)$	$r_0(\text{\AA})$	
S core – S core	3.0	2.198531	1.420177	
Three-body potential	$k(eV/\text{rad}^{-2})$		$\theta_0(^{\circ})$	
Co core – S core – S core	2.041		109.4666667	
S core – Co core – Co	0.694		109.4666667	

Table B3: Calculated structures and properties of the cubic Co₉S₈ phase for different potential models, including comparison versus experiment, where known.

	Experimental Observables [@]	Model 1	Model 2
C ₁₁	223.8	221.1	191.5
C ₁₂	80.3	80.4	88.9
C ₄₄	71.3	78.6	46.6
Bulk Modulus, <i>B</i> (GPa)	128.1	127.3	123.1
Shear Modulus, <i>G</i> (GPa)	71.5	48.5	75.3
Elastic Modulus, <i>E</i> (GPa)	180.8	188.7	128.6
Poisson Ratio, <i>v</i>	0.26	0.27	0.32
Volume (Å ³)	978.56 *	943.72	940.51
Lattice parameter, <i>a</i> (Å)	9.928*	9.809	9.798

*Ref. [89] and Ref [28] @DFT (VASP)

Appendix C

```

Miller Index:      1      1      1

Normal Axis  0.577350269189626      0.577350269189626
0.577350269189626
PLDRAW: Code (      33 ) with dipole =  8.047096322627567E-011
height      charge      atom arrangement
  0.0        4.8      CO--CO--CO--CO--CO--CO--CO--CO--CO--CO--CO--CO--
  0.2         0.0
  0.4         0.0
  0.6        -1.8      S--S--S--S--
  0.8        -5.4      S--S--S--S--S--S--S--S--S--S--S--S--
  1.0         0.0
  1.2         0.0
  1.4         1.6      CO--CO--CO--CO--
  1.6         0.0
  1.8         0.0
  2.0         0.0
  2.2         1.6      CO--CO--CO--CO--
  2.4         0.0
  2.6         0.0
  2.8         1.6      CO--CO--CO--CO--
  3.0         0.0
  3.2         0.0
  3.4        -5.4      S--S--S--S--S--S--S--S--S--S--S--S--
  3.6        -1.8      S--S--S--S--
  3.8         0.0
  4.0         0.0
  4.2         4.8      CO--CO--CO--CO--CO--CO--CO--CO--CO--CO--CO--CO--

```

Figure C1: Sketched representation of the atoms arrangement on the {111} surface

```

Miller Index:      1      0      1
Normal Axis 0.707106781186547      0.000000000000000E+000
0.707106781186547
PLDRAW: Code (      43 ) with dipole = -6.614264691506833E-011
height      charge      atom arrangement
0.0          -0.2      CO--CO--CO--CO--S--S--S--S--
0.2          0.0
0.4          0.0
0.6          0.0
0.8          0.0
1.0          0.0
1.2          0.0
1.4          0.0
1.6          0.0
1.8 1st line CO--S--S--CO--CO--CO--CO--CO--CO--CO--CO--CO--S--S--
1.8          0.4      S--S--S--S--
2.0          0.0
2.2          0.0
2.4          0.0
2.6          0.0
2.8          0.0
3.0          0.0
3.2          0.0
3.4          1.4      S--S--S--S--CO--CO--CO--CO--CO--CO--CO--CO--
3.6          -1.8     S--S--S--S--
3.8          0.0
4.0          0.0
4.2          0.0
4.4          0.0
4.6          0.0      |
4.8          0.0
5.0          0.0
5.2 1st line CO--CO--CO--CO--CO--CO--CO--S--S--S--S--CO--S--S--
5.2          0.4      CO--CO--S--S--
5.4          0.0
5.6          0.0
5.8          0.0
6.0          0.0
6.2          0.0
6.4          0.0
6.6          0.0
6.8          -0.2     S--S--S--S--CO--CO--CO--CO--

```

Figure C2: Sketched representation of the atoms arrangement on the {101} surface

```

Miller Index:      1      0      0
Normal Axis      1.0000000000000000      0.0000000000000000E+000
0.0000000000000000E+000
PLDRAW: Code (   13 ) with dipole = -4.685141163918161E-011
height  charge  atom arrangement
0.0     -1.8    S--S--S--S--
0.2      0.0
0.4      0.0
0.6      0.0
0.8      0.0
1.0      0.0
1.2      3.2    CO--CO--CO--CO--CO--CO--CO--CO--
1.4      0.0
1.6      0.0
1.8      0.0
2.0      0.0
2.2      0.0
2.4     -2.8    CO--CO--S--S--S--S--S--S--S--S--
2.6      0.0
2.8      0.0
3.0      0.0
3.2      0.0
3.4      0.0
3.6      3.2    CO--CO--CO--CO--CO--CO--CO--CO--
3.8      0.0
4.0      0.0
4.2      0.0
4.4      0.0
4.6      0.0
4.8     -2.7    S--S--S--S--S--S--
5.0     -0.9    S--S--
5.2      0.0
5.4      0.0
5.6      0.0
5.8      0.0
6.0      3.2    CO--CO--CO--CO--CO--CO--CO--CO--
6.2      0.0
6.4      0.0
6.6      0.0
6.8      0.0
7.0      0.0
7.2      0.0
7.4     -2.8    CO--CO--S--S--S--S--S--S--S--S--
7.6      0.0
7.8      0.0
8.0      0.0
8.2      0.0
8.4      0.0
8.6      3.2    CO--CO--CO--CO--CO--CO--CO--CO--
8.8      0.0
9.0      0.0
9.2      0.0
9.4      0.0
9.6     -0.9    S--S--
9.8     -0.9    S--S--

```

Figure C3: Sketched representation of the atoms arrangement on the {100} surface